

Cranfield University

Laura Chiriví

**Effect of Manufacturing Parameters on TBC
Systems Cyclic Oxidation Lifetime**

School of Applied Sciences

PhD Thesis

Cranfield University

School of Applied Sciences

PhD Thesis

Academic Year 2011

Laura Chiriví

Effect of Manufacturing Parameters on TBC Systems Cyclic Oxidation Lifetime

Supervisor: Professor John R Nicholls

December 2011

©Cranfield University 2011. All rights reserved. No part of this publication may be reproduced without the written permission of the copyright holder.

to Giuseppe

Abstract

Aero-gas turbine engines have to meet reliability, durability and fuel efficiency requirements. High turbine inlet temperatures may contribute to minimise fuel consumption and, in turn, environmental impact of the engine. Over the past few years, new designs and engine optimisation have allowed increase of such temperatures at a rate of 15°C per year, with maximum operating temperatures currently exceeding 1650°C . Ceramic coatings (also known as Thermal Barrier Coatings or TBCs) in conjunction with advanced cooling technologies are adopted to protect stator vanes and high pressure turbine blades from excessive thermal loads. Nevertheless, even with these protections in place, such components may experience a continuous service temperature of 1050°C , and peak temperatures as high as 1200°C . Therefore, it is vital that engine rotating components are able to maintain their mechanical properties at high temperature, while being able to withstand thermal loads and having sufficient oxidation resistance to preserve the integrity of the ceramic coating, and eventually reaching desired component lives.

Such strict requirements can be met with the use of complex *Thermal Barrier Coating systems* or TBC systems; these consist of a nickel-based superalloy component which is first coated with an environmental resistant layer (identified as *bond coat*) and then with a ceramic coating. As its name suggests, the bond coat must not only protect the metallic substrate against oxidation and/or corrosion but must also provide sufficient bonding of the ceramic top layer to the metallic substrate. This goal is achieved through the formation of a further layer between the bond coat and the ceramic. In gas turbine applications, such a layer (identified as *Thermally Grown Oxide* or TGO) is an alumina scale which is the result of the bond coat oxidation during the ceramic deposition.

During engine service, several time and cycle related phenomena occur within the TBC system which eventually lead the system to failure by spallation of the top coat.

This may have catastrophic consequences as the uncoated component would face temperatures higher than the melting point of the constituent metal. This is avoided by strict maintenance regimes based on the minimum expected life of the coating. While essential for safeguarding the aircraft, this approach prevents the TBC systems from being used to their full potential. This study investigates possible optimisation methods of the manufacturing process of TBC systems, with the aim of improving reproducibility in terms of time to failure, thereby extending their minimum life expectancy and reliability. Two different types of TBC systems are studied: a TBC system with a Platinum-diffused bond coat and a TBC system with a Platinum-modified aluminide bond coat. The work focuses on the effects due to modification of process parameters (varied within industrially accepted range) on the TBC systems lifetime in laboratory scale cyclic oxidation tests. Experimental results show that accurate monitoring of the metal substrate surface finish as well as of the *Pt* layer morphology and ceramic deposition temperature may result in a dramatic improvement in life expectancy of the system, up to sevenfold when compared to control samples, or threefold if compared to commercial coatings.

Acknowledgements

This research was funded by the EPSRC under the '*Luminescence Piezo-spectroscopy for Lifetime Assessment and Improvement of Thermal Barrier Coatings*' program.

I wish to thank my supervisor, Prof. John Nicholls for the advices, the scientific discussions, and the enthusiastic support during this project.

All my gratitude goes also to all the people that contributed to this work with their technical knowledge: Mr Tim Pryor, who helped with the cyclic oxidation tests and the high temperature facilities, Mr Tony Gray for his work on EB-PVD deposition, Dr Kevin Long who maintained and upgraded many of the coating equipments adopted in this work, Mr Andrew Baldwin for the samples substrate machining. Mr Andrew Dyer, Mrs Christine Kempston, Mr Colin Matthews, Dr Tracey Robers and Dr Matthew Kershaw for their support with the specimens metallographic preparation and with the analytical equipment. Dr Jeff Rao, Mr Ken Lawson, Dr Chris Show, Mr Mathew Taunt, Mr Andrew Stallard for their technical support in PVD coating manufacturing. And last but not least, I would like to acknowledge Mrs Sharon McGuire for the organizative support. I would like to acknowledge the many friends that were sharing with me the difficult journey to get a PhD and the support of which was fundamental to go through the difficulties. Finally, I would like to thank my family and my amazing husband.

Contents

Abstract	I
Acknowledgements	III
Contents	V
List of Figures	XI
List of Tables	XXIII
Acronyms	XXV
Nomenclature	XXVII
Introduction and thesis structure	1
I Literature review	6
1 Substrate alloys	7
2 Oxidation of metals	12
2.1 Oxidation process	12
2.2 Oxidation of alloys	15
2.3 Role of the alloy constituents	17
2.4 Role of sulphur	18
2.5 Oxidation testing	18
3 Diffusion coatings for oxidation resistance	20
3.1 Production of diffusion coatings	21

3.1.1	Pack cementation process	22
3.1.2	Out-of-pack process	23
3.1.3	Chemical Vapour Deposition	23
3.2	Aluminide coatings	23
3.2.1	Aluminising of Ni base alloys: microstructure and mechanism of coating formation	25
3.2.1.1	Outward diffusion coatings	26
3.2.1.2	Inward diffusion coatings	26
3.2.2	Platinum-modified aluminide coating	28
3.2.3	Mechanisms of coating degradation in service	30
3.3	Platinum-diffusion coatings	31
3.4	Physical Vapour Deposition	32
3.4.1	Evaporation	33
3.4.2	Sputtering	34
3.4.3	Ion plating	37
4	Thermal Barrier Coating	38
4.1	Ceramic top coat: material requirements	38
4.2	Stabilized zirconia alloys	39
4.3	Ceramic coating manufacture	40
4.3.1	Basic principle of EB-PVD process	41
4.3.2	EB-PVD TBC microstructure	42
4.4	Thermally Grown Oxide	47
4.5	TBC system degradation mechanisms	48
4.5.1	Erosion	48
4.5.2	Calcium-Magnesium-Alumino-Silicate (CMAS) attack	49
4.5.3	Bond coat oxidation	50
4.5.4	Residual stress	51
4.5.4.1	Stress within the TGO	51
4.5.4.2	Stress within the TBC	52
5	Life data analysis	53
5.1	Methodology	54
5.2	Collecting the life data	55
5.2.1	Types of data	56

5.3	Statistical distributions	57
5.3.1	The Weibull distribution	58
5.4	Effect of the parameters on the Weibull distribution characteristics . .	59
5.4.1	The shape parameter β	59
5.4.1.1	Influence of β on the Weibull pdf.	60
5.4.1.2	Influence of β on the reliability function	61
5.4.1.3	Influence of β on the failure rate function	62
5.4.2	The scale parameter η	64
5.4.3	The location parameter γ	64
5.5	Estimating the parameters of a distribution	65
5.5.1	The probability plotting method	65
5.5.2	The least squares method	66
5.6	Generating plots and results	67
5.7	Validating the model	68
5.8	An example of Weibull analysis	69
 II Materials and methods		71
 Introduction to the experimental procedure		71
 6 Nickel-based substrate machining		76
6.1	Substrate material characteristics	76
6.2	Substrate surface finish	76
6.2.1	Ground surface finishes	77
6.2.1.1	Coarse surface finish	79
6.2.1.2	Fine surface finish	80
6.2.2	Grit blasted surface finishes	80
6.3	Cleaning procedure	81
 7 Platinum deposition		82
7.1	Sputtering equipment	82
7.2	Platinum target and sputtering method	83
7.3	Sample holder	84
7.4	Calibration of deposition rates	84
7.4.1	Step measuring technique	85

7.4.1.1	Calibration run: substrate material	85
7.4.1.2	Calibration run: substrate preparation procedure	86
7.4.1.3	Calibration run procedure	87
7.4.2	Weight gain technique	88
7.5	Platinum deposition procedure	89
8	Bondcoat manufacturing	91
8.1	Vacuum furnace and heat treatment procedure	91
8.2	Production of a <i>Pt</i> -diffused bondcoat	92
8.3	Production of a <i>Pt</i> -modified Aluminide bondcoat	93
8.3.1	Pre-aluminising heat treatment	93
8.3.2	Aluminising by Chemical Vapour Deposition	93
8.3.2.1	CVD equipment	93
8.3.2.2	Reagents	97
8.3.2.3	CVD procedure	99
8.4	Post aluminising heat treatment	101
9	Ceramic deposition	102
9.1	Coating equipment	102
9.2	The EB-PVD substrates holders	103
9.3	The evaporation source	104
9.4	Ceramic deposition procedure	104
10	Testing methods	106
10.1	Surface texture characterisation	106
10.1.1	Profilometer	106
10.1.2	Procedure for surface texture assessment	107
10.2	Coating characterisation	108
10.2.1	Optical Microscopy	108
10.2.2	Scanning electronic microscopy (SEM) and Energy Dispersive X-ray Spectroscopy (EDS)	108
10.2.2.1	SEM samples preparation	109
10.2.3	Focused Ion Beam (FIB)	109
10.3	Cyclic oxidation	111
10.3.1	Cycling oxidation rig	111
10.3.2	Samples holder for cycling oxidation	112

10.3.3 Oxidation testing procedure	112
10.3.4 Oxidation rig programming	113
III Results and discussion	116
11 As-deposited platinum layer: coating morphology and density	118
11.1 Cartography of the platinum deposition	118
12 Effect of the platinum layer morphology on the lifetime of TBC systems with a $\gamma + \gamma'$ bond coat	122
12.1 Bond coat characterisation in as-deposited conditions	123
12.2 Oxidation test results	125
12.3 Conclusions on the role of <i>Pt</i> layer morphology on the lifetime of TBC systems with a $\gamma + \gamma'$ bond coat	129
13 Effect of the TBC deposition temperature on the lifetime of TBC systems with a $\gamma + \gamma'$ bond coat	130
13.1 Conclusions on the role of the TBC deposition temperature on the lifetime of TBC systems with a $\gamma + \gamma'$ bond coat	138
14 Influence of substrate surface preparation on the lifetime of TBC systems with a $\gamma + \gamma'$ bond coat	139
14.1 TBC systems characterisation at different stages of the manufacture	140
14.2 Cyclic oxidation test results	143
14.3 Post failure analysis	145
14.4 Conclusions on role of surface preparation on the lifetime of TBC systems with a $\gamma + \gamma'$ bond coat	148
15 Effect of substrate surface texture on the lifetime of TBC systems with a $\gamma + \gamma'$ bond coat	149
15.1 Surface texture assessment	150
15.2 Grit blasted surfaces	151
15.2.1 Before <i>Pt</i> deposition surface assessment: surface parameters versus grit blasting pressure	151
15.2.2 After <i>Pt</i> diffusion surface assessment: bond coat surface parameters versus grit blasting pressure	157

15.2.3	Surface texture evolution: comparison between substrate and bond coat surface parameters	160
15.2.4	Correlation between surface roughness parameters and TBC system lifetime	162
15.2.5	Lifetime analysis	166
15.3	Ground samples	171
15.3.1	Ground surface characterisation before <i>Pt</i> deposition	171
15.3.2	After heat treatment characterisation: bond coat surface assessment	175
15.3.3	Comparison between substrate and bond coat surface parameters in ground samples	177
15.3.4	Correlation between surface roughness parameters and TBC system lifetime	177
15.4	Conclusions on role of surface texture on the TBC system lifetime . . .	180
16	Effect of the platinum layer morphology on the lifetime of TBC systems with a <i>PtAl</i> bond coat	184
16.1	TBC system with <i>PtAl</i> bond coat	184
16.2	Bond coat characterisation in various stages of the manufacturing process	186
16.3	Post failure analysis	190
16.4	Conclusion on the role of <i>Pt</i> layer morphology on the lifetime of TBC systems with a <i>PtAl</i> bond coat	192
17	Conclusions	194
17.1	Contribution to knowledge	194
17.2	Suggestion for further work	197
	References	199
	Appendix A	217
	Appendix B	219
	Appendix C	221
	Appendix D	223

List of Figures

1	Potential benefits in gas turbines for the use of TBC: depending on operating conditions and requirements, TBC can improve engine performance and thrust as well as component lifetime [1]	2
2	Illustration of a typical coating system for a high pressure turbine blade. In red the schematic profile of temperature is highlighted; the drop of temperature close to the blade surface is due to the presence of a thin cooling air film [2]	3
3	SEM micrographs of the cross section of a TBC system with a <i>Pt</i> -diffused bond coat (A), and of a TBC system with a <i>Pt</i> -modified aluminide bond coat (B).	4
1.1	The different materials used in a Rolls Royce jet engine: titanium based superalloy (blue), nickel based superalloys (red), steel (orange), aluminium based alloy (yellow), composites (green) [3]	7
1.2	Temperature capability for several classes of alloys, adapted from [4]	8
2.1	Ellingham diagram of free energy of formation of oxides as a function of temperature [5, 6]	14
2.2	Binary alloy oxidation: A is more noble than B but B is more reactive than A. (a) B is diluted in A and oxidation results in the formation of BO precipitates dispersed in A. (b) B is concentrated in A and the amount of B is sufficient to form a continuous scale of BO. Adapted from [7].	16
2.3	Binary alloy oxidation: A and B form stable oxides but BO is more stable than AO. (a) B is diluted in A and the oxidation results in the formation of an outer layer of AO and an inner layer of BO precipitates dispersed in A. (b) B is concentrated in A and the amount of B is sufficient to form a continuous scale of BO. Adapted from [7].	16

3.1	Schematic diagram of a CVD process for co-deposition of Hf , Si and Al [8].	24
3.2	Schematic representation of the microstructure of a $NiAl$ outward diffusion coating (low activity process) [9]	26
3.3	nickel-Aluminum binary phase diagram [10]	27
3.4	Inward diffusion coating: formation of a $NiAl$ coating from a Ni_2Al_3 layer by diffusion heat treatment [9]	28
3.5	Schematic microstructures of different Pt -modified aluminide coatings, adapted from [11]	29
3.6	SEM micrographs showing degradation by rumpling of a Pt -modified aluminide coating, cyclically tested in air at a temperature of $1200^\circ C$ (one-hour cycles): (a) after 1 cycle; (b) after 10 cycles; (c) and (d) after 50 cycles [12].	31
3.7	Schematic representation of a planar diode sputtering process	34
3.8	Schematic of planar magnetron sputtering, showing the principle of trapping electrons to increase ionisation efficiency [13]	36
4.1	Phase diagram of $Zr_2O_3 - YO_{1.5}$ system adapted from Yashima <i>et al.</i> [14]	40
4.2	TBC microstructure: a) Columnar microstructure of a ceramic top coat manufactured by EB-PVD [15] b) Lamellar microstructure of a ceramic top coat manufactured by air plasma spray [16]	41
4.3	Schematic representation of an EB-PVD process; the whole assembly is under vacuum. A magnetic field is adopted to bend the path of the generated electron beam in order for it to focus on the source material [2]	42
4.4	Schematic of the TBC pores morphologies and spatial arrangements [17]	43
4.5	Movchan <i>et al.</i> structure zone model; T : substrate temperature, T_m : coating material melting point in K [18]	44
4.6	Model proposed by Thornton for sputtered metal coatings [19]	45
4.7	Schematic representation of the influence of rotational speed and absolute substrate temperature (expressed as a fraction of zirconia melting point T_m) on columnar microstructure evolution of EB-PVD TBCs [20].	45
4.8	SEM of the structure of zirconia columns taken in cross section in the plane perpendicular to the axis of rotation [21]	46
4.9	Schematic drawing of the rotation stage over the melt pool in the EB-PVD coater [22]	47

4.10	Cross-section SEM images of a TBC after exposure to CMAS at 1300°C for 4 hours. a) severe attack at the outer TBC surface; b) attack at the TBC/bond coat interface [23]	50
5.1	Probability density function, $f(t)$	57
5.2	Influence of the shape parameter β on the shape of the Weibull distribution function. In the diagram the three curves are plotted for $\beta < 1$, $\beta = 1$ and $\beta > 1$. The values of the other two parameters of the distribution are $\eta = 1$ and $\gamma = 0$	60
5.3	Effect of the shape parameter on the Weibull reliability function. $R(t)$ is plotted for three different values of β while the $\eta = 1$ and $\gamma = 0$	61
5.4	Effect of different values of β in the interval $]1, \infty[$ on the $R(t)$	62
5.5	Effect of the β value on the Weibull failure rate functions. In the diagram the three curves are plotted for $\beta < 1$, $\beta = 1$ and $\beta > 1$; the values of the other two parameters of the distribution are fixed to $\eta = 1$, and $\gamma = 0$	62
5.6	Effect of values of $\beta \in]1, \infty[$ on the failure rate. $\lambda(t)$ was plotted for $1 < \beta < 2$, $\beta = 2$ and $\beta > 2$; the values of the other two parameters of the distribution are fixed to $\eta = 1$, and $\gamma = 0$	63
5.7	Effect of the scale parameter on the Weibull pdf for fixed value of β and γ ; in particular $\beta = 3$ and $\gamma = 0$	64
5.8	Effect of a positive location parameter γ on the Weibull pdf.	65
5.9	Two different minimisations can be performed: A) Minimization in the vertical direction; B) Minimization in the horizontal direction.	66
5.10	Example of Weibull analysis. The diagram illustrates how/where to read β , η , and the B(10)life directly on the plot.	69
5.11	Flowchart ‘Level 0’: General description of the TBC systems production process	73
5.12	Flowchart ‘Level 1’: General description of the TBC systems production process	75
6.1	CMSX-4 coupons: A) Square coupons; B) Irregular shape coupons.	77
6.2	Grinding machine set up	78
6.3	Two CMSX-4 coupons fixed with wax on top of the component grinding support. A reference surface was used to simplify the alignment of one of the coupon edge with the rotation axis of the grinding wheel.	78

7.1	Sputtering apparatus overview	82
7.2	Samples holder for platinum deposition	84
7.3	Step measuring technique: substrate preparation procedure. A) Samples bonded to the aluminium plate. B) Automatic polishing machine . . .	86
7.4	Nimonic 75 coupons ready for the calibration run. A) The coupons surface is polished to ‘mirror finish’ and it is partially covered with Kapton® tape; B) Twenty-three Nimonic 75 coupons positioned in the samples holder.	87
7.5	A) Dektak® working principle. B) Typical step profile obtained with the Dektak®	87
8.1	Vacuum furnace chamber. The samples, loaded on the alumina plate, are placed between the two L-shaped carbon electrodes.	92
8.2	Bell Furnace on its trolley	94
8.3	Station A opened. A) Chamber bell shaped lid; B) Stand and the retort positioned on the chamber base	94
8.4	Stand	95
8.5	Retort. A) Retort closed; B) View from the top of the opened retort before loading the aluminising reagents and the tray with the samples. The picture shows: the sealing channel full of alumina granules, the three spacer bars and the ring shaped gases feeder; C) View from the top of the opened retort after loading. In the picture, the tray is the fully welded mesh and ring assembly. Underneath the tray, through the tray mesh, it is possible to see the aluminising reagents.	96
8.6	CVD equipment overview: the picture shows both the Station A and the five inlet/exit gases lines connected to it. (Adapted from material courtesy of Dr K. Long)	98
8.7	Aluminium-chromium alloy (40%Cr-60%Al) chips	99
9.1	EB-PVD working chamber layout. A) Two substrate holders fixed on the deposition chamber back wall, perpendicularly to the ceramic ingot. The red arrow indicates the rotation direction. B) The arc-shaped furnace placed over the sample holders.	103
9.2	EB-PVD substrates holders	104
10.1	Schematic representation of the profilometer while measuring a surface	106

10.2	Schematic of the interactions between the gallium ion beam (Ga^+) and the sample surface	110
10.3	Samples holder outside the furnace in the ‘cold position’: it is surrounded by four vertical nozzles connected to four electric fans.	112
10.4	Temperature evolution during a 79 minute cycle for the three thermocouples. ‘Sample-TC top’ and ‘Sample-TC bottom’ are the two signals recorded by the thermocouples welded to the samples on the top and middle plates, respectively. ‘Plain-TC top’ is the signal recorded by the thermocouple in the centre of the samples holder.	114
10.5	Details of the heating and cooling curves	114
11.1	Samples holder (left) and diagram with the cartography of a typical Pt deposition (right). In the diagram, samples positions are represented as squares, colour coded according to the Pt thickness obtained.	119
11.2	Micrographs of the topography (top row) and of FIB-milled sections (bottom row) of the as-deposited Pt layer on CMSX-4 substrate grit blasted at $0.2MPa$: Dense structure (A and B); Open structure (C and D); Electroplated Pt coating (E and F).	120
12.1	SEM micrographs of the DHR Pt structure on a ground surface after heat treatment: coating top surface (A) and cross section (B).	124
12.2	Oxidation test results for TBC systems with a Pt -diffused bond coat as a function of the Pt layer structure (DHR, open, or DLR) for two different substrate surface finishes ($0.2MPa$ or ground surface). For each TBC system, the number of specimens tested, the average, maximum and minimum lifetime values (expressed as number of oxidation cycles) are reported.	126
12.3	Weibull plots of the influence of the Pt layer morphology on the lifetime of TBC systems with grit blasted substrates and Pt -diffused BC. For each Weibull plot, the table reports the values of: β , η , B(10)life and R^2	128
13.1	Lifetime, expressed as average, maximum and minimum for each of the seven EB-PVD TBC run, as a function of the average ceramic deposition temperature.	131

13.2	Lifetime analysis conducted on a population of samples including specimens studied in the present work (<i>Cranfield data</i>) and results extrapolated from literature (<i>Wu et al. data</i> [24])	133
13.3	SEM micrographs of the top surface of TBC deposited at three different temperature: A) 1256K, B) 1278K, C)1289K.	133
13.4	Weibull plots of different families of samples, classified according to the nominal ceramic deposition temperature.	134
13.5	Weibull shape parameter versus TBC deposition temperature. The solid line in the diagram is an interpolation of the experimental data (β_{1276} and β_{1291}) while the dashed line is a linear extrapolation of the data to determine β_{1256}	135
13.6	Variation of characteristic life and B(10)life as function of the TBC deposition temperature	136
14.1	3D optical images of a ground (left) and grit blasted (right) substrate surface	141
14.2	SEM micrographs of the cross section of a $\gamma + \gamma'$ bond coat deposited on a ground surface (A) and on a grit blasted surface (B). The latter micrograph shows the presence of dark inclusions at a distance of approximately 50% from the TGO/bond coat interface. Such inclusions are residues of the alumina grits used during the substrate blasting process.	141
14.3	EDX compositional analysis of the cross section of a $\gamma + \gamma'$ bond coat deposited on a ground surface (A) and on a grit blasted surface (B). . .	142
14.4	SEM micrographs of the top surface of a EB-PVD TBC deposited on three different surfaces: A) fine ground surface; B) coarse ground surface; C) grit blasted surface.	143
14.5	Average lifetime as a function of surface preparation. Each column corresponds to a single type of surface and reports average, maximum, and minimum values of lifetime expressed as a number of cycles to failure. Columns are colour coded according to the category to which the type of surface belongs: ground, polished and grit blasted or grit blasted only.	144

14.6	Average lifetime as a function of the TBC deposition temperature for four different surface finishes. Each column reports the number of specimens tested as well as the average, maximum and minimum values of lifetime expressed as number of cycles to failure. Columns are colour coded according to the pressure adopted during the blasting procedure.	145
14.7	Post failure SEM analysis of a TBC system with a ground surface: A) substrate exposed surface and B) bottom side of the ceramic spalled fragment.	146
14.8	SEM micrographs of the cross section of a TBC system with a fine ground surface (A) and a coarse ground surface (B).	147
14.9	Post failure SEM analysis of a TBC system with a grid blasted surface: A) substrate exposed surface and B) bottom side of the ceramic spalled fragment.	147
15.1	Root mean square roughness (R_q) value of the grit blasted samples before <i>Pt</i> deposition: each column corresponds to one sample and plots the average, minimum and maximum R_q value.	152
15.2	Tortuosity (τ) value of the grit blasted samples before <i>Pt</i> deposition: each column corresponds to one sample and plots the average, minimum and maximum τ value.	152
15.3	Root mean square average wavelength (Rlq) value of the grit blasted samples before <i>Pt</i> deposition: each column corresponds to one sample and plots the average, minimum and maximum (Rlq) value.	153
15.4	R_q (measured before <i>Pt</i> deposition) for three batches of coupons plotted as a function of grit blasting pressure	154
15.5	τ (measured before <i>Pt</i> deposition) for three batches of coupons plotted as a function of grit blasting pressure	154
15.6	Rl_q (measured before <i>Pt</i> deposition) for three batches of coupons plotted as a function of grit blasting pressure	155
15.7	Profiles of a 0.05MPa surface (A) and of a 0.4MPa surface (B). The measures are in microns	156
15.8	Secondary electrons micrographs of the 0.05MPa surface (A) and of the 0.4MPa surface (B) inclined by 45°	156

15.9	R_q value of the grit blasted samples after heat treatment; each column corresponds to one sample and report the average, the minimum and the maximum R_q value.	158
15.10	Tortuosity (τ) value of the grit blasted samples after Pt diffusion: each column corresponds to one sample and plots the average, minimum and maximum τ value.	159
15.11	Root mean square average wavelength (Rlq) value of the grit blasted samples after Pt diffusion: each column corresponds to one sample and plots the average, minimum and maximum (Rlq) value.	159
15.12	R_q (measured after Pt diffusion) for three batches of coupons plotted as a function of the pressure adopted to grit blast the substrate before Pt deposition	160
15.13	τ (measured after Pt diffusion) for three batches of coupons plotted as a function of the pressure adopted to grit blast the substrate before Pt deposition	161
15.14	Rlq (measured after Pt diffusion) for three batches of coupons plotted as a function of the pressure adopted to grit blast the substrate before Pt deposition	161
15.15	Increment of the R_q value for three batches of coupons. The increment is determined as the difference between the R_q measured after Pt diffusion and the corresponding value measured before Pt deposition. ΔR_q is plotted as a function of the pressure adopted to grit blast the coupons before sputtering the Pt	162
15.16	Increment of the τ value for three batches of coupons. The increment is determined as difference between the τ measured after Pt diffusion and the corresponding value measured before Pt deposition. $\Delta\tau$ is plotted as a function of the pressure adopted to grit blast the coupons before sputtering the Pt	163
15.17	Increment of the Rlq value for three batches of coupons. The increment is determined as difference between the Rlq measured after Pt diffusion and the corresponding value measured before Pt deposition. ΔRlq is plotted as a function of the pressure adopted to grit blast the coupons before sputtering the Pt	163
15.18	Variation of the TBC system lifetime as a function of the substrate surface Rlq , for three different TBC deposition temperatures.	164

15.19 Weibull plots including the lifetime of specimens with $Rlq < 15$ (empty symbol) and $15 < Rlq < 22$ (filled symbol). Ceramic deposition temperature was 1276K. For each Weibull plot, the table reports the values of β , η , B(10)life and R^2	167
15.20 Weibull plot including the lifetime of specimens with $22 < Rlq < 36$; the plot includes specimens which were coated at three different TBC deposition temperatures. The table reports the values of β , η , B(10)life and R^2	168
15.21 Weibull plots including the lifetime of specimens with $36 < Rlq < 43$ (empty symbol) and $Rlq < 43$ (filled symbol); each plot includes specimens coated at three different TBC deposition temperatures. For each Weibull plot, the table reports the values of β , η , B(10)life and R^2 . . .	169
15.22 Characteristic life and B(10)life for the Weibull distribution as a function of Rlq intervals	170
15.23 Shape parameter for the Weibull distribution as a function of Rlq intervals	171
15.24 Weibull plots including the lifetime of specimens with $22 < Rlq < 36$; each plot includes specimens which were coated at a similar TBC deposition temperatures. For each Weibull plot, the table reports the values of β , η , B(10)life and R^2	172
15.25 Characteristic life and B(10)life for the Weibull distribution for the five Rlq intervals and for three different TBC deposition temperature . . .	173
15.26 Shape parameter for the Weibull distribution for the five Rlq intervals and for three different TBC deposition temperature	173
15.27 R_q value of the ground samples before Pt deposition; each column corresponds to one sample and report the average, the minimum and the maximum R_q value.	174
15.28 Rlq value of the ground samples before Pt deposition; each column corresponds to one sample and report the average, the minimum and the maximum Rlq value.	174
15.29 τ value of the ground samples before Pt deposition; each column corresponds to one sample and report the average, the minimum and the maximum τ value.	175
15.30 R_q value of the ground samples after heat treatment; each column corresponds to one sample and reports the average, the minimum and the maximum R_q values.	176

15.31	τ value of the ground samples after heat treatment; each column corresponds to one sample and reports the average, the minimum and the maximum τ values.	176
15.32	Rlq value of the ground samples after heat treatment; each column corresponds to one sample and reports the average, the minimum and the maximum Rlq values.	177
15.33	Comparison of R_q (averaged for fine and coarse surface finish) measured before Pt deposition and after heat treatment	178
15.34	Comparison of τ (averaged for fine and coarse surface finish) measured before Pt deposition and after heat treatment	178
15.35	Comparison of Rlq (averaged for fine and coarse surface finish) measured before Pt deposition and after heat treatment	179
15.36	Variation of the TBC system lifetime as a function of the substrate surface Rlq for ground specimens.	180
15.37	Weibull plots including the lifetime of fine and coarse ground specimens. For each Weibull plot, the table reports the values of β , η , B(10)life and R^2	181
16.1	Oxidation test results for TBC systems with a $PtAl$ bond coat as a function of the Pt layer structure (DHR, open, or DLR) for two different substrate surface finishes (0.2MPa grit blasted and ground surface). For each TBC system, the number of specimens tested, the average, maximum and minimum lifetime values (expressed as number of oxidation cycles) are reported.	186
16.2	SEM micrographs of the coating cross section at various stages of the manufacturing process. Proceeding from the top row to the bottom, the pictures show: the coating after Pt deposition and pre-aluminising heat treatment, after aluminising and at the end of $PtAl$ bond coat manufacturing (therefore after post-aluminising heat treatment). Pictures A, B, C (left column) are relative to specimens with a DHR Pt structure while picture D, E, F (right column) are relative to specimens with an open Pt structure.	187

16.3	EDX compositional analysis of the cross sections of specimens with either a DHR or an open <i>Pt</i> structure at two different stages of the bond coat production: after <i>Pt</i> deposition and heat treatment at 1040°C (A and D) and at the end of <i>PtAl</i> bond coat manufacturing (C and F). Pictures A and C (left column) are relative to specimens with a DHR <i>Pt</i> structure while picture D and F (right column) are relative to specimens with an open <i>Pt</i> structure.	189
16.4	Cross section micrograph of the failed specimens. A) <i>PtAl</i> bond coat with a DHR <i>Pt</i> structure B) <i>PtAl</i> bond coat with an open <i>Pt</i> structure	191
16.5	Damage evolution in a <i>PtAl</i> bond coat with a dense <i>Pt</i> structure. In the first stage, isolated voids are formed along the original grit line, with fully bonded material between them. With thermal cycling and/or oxidation time the voids grow and merge together. The voids surface oxidise due to oxygen penetration into the coating from the coating edges. Subsequently, the volume increase due to the oxidation causes the coating to swell until failure.	192
17.1	Root mean square roughness (R_q) value of the polished plus grit blasted samples before <i>Pt</i> deposition: each column corresponds to one sample and plots the average, minimum and maximum R_q value	217
17.2	Tortuosity (τ) value of the polished plus grit blasted samples before <i>Pt</i> deposition: each column corresponds to one sample and plots the average, minimum and maximum τ value.	218
17.3	Root mean square average wavelength (Rlq) value of the polished plus grit blasted samples before <i>Pt</i> deposition: each column corresponds to one sample and plots the average, minimum and maximum (Rlq) value.	218
17.4	Root mean square roughness (R_q) value of the polished plus grit blasted samples after <i>Pt</i> diffusion: each column corresponds to one sample and plots the average, minimum and maximum R_q value	219
17.5	Tortuosity (τ) value of the polished plus grit blasted samples after <i>Pt</i> diffusion: each column corresponds to one sample and plots the average, minimum and maximum τ value.	220
17.6	Root mean square average wavelength (Rlq) value of the polished plus grit blasted samples after <i>Pt</i> diffusion: each column corresponds to one sample and plots the average, minimum and maximum (Rlq) value.	220

17.7	Variation of the TBC system lifetime as a function of the substrate surface R_q , for three different TBC deposition temperatures	221
17.8	Variation of the TBC system lifetime as a function of the substrate surface τ , for three different TBC deposition temperatures	222
17.9	Variation of the TBC system lifetime as a function of the substrate surface R_q	223
17.10	Variation of the TBC system lifetime as a function of the substrate surface τ	224

List of Tables

1.1	Nominal composition in weight percentage of four generations of commercially available single crystal <i>Ni</i> -base superalloys (nickel content is to balance)	11
3.1	Commercially available <i>Pt</i> -modified aluminide coatings	29
5.1	List of operations that were carried out, on the specimens, between two consecutive manufacturing steps	75
6.1	Nominal composition (wt%) of CMSX-4 [25]	76
6.2	FEPA identification for the two grinding wheels adopted in the program. The achieved type of surface finish is indicated in the top row.	79
7.1	NIMONIC alloy 75 chemical composition (wt%) (Special metals)	85
7.2	Polishing procedure	86
8.1	Heat treatment procedure	92
8.2	Aluminising process divided into phases. For each phase are indicated: sample temperature, position of the furnace, gas flows, in the retort and in the chamber.	100
9.1	Dimensions and nominal chemical composition of Y-PSZ ingot	104
10.1	Heating and cooling rate during the first and last 3 minutes of the cycle, recorded for the three thermocouples. Identification of the thermocouple position is described in figure 10.4.	115
11.1	Sputtering parameters and deposition run characteristics to deposit a nominal $10\mu m$ coating thickness	119

12.1	Results of visual inspection of coatings after diffusion: the DHR coating, when deposited on ground surface, was affected by blistering. The <i>Pt</i> with an open structure was not deposited on samples with a ground surface.	123
12.2	Roughness parameters values for a ground and grit blasted surface finish; the chosen set of parameters is the one usually adopted to describe surfaces.	124
13.1	Details of the EB-PVD runs carried out for depositing TBC on 26 specimens with a <i>Pt</i> -diffused bond coat	131
14.1	Summary of specimens surface preparation including total number of samples manufactured for each surface finish and samples identification codes	140
16.1	Results of visual inspection of the coating after diffusion: the dense high rate coating, when deposited on the ground surface, failed the inspection due to the presence of blisters. The <i>Pt</i> with an open structure was not deposited on ground surface.	185
16.2	Average composition of the cross section of coatings, with either a DHR or an open <i>Pt</i> structure, at different stages of the bond coat manufacture. The EDX analysis was performed on areas of the coatings having a $10\mu m$ x $5\mu m$ dimension and set at a distance of $5\mu m$ from the coating surface. The coating composition was determined as the average composition over three areas.	190

Acronyms

BC	Bond Coat
CBN	Cubic Boron Nitride
cdf	cumulative distribution function
CMAS	Calcium-Magnesium-Alumino-Silicate
CMC	Ceramic Matrix Composite
CMSX	Cannon Muskegon Single Crystal
CTE	Coefficient of Thermal Expansion
CVD	Chemical Vapour Deposition
DC	Direct Current
DHR	Dense High Rate
DLR	Dense Low Rate
DOC	Depth of Cut
EB	Electron Beam
EB-PVD	Electron Beam Physical Vapour Deposition
EZ	External Zone
FCC	Face Centered Cubic
FEPA	Fédération Européenne des Fabricants de Produits Abrasifs
FIB	Focussed Ion Beam
FOD	Foreign Object Damage
FSZ	Fully Stabilized Zirconia
HP	High Pressure
IDZ	Interdiffusion Zone
IG	Inward Grown
MFC	Mass Flow Controller
OG	Outward Grown
pdf	probability density function

PLPS	Photoluminescence Piezo Spectroscopy
PSZ	Partially Stabilized Zirconia
PTM	Pressure type machine
PVD	Physical Vapour Deposition
RF	Radio Frequency
TBC	Thermal Barrier Coating
TCP	Topologically Close-Packed phase
TGO	Thermally Grown Oxide
Y-FSZ	Yttria Fully Stabilized Zirconia
Y-PSZ	Yttria Partially Stabilized Zirconia
WEDM	Wire Electrical Discharge Machining

Nomenclature

β	Shape parameter in the Weibull distribution
B(10)life	Estimated time when the probability of failure will reach 10%
γ	Location parameter in the Weibull distribution
γ	Gamma phase
γ'	Gamma prime phase
η	Characteristic life in the Weibull distribution
<i>PtAl</i>	<i>Pt</i> -modified aluminide
R_a	Arithmetical mean deviation of the roughness profile
R_q	Root mean square deviation of the roughness profile
R_v	Maximum roughness profile valley depth
R_p	Maximum roughness profile peak height
R_{sk}	Skewness of the roughness profile
R_{ku}	Kurtosis of the roughness profile
RSm	Mean width of the roughness profile elements
Rlq	Root mean square average wavelength of the roughness profile
t	Nominal layer thickness
τ	Tortuosity

Introduction and thesis structure

A gas turbine engine has to be not only reliable, economical on fuel and profitable but also environmentally acceptable. The pressure in this sector is so high that in March 2000 the European Commission has launched a large program, '*Efficient and Environmentally Friendly Aircraft Engine (EEFAE)*', aiming at mitigating the impact of aviation on the global warming and climate change [26, 27]. The project pursued the validation of new technologies that would allow a reduction of emission of carbon dioxide (CO_2) by 20% and nitrogen oxides (NO_x) by 80% relatively to the ICAO¹ 1996 standard. This means that future aircraft gas turbine engines must provide increasing cycle performance at reduced weight (i.e. increased thrust to weight ratio), which will minimize fuel consumption and consequently reduce emission of greenhouse gases. Producing more thrust while burning less fuel translates into increasing the operating temperatures within the turbine section of the engine. In modern gas turbine such temperature can exceed $1650^\circ C$, with cooled components reaching temperatures as high as $1200^\circ C$. To meet the engine performance, while operating in such environment, the alloys used for parts construction must be able to maintain their mechanical properties up to extraordinary high temperatures. Creep, fatigue and tensile strength are optimised for maximum load-carrying capability, usually at the expense of the alloys environmental resistance. As a consequence, the structural material of a component exposed to the high pressure turbine environment will quickly degrade due to oxidation, corrosion and cyclic fatigue.

Overall protection against heat-related damage can be provided by *environmental resistant coatings*. These are produced by means of specialised surface treatments of the structural material and provide a barrier between the alloy and the outer environment. Such coatings do not need to have load-bearing capability, and their composition and properties can be tailored to meet specific environmental resistance requirements. A

¹International Civil Aviation Organization

further contribution to the reduction of the heat damage to the alloy is provided by TBCs, which allow a reduction in the overall metal surface temperature. This class of ceramic coatings provides thermal insulation for the component, allowing a high thermal gradient to be subtended across the coating thickness.

Although reducing the metal surface temperature results in an increment of the component life without sacrificing the performance of the turbine, more often TBCs are applied to either improve the engine performance or the thrust to weight ratio (see figure 1). Thermal Barrier Coatings, in fact, offer the potential of either reducing the cooling air flow by about 36%, whilst maintaining the operating temperature of the turbine, or increasing the turbine entry temperature up to 150°C without any increase in the metal surface temperature [28, 29].

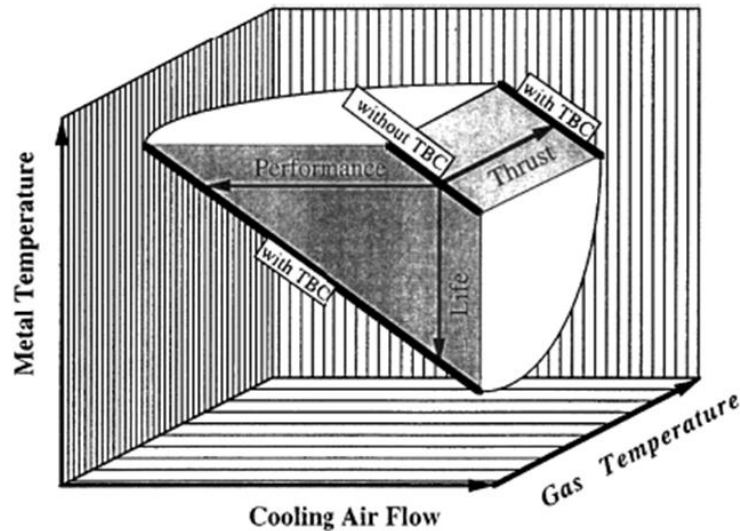


Figure 1: Potential benefits in gas turbines for the use of TBC: depending on operating conditions and requirements, TBC can improve engine performance and thrust as well as component lifetime [1]

Due to the thermal mismatch between the ceramic and the component structural material, TBC cannot be deposited directly on bare alloys. To provide the necessary adhesion, the ceramic is deposited on the metal component as the top layer of a complex structure called TBC system. This consists of three layers, two ceramics and one metallic, which are, from the metallic substrate outwards: bond coat, Thermally Grown Oxide (TGO) and TBC (figure 2). The bond coat and the TBC are deliberately deposited on the metal substrate, while the TGO is the result of bond coat oxidation during the TBC deposition.

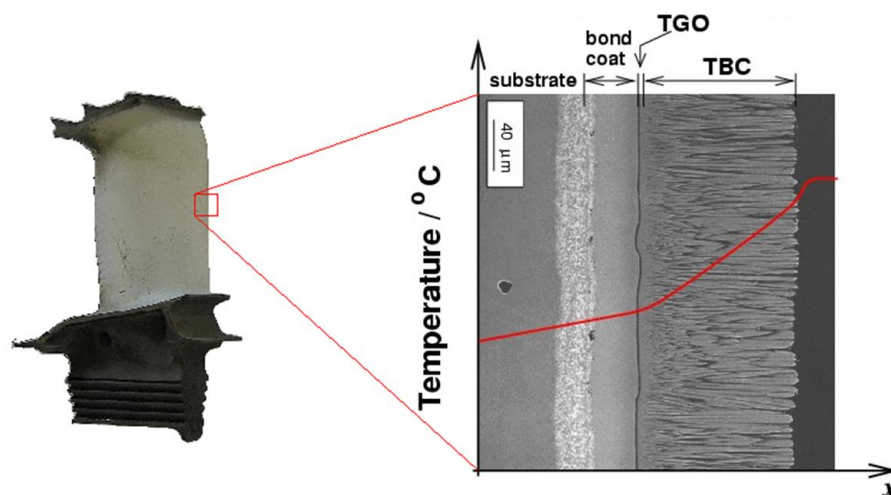


Figure 2: Illustration of a typical coating system for a high pressure turbine blade. In red the schematic profile of temperature is highlighted; the drop of temperature close to the blade surface is due to the presence of a thin cooling air film [2]

Purpose and structure of the thesis

During engine operations, several time and cycle related phenomena occur within the TBC system which eventually result in the system failure by spallation of the top coat. Moreover, TBC systems show a large variability in time to failure which prevents the use of these coatings to their full potential. A possible approach to meet the requirements for higher durability, reproducibility and energy efficiency is the development of both new substrate and coating materials. The approach adopted in this study, instead, consists of optimizing the existing TBC systems manufacturing process. Two types of TBC systems were studied: a TBC system with a *Pt*-diffused bond coat and a TBC system with a *Pt*-modified aluminide bond coat; the two systems are shown in figure 3A and B, respectively. The production of these systems involved several steps which were entirely carried out within the National High Temperature Surface Engineering Centre facilities in Cranfield University. The optimization process was articulated in two phases:

1. studying the effect that a variation in one or more process parameters, for each manufacturing step, has on the TBC system lifetime measured in cyclic oxidation test;
2. modelling, where possible, the life data with Weibull distribution in order to

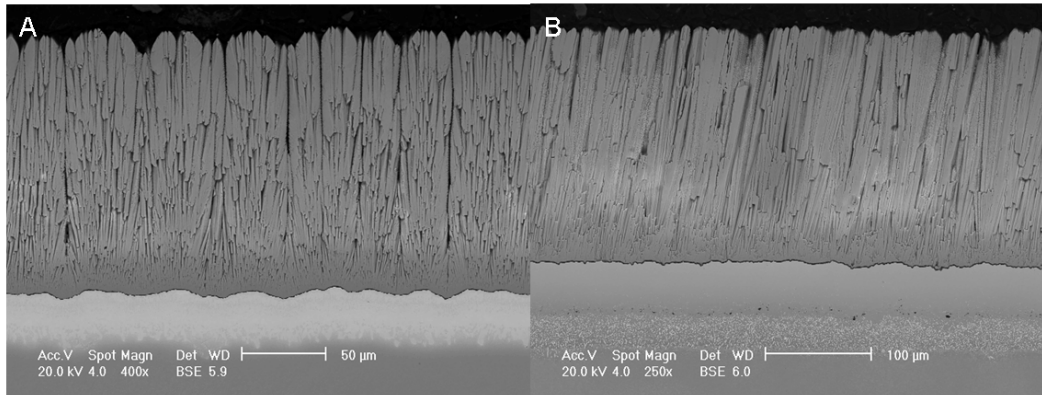


Figure 3: SEM micrographs of the cross section of a TBC system with a *Pt*-diffused bond coat (A), and of a TBC system with a *Pt*-modified aluminide bond coat (B).

quantify the TBC system durability and reproducibility.

Given the complexity of the processes and manufacturing procedures analysed in this thesis, as well as the large number of variables and parameters investigated, it was decided to organize the document into three Parts, each comprised of several chapters, rather than according to the more ‘classical’ layout. This has given the author the possibility of addressing relevant topics and aspects independently, hopefully improving the thesis clarity and accessibility. The document overall structure is as follows:

Part I consists of the literature review, which provides a theoretical background to the present study and discusses the state-of-the-art in high temperature coating manufacturing and their degradation mechanisms, mainly focussing on the processes relevant to the specific systems investigated in this work. This thesis does not aim to provide an exhaustive review on the knowledge of production and degradation of coatings in general. An overview of the methods adopted for the statistical analysis of life data is also presented.

Part II describes the experimental procedure followed to develop, produce, test, and characterise the two types of TBC systems studied. Each step is independently addressed in a separate chapter, from chapter 6 to 10. Due to the complexity of the manufacturing process, an ‘*Introduction to the experimental procedure*’ has been added too, in order to provide an overview of the whole manufacturing procedure.

Part III collects several chapters presenting and discussing the experimental results. Each chapter in this section is dedicated to a single process parameter which was found to have an effect on the life of the coating system. The performance of the custom made TBC systems are evaluated and when possible compared to that of commercial TBC systems.

Part I

Literature review

Chapter 1

Substrate alloys

Despite Goulette's forecasts regarding the gas turbine materials usage [30], and despite the increasing interest in ceramic matrix composites (CMCs), both for rotating and static components [31], four classes of alloys based on the metals aluminium, iron, titanium and nickel continue to be the major constituents of aero engines (figure 1.1). Figure 1.2 shows the density-corrected strengths for these four groups of alloys as a

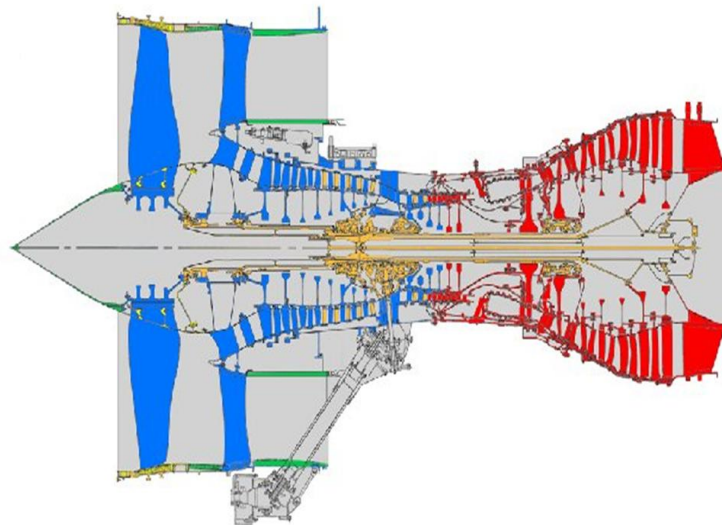


Figure 1.1: The different materials used in a Rolls Royce jet engine: titanium based superalloy (blue), nickel based superalloys (red), steel (orange), aluminium based alloy (yellow), composites (green) [3]

function of the temperature. Aluminium and *Al*-base alloys cannot be used for high temperature applications due to the relatively low melting point of the pure metal (660°C) and to the limited temperature capability of its alloys. Titanium is a very

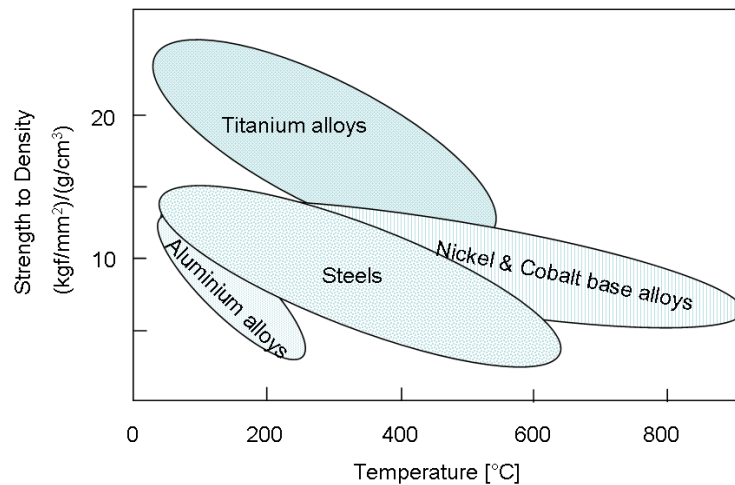


Figure 1.2: Temperature capability for several classes of alloys, adapted from [4]

attractive alloy base metal due to its low density ($4.54 \frac{g}{cm^3}$, about 40% less than steel, cobalt and nickel based superalloys), high melting point ($1668^\circ C$), and excellent corrosion resistance. *Ti*-base alloys exhibit high strength and low density, therefore they are adopted for manufacturing fan and compressor blades of gas turbine engines. When exposed to a temperature above $600^\circ C$, titanium alloys tend to form interstitial phases which compromise the mechanical properties, making these alloys unsuitable for high temperature applications. Steel is an iron-carbon alloy which has a carbon content between $0.2wt\%$ and $2.1wt\%$, depending on the grade. To achieve a broad range of physical and structural properties, various alloying elements (e.g. *Cr*, *Mo*, *Ni*, *V*, *Ti*) besides carbon are added to the alloy. For low temperature applications, steels are preferred to *Ni*-base alloys because of their comparable mechanical properties and lower price. At higher temperature the density-corrected strengths of these alloys drops below those of *Ni*-base superalloys; therefore for applications under stressed conditions steels are adopted up to $650^\circ C$.

A material for load-bearing applications at high temperature is required to have high strength and to maintain it across a wide range of temperatures. Only two types of alloys satisfy such requirements: cobalt and nickel based superalloys, the latter being best suited for aeroengine applications. Nickel is characterized by high melting point ($1455^\circ C$) and face centered cubic (FCC) crystal structure, which makes the pure metal suitable for extensive alloying. *Ni*-base superalloys have two essential alloying constituents: aluminium and/or titanium, with a typical total concentration below $10at\%$. These solutes generate a two-phase equilibrium microstructure consisting of a matrix,

γ – phase, which is strengthened by the precipitation of a second phase: γ' – phase.

The γ – phase is a solid solution with a FCC crystal structure. Several alloying elements such as *Cr*, *Co*, *Fe*, *Mo*, *Ta*, *W*, and *Re* dissolve in the γ – phase randomly replacing the *Ni* atoms without changing the crystal structure. Due to the difference in size between the solute atoms and the *Ni* atoms, a stress field is generated inside the matrix impeding the dislocation motion and increasing the strength of the alloy. However, the main phase responsible for the elevated-temperature strength of the *Ni*-base superalloys and their outstanding resistance to creep deformation is the precipitation of the γ' – phase into the γ matrix.

The γ' – phase is an intermetallic compound with $L1_2$ crystal structure (ordered FCC). *Al* or *Ti* atoms are placed at the vertices of the cubic cell and form the sublattice A. *Ni* atoms are located at the centre of each face and form the sublattice B. This atomic arrangement corresponds to the chemical formula Ni_3Al , Ni_3Ti , or $Ni_3(Al, Ti)$. The phase is not strictly stoichiometric; deviations from stoichiometry result from an excess of vacancies which may exist in one of the two sublattices. Sublattices A and B of the γ' – phase can accommodate a considerable proportion of other elements: the *Ni* sites may also contain *Co*, *Cr* and *Mo* while the *Al* sites may contain *Hf*, *Ta*, and *Nb*.

The phases γ' and γ do not share only the same cubic structure but also similar lattice parameters, therefore γ' precipitates in a cube-cube relationship with γ . This means that the edges of the γ' cell are exactly parallel to the corresponding edges of the γ phase. Besides, due to the similarity in the lattice parameters, γ' is coherent¹ with the γ matrix when the precipitate size is small. Coherent interfaces have low energy, hence the precipitates have little driving force to grow in size. The presence of these fine and hard precipitates, over a wide range of temperatures, results in the impediment for dislocation motion and in the increment in strength of the alloy.

The size and the volume fraction of γ' in the alloy affect the creep and the fatigue strength of the material. The precipitates size ranges between $0.2\mu m$ and $0.5\mu m$ and their shape evolves from a spherical morphology for the smallest size to the cuboidal morphology for the largest size. Depending on the application, the minimum volume fraction of γ' in the alloy may range from 0.2, when the alloy is designed for service at relatively low temperatures (e.g. $750^\circ C$), to 0.6, in turbine blades for modern turbine engines [32].

To further improve their high temperature capability, over the years the *Ni*-base

¹A precipitate whose crystal structure and atomic arrangement has a continuous relationship with the matrix from which the precipitate is formed is defined as coherent.

superalloys evolved from wrought to cast, then to directionally solidified alloys and finally to single crystal material [15, 33]. When adopted for turbine blade manufacturing, the *Ni*-base superalloys in polycrystalline form tend to fail along the grain boundaries orientated transversely to the blade axis which is the direction of the centrifugal force of rotation. The creep properties of the alloy improved considerably with the introduction of the directionally solidified alloys which are characterized by columnar grains orientated parallel to the blade axis. A further increase in creep strength was achieved when the grain boundaries were eliminated altogether in a single crystal material. The single-crystal superalloys are often classified into first, second, third, and fourth generation alloys. The first generation of single crystal nickel based superalloys contained concentrations of aluminium in excess of 10wt% or chromium in excess of 16wt%; this in the aim to combine excellent mechanical properties at elevated temperatures with a certain oxidation/corrosion resistance. In an oxidizing atmosphere, in fact, these alloys are able to establish a protective scale (alumina and/or chromia) capable of decreasing further substrate attack. Second, third, and fourth generations of superalloys for single crystal turbine blades, contain as many as 5 to 12 additional elements; among them relatively high percentages of refractory elements such as *Ta*, *W*, *Re* or *Ru* which enhance the high temperature mechanical properties. Unfortunately, this is done at the expense of environmental resistance as the percentage of *Cr* and *Al* is decreased. Table 1.1 includes the composition, in weight percentage, of some commercially available nickel-base superalloys which have been developed for use as single-crystal turbine blades and vanes.

Alloy	Cr	Co	Mo	W	Ta	Re	Ru	V	Nb	Al	Ti	Hf
1 st generation [34]												
PWA 1480	10	5	-	4	12	-	-	-	-	5.0	1.5	-
PWA 1483	12.8	9	1.9	3.8	4	-	-	-	-	3.6	4.0	-
Rene N4	9	8	2	6	4	-	-	-	0.5	3.7	4.2	-
SRR 99	8	5	-	10	3	-	-	-	-	5.5	2.2	-
RR 2000	10	15	3	-	-	-	-	1	-	5.5	4.0	-
AM1	8	6	2	6	9	-	-	-	-	5.2	1.2	-
AM3	8	6	2	5	4	-	-	-	-	6.0	2.0	-
CMSX-2	8	5	0.6	8	6	-	-	-	-	5.6	1.0	-
CMSX-3	8	5	0.6	8	6	-	-	-	-	5.6	1.0	0.1
CMSX-6	10	5	3	-	2	-	-	-	-	4.8	4.7	0.1
CMSX-11B	12.5	7	0.5	5	5	-	-	-	0.1	3.6	4.2	0.04
CMSX-11C	14.9	3	0.4	4.5	5	-	-	-	0.1	3.4	4.2	0.04
AF 56 (SX 792)	12	8	2	4	5	-	-	-	-	3.4	4.2	-
SC 16	16	-	3	-	3.5	-	-	-	-	3.5	3.5	-
2 nd generation [34]												
CMSX-4	6.5	9	0.6	6	6.5	3	-	-	-	5.6	1.0	0.1
PWA 1484	5	10	2	6	9	3	-	-	-	5.6	-	0.1
SC 180	5	10	2	5	8.5	3	-	-	-	5.2	1.0	0.1
MC2	8	5	2	8	6	-	-	-	-	5.0	1.5	-
RENE N5	7	8	2	5	7	3	-	-	-	6.2	-	0.2
3 rd generation [34]												
CMSX-10	2	3	0.4	5	8	6	-	-	0.1	5.7	0.2	0.03
RENE N6	4.2	12.5	1.4	6	7.2	5.4	-	-	-	5.75	-	0.15
4 th generation [35]												
TMS-138	2.9	5.9	2.9	5.9	5.6	4.9	2	-	-	5.9	-	0.1

Table 1.1: Nominal composition in weight percentage of four generations of commercially available single crystal *Ni*-base superalloys (nickel content is to balance)

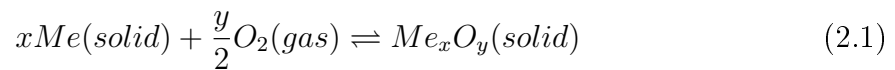
Chapter 2

Oxidation of metals

Oxidation consists in the conversion of a metallic element into its oxides; such a process occurs when a pure metal or an alloy are exposed to an oxygen containing gas at high temperature. The formed oxide can either be a continuous adherent layer that acts as an oxygen diffusion barrier, thus reducing further oxidation of the metal, or a brittle scale that continuously spalls leaving fresh metal exposed. In the latter case, the component experiences continuous metal loss which may result in loss of load-bearing capability and eventually in component failure. Oxidation studies consist of monitoring either the oxygen uptake, the metal weight loss or the metal thickness loss when the component is exposed, at high temperature, to an oxidising environment containing O_2 , CO_2 , H_2O , NO_2 or their combinations.

2.1 Oxidation process

The oxidation process occurs according to a solid-gas reaction between the metal and the oxygen to form the oxide layer. In its general form, the reaction is:



where Me stands for metal. The change in *Gibbs free energy* (ΔG) associated with the reaction determines how prone the metal is to oxidise; in particular the reaction spontaneously proceeds from left to right if $\Delta G < 0$; the system reaches the *equilibrium* when $\Delta G = 0$ [36]. The ΔG associated to the oxidation reaction is:

$$\Delta G = \Delta G(products) - \Delta G(reactants) = \Delta G^\circ + RT \ln K \quad (2.2)$$

where ΔG° is the free energy change involving reactants and products in their standard state¹, R is the gas constant, T the temperature in Kelvin, and K is the equilibrium constant of the reaction, given by:

$$K = \frac{a_{Me_xO_y}}{a_{Me}^x * a_{O_2}^{\frac{y}{2}}} \quad (2.3)$$

where a_n is the *activity* of the species n . The activity is defined by:

$$a_n = \frac{P_n}{P_n^\circ} \quad (2.4)$$

where P_n is the partial pressure of the species n in the alloy, while P_n° is the vapor pressure of the species n over pure n at the same temperature. Equation 2.4 shows that the activity of pure substances is 1, while for gases the activity corresponds to their partial pressure. From equation 2.2, at equilibrium:

$$\Delta G = \Delta G^\circ + RT \ln K = 0, \quad (2.5)$$

and, by combining equations 2.3, 2.4, and 2.5:

$$\Delta G^\circ = RT \ln P_{O_2}. \quad (2.6)$$

At a given temperature, equation 2.6 allows to determine the equilibrium partial pressure of oxygen ($P_{O_2, \text{equil}}$) from the value of ΔG° :

$$P_{O_2, \text{equil}} = \exp\left(\frac{\Delta G^\circ}{RT}\right). \quad (2.7)$$

$P_{O_2, \text{equil}}$ is the value of the partial pressure of oxygen at which the driving force for the reaction is zero. This means that, at a given temperature T , reaction 2.1 will take place (namely the metal will oxidise) if $P_{O_2} > P_{O_2, \text{equil}}$ while, the oxidation will be avoided if $P_{O_2} < P_{O_2, \text{equil}}$. In this case, the metal oxide will dissociate to form metal plus oxygen gas. The variation of ΔG° with temperature for several reactions can be read on the Ellingham diagram (figure 2.1).

One should be aware that thermodynamic considerations based on the free energy change predict how favorable the reaction is, but does not provide any information about the rate at which the reaction occurs. Moreover, thermodynamic calculations

¹The standard state is defined as the state in which the pure substance (solid, liquid or gas) exists at a pressure of 1 atmosphere and a temperature of 298K (25°C).

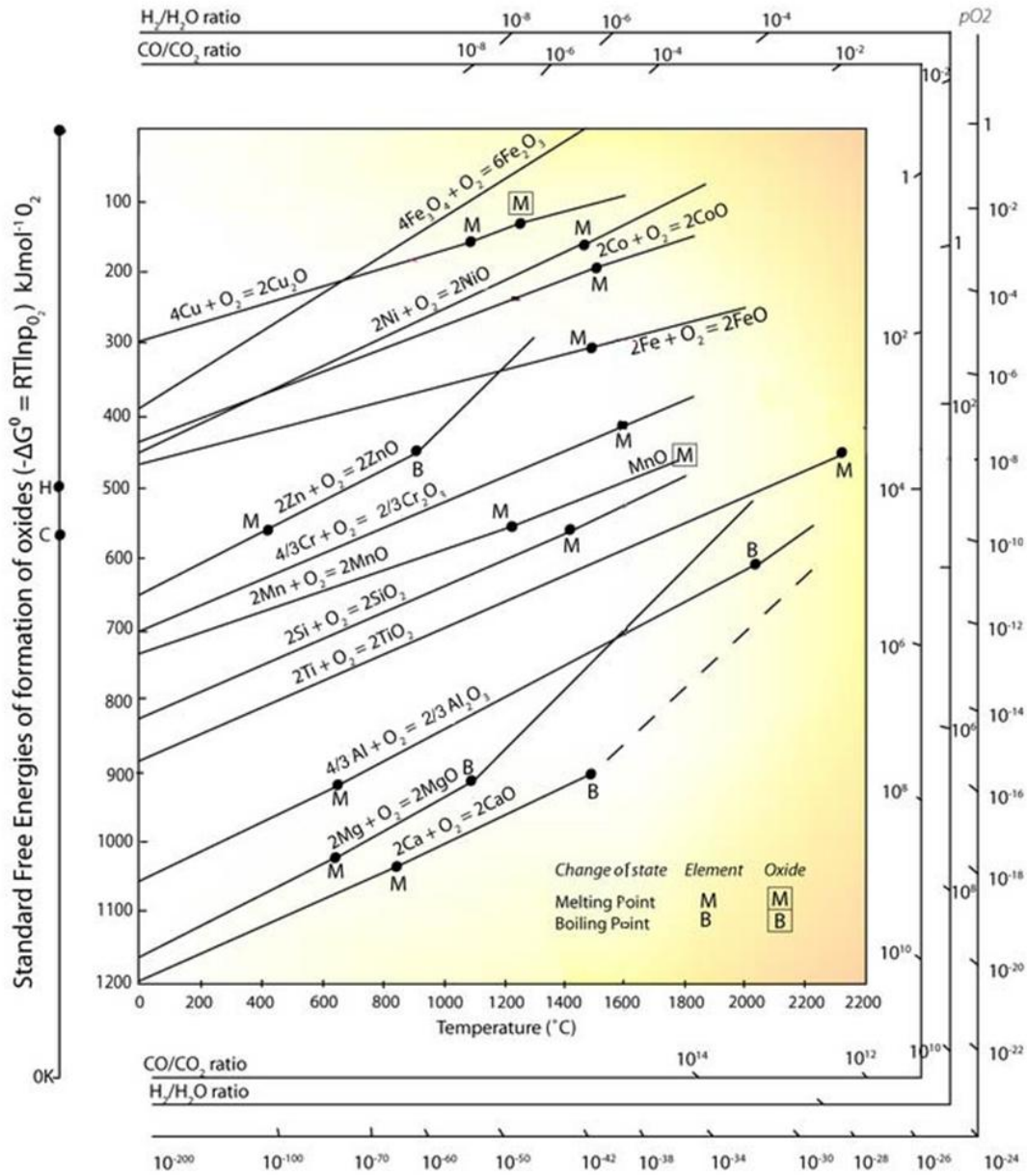


Figure 2.1: Ellingham diagram of free energy of formation of oxides as a function of temperature [5, 6]

do not take into account the individual steps that lead to the oxide formation, such as oxygen adsorption on the metal surface, oxide nuclei formation and oxide film growth [37].

2.2 Oxidation of alloys

Generally speaking, the oxidation of alloys is a more complex phenomenon than the oxidation of a pure metal. The complications arise from the formation of internal oxides, mixed oxides, and from the diffusion interaction within the metal. The alloying effect, on oxidation behaviour, was studied by Wagner [38] adopting a binary alloy model AB where, A is the major alloying component and B is the minor component. Two different cases [39] occur, the oxidation mechanism of which is described in the following paragraphs.

Case 1 This case represents the situation in which A is more noble than B but B is more reactive than A. This means that, in an oxidising environment², A does not oxidise while B forms BO. In practice, this case depicts the oxidation behaviour of a *Pt*-modified aluminide bond coat where A is the *Pt* and B is *Al*, *Cr*, or *Ti*. Case 1 includes two different scenarios depending on the concentration of B in A. If B is diluted in A, and oxygen is soluble in A, then B oxidises to form internal precipitates (BO) dispersed in A (figure 2.2a). The amount of B is in fact insufficient to form a continuous layer of BO. The oxidation results in the formation of a continuous oxide scale only if B is concentrated in A (figure 2.2b).

Case 2 This case illustrates the situation in which A and B both form stable oxides but BO is more stable than AO. When an alloy containing more than one constituent capable of forming a stable oxide, is exposed to an oxidising environment, the oxygen is adsorbed on the metal surface and nuclei of all the stable oxides are formed on the alloy. These nuclei start growing laterally until the oxide with the greatest stability covers the entire alloy surface with a continuous scale. At this stage, the growth of the other metal oxides stops and the oxidation rate is controlled by the growth of (and the transport through) the predominant oxide film. In the simplest case of a binary system, where BO is more stable than AO, this mechanism would result in the formation of a continuous layer of BO on the

²An atmospheric pressure of oxygen is assumed

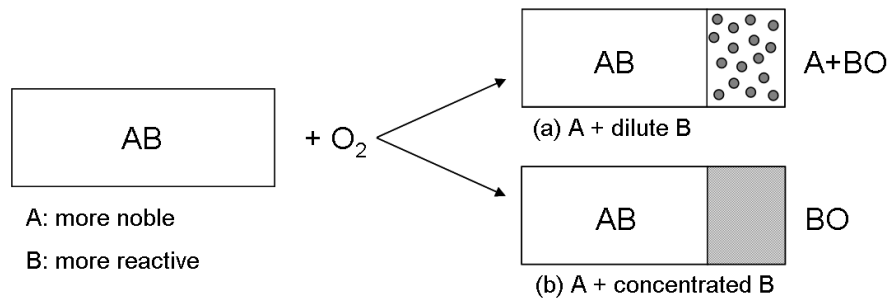


Figure 2.2: Binary alloy oxidation: A is more noble than B but B is more reactive than A. (a) B is diluted in A and oxidation results in the formation of BO precipitates dispersed in A. (b) B is concentrated in A and the amount of B is sufficient to form a continuous scale of BO. Adapted from [7].

alloy surface (figure 2.3b). If B is diluted in A with a concentration lower than the critical value needed to form a continuous layer of BO, then a stable oxide AO is formed as an outer oxide scale instead. Underneath the AO layer, at the oxide layer/alloy interface, B converts into BO precipitates dispersed in A as illustrated in figure 2.3a.

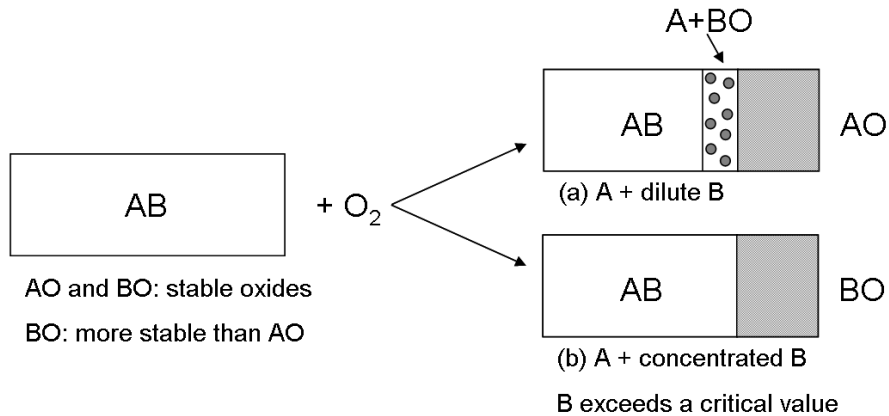


Figure 2.3: Binary alloy oxidation: A and B form stable oxides but BO is more stable than AO. (a) B is diluted in A and the oxidation results in the formation of an outer layer of AO and an inner layer of BO precipitates dispersed in A. (b) B is concentrated in A and the amount of B is sufficient to form a continuous scale of BO. Adapted from [7].

Case 2 mirrors the behaviour of *NiAl* coatings (see section 3.2) where aluminium oxides are more stable than nickel oxides. Depending on the *Al* concentration, the alloy may follow three different oxidation behaviours [7]:

- $Al < 6\text{at}\%$: the alloy oxidation mechanism follows the scheme pictured in figure 2.3a, with the formation of an outer layer of NiO and an inner layer of Al_2O_3 and $NiAl_2O_4$.
- $6\text{at}\% < Al < 17\text{at}\%$: this alloys form an Al_2O_3 oxide layer in the initial phase of oxidation. Subsequently, a prolonged exposure to the oxidising environment causes the oxide layer to degenerate in a mixture of NiO and $NiAl_2O_4$ spinel, resulting from the combination of NiO and Al_2O_3 . Over time, in fact, the Al concentration in the alloy adjacent to the oxide scale drops below the critical value required to form a continuous layer of Al_2O_3 thus NiO starts forming.
- $Al > 17\text{at}\%$: the Al reservoir in the alloy is sufficient to maintain a continuous alumina layer. The oxidation mechanism for these alloys is given in figure 2.3b.

2.3 Role of the alloy constituents

Nickel based superalloys for single crystal turbine blades contain several additional constituents (table 1.1); what is their role in terms of alloy oxidation resistance? Aluminium is the alloying element that provides the greatest effect on oxidation resistance at elevated temperatures: it allows the formation of a protective scale of alumina which decreases further substrate attack. Chromium provides oxidation resistance at intermediate temperatures and is usually added to the alloy to withstand corrosive environments at these temperatures. When chromium and aluminium are present in combination, Cr increases the Al activity in the alloy, therefore the Al content required to form an alumina scale is reduced from $10\text{wt}\%$ to $5\text{wt}\%$ within $NiCrAl$ alloys[40].

Additions of Co , Ti , Re , W , V , Nb , and Mo may be detrimental for the oxidation resistance of the alloy. Cobalt oxide has a higher growth rate than nickel oxide, therefore, when the alloy area in contact with the oxide scale is depleted in Al after a prolonged exposure to high temperature, high concentrations of Co cause the formation of a faster growing CoO scale. When added to Ni-base superalloys, titanium increases the growth rate of alumina and reduces its scale adherence. However, Sarioglu *et al.* [41] showed that, if a similar amount of Ti is added to a $FeCrAl$, the alloy oxidation resistance improves.

Refractory elements, in principle, have a detrimental effect on the alloy oxidation resistance because they reduce the Al diffusivity to the surface. Moreover, some of

the refractory metals, such as ruthenium and rhenium, form highly volatile oxides, the vapourisation of which makes the alumina scale structure uneven, causing scale spallation. An exception to this is tantalum: small additions of this element, in fact, improve the oxidation resistance of the alloy [42].

Hafnium additions to *Ni*-base alloys, improves the Al_2O_3 scale adhesion [43, 44] while, when this element is added to *Pt*-modified $\gamma + \gamma'$ alloys, it results in a significant reduction in scale growth [43, 45, 46].

2.4 Role of sulphur

Sulphur is not deliberately added to coatings or alloys, nevertheless, it is always present in tens of part per million. This contamination may result from the alloy casting process, the aluminising equipment, the *Pt* deposition via electroplating or simply from the component handling and storing [47, 48, 49]. During oxidation, sulphur segregates at the alloy/oxide interface reducing the adhesion of the oxide scale to the alloy eventually triggering early oxide spallation [50, 51, 52]. The detrimental effect of sulphur can be reduced either by physically removing it from the alloy or by ‘trapping’ it away from the alloy/oxide interface. The removal methods aim at reducing the S content below *1ppm* and consist of repeated oxidation and polishing, high temperature annealing in vacuum or annealing in H_2 at a temperature between $1100^\circ C$ and $1200^\circ C$ [53]. The addition of reactive elements instead trap the sulphur at the alloy grain boundaries. For example, yttrium additions tie up the sulphur forming yttrium sulphides or complexes [54, 55, 56].

2.5 Oxidation testing

Oxidation studies involve monitoring either the oxygen uptake, the metal weight gain or the metal thickness loss when a component is exposed to an oxidising environment; two types of test are adopted commonly: *isothermal tests* and *cyclic tests*. Isothermal tests are usually conducted in a tube furnace and consist of three phases:

- a heating up phase to test temperature, which can last 10 to 15 minutes depending on sample size;
- hold time at the test temperature, for various times from minutes to thousands of hours;

- a cool down phase to room temperature with a controlled cooling rate (typically between $10^{\circ}\text{C}/\text{min}$ and $15^{\circ}\text{C}/\text{min}$).

The tested samples are typically disk-shaped coupons the surface of which is ground with 600 grit abrasive paper before testing. During the test, an oxide scale forms on the alloy surface. Microbalances can be used to record the coupons weight change during the test and the oxide growth is plotted as a function of the exposure time. At the test completion, the oxide thickness and composition may be determined by SEM and EDX analysis conducted on the metallographically prepared cross section of the coupons.

While every effort is made to replicate the gas temperature and the conditions that a component would experience in real-life applications, gas velocities in a laboratory test are considerably lower than those in the high pressure turbine section of a gas turbine engine ($\sim 1000\frac{\text{m}}{\text{s}}$ at 1093°C). This means that isothermal tests provide an excellent instrument to study the fundamental processes involved in oxidation but they cannot be used to predict reliably the oxidation life of the component in service [7].

Cyclic oxidation tests consist of cyclically moving the specimens in and out of a furnace. In one typical cycle, disk-shaped samples may alternate 50 minutes in the furnace hot zone to 10 minutes outside of the furnace, in the laboratory environment. The cool down phase, down to a temperature below 100°C , is usually performed either in still air or forced ventilation. The samples should be visually monitored at regular interval during the whole test, and their weight change regularly recorded. Guidelines for cyclic oxidation test standardization were outlined by Nicholls and Bennett [57]. Cyclic oxidation tests can be performed also in burner rigs [58]. Such a setup is more versatile, in that it allows the analysis of the combined effects on the durability of coupons (or components) of cyclic oxidation, hot corrosion, and erosion. While the tested specimens are thermally cycled in the rig to simulate the start-up and shut-down conditions in the engine, hot corrosion and high temperature erosion investigations can be performed by adding a controlled amount of contaminants and solid particulate to the fuel and to the combustion air.

Chapter 3

Diffusion coatings for oxidation resistance

The composition of superalloys for high temperature applications has been optimised to achieve high temperature mechanical properties; unfortunately, this has been done at the expense of the environmental resistance of the alloy. The environmental protection, therefore, has to be provided by an external *coating*, compatible with the alloy, and the composition and microstructure of which have to be tailored to provide good oxidation and corrosion resistance. The primary aim of the coating is to produce a stable, adherent, slow growing surface oxide capable of providing a barrier between the coating alloy and the environment [40, 59].

A large number of coatings and coating processes are available to provide surface protection. In principle, the coating selection depends on the component design and application, but it is difficult to draw general rules. Even for the same application and the same engine, in fact, different commercial strategies could result in different choices of coating: opting for a higher efficiency and, as a consequence, higher temperatures at the expense of long life, could imply a change in the operating conditions, and therefore a change in the dominant degradation mechanisms.

The numerous types of environmental protective coatings can be divided into two main categories: *overlay coatings* and *diffusion coatings*, only the latter are described here, with particular attention to the *Pt-modified aluminide* and *Pt-diffused* coatings. When the protective coatings are used with a thermal barrier, they are also called *bond coats* because they provide a ‘transition’ layer on which the ceramic top coat adheres better than on the substrate.

3.1 Production of diffusion coatings

Diffusion coatings [60, 61] are formed by the surface enrichment of an alloy with an oxide scale former such as aluminium, chromium, Silicon or their combination. These elements react with the substrate alloy constituents to form an intermetallic layer, which has a thickness between $10\mu m$ and $100\mu m$, depending on the application, and a significantly high level of the enriching elements.

Three main techniques are available to manufacture diffusion coatings: *pack cementation process*, *out-of-pack process*, and *Chemical Vapour Deposition (CVD)* [62]. All of them require exposure to high temperature of the components to be coated and consist of five main steps:

1. generation of the vapour containing *Al*, *Cr*, or *Si*;
2. transport of the vapour to the component;
3. reaction of the vapour with the elements of the substrate alloy to form various intermetallics;
4. diffusion in the alloy;
5. post-processing heat treatments with the double aim of achieving a coating with the desired composition and microstructure and of recovering the mechanical properties of the substrate alloy.

The differences among the three processes listed above lie in the way the vapour is generated and transported to the components. In the pack cementation process the components are in contact with a pack mixture in a heated retort. The vapour is generated inside the pack. In the out-of-pack process, the parts are still placed in the retort, but not in direct contact with the pack. The vapour is adequately conveyed to reach the external and internal surfaces of the components. In the CVD process, the vapour is generated in a retort physically separated from the deposition chamber and then it is circulated around and onto the components.

Some pre-processing procedures are carried out on the component before the coating deposition. These consist of:

1. cleaning the component surface;
2. a masking procedure.

Cleaning involves grit blasting of the surface with alumina grits, the purpose being to remove oxides and contaminants. Masking has the aim of protecting some areas of the component which are not intended to be coated. For instance, when coating turbine blades via aluminium enrichment, only the aerofoils have to be exposed, while the remaining areas of the blades must be screened. The maskant is usually a nickel-based paste that solidifies upon application and that is able of withstanding process temperatures without degrading.

3.1.1 Pack cementation process

In the pack cementation process[63, 64], the parts to be coated are placed in a sealed or semi-sealed retort, and are embedded in a powder mixture containing: a source of coating material, a halide salt, and an inert filler material. The source material, identified as the *master alloy*, can be either pure or alloyed. The halide salt can be either a stable or an unstable halide salt such as AlF_3 , $NaCl$, NH_4Cl , and NH_4F . It is usually added to the powder mixture in small quantities (2wt% to 5wt%) and it acts as an activator in the chemical reactions which promote the coating deposition. The filler material, usually alumina, has the dual purpose of preventing the pack from sintering and of suspending the components to be coated during deposition. The process is carried out at a temperature between $700^\circ C$ to $1100^\circ C$, under a protective Argon atmosphere, or an $Ar + H_2$ atmosphere.

Although the pack cementation is extensively used and covers the need of 80-90% of the market, it has several drawbacks. The process requires a direct contact between the components and the pack powder, therefore, small or inaccessible passages cannot be coated. Even when the internal passages are accessible, it is difficult to obtain a uniform coating thickness and microstructure. Morphology and thickness of the internal coating are, in fact, a function of the ratio between the surface area and the pack powder available. Besides, the required intimate contact between the pack and the component causes some powder particles to become entrapped within the coating, acting as stress concentrators, thus increasing the risk of fatigue cracking.

A variant of this method which aims at reducing the limitations of the standard pack technique is the *slurry process*: in this case the coating material is mixed with a carrier fluid to form a slurry which is injected into cavities or is painted on the accessible surfaces to be coated [65].

3.1.2 Out-of-pack process

Most of the disadvantages of the pack cementation process have been overcome by the introduction of the out-of-pack process [66, 67], which does not require any contact between the components and the pack mixture. In this process, the parts to be coated are placed in a retort, above a tray containing the pack mixture; the retort is designed to allow the flowing of an inert gas, usually Argon or an Argon/Hydrogen mixture. Such gases work as a carrier for the halide vapors generated inside the pack, which can then easily access both the external and the internal surfaces of the component.

A variant of this type of process is the *vapour phase process*, which has been developed by SNECMA to produce aluminide protective coatings for military and civil applications [68]. The main novelty of the vapour phase process is the nature of the vapour source: the powder pack is replaced by *Al-Cr* alloy in the form of solid granules on which the activator is sprinkled. The absence of powder and the possibility to re-use the granules up to 50 times makes the process more environmentally friendly.

3.1.3 Chemical Vapour Deposition

In the CVD process, the halide vapour is generated in a reactor placed remotely from the deposition zone and then it is transported by gas flow, as well as diffusion, to the deposition reactor, which is held at a temperature between 1000°C and 1100°C . In comparison to the other techniques available to deposit diffusion coatings, the CVD process has several advantages. The coating can be formed over a wider range of distances, up to $1 - 2000\text{mm}$ against the 300mm max of the out-of-pack process, allowing to coat uniformly long internal passages. The CVD process gives greater control over the concentration of the halide vapour, which in turn gives greater control over composition and coating growth rate. It allows also to introduce multiple elements in the coating adopting independent reactors [8] (see figure 3.1). Finally, the post coating heat treatment can be carried out without removing the components from the deposition chamber reducing the manufacturing time and cost [69].

3.2 Aluminide coatings

Aluminide coatings are a particular type of diffusion coatings where the alloy surface is enriched with aluminium. These are the coatings of choice for protecting superalloy

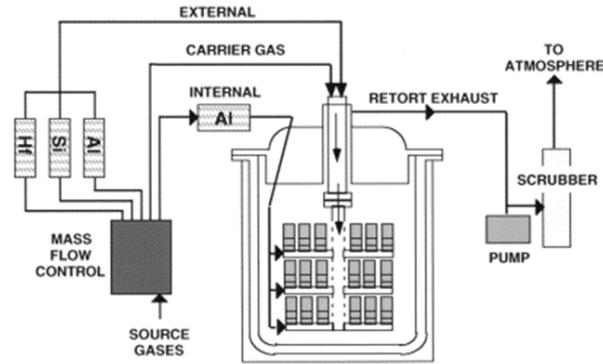


Figure 3.1: Schematic diagram of a CVD process for co-deposition of Hf , Si and Al [8].

components in oxidizing environments; they offer satisfactory performance in many marine, aeronautical and industrial applications if adopted at temperatures below $1100^{\circ}C$. For applications in oxidising-corrosive environments, the resistance of the aluminide coatings is improved by the addition of alloying elements such as Cr , Si , Ta , Hf , Zr , Rare Earth elements (e.g. Y), and precious metals (e.g. Pt and Pd). These *modified aluminide* coatings may be deposited in several ways: co-deposition of elements from the pack or slurry, suitable pre-treatment of the superalloy before pack aluminising, or deposition of a metallic layer using electroplating or Physical Vapour Deposition (PVD, see section 3.4 for more details) [40]. The industrial success of the aluminising processes depends on the low cost of the raw materials, the ability to coat at one time large batches of parts and the possibility to strip and recoat out-of-tolerance and used parts.

The morphology, the thickness and the Al activity in the coating depend on the process parameters, the post-processing heat treatment and the substrate alloy composition. The Aluminide coating, as any other type of diffusion coating, can be deposited only in a limited range of thicknesses, typically between $30\mu m$ and $70\mu m$ [70], depending on the type of aluminide formed. This is linked to two main factors: the progressively reduced activity of the pack, due to its continuous depletion in source material, and the growth rate of the coating. The coating growth is diffusion controlled, hence the coating thickness increases roughly as the square root of the time [71, 72]:

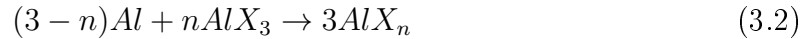
$$x \approx \sqrt{Dt} \quad (3.1)$$

where x is the coating thickness, D is the relevant diffusion coefficient and t is the

exposure time at the processing temperature. Relation 3.1 shows that progressively more time is required to achieve the same increment in coating thickness. Typically, aluminide coatings contain in excess of 30wt% aluminium [70].

3.2.1 Aluminising of Ni base alloys: microstructure and mechanism of coating formation

Aluminide coatings can be applied with one of the techniques described in section 3.1: pack cementation, out-of-pack or CVD. All of these processes are based on the same chemical reactions, and all of them operate through a similar mechanism in the gas phase, although the range of transport in the pack process is rather small. At the process temperature the activator reacts with the metallic component of the pack, pure aluminium or aluminium alloy, to form a mixture of volatile aluminium subhalides (AlX_n) according to the reaction:



where AlX_3 is the halide salt, X is usually F , Cl , or Br and $n < 3$. AlX_n is more thermodynamically stable than AlX_3 as the temperature increases. The AlX_n mixture diffuses in the vapour phase to the surface of the component to be coated, and reacts with the nickel in the alloy, to form an intermetallic compound and the halide salt in gaseous form, according to the following reaction:



where $AlNi_y$ is the intermetallic compound and $\frac{1}{3} \leq y \leq 3$. The produced activator, AlX_3 , can diffuse back to the aluminium source to continue the process.

The mechanism of formation and the microstructure of two major variants of aluminide coatings were modelled, for the first time, by Goward and Boone in 1971 [73]. Depending on the aluminium content in the pack and the processing temperature, the formed intermetallic on Ni -base superalloys, $AlNi_y$, is either $\beta - NiAl$ or $\delta - Ni_2Al_3$. In the first case the aluminising process is termed as a *low-activity process* and the resulting coating as *outward diffusion coating*; in the second case the process is identified as a *high-activity process* and the coating as *inward diffusion coating*. The coatings identification name is linked to the predominant diffusion process that occurs in the alloy during deposition; such a process can be either the inward diffusion of aluminium

or the outward diffusion of nickel.

3.2.1.1 Outward diffusion coatings

When the Al activity in the pack is low and the process temperature is higher than $1000^{\circ}C$, the diffusivity of Ni (D_{Ni} , as defined in [74]) in the alloy is greater than that of the Al , consequently the Ni preferentially diffuses out from the substrate producing an outward diffusion coating. The combination of the Ni with the Al results in the formation of a $\beta - NiAl$ intermetallic layer that builds up on the component surface. Near the original interface, the alloy, depleted in Ni , evolves from a $\gamma + \gamma'$ microstructure into a $\beta - NiAl$ phase. This compound has a very low solubility for the constituents of the alloy which therefore precipitate out. The obtained outward diffusion coatings are characterized by two zones: an external zone (EZ) and an internal zone, identified as an interdiffusion zone (IDZ). Both zones are $\beta - NiAl$ but only the IDZ includes the presence of second phase precipitates. Due to the difference in diffusion coefficient ($D_{Ni} > D_{Al}$, as defined in [74]), outward diffusion coatings can present Kirkendall porosity below the original interface. Figure 3.2 shows the typical microstructure of a $NiAl$ outward diffusion coating.

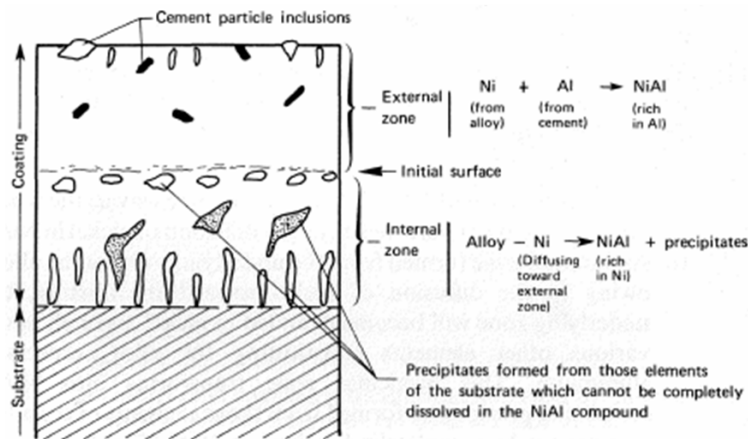


Figure 3.2: Schematic representation of the microstructure of a $NiAl$ outward diffusion coating (low activity process) [9]

3.2.1.2 Inward diffusion coatings

When the Al activity in the pack is high and the temperature is in the range $750-950^{\circ}C$ the diffusion rate of Al (D_{Al}) is greater than that of Ni , thus the Al diffuses inward and

an inward diffusion coating is produced. As a direct consequence of $D_{Al} > D_{Ni}$, the original surface of the alloy becomes the external surface of the coating and Kirkendall voids are not generated.

Depending on the Al activity, three different types of microstructures and coating compositions can be achieved (see the $Ni-Al$ phase diagram in figure 3.3):

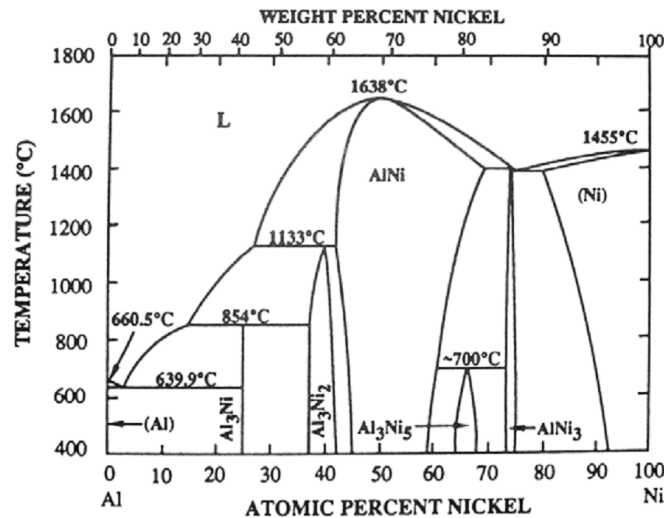


Figure 3.3: nickel-Aluminum binary phase diagram [10]

1. if Al activity is very high: a $\delta - Ni_2Al_3$ phase forms;
2. if Al activity is high: a two-layer structure forms with an outer layer of $\delta - Ni_2Al_3$ phase and an inner layer of Al rich $\beta - NiAl$ (Al content $>50at\%$);
3. if Al activity is moderate: a $\beta - NiAl$ phase forms with high Al content.

As a consequence of the inward growth, slow diffusing constituents of the alloy such as W , Mo , Ta , Re are trapped in the coating as precipitates and in solid solution in the coating matrix. $\delta - Ni_2Al_3$ is a brittle phase, therefore the component requires a further heat treatment after aluminising in order to achieve an acceptable performing coating. This additional step allows the Ni from the substrate to diffuse outwards so that the $\delta - Ni_2Al_3$ phase is transformed into a less brittle Al rich $\beta - NiAl$ (Al content $>50at\%$). Figure 3.4 illustrates the formation of a $NiAl$ coating from a Ni_2Al_3 layer by diffusion heat treatment.

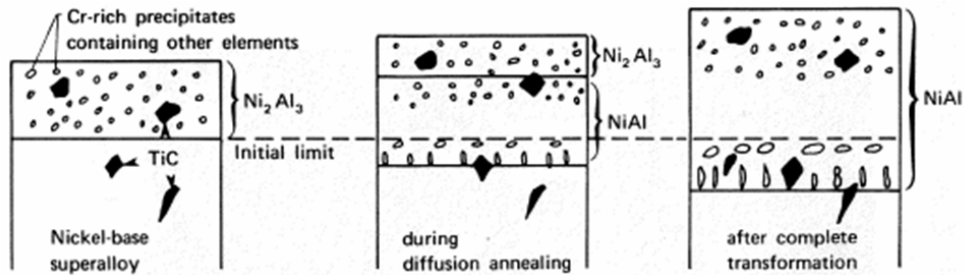


Figure 3.4: Inward diffusion coating: formation of a $NiAl$ coating from a Ni_2Al_3 layer by diffusion heat treatment [9]

3.2.2 Platinum-modified aluminide coating

Aluminide coatings can be modified by Pt addition to improve the coating hot corrosion and oxidation resistance [75]. The first commercial Pt -modified Aluminide coating was identified as LDC-2 [76]. The production method consisted of: depositing a Pt layer by electroplating, typically between $6\mu m$ and $10\mu m$ thick, aluminising by pack cementation and heat treating the blades to diffuse the Pt and the Al into the surface. The manufacturing method adopted nowadays has not changed significantly; the main differences lie into the possibility of adopting, for the Al deposition, not only pack cementation, but all the aluminising methods described in section 3.1, and into splitting the heat treatment into two steps. In fact, the components may receive a first diffusion heat treatment after plating to improve the Pt layer adherence to the substrate alloy, and to a second heat treatment after aluminising to achieve the required microstructure and phase distribution in the coating.

Depending on the Pt layer thickness, the aluminising process parameters and the consequent heat treatment, Pt -modified aluminide coatings can have different microstructures and compositions [77, 78]. The Pt enters the coating as a single-phase solid solution $\beta - (Pt, Ni)Al$, as a single phase $PtAl_2$, or as a two-phase $PtAl_2$ and $\beta - (Pt, Ni)Al$ solid solution. A schematic representation of different Pt -modified aluminide coating microstructures is provided in figure 3.5. The coating may include up to four zones including the IDZ. The latter consists of a $\beta - (Ni)Al$ matrix with elongated Cr -rich α -phase and refractory element precipitates [79]. Table 3.1 reports the coating designation of some commercially available Pt -modified aluminide coatings.

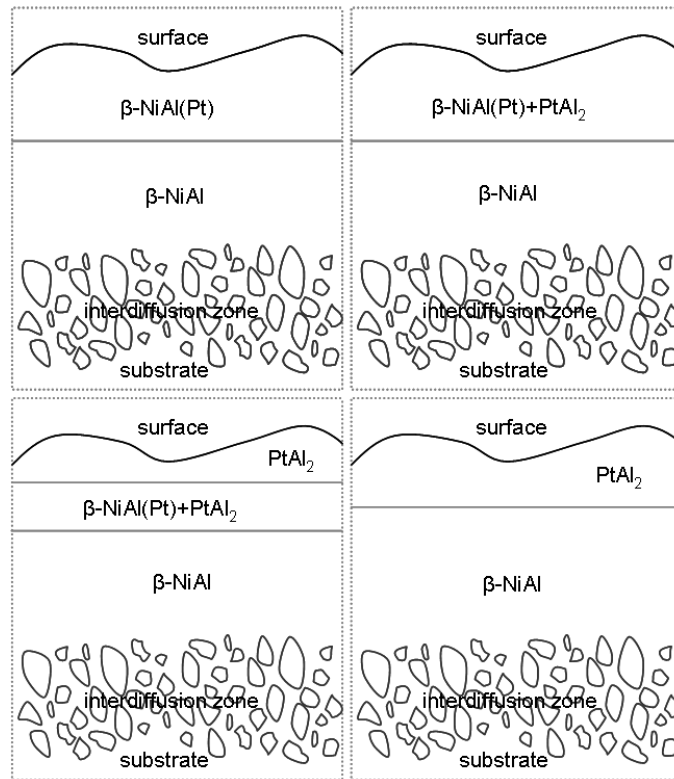


Figure 3.5: Schematic microstructures of different *Pt*-modified aluminide coatings, adapted from [11]

COATING DESIGNATION	MANUFACTURER	COMPOSITION	ALUMINISING PROCESS
RT22	Chromalloy	High activity	in pack
CN91	Chromalloy	Low activity	CVD
LDC 2E	Howmet	High activity	in pack
MDC 150	Howmet	High activity	CVD
MDC150L	Howmet	Low activity	CVD
PS 138	Turbine Metal Technology	High activity	in pack
SS82A	Turbine Component Corp.	High activity	out-of-pack

Table 3.1: Commercially available *Pt*-modified aluminide coatings

3.2.3 Mechanisms of coating degradation in service

During service at high temperature, between 950°C and 1250°C , the compositional differences between the coating and the substrate provide the driving force for various elements interdiffusion and, consequently, for several microstructural changes [80, 81, 79, 82]. The EZ of the coating becomes depleted in Al due to its diffusion towards the coating surface to form or replenish the Al_2O_3 scale. In the resulting hypostoichiometric $\beta - \text{NiAl}$, Ni is the predominant diffusion specie therefore, it diffuses outwards from the substrate causing the nucleation of $\gamma' - \text{Ni}_3\text{Al}$ in the EZ. The Ni flux depletes the substrate below the IDZ in Ni and, in turn, results in the precipitation of the Topologically Close-Packed (TCP) phases [83]. These precipitates are rich in refractory elements, the solubility of which decreases in the alloy due to the Ni depletion. The latter, plus the fact that the TCP phases incorporate very little Al , causes the matrix around the precipitate to transform from $\gamma + \gamma'$ into $\beta - \text{NiAl}$. After long term oxidation, more Ni diffuses from the substrate causing the $\beta - \text{NiAl}$ phase to transform back to $\gamma' - \text{Ni}_3\text{Al}$. As a consequence, the Ni depleted area extends deeper causing the TCP phases to grow inward into the substrate. The TCP phases are brittle with a needle-like morphology, the formation of which reduces the concentration of refractory elements in the alloys. The loss in strengthening constituents results in the reduction of the load-bearing cross section of the component, while the TCP precipitates, with their large-angle grain boundaries, may contribute to the generation of fatigue cracks.

$\beta - \text{NiAl}$ and $\beta - (\text{Ni}, \text{Pt})\text{Al}$ coatings may undergo a reversible martensitic transformation when they are cooled down from temperatures exceeding 1100°C [84, 85]. The martensitic reaction occurs when the coating becomes rich in nickel due to Al depletion to form the Alumina scale [84], or after Ni outward diffusion from the substrate [86]. This transformation does not require diffusion and takes place by atom coordinated displacement (a shear transformation): the high temperature phase, with body centered structure, changes into a low temperature phase with face centered tetragonal structure. The transformation occurs with an associated volume change of $\sim 2\%$ which corresponds to linear strain of $\sim 0.7\%$ [85, 87]. This value is higher than the value of the thermal expansion mismatch strain between the substrate and the coating generated upon heating ($\sim 0.1\%$). The strain induced by the transformation is believed to be one of the causes triggering bondcoat *rumpling*. This term is adopted to describe a phenomenon affecting aluminide and overlay (MCrAlY) coatings; it results in an increase of coating surface roughness following thermal cycling [12, 88, 89] and eventually into

TBC failure if the coating is used as bond coat. Figure 3.6 shows an example of coating degradation by rumpling.

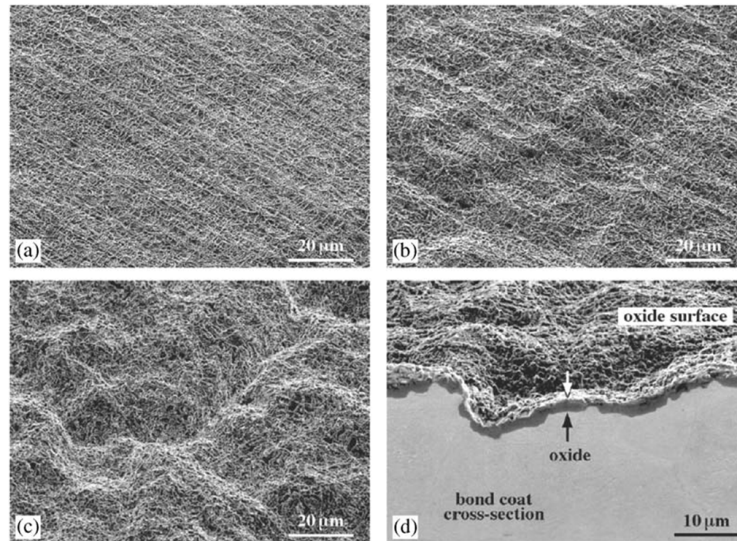


Figure 3.6: SEM micrographs showing degradation by rumpling of a *Pt*-modified aluminate coating, cyclically tested in air at a temperature of 1200°C (one-hour cycles): (a) after 1 cycle; (b) after 10 cycles; (c) and (d) after 50 cycles [12].

3.3 Platinum-diffusion coatings

Platinum-diffusion coatings belong to the category of diffusion coatings but exhibit some peculiar aspects which characterise them as a class of their own. In contrast to other diffusion coatings, manufacturing of *Pt*-diffusion coating follows different processes to those described in section 3.1 and involves only the deposition of platinum either by PVD or by electroplating, as detailed in the next paragraph, and heat treatment. The enriching element, in this case platinum, is not an oxide scale former and does not modify the $\gamma + \gamma'$ microstructure of the *Ni* base substrate. The *Ni* base superalloys exhibit high creep strength, therefore a coating based on an equivalent structure is expected to be resistant to creep-induced rumpling. Moreover, the similarity of the microstructure between substrate and coating makes the latter less prone to microstructural changes due to elements interdiffusion.

A coating based on a $\gamma + \gamma'$ structure was patented by Rickerby *et al.* in 1999 [90, 91, 92, 93, 94]. It consists of a *Pt* enrichment of the alloy and it is produced

by depositing a 8 – 10 μm thick layer of *Pt* by electroplating, or PVD, followed by a diffusion heat treatment in vacuum or inert atmosphere at a temperature between 1100°C and 1200°C. The beneficial effect of the *Pt* additions to coatings have been investigated by Gleeson’s research group [93, 95, 96, 97, 98]. Studies conducted on $\gamma - Ni$ and $\gamma' - Ni_3Al$ single phase alloys show that the *Pt* addition promotes the establishment of a continuous Al_2O_3 scale by suppressing the *Ni* oxide growth in both alloys [97]. In case of the γ' alloy, this can be linked to the strong preference that the *Pt* atoms have for the *Ni* sites in the Ni_3Al crystal lattice; which results in an *Al* enrichment of the γ' surface and, in turn, in the preferential formation of Al_2O_3 over *NiO* [99]. Moreover, when added to the coating in a percentage higher than 15at%, *Pt* increases the *Al* supply to the Alumina scale. The presence of *Pt* decreases the *Al* activity in the coating, thus generating an activity gradient between the substrate and the coating itself; consequently an uphill diffusion of *Al* occurs from the substrate to the coating and, eventually, to the alumina scale [96, 100, 101]. Studies conducted on TBC systems with $\gamma + \gamma'$ bond coat showed that the *Pt* can inhibit, although not eliminate, the segregation of *S*, *C*, and refractory elements at the TGO/bond coat interface and therefore extend the TBC system lifetime [102].

3.4 Physical Vapour Deposition

The term Physical Vapor Deposition or PVD refers to a variety of methods for the deposition of thin films on various surfaces involving only physical processes. Generally speaking, the PVD techniques allow the deposition of several types of materials ranging from metals to ceramics, from intermetallics to some polymers. For their versatility the PVD processes find application in tool coating and microelectronic industries (e.g. deposition on semiconductor wafers), as well as for the production of optic and decorative films. In the context of this thesis, PVD processes are particularly relevant in that they are used for the production of *Pt*-diffusion coatings (see section 3.3) and in the modification of aluminide coatings via the addition of platinum (see section 3.2.2).

A PVD process is carried out in a vacuum chamber, where the source material and the substrate to be coated are held, and follows four main steps [103]:

1. synthesis of the coating vapour;
2. transport of the vaporized material to the substrate;

3. adsorption of the atoms onto the substrate surface;
4. film nucleation and growth.

The synthesis of the coating material involves a phase change of the source material from a solid/liquid state to the vapour state. The vapour diffuses across the coating chamber to reach the substrate surface; here, the atoms are either bounced off or adsorbed. In the latter case, atoms are identified as *adatoms*, and they move on and across the substrate surface by surface diffusion to seek low energy sites where they become attached to the surface allowing the formation of *nuclei*. These are identified as quasi-stable islands of deposited material. The atoms that reach the surface next can either contribute to the growth of the primary formed nuclei, or allow the formation of new ones. In a later stage of deposition the islands coalesce into a continuous film.

The major advantages of adopting PVD processes instead of other film deposition techniques such as electroplating, CVD or plasma spray consist of [104]:

- flexibility in the composition of the deposit;
- ability to manufacture deposits with unusual microstructures and crystallographic properties;
- possibility to vary the temperature of the substrate over a very wide range;
- very high purity of deposit;
- excellent control of the film thickness down to the nanometric scale;
- excellent surface finish which can be equal to that of the substrate.

The main limitation of this technique comes from it being a *line of sight* process; this prevents its use in those cases where the substrate has complex geometry or internal passages, which would remain uncoated due to the shadowing effects occurring during deposition.

All PVD methods can be classified into three main categories: evaporation, sputtering and ion plating techniques [105].

3.4.1 Evaporation

In evaporation processes, the material to be deposited is placed in a crucible that can be either made of a refractory metal (such as *Mo*, *W*, or *Ta*) or of a metal coated

with alumina. The crucible is heated to melt the evaporant, thus creating the atomic vapour. A variety of heating systems can be adopted for this purpose, such as electric resistance, radiation, induction, etc. The use of electron beams as a heating source allows evaporation of high melting point materials (like ceramics) while achieving high deposition rates [104, 106]. Modern electron beam coaters can reach a deposition rate of $75 \frac{\mu m}{min}$. A detailed description of a PVD process where an electron beam is adopted as a heating source is given in section 4.3.1, when discussing the deposition of Thermal Barrier Coatings.

3.4.2 Sputtering

In sputtering processes the coating material is originated, in the form of atoms, from a *target*¹. Atom emission is caused by the bombardment of the target by high energy particles. Figure 3.7 shows a schematic representation of a typical sputtering equipment.

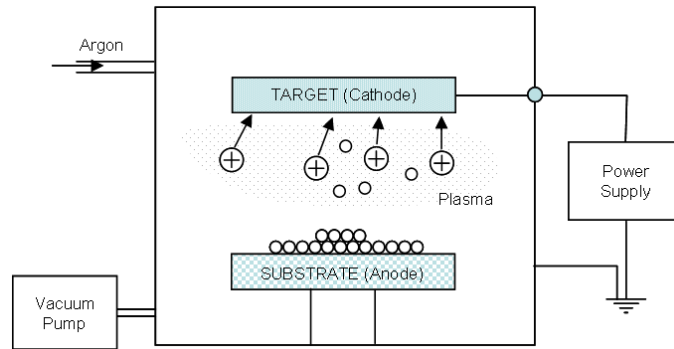


Figure 3.7: Schematic representation of a planar diode sputtering process

The working principle is relatively simple: the sputtering unit consists of a chamber, evacuated to low pressure, which is equipped with inlet/outlet gas valves and contains the target and a holder locating the substrate to be coated. The working gas is a heavy and inert gas, typically Argon, which is introduced in the sputtering chamber and ionised to form a *plasma*, namely a collection of neutral atoms, electrons and ions. A power supply is connected to the target and substrate in such a way that the former acts as a cathode relatively to the grounded substrate. Such a setup accelerates the gas ions (Ar^+) towards the negatively charged target, so that they impinge its surface with high energy, transferring their large momentum. This energy transfer may cause different phenomena:

¹In this context *target* is the source of the coating material

- direct ejection of the impacted atom from the target surface;
- a cascade effect in which a series of collisions between atoms in the first few atomic layers of the material lattice is initiated, which eventually leads to the ejection of another atom, other than the impacted one;
- ion implantation;
- ion reflection;
- emission of a secondary electron.

Only the first two events lead to proper sputtering of the target material, while the others are ineffective in this respect. Ion implantation or reflection can occur with or without neutralisation, with loss of kinetic energy. The emission of a secondary electron is the result of an impact causing extraction of an electron from an external orbital of a surface atom. Only $\sim 1\%$ of the impact energy produces ejected atoms, while $\sim 75\%$ is dissipated as heat and the remaining portion generates secondary electron emission [7]. The sputtering process efficiency is measured as *sputtering yield*, defined as the number of target particles ejected per incident particle of plasma. The yield depends on the source material, the impact angle of the particles, and the nature of the target surface, while it is independent of the charge of the impacting particles [107]. The sputtering rate according to Thornton [107] is given by:

$$R = 6.23IS \frac{M}{\rho} \quad (3.4)$$

where R is expressed in $\frac{nm}{min}$, I is the ion current in $\frac{mA}{cm^2}$, S is the sputtering yield as atoms ejected per ion, M is the atomic weight of the target in grams, and ρ is the density of the sputtered material in $\frac{g}{cm^3}$. Equation 3.4 highlights that R increases with ion current and with materials characterized by higher $\frac{M}{\rho}$ ratio.

Several variants of the sputtering method have been developed to increase the sputtering yield or to address special requirements, such as the sputtering of non-conductive materials. The sputtering process most widely used is the Direct Current (DC) planar diode setup (illustrated in figure 3.7). In this configuration the target and the substrate are held parallel to each other at a distance between 5 and 10 cm. The working chamber is evacuated to a pressure between 10^{-5} and 10^{-7} Torr and backfilled with Argon at a pressure between 10^{-1} and $2 * 10^{-2}$ Torr. During the process, a DC power supply keeps

the target at a high negative bias ($\sim -3kV$), while the chamber and the substrate are earthed. This process can achieve only extremely low deposition rates, in the region of $40 \frac{nm}{min}$ for a cathode bias of $-3kV$ and an Argon pressure of $75mTorr$ [107]. A higher deposition rate, at a given voltage, can be achieved by increasing the gas pressure, which translates in a higher number of impacting ions. It should be noted, nevertheless, that too high pressure may reduce the deposition rate because of scattering effects in the gas.

An alternative and more effective way to enhance the deposition rate is based on the use of the *magnetron sputtering* method, which adopts a magnetic field, generated by a permanent magnet placed under the target, to increase the ionisation efficiency of the electrons. Deposition rates in this case can reach $1 \frac{\mu m}{min}$, even at relatively low working pressures. The magnetic field combined with the electric field between the cathode and anode traps the electrons in a coil path around the magnetic field lines as illustrated in figure 3.8. In this way, the path length of each electron is significantly increased: it has

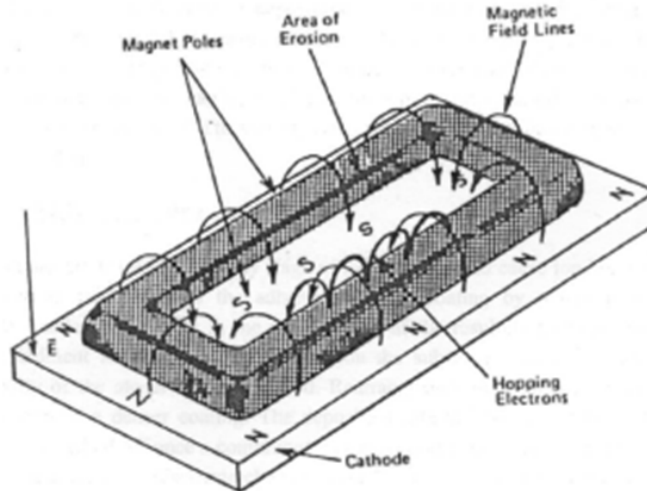
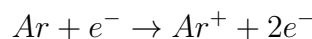


Figure 3.8: Schematic of planar magnetron sputtering, showing the principle of trapping electrons to increase ionisation efficiency [13]

to travel along a helical path even for covering short linear distances. This results in a longer permanence of the electron in the gas and, in turn, in an increased possibility to ionise the Argon gas by inelastic collision:



The main disadvantage of this technique is a heterogeneous erosion of the target, if planar magnetrons are adopted. The electrons, trapped in a ring of plasma, concentrate target consumption along an erosion track, limiting the life span of the target and leaving most of its bulk material unused.

3.4.3 Ion plating

The ion plating process can be seen as a combination of evaporation and sputtering techniques. The metal is still evaporated but, as in the sputtering method, the vapour is ionised by a plasma. The main advantage of this technique is the good adhesion of the deposit obtainable at low substrate temperature. The evaporants ions, in fact, bombard the substrate surface with such a high energy that the ions themselves implant into the substrate.

Chapter 4

Thermal Barrier Coating

Thermal Barrier Coatings (TBCs) are a class of ceramic coatings which provides thermal insulation for the coated component, allowing a high thermal gradient to be subtended across the coating thickness, and in turn lowering the metal surface temperature. This results in an enhancement of the thermal fatigue and creep capability of the coated component without sacrificing the performance of the turbine. Although TBC do not provide significant reduction in oxygen physically transported to the substrate, the lower temperature in the metal substrate can lead to a reduction in the damage due to oxidation and hot corrosion.

4.1 Ceramic top coat: material requirements

The material selection for Thermal Barrier Coating applications is restricted by some basic requirements: high melting point, no phase transformation between room temperature and component operation temperature, low thermal conductivity, chemical inertness, a thermal expansion coefficient close to that of the metal substrate, good adherence to the metallic substrate and low sintering rate of the porous microstructure [108]. The physical properties of zirconia (ZrO_2) make it ideal for TBC applications. This oxide has a very low thermal conductivity (one and half orders of magnitude lower than that of a typical superalloy, such as MAR M 247) [109, 110], high melting point, inertness and a relatively high coefficient of thermal expansion. However, zirconia undergoes a polymorphic phase transformation when cooled from high temperature. The pure oxide, in fact, can exist in three crystal forms, a cubic structure stable at the highest temperatures, between the melting point ($2710^\circ C$) and $2369^\circ C$ [111], a tetragonal

form stable at intermediate temperatures (2369°C to 1114°C) [14] and a monoclinic form stable at lower temperatures. The tetragonal→monoclinic transformation (t→m) is a martensitic phase transformation and occurs with a large volume expansion, of about 3-5% [112], which compromises the mechanical integrity of the coating. The t→m transformation can be suppressed by total stabilisation of the zirconia in the cubic form, in a material called *Fully Stabilized Zirconia* (FSZ), although the most useful mechanical properties are obtained in a non-equilibrium tetragonal phased material known as *Partially Stabilized Zirconia* (PSZ) [113].

4.2 Stabilized zirconia alloys

Various divalent (e.g. Ca^{2+} , Mg^{2+}), trivalent (e.g. Y^{3+} , Sc^{3+} , Ln^{3+})¹ or tetravalent (e.g. Ce^{4+}) oxides of cubic symmetry can be added to zirconia to stabilize its high temperature phase, inhibiting the t→m phase transformation and the related volume change [114, 115]. Of these stabilizers, yttria (Y_2O_3) is the most widely used; it has a vapour pressure very similar to that of zirconia [116] which is an advantage when the TBC are manufactured by vapour deposition.

Yttria additions between 7wt% and 20wt% lead to Yttria Partially Stabilized Zirconia (Y-PSZ) while additions higher than 20wt% lead to Yttria Fully Stabilized Zirconia (Y-FSZ). The fully stabilized material has, at room temperature, a 30% lower thermal conductivity than the partially stabilized material [117]. Moreover, at temperature above $\sim 1000^\circ C$, it occurs as an equilibrium single cubic phase which is kinetically constrained from transforming at lower temperatures. Despite these advantages, nowadays the 8wt% yttria PSZ, have become the industrial standard to reduce the heat flux into hot-path components within gas turbine engines [118, 119]. Durability studies, in fact, revealed that the Y-PSZ has a cyclic life much longer than the ‘stable’ cubic coatings [120, 121].

Figure 4.1 shows the phase diagram of the $ZrO_2 - YO_{1.5}$ system. The continuous lines indicate the boundaries of the equilibrium phases, while the discontinuous lines indicate the non-equilibrium phase transformations. The standard composition for Y-PSZ is indicated as composition 1². Y-PSZ consists of a metastable tetragonal solid solution, known as t' , which can be thermally cycled without undergoing the disruptive t→m transformation. Although t' is a non-equilibrium phase, the alloy retains its

¹Ln= Lanthanide group metals

² $ZrO_2+6 - 8wt\% Y_2O_3$ corresponds to $ZrO_2 + 7.6 \pm 1mol\%YO_{1.5}$

state, without transforming into a tetragonal+cubic (t+c) assemblage, and without precipitating yttria from the solution for extended periods of exposure at temperature up to 1200°C [115, 122, 123, 124].

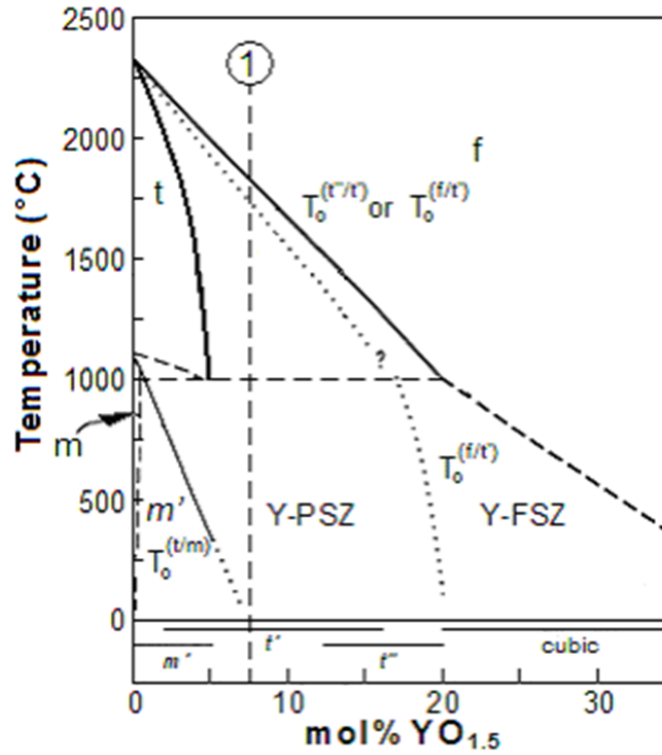


Figure 4.1: Phase diagram of $\text{Zr}_2\text{O}_3-\text{YO}_{1.5}$ system adapted from Yashima *et al.* [14]

4.3 Ceramic coating manufacture

Thermal barrier coatings can be manufactured by different processes, such as Electron Beam Physical Vapour Deposition (EB-PVD) or Air Plasma Spray [125, 126]. Different techniques result in significantly different physical properties and microstructures of the coating [92, 127, 128]. Although more costly than Air Plasma Spray, EB-PVD is the preferred method for high pressure turbine blades, where a good surface finish is paramount and excellent strain compliance and adhesion are required. Only the EB-PVD process and resulting coating microstructure will be covered here in detail.

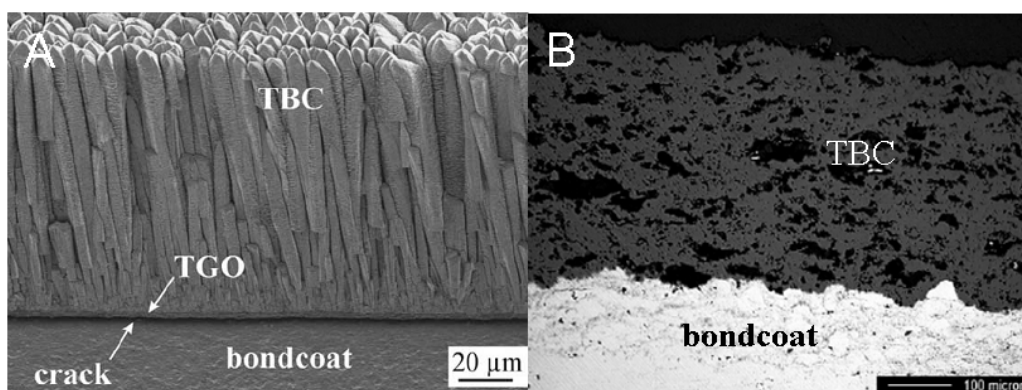


Figure 4.2: TBC microstructure: a) Columnar microstructure of a ceramic top coat manufactured by EB-PVD [15] b) Lamellar microstructure of a ceramic top coat manufactured by air plasma spray [16]

4.3.1 Basic principle of EB-PVD process

The first application of an Electron Beam (EB) heating source for material evaporation under vacuum is dated in the 1930s. In the 1960s high power EB guns were used to develop equipment for high speed evaporation of metallic substances under vacuum. In the 1980s, a modification of such technology allowed the introduction of a new class of protective coatings for gas turbines, known as the Electron Beam Physical Vapour Deposition Thermal Barrier Coating (EB-PVD TBC) [129].

Figure 4.3 shows a schematic representation of an EB-PVD process. In the deposition chamber, the electron beam hits the surface of a sintered Y-PSZ ingot to generate a melt pool under vacuum. In industrial setups the substrates are positioned above the melt only after being preheated at a suitable temperature. The flux of vapour from the pool impinges onto the substrates where it condenses to form the coating. The EB-PVD is a line of sight process, thus, in order to guarantee the coating uniformity, the substrate rotates in the vapour cloud. During evaporation the ingot is bottom fed into the crucibles to ensure continuous coating growth. Oxygen is also bled into the Y-PSZ vapour cloud to minimize any deviations from stoichiometry during coating deposition. This is required since ZrO_2 becomes somewhat oxygen deficient as a result of partial dissociation during evaporation in a vacuum [28]. A typical thickness for an EB-PVD TBC is between $125\mu m$ and $250\mu m$.

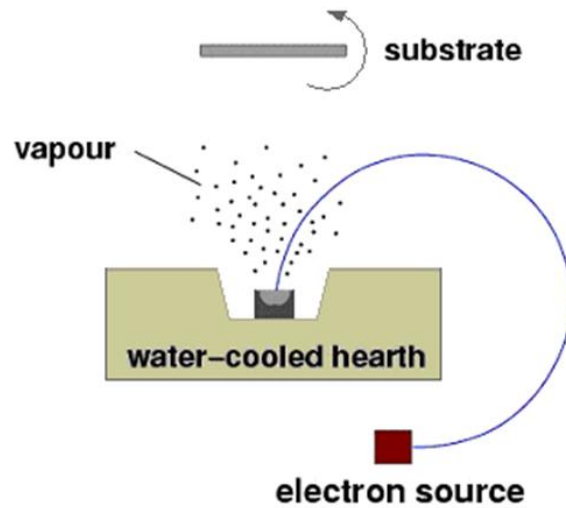


Figure 4.3: Schematic representation of an EB-PVD process; the whole assembly is under vacuum. A magnetic field is adopted to bend the path of the generated electron beam in order for it to focus on the source material [2]

4.3.2 EB-PVD TBC microstructure

The EB-PVD TBC microstructure is characterized by a thin region of polycrystalline Y-PSZ with equiaxed grains (size $\leq 50nm$) at and near the metal/ceramic interface, and by columnar Y-PSZ grains ($5 - 10\mu m$ diameter at the column tops) growing out of the equiaxed grain region to the top coat surface (figure 4.2a) [130, 131]. During deposition, three different scales of porosity are introduced in the coating, as illustrated in figure 4.4.

1. The largest scale of porosity, Type A in figure 4.4, consists of the intercolumnar gaps ($\sim 125nm$), perpendicular to the metal/ceramic interface, separating the columnar grains. Each of these columns exhibit a featherlike structure, which is the result of shadowing, by growth steps, on the column tips near the centre of the column.
2. The second scale of porosity, Type B in figure 4.4, is incorporated within the featherlike structures, and it appears as the segmentation that defines the ‘branches’ of the feather. Such ‘branches’ can be visualized as microcolumns aligned at approximately 50° towards the main column axis. This type of porosity ($5 - 20nm$ across) extends inward for about $200 - 250nm$ and then evolves into discrete pores, typically of high aspect ratio, still aligned along the ‘branches’ plane.

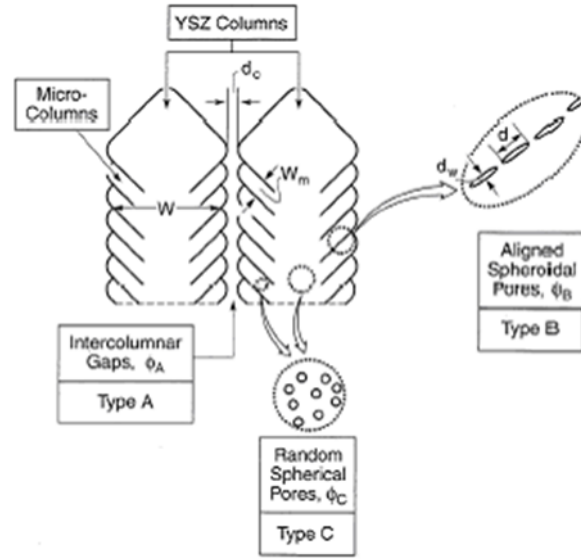


Figure 4.4: Schematic of the TBC pores morphologies and spatial arrangements [17]

3. The last scale of porosity, Type C in figure 4.4, consists of randomly distributed nanoscale spherical pores, more evident near the core of the columns [17, 131, 116]. These pores are generally $20nm$ wide and are the consequence of the substrate rotation during deposition.

The growth morphologies and kinetics of the zirconia columns are strongly influenced by the deposition process parameters, the variation of which results in the production of coatings with different degrees of packing and interaction between columns. The effect of temperature on a PVD layer morphology was investigated for the first time in 1969 by Movchan and Demchishin [18]. They found a clear dependency of the structure of the deposited film on the T/T_m ratio, where T is the substrate temperature and T_m the coating material melting point in K (figure 4.5). Two critical values of such ratio were identified: 0.3 and 0.5; each of them constituting the boundary between two different types of coating structures, or Zones, according to their model. Therefore, three different morphologies could be formed, depending on the T/T_m ratio:

The *Zone 1* type of structure is formed when $0 < T/T_m < 0.3$. At this low temperature, the coating growth is controlled by the transport of the vapourised material to the substrate; the adatoms in fact have insufficient energy to diffuse across the substrate surface very far. Due to their low mobility, the adatoms are unable to overcome the shadowing effect produced by existing grains on the inter-grains areas. This results in

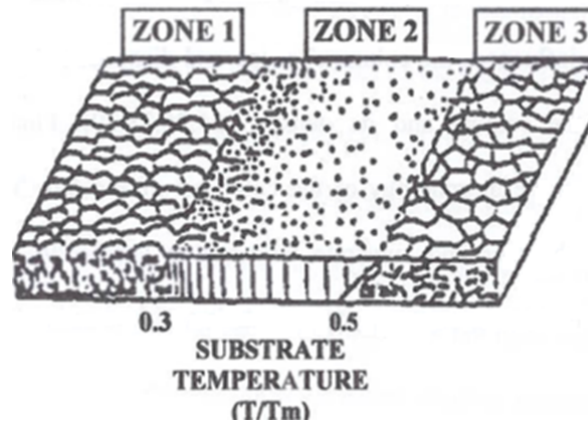


Figure 4.5: Movchan *et al.* structure zone model; T : substrate temperature, T_m : coating material melting point in K [18]

a porous structure consisting of tapered crystallites, with domelike tops, separated by voids. The diameter of the crystallites increases with the coating thickness and with the value of T/T_m ratio. Usually these films carry residual tensile stress after deposition.

The *Zone 2* type of structure is formed when $0.3 < T/T_m < 0.5$. At intermediate temperatures, due to the high thermal energy, the structure growth is controlled by the surface diffusion of adatoms. The result is a structure with faceted columnar grains with dense interfaces.

The *Zone 3* type of structure is formed when $0.5 < T/T_m < 1$. At such high temperature, the thermal energy available to the adatoms allows bulk diffusion that, in turn, controls the structure. This is characterized by equiaxed grains with a smooth surface.

In 1974, Thornton modified the Movchan and Demchishin model adding the effect of the chamber pressure, or Argon pressure, on the film microstructure (figure 4.6) [19]. The resulting model included a fourth zone, *Zone T*, defined as a transition structure between the *Zone 1* and *Zone 2* types of structure. *Zone T* is characterized by densely packed fibrous grains; films with such a structure exhibit high compressive internal stress.

Rigney *et al.* investigated the combined effect on the EB-PVD TBC microstructure of substrate rotation rate and temperature [21], while Kaysser *et al.* examined the effect of vapour incidence angle [20]. Substrate temperature and rotational speed are process parameters that, within certain limits, affect the same microstructural TBC features (figure 4.7). At low temperature and low rotational speed columns often vary

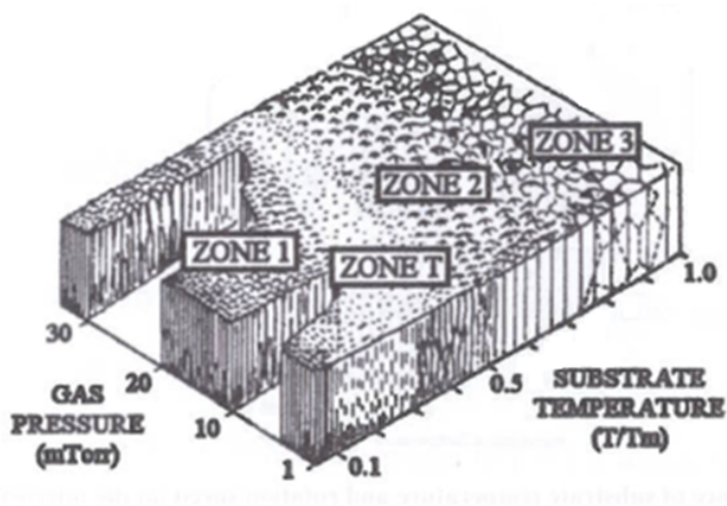


Figure 4.6: Model proposed by Thornton for sputtered metal coatings [19]

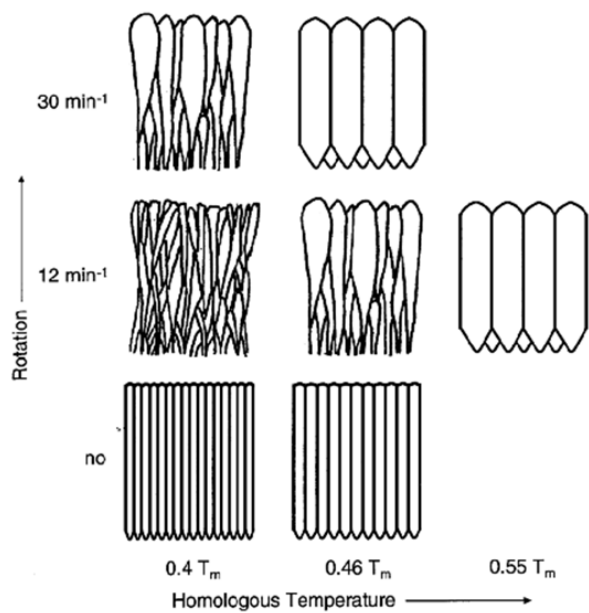


Figure 4.7: Schematic representation of the influence of rotational speed and absolute substrate temperature (expressed as a fraction of zirconia melting point T_m) on columnar microstructure evolution of EB-PVD TBCs [20].

in diameter from root to top or from one column to the other. Columns at the root section are much thinner than at the top and they are enlarging conically from root to top. Increasing both temperature and rotational speed improves the regularity and parallelism of the microstructure and enlarge the column diameter; this microstructure results in coatings with higher density and higher hardness than the previous one [20]. A rotational speed reduction, whilst keeping the deposition temperature constant, facilitates the formation of the so called bent or C-shaped structure in the columns. Such feature can be clearly observed (by scanning electron microscopy) cross sectioning a TBC perpendicularly to the rotation axis (figure 4.8).



Figure 4.8: SEM of the structure of zirconia columns taken in cross section in the plane perpendicular to the axis of rotation [21]

The C-shaped structure is due to the continuous change, during each revolution, both of the vapour impact angle and of the amount of vapour particles that adhere on the sample surface. These variations would be less evident at higher rotational speed. In a C-shaped coating the curved section is periodic through the thickness of the deposited material with a period equal to one revolution of the substrate in the coater. On the other hand, by sectioning the same sample along the direction parallel to the rotation axis (as illustrated in figure 4.9), only a little curvature in the grains of the columns would be observed. This is due to the fact that, in this direction, the angle variation between the substrate surface and the centre of the melt pool during rotation is much smaller than in the previous case [22].

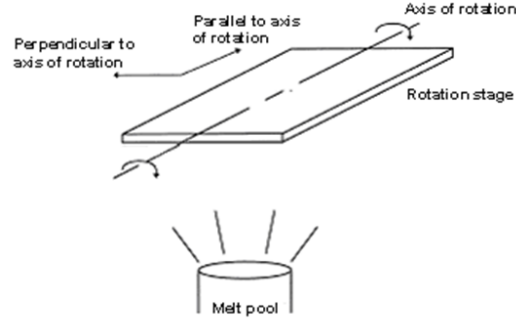


Figure 4.9: Schematic drawing of the rotation stage over the melt pool in the EB-PVD coater [22]

4.4 Thermally Grown Oxide

During the Y-PSZ deposition by EB-PVD process, a gas blend rich in oxygen (flux composition 10%Ar-90%O₂) is introduced in the working chamber to maintain the ZrO₂ stoichiometry. The resulting oxidising environment is sufficient to allow the oxidation of the bond coat during the pre-heating stage of the TBC deposition process. A layer of oxide scale, typically alumina, is then formed at the metallic/ceramic interface; such layer is usually known as a Thermally Grown Oxide (TGO).

The TGO continues to grow during operating conditions in gas turbine engines [132]; the interconnected porosity that always exists in the top coat allows easy ingress of oxygen from the engine environment to the bond coat. It should be pointed out that, even if the top coat was fully dense, the oxygen would still have an easy access: the extremely high ionic diffusivity of oxygen in the ZrO₂-base top coats ($10^{-11} \frac{m^2}{s}$ at 1000°C) [127] renders them essentially ‘oxygen transparent’.

The TGO growth is generally controlled by the inward diffusion of the oxygen through the TGO into the bond coat. Only in some cases it is controlled by the outward diffusion of Al, which leads to the formation of new TGO at the TGO/top coat interface or at the $\alpha - Al_2O_3$ grain boundaries within the TGO [132].

Schulz *et al.* studied the kinetics of the TGO growth on a NiCoCrAlY coating on different substrates tested under cycling oxidation. The growth rate of the TGO can be expressed by the equation:

$$d^n = k'_p t \quad (4.1)$$

where d is the thickness of the TGO, t the time at temperature of test, k'_p the growth

constant and n the exponent. The experimental work showed that the TGO thickness follows nearly the same growth kinetics regardless of the substrate alloy. Moreover, the classical parabolic law [39], with $n = 2$ and $k'_p = 1.5 * 10^{-17} \frac{m^2}{s}$, works well only for short duration tests, while a reasonable agreement with experimental data is obtained with values $n = 3.33$ and $k'_p = 2 * 10^{-16} \frac{m^{3.33}}{s}$ for longer duration tests [44].

TGO growth has to be carefully controlled: the interfacial alumina is designed to act as an oxygen diffusion barrier that retards further bond coat oxidation. Any unwanted excessive TGO growth would cause volumetric expansion which would eventually disrupt by spallation the overlying ZrO_2 layer (see section 4.5.3). The amount of oxidation depends on the time spent at high temperatures. It has been shown that spallation occurs when the oxide at the interface reaches a critical thickness of about $4 - 6 \mu m$ [133]. This means that the ideal bond coat is engineered to ensure that the TGO forms as highly adherent $\alpha - Al_2O_3$ with a slow, uniform, and defect free growth. The TGO plays an important role for TBCs performance: failure in TBCs is almost always initiated at or near the TGO, mostly between the TGO and the bond coat. Although TBC spallation cannot be correlated simply to the TGO thickness [44], control of the growth rate of this oxide should allow an increase in the life of the system.

4.5 TBC system degradation mechanisms

In service, the TBC systems are affected by several degradation modes: they all affect the system performance but only few of them are life limiting. Failure of a TBC system occurs when a significant part (generally indicated as a percentage of the total coated area) of the ceramic coating is lost. This phenomenon, named as *TBC spallation*, results in the exposure of the underlying component to the hot-gas environment. Without its thermal protection, the exposed metal rapidly deteriorates, eventually causing the failure of the component. The individual failure modes are treated in the following paragraphs.

4.5.1 Erosion

During the operations of takeoff and landing the gas turbine engines of an aircraft are exposed to sand and debris ingestion. These solid particulates, together with hard carbon (particles that may be produced in the combustor), are trapped within the gas flow and are likely to hit engine components when the gas passes through the engine.

The impact of this fine particulate causes gradual material removal from the impacted component. This erosion process results in the deterioration of the surface finish which is accompanied by a change in blade geometry [134] and thus in aerodynamic efficiency loss. Moreover, it causes a local reduction of the ceramic thickness which may lead to a local increase of the heat transfer to the component and of the bond coat oxidation rate. EB-PVD TBC erosion depends on the temperature, the velocity, the impingement angle and the size of the impacting material relative to the column diameter [133, 135, 136, 137, 138]. The interaction of these factors generates three different erosion modes:

- *Mode I* erosion occurs both at room and high temperature when the impacting particles are small ($< 100\mu\text{m}$). It results in crack initiation at the elastic/plastic interface due to the impact on individual columns.
- *Mode II* erosion is characterized by the absence of near surface cracking or gross plastic deformation and by the densification of the individual columns. This mode was observed for larger particles and intermediate velocity both at room and high temperature.
- *Mode III* erosion or Foreign Object Damage (FOD) occurs when a limited number of large particles impinge on the ceramic coating at low velocity. This erosion mode causes the highest degree of damage with an extensive compression and ceramic densification. Moreover, outside the TBC compacted area, cracks form and extend to run parallel to the TGO [139].

4.5.2 Calcium-Magnesium-Alumino-Silicate (CMAS) attack

The ingestion of sand, dust and ashes causes ceramic erosion and FOD damage at temperatures below 1100°C , while inducing ceramic fluxing above 1200°C . At this temperature CMAS compounds contained in the ingested debris melt and infiltrate the ceramic layer, and may penetrate down to the TGO layer causing chemical attack to the TBC (figure 4.10). Aluminosilicate compounds attack the TBC grain boundaries leaching yttria out of the zirconia which leads to the detrimental tetragonal/monoclinic transformation into the coating. Moreover, during the engine cool down phase the melt re-solidifies, leading to the introduction of large stresses in the coating which can result in TBC delamination [140, 141].

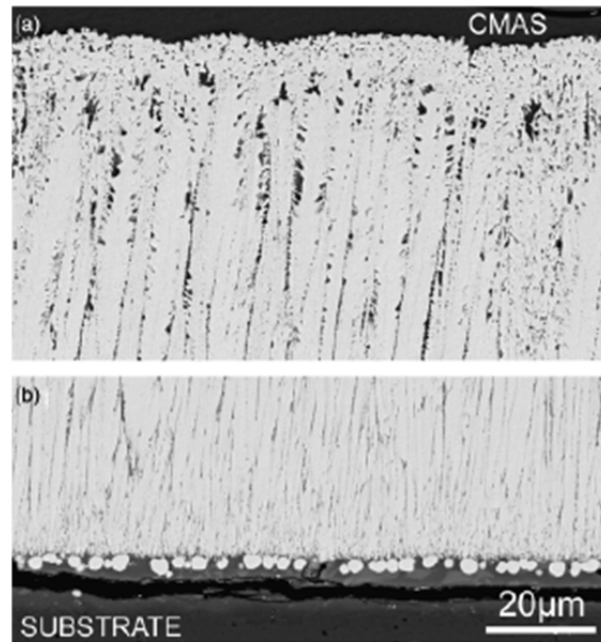
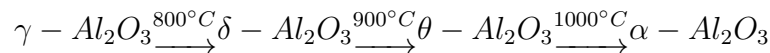


Figure 4.10: Cross-section SEM images of a TBC after exposure to CMAS at 1300°C for 4 hours. a) severe attack at the outer TBC surface; b) attack at the TBC/bond coat interface [23]

4.5.3 Bond coat oxidation

Another source of TBC damage are the changes within the TGO both during the initial scale formation and later due to aluminium depletion in the bond coat. The bond coat composition is tailored to form a continuous layer of $\alpha - \text{Al}_2\text{O}_3$ which is the most stable and slow growing form of alumina out of the several existing aluminium oxide phases. Although the formation of a pure $\alpha - \text{Al}_2\text{O}_3$ layer is desirable, meta-stable alumina phases such as δ , γ or θ are formed in the initial stage of oxidation between 800°C and 1000°C . The formation of these transient alumina is proposed to be, with increase in temperature [142, 143, 144]:



Transitional alumina phases have a detrimental effect on the TBC system life. They do not form an efficient diffusion barrier, hence their presence leads to a greater oxidation rate which, in the case of $\theta - \text{Al}_2\text{O}_3$, is two order of magnitude greater than that of $\alpha - \text{Al}_2\text{O}_3$ [145]. Moreover, transient aluminas have lower density than $\alpha - \text{Al}_2\text{O}_3$ thus the phase transformation from θ to $\alpha - \text{Al}_2\text{O}_3$ is associated to a 10% volume shrinkage.

The localised volume reduction allows residual stresses to be built in the TGO which eventually may cause TBC spallation.

In service, the continuous oxidation and growth of the TGO results in the aluminium depletion of the bond coat. When the aluminium activity in the alloy adjacent to the oxide scale drops below the critical value required to form a continuous layer of Al_2O_3 , oxides of other alloying constituents start forming. The oxide scale degenerates into a mixture of NiO and $NiAl_2O_4$ spinel resulting from the combination of NiO and Al_2O_3 . In comparison with alumina, these oxides are characterized by a lower bond strength with both the TBC and the bond coat which lead to TBC failure by delamination.

4.5.4 Residual stress

The durability of EB-PVD TBC systems is strongly influenced by the residual stress built in the ceramic layer and in the TGO. Moreover, the difference in level of stress between the TBC and the oxide scale control the failure onset and mechanism. EB-PVD TBCs tend to fail at the TGO/bond coat interface; this failure path is due to a significantly higher stress value measured within the TGO in comparison to that measured within the ceramic layer [146].

4.5.4.1 Stress within the TGO

The TGO exhibits, at room temperature, an in-plane compressive stress with a magnitude between $2.4GPa$ and $5GPa$ [88, 147, 148]. This stress has two main contributing components:

- the stress resulting from the thermal mismatch between the bond coat and the oxide scale;
- the stress related to TGO growth.

The TBC system can be assumed to be stress free at high temperature. On cooling to room temperature, a residual stress arises due to the mismatch in the coefficient of thermal expansion (CTE) between the alumina and the metallic bond coat. The contribution of this component to the total residual stress in the TGO has been estimated by Christensen *et al.* to be $\sim 3.5GPa$ in compression, for a system consisting of alumina on Ni_3Al [149].

The exposure to an oxidising environment results in the oxidation of the bond coat. A residual stress arises from the volume increment related to the conversion of a high

density intermetallic to a low density oxide. The compressive stress associated with the TGO growth has been estimated by Cannon *et al.* to be $\sim 3GPa$ [150]. This value is significantly higher than the typical value of approximately $1GPa$ determined by subtracting the calculated thermal mismatch stress from the value of total residual stress determined experimentally. Such a discrepancy may be due to either a theoretical overestimation or to a partial stress relaxation within the TGO. The stress, in fact, exceeds the TGO creep strength, thus part of the stress may be relieved through plastic deformation of the TGO [151].

4.5.4.2 Stress within the TBC

The residual stress within the ceramic layer depends on the manufacturing conditions. Jordan and Faber measured the residual stress of an EB-PVD TBC deposited on platinum aluminide bond coat reporting a value between 270 ± 9 and $304 \pm 15MPa$ in the as-deposited conditions [152]. Upon thermal cycling, these values decrease, hence the stress in the TBC is always significantly lower than that measured in the TGO, and it is unlikely to be the sole cause of TBC failure[151].

Chapter 5

Life data analysis

The *reliability* of a system or a component is defined as its ability to perform the required functions, without failure, under stated conditions for a specified period of time [153]. Each product is required to have a known level of reliability; a failure before the mission duration can have varying effects, ranging from catastrophic consequences, such as an aircraft accident, to minor inconvenience, such as the failure of a washing machine. From a manufacturer point of view both types of failures have to be avoided; the first one because it causes loss of life and property, the second one because it causes customer dissatisfaction that in turn can have disastrous financial effects on the manufacturer. As a consequence, in today's highly competitive environment, a company can succeed only if it knows the reliability of its products and it is able to control it. Ideally, the reliability of a product should coincide with its designed life, in fact, producing a product that operates much past its intended life would impose additional costs on the manufacturer.

Reliability engineering is the branch of engineering that studies the reliability of a population of products by performing *life data analysis*; this allows to estimate the life characteristics of the entire population based on the *life data* or *lifetime* of a sample from the same population. In the context of this thesis life data analysis is important because it constitutes a fundamental tool for investigating the influence of the manufacturing conditions on the lifetime of the TBC systems. In fact, by providing the means for modelling the behaviour of the coatings, life data analysis allows to predict the effects that variations in the deposition procedure will have on the reliability of the coatings when in service. The possibility of modelling the life of the turbine blades and of validating the accuracy of such models has obvious benefits on the maintenance schedule

(and costs) of the jet engine in real life applications. Given the relevance of this topic, its presentation in this chapter is important but it is limited to relevant methods for TBC system lifetime assessment. A thorough review of all possible methods and techniques for modelling experimental data sets and/or validating the models falls outside the remit of this study. The author has purposely avoided discussing all the limitations of the presented methods when not directly relevant to the analysis conducted in this thesis.

5.1 Methodology

Lifetime is defined as the time a component or a system operates before failure; for example it can be measured in hours, miles, cycles-to-failure. The life data analysis of a population of products consists in four main steps [154]:

1. Collecting the life data;
2. Selecting a statistical distribution that can fit the data and model the life of the products;
3. Estimating the parameters of the distribution;
4. Generating predictive plots and results.

The lifetimes are collected by testing, under operative conditions or simulated operative conditions, a sample of units from a population of products. The statistical distribution chosen to model the data consists of a mathematic parametric function called *probability density function* (pdf). The estimate of the parameters allows the distribution to fit the data. The pdf plot can then be used to determine the life characteristics of the entire population of products, such as reliability or probability of failure at a specific time, mean life, $B(X)\text{life}^1$ and failure rate.

¹ $B(X)\text{life}$ is defined as the estimated time when the probability of failure will reach a specified point (X%). For example, if the $B(10)\text{life}$ of a population of products is 2 years, it means that 10% of the population is expected to fail by 2 years of operation; in the same way this means that, after 2 years of operation, is estimated that 90% of the population is still working, therefore $B(10)\text{life}$ is equivalent to 90% reliability.

5.2 Collecting the life data

Life data analysis consists of analysing the lifetime of a sample of units, from a population of products, in order to estimate the life characteristics of the entire population. To make a good prediction, the life data need to be collected following testing of the units under operative conditions; however, in many cases such data are either not available or very difficult to obtain. Most products in fact are expected to have a very long life and often there is not enough time, between the design stage and the release of the product on the market, to collect the data. In order to overcome such difficulties, the reliability engineers design alternative testing methods that, on the one hand accelerate the failure of the tested product, and on the other allow to obtain information or even to quantify the life characteristics of the product under normal use conditions [155]. Such methods, identified as *accelerated life testing*, can be divided into two main categories: *qualitative* accelerated life testing and *quantitative* accelerated life testing.

Qualitative accelerated tests have the only purpose of identifying the failure modes that will occur during the use of the product under operative conditions. During the test, samples are subjected to different type/level of stress such as: a single severe stress, a combination of different stresses or a cyclic stress. The sample passes the test if it does not fail. The sample failure provides useful information about the probable failure mode and the types and level of stresses which need to be employed during the subsequent quantitative accelerated test.

Quantitative accelerated life tests are designed to estimate the life characteristic of the product under normal use conditions. Quantitative accelerated life testing can take the form of *usage rate acceleration* or *overstress acceleration*. The usage rate acceleration test is applied to products that under normal condition do not operate continuously. In this case it is sufficient to operate the tested unit continuously in order to accelerate the failure. Data obtained through usage rate acceleration can be analyzed with the same methods used to analyze regular life data. The overstress acceleration test is applied when the tested product normally has a very high or continuous usage. In this case the product is forced to fail by applying a stress, or a combination of stresses, that exceed the level of stress that the product will encounter under normal use conditions [156]. The obtained overstress life data are then adopted to extrapolate the life data relative to normal use conditions. The main risk involved in the adoption of this mode accelerated life test, is linked to the possibility of choosing stress levels which introduce failure modes that would otherwise never occur under normal use

conditions. To mitigate this issue, while both the type and the level of stress are chosen to fall outside the product specification limits, they will be selected to guarantee that the product is still operating within its design limits [156]. In this study, the accelerated stress is generated through the thermal cyclic testing of the TBC systems at higher temperatures than those normally expected in service; however, temperatures are selected in order not to trigger any failure mechanism not observed in service.

5.2.1 Types of data

The life data collected during an accelerated test can be divided in two main categories:

- complete data,
- censored data.

A set of data is defined *complete* if the life data relative to each tested unit is observed or known. If the set contains uncertain data, for example the exact failure time for the units is unknown, the set is called *censored*. There are three types of censored data:

- right censored,
- interval censored,
- left censored.

Right censored or suspended data are those relative to the units that have not yet failed when the life data are analyzed. The data are defined as *interval censored* if the exact time of failure is uncertain but the interval of time in which the failure occurred is known. This type of data usually comes from tests in which the tested units are not constantly monitored and, as a result, the only information available is a failure that happened between two successive inspections. A particular case of interval censored data is the *left censored* data. In this case the failure time is only known to be before a certain time, which means that the failure occurred at any time between the start of the test and the first inspection. It should be observed that left censored data coincide to interval censored data when the starting time for the interval is zero.

5.3 Statistical distributions

In reliability engineering, the failure of a product is expected to be a random phenomenon, that could happen at any time after the operation start, which is assumed to occur at time zero. The product lifetime can then be indicated as a variable (T) that could take any value bigger than zero; in mathematical terms $T \in [0, \infty[$. Given a random variable T , it is possible to define [157]:

- the probability density function (pdf), of T : $f(t)$ and
- the cumulative distribution function (cdf), of T : $F(t)$.

The pdf, of T , is a function $f(t)$ such that for two numbers, a and b with $a \leq b$, the probability that T takes on a value in the interval $[a, b]$ is given by the area under the function itself from a to b (figure 5.1). In mathematical terms:

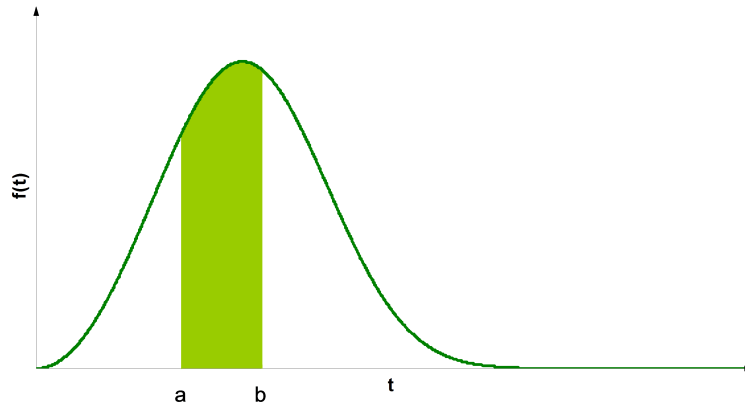


Figure 5.1: Probability density function, $f(t)$

$$P(a \leq T \leq b) = \int_a^b f(t)dt$$

with $f(t) \geq 0 \forall t \in [0, \infty[$.

The cdf, of T , is a function $F(t)$ such that, for a given value t , $F(t)$ is the probability that the observed value of T will be at most t . In mathematical terms:

$$F(t) = P(T \leq t) = \int_{0, -\infty}^t f(s)ds$$

where the limits of integration depend on the domain of $f(s)$.

The mathematical relationships between the pdf and the cdf is given by:

$$F(t) = \int_{-\infty}^t f(s)ds$$

and conversely:

$$f(t) = \frac{d(F(t))}{dt}.$$

This means that the value of the cdf at t is the area, up to t , under the pdf. In other words, for a given time t , the cdf indicates the probability that a random selected unit in the population will fail by the time t . The pdf function takes only positive values and decreases towards 0 as the t increases. The cdf function instead increases monotonically and goes asymptotically to 1 as t approaches infinity. This means that the the total area under the pdf is always equal to 1.

The pdf, $f(t)$, is a parametric function that can have in principle any number of parameters, however, the distributions used in life data analysis have usually a maximum of three parameters. These are known as the *scale parameter*, the *shape parameter* and the *location parameter*. The scale parameter defines where the bulk of the distribution lies. The shape parameter helps defining the shape of a distribution. The location parameter, indicated as γ , defines the location of the origin of the distribution. For a lifetime distribution, the introduction of a location parameter allows to shift the distribution on the time scale; this means that a pdf with a domain on $[0, \infty[$ will have its domain changed to $[\gamma, \infty[$. The location parameter can have both positive and negative values. A positive location parameter indicates that up to the point γ the component is never going to fail. A negative location parameter states that the component failure occurs before time zero, i.e. before the operation start. Although a negative location parameter might be considered meaningless at first, as it represents an apparently unrealistic condition, it indicates a failure that may occur before the component is used the first time, with problems linked, for example, to manufacturing, handling or shipping of the item.

5.3.1 The Weibull distribution

A type of pdf commonly used for analysing life data is the Weibull distribution. This category of analysis is named after Waloddi Weibull who conceived it in 1937. It was described in detail in a paper presented to the American Society of Mechanical Engineers (ASME) in 1951 [158]. According to Weibull, his distribution applies to a wide range of problems and he used seven case studies to demonstrate it.

The three-parameter Weibull pdf is defined by:

$$f(t) = \frac{\beta}{\eta} \left(\frac{t - \gamma}{\eta} \right)^{\beta-1} e^{-\left(\frac{t-\gamma}{\eta}\right)^\beta}$$

for $t \geq \gamma$ and

$$f(t) = 0$$

for $t < \gamma$ where $\beta > 0$, $\eta > 0$, and $-\infty < \gamma < \infty$.

In the Weibull pdf, β is the shape parameter, also known as the *Weibull slope*, η is the scale parameter, and γ is the location parameter of the distribution.

When $\gamma = 0$, the distribution becomes the two-parameter Weibull or:

$$f(t) = \frac{\beta}{\eta} \left(\frac{t}{\eta} \right)^{\beta-1} e^{-\left(\frac{t}{\eta}\right)^\beta}.$$

The adoption of the Weibull distribution in life data analysis has three main advantages: it works with extremely small samples, its output is easy to interpret and informative in a graphical plot (see section 5.8), and it usually provides the best fit of the life data. Studies conducted by R. Abernethy at Pratt & Whitney Aircraft [159] show that even two or three failures, in a population of units, can provide a reasonable failure analysis and failure forecast. This allows to reduce the cost and the time required for a product testing and to start working to a solution at the earliest indication of a problem without waiting for the test completion. Of course, in order for the analysis to have statistical relevance, a larger number of failures is needed.

5.4 Effect of the parameters on the Weibull distribution characteristics

5.4.1 The shape parameter β

The parameter β [160] is a pure number that can assume only positive values. It is called ‘shape parameter’ because changing its value has an effect on the shape of the Weibull pdf. This section describes the influence of the shape parameter on the Weibull pdf, the reliability and the failure rate function. Such functions will be plotted for three different values of β and a fixed value of both the scale parameter ($\eta = 1$) and the location parameter ($\gamma = 0$).

5.4.1.1 Influence of β on the Weibull pdf.

The effect of β on the shape of the Weibull pdf is shown in figure 5.2.

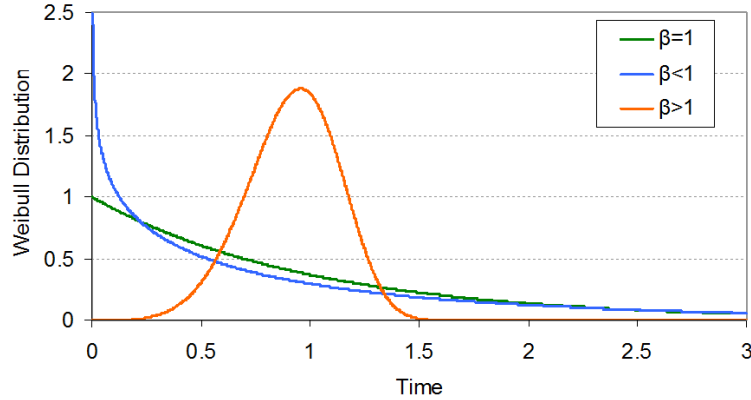


Figure 5.2: Influence of the shape parameter β on the shape of the Weibull distribution function. In the diagram the three curves are plotted for $\beta < 1$, $\beta = 1$ and $\beta > 1$. The values of the other two parameters of the distribution are $\eta = 1$ and $\gamma = 0$.

When $0 < \beta < 1$ the Weibull pdf is a monotonic decreasing function for increasing values of t : $f(t) \rightarrow \infty$ for $t \rightarrow 0$ (or for $t \rightarrow \gamma$) while $f(t) \rightarrow 0$ for $t \rightarrow \infty$.

When $\beta = 1$ the Weibull pdf decreases monotonically: $f(t) = 1$ for $t = 0$ (or for $t = \gamma$) while $f(t) \rightarrow 0$ for $t \rightarrow \infty$.

When $\beta > 1$ the Weibull pdf has a maximum for $t = t_{max}$ where $t_{max} = \gamma + \eta \left(\frac{\beta-1}{\beta}\right)^{\frac{1}{\beta}}$: $f(t) = 0$ for $t = 0$ (or for $t = \gamma$) and for $t \rightarrow \infty$. The value t_{max} is also called the *mode* of the distribution.

For some specific values of the shape parameter the equation of the Weibull distribution is reduced to those of other distributions. In particular, the Weibull pdf becomes:

- the *exponential distribution* [161] for $\beta = 1$ and
- the *Rayleigh distribution* for $\beta = 2$.

For values of β in the interval $]2.6, 3.7[$ the Weibull distribution approximates the *Normal distribution* [162]. In such interval the coefficient of skewness of the distribution approaches zero, thus the Weibull pdf becomes almost symmetrical. The Weibull distribution is positively skewed and it has a right tail for $\beta < 2.6$ whereas it is negatively skewed and it has a left tail for $\beta > 3.7$.

5.4.1.2 Influence of β on the reliability function

The reliability function $R(t)$ [163] represents the probability that a component has to perform successfully a mission of a prescribed duration. The mathematical expression of the Weibull $R(t)$ can be derived from the cdf. As seen in section 5.3, given a time t , the $F(t)$ indicates the probability that a random selected unit in the population will fail by the time t ; as a consequence, the probability that the same unit will survive by the time t can be expressed as:

$$R(t) = 1 - F(t) = e^{-\left(\frac{t-\gamma}{\eta}\right)^\beta}$$

The effect of the shape parameter on the reliability function is shown in figure 5.3.

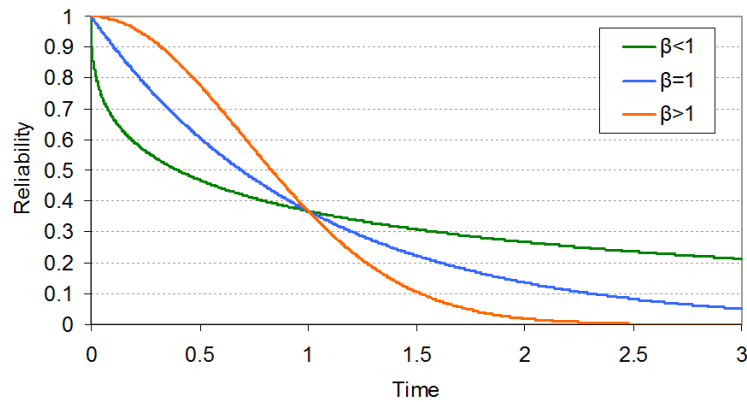


Figure 5.3: Effect of the shape parameter on the Weibull reliability function. $R(t)$ is plotted for three different values of β while the $\eta = 1$ and $\gamma = 0$.

For $0 < \beta \leq 1$, $R(t)$ is a convex function and decreases monotonically as t increases.

For $\beta > 1$, $R(t)$ decreases as t increases. For $t = t_0$ the function has an inflection point $R''(t_0) = 0$ and changes its shape from a concave to a convex function.

Figure 5.4 shows the influence on $R(t)$ of different values of β in the interval $]1, \infty[$. A high value of the shape parameter is desirable since the reliability increases as β increases.

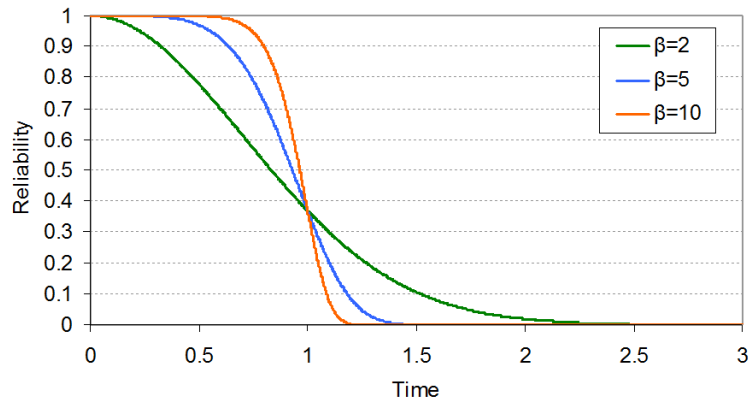


Figure 5.4: Effect of different values of β in the interval $]1, \infty[$ on the $R(t)$

5.4.1.3 Influence of β on the failure rate function

The failure rate is defined as the frequency with which a system or component fails. It is denoted by the Greek letter λ and its mathematical expression is [163]:

$$\lambda(t) = \frac{f(t)}{R(t)} = \frac{\beta}{\eta} \left(\frac{t - \gamma}{\eta} \right)^{\beta-1}.$$

As illustrated in figure 5.5, the value of β has a marked effect on the failure rate of the Weibull distribution. In particular:

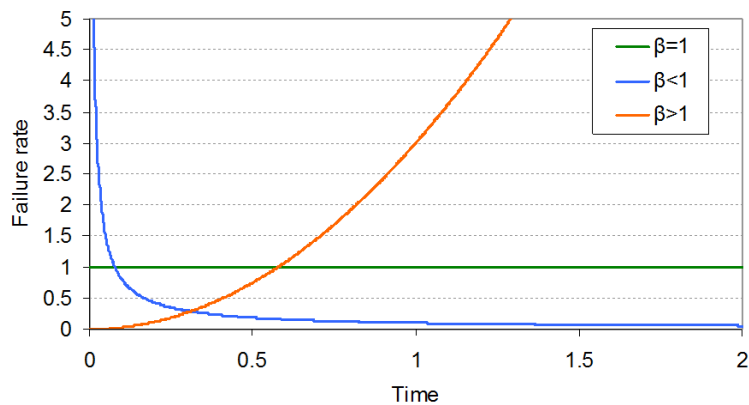


Figure 5.5: Effect of the β value on the Weibull failure rate functions. In the diagram the three curves are plotted for $\beta < 1$, $\beta = 1$ and $\beta > 1$; the values of the other two parameters of the distribution are fixed to $\eta = 1$, and $\gamma = 0$.

- for $0 < \beta < 1$ the failure rate decreases monotonically: $\lambda(t) \rightarrow \infty$ for $t \rightarrow 0$ (or for $t \rightarrow \gamma$), while $\lambda(t) \rightarrow 0$ for $t \rightarrow \infty$;

- for $\beta = 1$ the failure rate is constant over time;
- for $\beta > 1$ the failure rate increases with time.

A high failure rate shortly after the operation start is generally indicated as ‘infant mortality’; this type of trend usually highlights problems in production, in the burn-in period, in the packaging or in the delivery methods. A constant failure rate suggests that an old component is as good as a new one. It means that the failure is caused by random events, such as natural causes, like a flooding or a lightning strikes, or human error, like errors in the product maintenance. The most desirable failure rate trend is the one generated by a $\beta > 1$. In this case the failure is due to a wear-out process, thus the probability of failure in the early stage of the component life is very low.

Although for $\beta \in]1, \infty[$ the $\lambda(t)$ function increases as t increases, its rate changes for different values of β . Figure 5.5 shows $\lambda(t)$ plotted for $1 < \beta < 2$, $\beta = 2$ and $\beta > 2$. In particular:

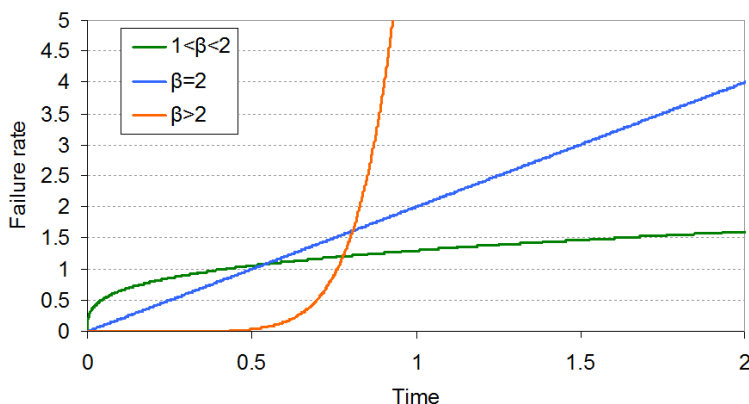


Figure 5.6: Effect of values of $\beta \in]1, \infty[$ on the failure rate. $\lambda(t)$ was plotted for $1 < \beta < 2$, $\beta = 2$ and $\beta > 2$; the values of the other two parameters of the distribution are fixed to $\eta = 1$, and $\gamma = 0$.

- For $1 < \beta < 2$, the $\lambda(t)$ curve is concave thus the rate at which the function increases decreases as t increases ($\lambda'(t) < 0$ for $t > 0$).
- For $\beta = 2$, $\lambda(t)$ becomes a straight line ($\lambda'(t) = const$). The function takes the value of $\lambda(t) = 0$ for $t = 0$ or for $t = \gamma$ and then increases at constant rate with a slope of $\frac{2}{\eta^2}$.
- When $\beta > 2$, the $\lambda(t)$ curve is convex thus the failure rate increases at an increasing rate as t increases ($\lambda'(t) < 0$ for $t > 0$).

5.4.2 The scale parameter η

Figure 5.7 shows the effects of η on the Weibull pdf for a fixed value of β and γ [160]. The area under the pdf has a constant value of one (see section 5.3), thus a change in η ,

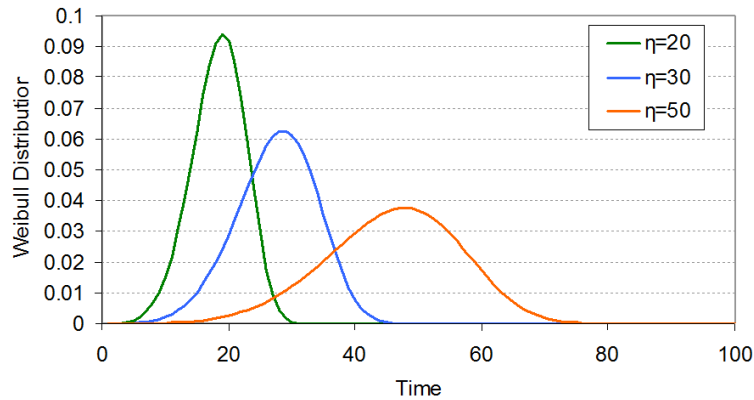


Figure 5.7: Effect of the scale parameter on the Weibull pdf for fixed value of β and γ ; in particular $\beta = 3$ and $\gamma = 0$.

while keeping the same shape and location parameters, results in either the ‘stretching’ or the ‘compressing’ of the pdf along the abscissa. In particular:

- for increasing value of η the pdf stretches out on the right and the maximum value of the distribution decreases;
- for decreasing value of η the pdf gets compressed to the left and the maximum value of the distribution increases.

The scale parameter η has the same units as the abscissa of the Weibull pdf (t).

5.4.3 The location parameter γ

As mentioned in section 5.3, the location parameter γ locates the distribution along the abscissa hence changing its value has the effect of ‘shifting’ the pdf along the t axes. Despite γ has the same unit as a time, it can take any value in the interval $]-\infty, \infty[$; where a value of $\gamma < 0$ indicates the failure of the component before the operation start off. Figure 5.8 shows the effect of a positive location parameter on the position of the Weibull pdf. When $\gamma > 0$, it gives an estimation of the first failure in a population of products; a shift on the right of the pdf, in fact, implies that there are no failures for $t \in [0, \gamma[$ [160].

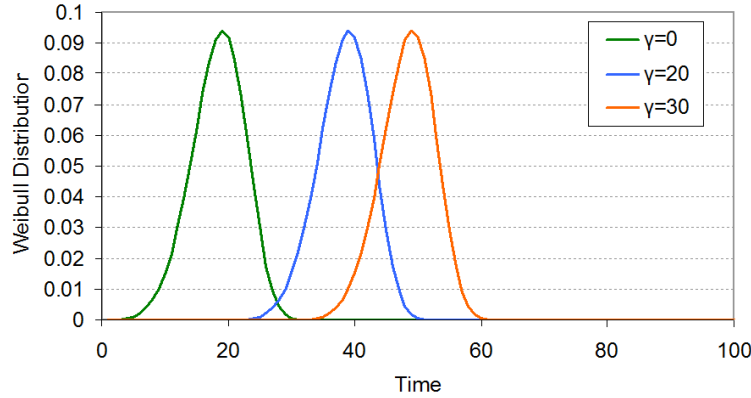


Figure 5.8: Effect of a positive location parameter γ on the Weibull pdf.

5.5 Estimating the parameters of a distribution

Once the distribution has been selected, correct estimate of the parameters allows the pdf to fit the data. The following sections describe parameter estimation by the *probability plotting* method and the *least squares* method [160].

5.5.1 The probability plotting method

The probability plotting method consists of two steps:

1. plotting the life data on a specially constructed *probability plotting paper*;
2. reading the parameters directly from the plot.

This method aims to transform the cdf in the form of a straight line: $Y = mX + c$ [160]. The linearisation procedure in the case of the two-parameter Weibull distribution is:

$$F(t) = 1 - R(t) = 1 - e^{-\left(\frac{t}{\eta}\right)^\beta}$$

$$1 - F(t) = e^{-\left(\frac{t}{\eta}\right)^\beta} \rightarrow \ln(1 - F(t)) = -\left(\frac{t}{\eta}\right)^\beta$$

$$-\ln(1 - F(t)) = \left(\frac{t}{\eta}\right)^\beta \rightarrow \ln(-\ln(1 - F(t))) = \ln\left(\frac{t}{\eta}\right)^\beta \rightarrow \ln(-\ln(1 - F(t))) = \beta \ln(t) - \beta \ln(\eta)$$

$$\ln\left(\ln\left(\frac{1}{1 - F(t)}\right)\right) = \beta \ln(t) - \beta \ln(\eta) \quad (5.1)$$

Setting $y = \ln(\ln(\frac{1}{1-F(t)}))$ and $x = \ln(t)$ the equation 5.1 is transformed in:

$$y = \beta x - \beta \ln(\eta)$$

which is in fact the equation of a straight line. This means that when plotting the life data on a chart with the appropriate x and y axes as those provided by the specially constructed probability plotting paper, they will be arranged approximately along a line indicated as the *Weibull plot*. The parameters of the pdf can be read directly from the plot: the shape parameter is given by the slope of the plot while the characteristic life can be determined from the intercept of the line with the x axis ($y = 0$).

5.5.2 The least squares method

The least squares method is based on the same idea as the probability plotting method but rather than fitting the best straight line through the set of points by eye, the best approximation is determined by regression analysis. The main consequence of an analytical approach is the possibility of evaluating quantitatively how well the model fits the experimental data. With this method the line is determined minimizing the sum of the squares of the distance of the data points to the fitted line. Two different minimisations can be performed achieving different results (see figure 5.9). The regression X on Y is the minimization in the vertical direction; it consists of minimizing the distance of the vertical deviations from the points to the line. The regression Y on X is the minimization in the horizontal direction; it involves minimizing the distance of the horizontal deviations from the points to the line. Research conducted by Berkson

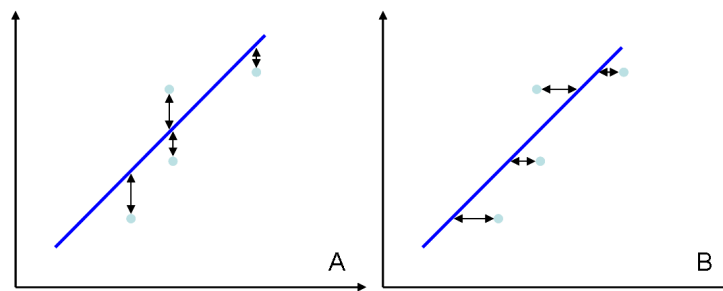


Figure 5.9: Two different minimisations can be performed: A) Minimization in the vertical direction; B) Minimization in the horizontal direction.

recommends selecting the scale with the larger variation as the dependent variable. In the typical Weibull plots, the X variable has more scatter and error than the Y variable.

Consequently the most used method for fitting the life data in a Weibull plot involves regressing X on Y [164].

5.6 Generating plots and results

In order to predict the life of a population of components, N units from the same population have to be tested to failure and their lifetimes ($t_1, t_2, t_3, \dots, t_N$) collected. Building the Weibull plot consists of three steps [164]:

- ranking the data from the shortest lifetime to the longest;
- estimating the $F(t_i)$ for each lifetime t_i , where $1 \leq i \leq N$;
- plotting the data and estimating the distribution parameters.

Ranking the samples allows to determine the position along the abscissa (t axis) for each unit, while estimating $F(t_i)$ provides the percentage of the entire population failing before t_i . It should be noted that the real value of $F(t_i)$ is unknown unless the entire population of components is tested. Several different approaches can be used to estimate $F(t_i)$. In his paper in 1951 [158], Weibull adopted the *mean ranks method*. This consisted of estimating $F(t_i)$ using $F(t_i) = \frac{i}{N+1}$. Later, Johnson [165] suggested an alternative method, the *median ranks method*, as more accurate. The latter requires estimating $F(t_i)$ by setting, for each i , the cumulative binomial distribution equal to 0.5 and solving the equation for the variable MR as defined by the following equation:

$$\sum_{k=i}^N \binom{N}{k} (MR)^k (1 - MR)^{N-k} = 0.5$$

where N is the number of samples, MR is the median ranks and i is the order number. Today the adoption of the median ranks is considered the best practice; although, when a reasonable volume of data is available, the different methods of estimating bring very little difference in the results [159].

The $F(t_i)$ values are used eventually to calculate $\ln(\ln(\frac{1}{1-F(t_i)}))$ which, in turn, provides the parameters of the distribution, when processed with one of the two methods described in section 5.5.

5.7 Validating the model

In practical terms, the fact that the plotted data cluster around a straight line signifies that the Weibull distribution is modeling the life data closely. However, the goodness of fit can be, in general, measured quantitatively by calculating the *Pearson product-moment correlation coefficient* [166]. Such a coefficient, typically denoted by r , is a measure of the correlation or linear dependence between two variables X and Y . For a sample of units from a population, r is calculated as:

$$r = \frac{\sum_{i=1}^N (X_i - \bar{X})(Y_i - \bar{Y})}{\sqrt{\sum_{i=1}^N (X_i - \bar{X})^2} \sqrt{\sum_{i=1}^N (Y_i - \bar{Y})^2}}$$

where N is the number of units, X and Y are the two variables and \bar{X} and \bar{Y} are defined by:

$$\bar{X} = \frac{1}{N} \left(\sum_{i=1}^N X_i \right)$$

and

$$\bar{Y} = \frac{1}{N} \left(\sum_{i=1}^N Y_i \right).$$

In principle, r can assume values between $+1$ and -1 ($r \in [-1, 1]$) depending on the line slope. An r value close to $|1|$ indicates a good fit while a value close to zero indicates that the data are randomly scattered and that they do not have any pattern or correlation in relation to the regression line model. In the particular case of a Weibull analysis, r assumes only positive values (the plot has always a positive slope) and it can be seen as a measure of the strength of the linear relationship between the median ranks and the life data [166].

In many cases, statisticians adopt the *coefficient of determination* R^2 instead of r to measure the goodness of fit. In case of a linear model fitted by a least squares regression, R^2 is defined by the square of the sample correlation coefficient between the observed and modelled (predicted) data values. In this case, R^2 can assume values between 0 and 1 ($R^2 \in [0, 1]$). The value is not directly a measure of how good the modelled values are, but it is equal to the percentage of the variation in the data that is explained by the fit to the distribution. In other words, if R^2 is 0.9, then it means

that 90% of the variation in the data set can be accounted for by the statistical model. Moreover, an R^2 of 1 indicates that the regression line perfectly fits the data.

5.8 An example of Weibull analysis

Figure 5.10 shows an example of Weibull analysis, not referring to any meaningful experimental case, but only provided here to clarify the concepts presented in this chapter. The plot has been obtained by implementing in Microsoft Excel the probability plotting method (section 5.5.1) [167]. The horizontal scale is a measure of life while

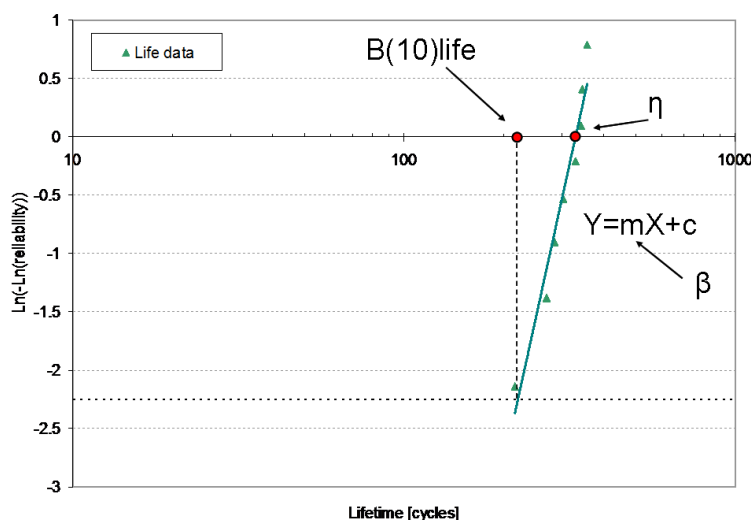


Figure 5.10: Example of Weibull analysis. The diagram illustrates how/where to read β , η , and the B(10)life directly on the plot.

the vertical scale gives a measure of the cumulative percentage of samples failed in the analysed population of products. Each green triangle represents the time to failure of a single product, while the green line (determined as an interpolation of the experimental data) is the actual Weibull plot. The two defining parameters of the Weibull distribution and the B(X)life can be directly read on the plot. The shape parameter β is the slope of the line that interpolates the data, while the scale parameter η is the intersection of this line with the X axis. B(X)life is defined as the estimated time by which the probability of failure has reached the specified level of X%.

In order to choose the unit of the horizontal axis the physics of failure must be analysed; turbine parts usually fail as a function of time at high temperature or as the number of hot-to-cold cycles. In this work, TBC systems were tested in cyclic oxidation,

therefore, the chosen units of age was the number of cycles.

The quality of the data interpolation was determined by the calculation of R^2 , and by comparing this value with the critical R^2 ($R_{critical}^2$) [166]: if $R^2 > R_{critical}^2$ the quality of fit is considered good. In case the Weibull analysis were to provide a poor data fit, other distributions should be taken in consideration, like the *lognormal distribution* [168]: the data should be plotted on other probability papers and the distribution that provides the best fit should be chosen. In reality, in order to accurately discriminate between the Weibull and other distributions, a data set with at least twenty failures is needed; therefore for small data set the Weibull distribution is generally considered as the best choice [166].

Part II

Materials and methods

Introduction to the experimental procedure

In this program two different Thermal Barrier Coating (TBC) systems were studied:

- A TBC system with a *Pt*-diffused bond coat
- A TBC system with a *Pt*-modified aluminide bond coat.

The aim of this part of the thesis is to describe the experimental procedure followed to develop, produce, test, and characterise the two TBC systems. Given the level of complexity of such procedures, their description is supported by two flowcharts with an increasing level of detail. Each flowchart consists of a schematic diagram in which each block represents either one or a series of experimental steps; a colour scheme, adopted for the blocks, visually allows making a distinction between these two cases.

Blocks representing an experimental step that includes sub-steps are green, blocks which do not include sub-steps are red. The flowcharts are labeled as:

- Level 0
- Level 1

Figure 5.11 shows the flowchart ‘Level 0’ which represents the most basic description of the experimental procedure and will be introduced here to start familiarisation with the process. Nickel-based superalloy coupons were used as substrates for the production of the two TBC systems. After surface finish preparation, all coupons were coated with *Pt* and then divided into two sets of samples. One set followed the manufacturing route to obtain a *Pt*-diffused bond coat, while the other followed the production route to obtain a *Pt*-modified aluminide bond coat. When the production of the two bond coats was completed, the two sets of samples were put together for the ceramic deposition and then, eventually, tested.

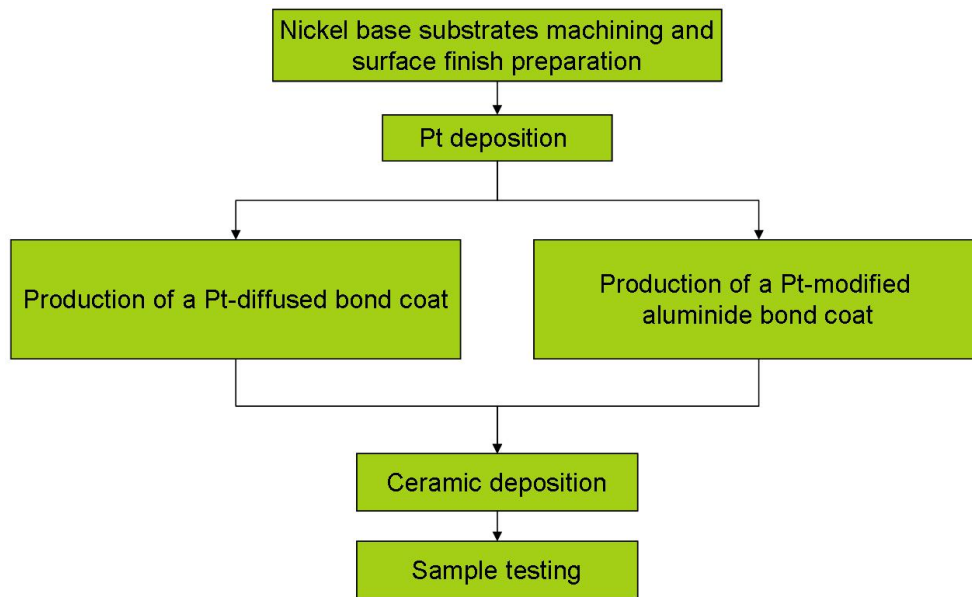


Figure 5.11: Flowchart ‘Level 0’: General description of the TBC systems production process

Figure 5.12 shows the flowchart ‘Level 1’, which is used as a graphical support for the description of both apparatus and procedures adopted for specimens manufacturing, analysis, and testing. The red coloured blocks signify that each of them represents a single experimental step. The diagram includes three main elements: the blocks, which give information about the steps in the experimental procedure, the connectors, which show the sequential order of the manufacturing/testing steps, and one or more symbols pictured next to the block connectors. Each symbol is a schematic representation of a complementary operation that was carried out on the specimens between two consecutive manufacturing steps. Table 5.1 illustrates these symbols (left-hand column) and their meaning (right-hand column).

CMSX-4 is the code of the *Ni*-based superalloy used as a substrate for the two TBC systems. The composition of CMSX-4 is given later in table 6.1. The surface of the CMSX-4 coupons was either grit blasted or ground to achieve the requested surface finish. After cleaning and characterising the surface texture, the coupons were coated with platinum by Physical Vapour Deposition (PVD). The samples were weighed before and after *Pt* deposition with the aim of controlling the amount of *Pt* deposited. At this point half of the samples was heat treated to obtain a *Pt*-diffused bondcoat, while the other half was heat treated, aluminised by Chemical Vapour Deposition (CVD) and heat treated again to obtain a *Pt*-modified aluminide bondcoat. The samples surface

texture was assessed after the completion of each of these steps. Following bondcoat manufacturing, all samples underwent a deposition of Yttria Partially Stabilized Zirconia (Y-PSZ) by Electron Beam Physical Vapour Deposition (EB-PVD). The sample weight gain was used to monitor the amount of ceramic material deposited. After completion of the manufacturing process, the TBC systems were tested using a cyclic oxidation test. Some of the samples were analysed to characterise the coating, using various techniques, described in detail in section 10.2. Such characterisation processes were performed at various stages both during the manufacturing procedure and after testing.

Part II structure

The experimental procedure briefly described in the previous section is explained more in depth in the following chapters. Given the large amount of experimental details to be presented, the whole of part II has been divided into several chapters, in which the single steps are individually discussed:

Chapter 6: Nickel-based substrates machining;

Chapter 7: Platinum deposition;

Chapter 8: Bondcoat manufacturing;

- Production of a *Pt*-diffused bondcoat
- Production of a *Pt*-modified aluminide bondcoat

Chapter 9: Ceramic deposition;

Chapter 10: Testing methods.

The first four chapters correspond to the various production phases, while the fifth to the testing procedure. Each of these chapters describes materials, procedures for samples preparation, and the pieces of equipment necessary for coating manufacture. All test results will be listed and discussed in part III.


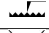


SYMBOL	MEANING
	Cleaning procedure
	Surface texture characterization
	Weight assessment
	Coating characterization (FIB, XRD EDS, SEM)

Table 5.1: List of operations that were carried out, on the specimens, between two consecutive manufacturing steps

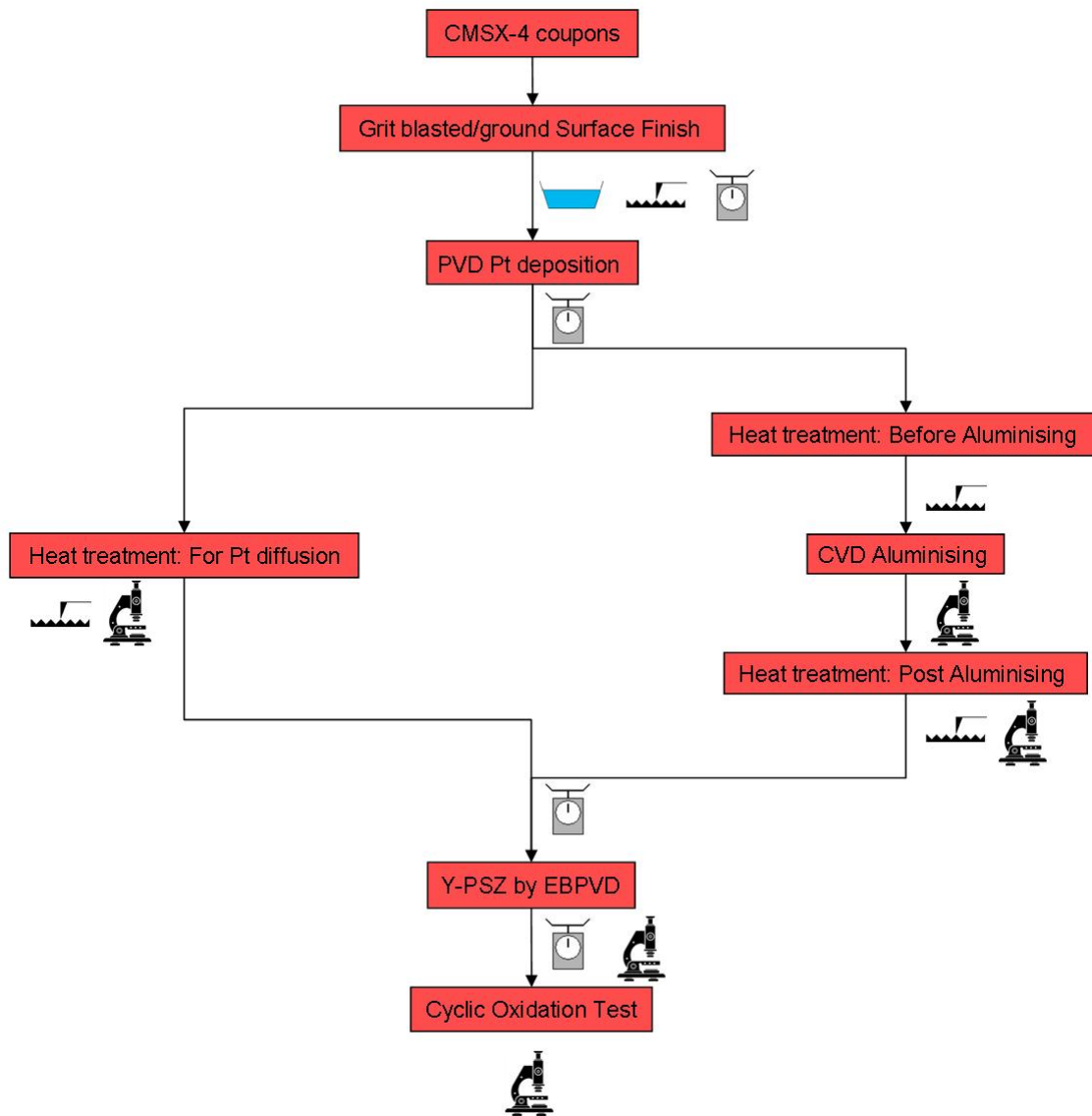


Figure 5.12: Flowchart 'Level 1': General description of the TBC systems production process

Chapter 6

Nickel-based substrate machining

6.1 Substrate material characteristics

CMSX-4 is the material used as a substrate for the two TBC systems produced. CMSX-4, developed by Cannon Muskegon Corporation, is a second generation nickel-based single crystal alloy. This rhenium-containing alloy is characterised by ultra high strength and it is capable of peak temperature/stress operation of at least $1163^{\circ}C$. The alloy microstructure consists of two main equilibrium phases: the γ' phase - Ni_3Al , Ni_3Ti or $Ni_3(Al, Ti)$ - as a precipitate and the γ phase - Ni - as a matrix. The nominal composition of the alloy is given in table 6.1.

Element	Ni	Al	Cr	Co	Ti	W	Re	Ta	Mo	Hf
Weight percent	61.7	5.6	6.5	9.0	1.0	6.0	3.0	6.5	0.6	0.1

Table 6.1: Nominal composition (wt%) of CMSX-4 [25]

6.2 Substrate surface finish

CMSX-4 rods with various diameters were cast at Rolls-Royce, with the same procedure as High Pressure (HP) single crystal blades. Using a wire Electrical Discharge Machining (also known as Spark EDM), each rod was first machined along the length to obtain a block with at least 2 perpendicular surfaces, and then it was sliced into $3mm$ thick coupons. The resulting shape of the coupons was linked to the original dimension of the rod: some of the coupons were square with $15mm$ edge (figure 6.1A), while others had a more irregular shape with two perpendicular edges (figure 6.1B).

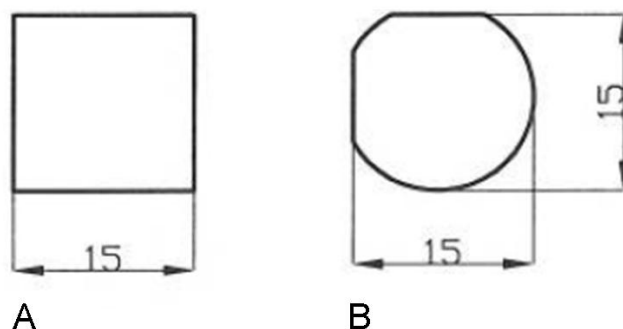


Figure 6.1: CMSX-4 coupons: A) Square coupons; B) Irregular shape coupons.

The specimens were either ground or grit blasted prior to Pt deposition. Six different surface finishes are considered: 2 ground surfaces and 4 grit blasted surfaces. The two ground surfaces were labelled respectively as:

- Coarse surface finish (or simply Coarse ground),
- Fine surface finish (or simply Fine ground).

The four grit blasted surfaces were named according to the blasting pressure that was used during the blasting procedure, as follows:

- $0.05MPa$,
- $0.1MPa$,
- $0.2MPa$,
- $0.4MPa$.

6.2.1 Ground surface finishes

The two different ground surfaces were prepared using a Edgetek 5 axis SAM (SuperAbrasive Machining) manufactured by Holroyd. The machine was equipped with a grinding wheel, a component support and a nozzle for the refrigeration fluid outlet (figure 6.2). The samples, in couples, were fixed using wax on the component support (figure 6.3). The latter consisted of a stainless steel plate provided with a reference surface; such reference allowed the alignment of at least one of the coupon edges to the rotation axis of the grinding wheel. In fact, the pattern eventually ground on the

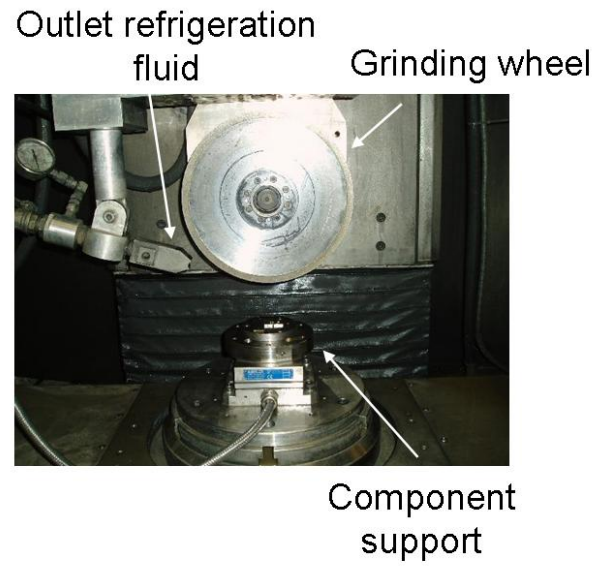


Figure 6.2: Grinding machine set up

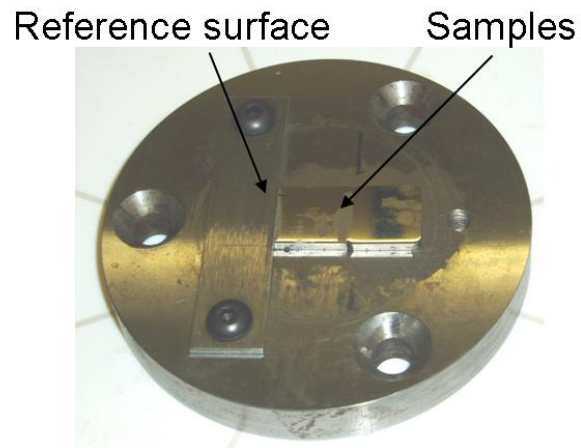
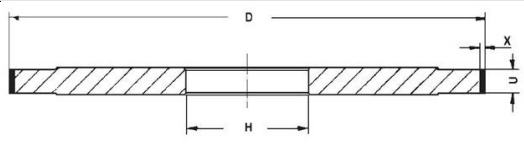


Figure 6.3: Two CMSX-4 coupons fixed with wax on top of the component grinding support. A reference surface was used to simplify the alignment of one of the coupon edge with the rotation axis of the grinding wheel.

sample surface is directional and, using the reference surface, allowed to define a consistent pattern direction for all samples. The samples were cut moving the grinding wheel across the sample surface. The grinding machine was capable of working independently in automatic mode according to a preloaded program specifying the rotation speed of the wheel (V_w), its feeding rate (F), the depth of the cut (DOC), and the number of cuts. A Castrol Hysol XH (2% oil in water) was used as a cooling fluid during all grinding procedures. The resulting surface finish consisted of a series of groves running parallel to each other and, because of the selected sample position, parallel to at least one of the coupons edges.

6.2.1.1 Coarse surface finish

Sixty CMSX-4 coupons were ground to obtain the desired coarse surface finish. The cutting tool was a grinding wheel manufactured by Winter; it consisted of a single layer of Cubic Boron Nitride (CBN) as abrasive, bonded to the wheel body by electro-deposition. The FEPA (Fédération Européenne des Fabricants de Produits Abrasifs) designation for the grit size is B91 (see table 6.2 for full wheel identification). The



Surface finish	Coarse	Fine
Wheel type	1A1	K1A1
Diameter (D)	275mm	300mm
Bore size (H)	76.2mm	76.2mm
Abrasive rim dimensions	U=20mm, X=5mm	U=20mm, X=3mm
Grit size	B91	B46
Bond	GSS	KSS 10N
Concentration	N/a	V180K

Table 6.2: FEPA identification for the two grinding wheels adopted in the program. The achieved type of surface finish is indicated in the top row.

grinding procedure consisted of three steps:

1. One cleaning cut with $20\mu m$ DOC;
2. One cut with $10\mu m$ DOC;

3. Two cuts with $5\mu\text{m}$ DOC.

All steps were carried out using a $V_w=30\text{m/s}$ (2084 rpm) and a $F = 100\text{mm}/\text{min}$. Before starting the grinding process, the wheel was conditioned by means of 5 cuts, with 1mm DOC and $F = 100\text{mm}/\text{min}$, on 60HRC M50 steel.

6.2.1.2 Fine surface finish

Out of the sixty specimens machined as described above, twenty-six coupons underwent a further automatic grinding process to obtain a fine surface finish. The samples were ground in pairs using a Winter CNB resin bond wheel; the grit size designation according to the FEPA standard was B46 (see table 6.2 for complete wheel identification). The grinding procedure consisted of two steps:

1. Eight cuts with $5\mu\text{m}$ DOC and $F = 100\text{mm}/\text{min}$;
2. Two cuts with $5\mu\text{m}$ DOC and $F = 50\text{mm}/\text{min}$.

For both steps the rotation speed of the wheel was $V_w = 40\text{m/s}$ (2546rpm).

The nature of this wheel required, as a part of the grinding procedure, performing a dressing cycle on the wheel. This operation aimed at keeping the wheel efficient, removing the bonding material and exposing the abrasive particles. In order to maximise its performance, the wheel was dressed always after use. The dressing procedure consists of 3 cuts, with a 0.25mm DOC, on an alumina bar (AA220 L VL (ZZ)); the feeding rate and the rotation speed of the wheel in the dressing stage were $1\text{mm}/\text{min}$ and 40m/s , respectively.

6.2.2 Grit blasted surface finishes

Four different grit blasted surfaces were prepared using a pressure-type machine (PTM) manufactured by Guyson International Limited. The grit blasting was performed for approximately 10 seconds per sample, keeping a distance of roughly 15cm between the nozzle and the sample. The blasting medium was 220grit brown alumina and four different blasting pressures were used: 0.05MPa , 0.1MPa , 0.2MPa , and 0.4MPa . Each of these values was used to identify the specimens produced at that specific blasting pressure.

It should be pointed out that a grit blasting procedure is adopted commercially to prepare the surface of the blades before Pt deposition, although details of such a

procedure, including the values for the blasting pressure and the medium grit size, are sensitive data and cannot be disclosed freely. Nevertheless, the blasting procedure chosen in this work can be considered representative of the method adopted industrially; in fact, the actual blasting pressure used in commercial operation is within the range used here.

Ground surfaces, instead, are not commercially used. The study conducted on this type of surfaces aims at understanding a possible effect of the groves on the TBC systems performance. The grinding procedure adopted here was conceived in order to achieve two types of ground surfaces showing a similar pattern in the surface irregularities but having different roughness values. Both coarse and fine surfaces show, in fact, a series of groves running parallel to each other but the roughness values are significantly different, with the coarse surface showing an R_a value which is double the value of the fine surface (see section 12.1). The grit size for the grinding wheels was chosen in order to achieve a surface finish having a roughness comparable with the surface roughness achieved via the grit blasting procedure. This will allow to study the effect on TBC systems performance of surface having similar roughness but showing either a directional (ground surfaces) or an even (grit blasted) pattern.

6.3 Cleaning procedure

After surface machining and finishing the substrates were brushed, to remove any debris from the grinding/grit blasting procedure, and cleaned by means of organic solvents in an ultrasonic bath. The cleaning procedure consisted of three steps:

- 30 minutes in ultrasonic bath with acetone,
- 30 minutes in ultrasonic bath with isopropanol,
- 30 minutes in ultrasonic bath with Analar¹ isopropanol.

The samples were rinsed after each step with Analar isopropanol.

¹An Analar product is a chemical reagent of high purity generally for use in chemical analyses.

Chapter 7

Platinum deposition

7.1 Sputtering equipment

In order to cover a wider range of process conditions, two different sputtering apparatus were used to deposit the platinum layer: a Nordiko2500 unit, and a custom designed 840 four magnetron sputter deposition coater. The two machines work according to the same principle which is schematically presented in figure 7.1. Sputtering is a process

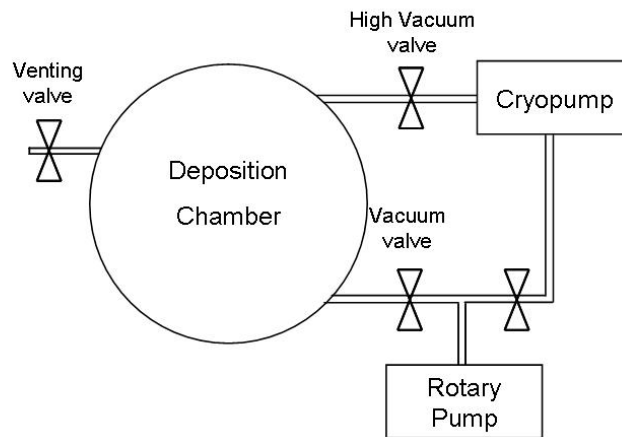


Figure 7.1: Sputtering apparatus overview

carried out under vacuum, thus the deposition chamber is connected to a pumping system consisting of:

- a rotary pump, which evacuates the deposition chamber down to $10^{-1}mbar$;

- a cryopump, which evacuates the deposition chamber down to 10^{-6} mbar . This pump is manually connected to the chamber through the high vacuum valve when the pressure in the chamber reaches 10^{-1} mbar .

As well as the connections to the vacuum apparatus, the deposition chamber is provided with a water cooling system for the walls and the base, a gas inlet, which allows argon injection during deposition, and a venting valve. The chamber is, in fact, kept constantly under vacuum and the venting valve allows access to atmospheric pressure when loading and unloading the samples. Inside, the deposition chamber can hold several different targets: up to 4 in the 840 sputter and up to 6 in the Nordiko2500. Each target is clamped onto a water cooled magnetron and connected to a power supply that can be Direct Current (DC), pulsed DC or Radio Frequency (RF). A copper plate is placed between the target and the magnetron to prevent the direct contact with the cooling water, which might cause corrosion and/or contamination of the target. The choice of copper for this purpose is due to its very good thermal conductivity as well as on its minimal influence on the magnetic field generated by the magnetron. The chamber is also equipped with a substrate holder rotation system which allows changing the position of the specimens in order to place them, in turn, in front of each target. As a result, in both the sputtering units, it is possible to produce multi-layer coatings without the need of opening the chamber during the process and, therefore, without breaking the vacuum, between the deposition of the subsequent layers.

7.2 Platinum target and sputtering method

Only a single type of target was used for the purpose of this study: a 99.99% pure, $101.6 \text{ mm} \times 203.2 \text{ mm}$, platinum target. The same target was used in both sputtering units. The *Pt* was deposited at room temperature by DC magnetron sputtering; the power supply was operated in current regulation mode and the magnetron power during sputtering ranged between 70 and 350W depending on the deposition rate desired. This method has the advantage of a high deposition rate; the magnetic field generated by the magnetron enhances the plasma density increasing, as a consequence, the deposition rate. On the other hand, the magnetic field created a ‘doughnut’ shape of the plasma, which resulted in an inhomogeneous metal consumption on the target and, hence, in the formation of an erosion track on the metal target surface.

7.3 Sample holder

A suitable specimens holder was designed and built to hold the samples during deposition (figure 7.2). It consists of a square Aluminum plate in which 23 holes were



Figure 7.2: Samples holder for platinum deposition

machined to accommodate the specimens. Each hole has an inner lip that allows holding the sample both in vertical and face-down position.

7.4 Calibration of deposition rates

Although sputter deposition is a line of sight deposition process, the position of each specimen with respect to the target has an effect on the amount of platinum deposited; as a consequence, the deposition rate is not constant across the holder. Two different methods were adopted in order to evaluate the deposition rate:

- a *step measuring* technique,
- a *weight gain* technique.

The two techniques are illustrated in the following paragraphs, while the results of the calibrating depositions are shown in detail in chapter 11. Both the methods involve running a calibrating deposition, the first measures the thickness of the deposited *Pt* layer, the second its weight. When comparing structures obtained using different sputtering parameters, as in this study, it is fundamental to have both these pieces of information as the microstructure and density of the *Pt* layer strictly depends on the deposition settings.

7.4.1 Step measuring technique

This technique allows to determine the deposition rate as $\mu m/minutes$ and it involves three steps:

1. running a calibrating run for each set of process conditions adopted in the study,
2. measuring the thickness of the deposited layer for each sample position in the holder,
3. dividing this value in μm by the deposition time in minutes to determine the deposition rate.

7.4.1.1 Calibration run: substrate material

An established practice in the group indicates glass slides as a suitable material for calibration runs; their smooth surface, in fact, allows easy measurement of the coating thickness (see 7.4.1.3). Nevertheless, glass plates were used only in one trial and were subsequently replaced by Nimonic 75, *NiCr* alloy believed to be more suitable for this use as more similar material to CMSX-4. This particular alloy was selected after taking into consideration both availability and cost. Its chemical composition is reported in table 7.1. Nimonic 75 has the following advantages over glass:

- reduces the error in deposition rate assessment because glass is not conductive and the charging effect in the early stage of deposition affects the deposition rate;
- excellent adhesion of the *Pt* layer with 0% spallation of the coating.

Element	Ni	Cr	Ti	Si	Cu	Fe	Mn	C
Weight percent	Base	18-21	0.2-0.6	≤1.0	≤0.5	≤5.0	≤1.0	0.08-0.15

Table 7.1: NIMONIC alloy 75 chemical composition (wt%) (Special metals)

The use of metal as a calibration substrate has the drawback of requiring a complex surface preparation before each calibration run. In order to measure the coating thickness, in fact, the *Pt* layer has to be deposited on a smooth surface, which means that the Nimonic 75 samples needed to be polished to a ‘mirror finish’ before every single run.

7.4.1.2 Calibration run: substrate preparation procedure

The aim of the calibrating runs was to assess the deposition rate for each of the 23 substrates positions in the samples holder. For this purpose, 15mm sided square coupons were cut from a, 1.5mm thick, sheet of Nimonic 75. Using melted wax, the specimens were bonded to an aluminium plate (figure 7.3A); this operation ensured a good contact between the sample surface and the grinding media during the polishing procedure. Once the wax was solidified, the aluminium plate was attached to a polishing plate with

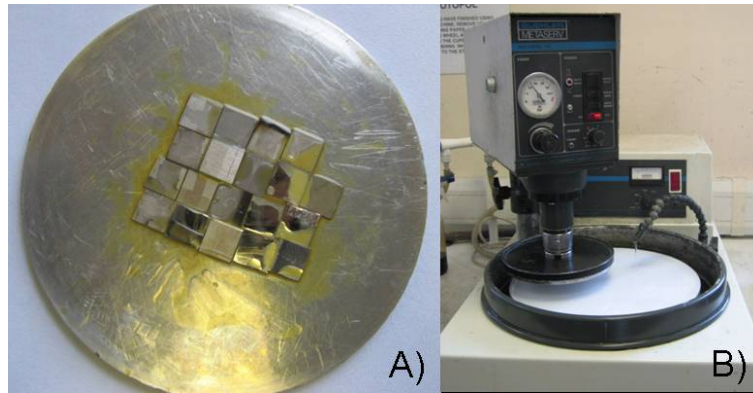


Figure 7.3: Step measuring technique: substrate preparation procedure. A) Samples bonded to the aluminium plate. B) Automatic polishing machine

bi-adhesive tape. The polishing procedure was carried out using an automatic machine (figure 7.3B) and it consisted of several grinding steps, progressively decreasing the grit size of the grinding medium. The polishing procedure is summarized in table 7.2.

MEDIUM	LUBRICANT	TIME [MIN]
120 grit paper	water	until flat
240 grit paper	water	4
1200 grit paper	water	2
2500 grit paper	water	2
4000 grit paper	water	2
Colloidal silica suspension on Microcloth [®] disc by Buehler [®]	water	1

Table 7.2: Polishing procedure

Once the polishing was completed, the aluminium plate was heated to melt the wax and remove the coupons. Samples were cleaned using a non-solvent cleaning fluid (Eccoclear[®]) to remove any remaining trace of wax, and then decreased with acetone; both operations were carried out in an ultrasonic bath.

7.4.1.3 Calibration run procedure

The polished Nimonic 75 coupons were partially covered with a high temperature adhesive tape (Kapton[®] tape) (figure 7.4A), then they were placed in the samples holder (figure 7.4B) and finally used as substrates for the calibration run. The coating-free

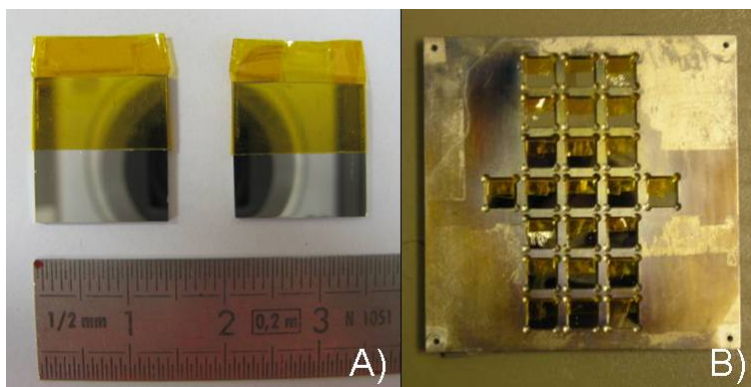


Figure 7.4: Nimonic 75 coupons ready for the calibration run. A) The coupons surface is polished to ‘mirror finish’ and it is partially covered with Kapton[®] tape; B) Twenty-three Nimonic 75 coupons positioned in the samples holder.

zone obtained by removing the tape allowed measuring the step between the coated and uncoated areas. This was done using a Veeco Dektak[®] 3ST stylus profiler. This machine measures the step by drawing a diamond-tipped stylus across the surface and assessing its vertical displacement as a function of the position. Figure 7.5A and 7.5B show the Dektak[®] working principle and the obtained typical step profile, respectively. For each sample position in the holder, the coating thickness was assessed as an aver-

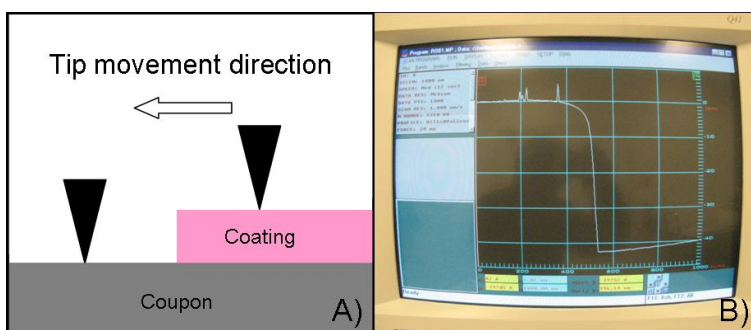


Figure 7.5: A) Dektak[®] working principle. B) Typical step profile obtained with the Dektak[®]

age of four thickness measurements equally distributed along the sample surface. The

deposition rate was determined for each sample position simply by dividing the average coating thickness by the deposition duration. This was done on the assumption that the coating thickness is a linear function of the deposition time, which is only true in case of thick coatings (in the μm scale), when it is acceptable to ignore the non-linear early stage of the deposition. The thickness values determined with this method were consistent with the values measured through SEM observations of the sample cross section.

The step measuring technique is a non-destructive technique, hence, after measuring the coating thickness, the *Pt* layer could be removed and the Nimonic 75 coupons reused.

7.4.2 Weight gain technique

This technique allows determining the deposition rate as *mg/minutes*. It involves four steps:

1. weigh the substrates before the run,
2. running a calibration run for each set of process conditions adopted in the study,
3. weigh the coated substrates and determine the *Pt* weight gain,
4. dividing this value in *mg* by the deposition time in minutes.

Substrates preparation before *Pt* deposition was very limited for this method as no profilometer measurement had to be taken after deposition. The surface of the Nimonic 75 coupons needed only to be grit blasted and cleaned in ultrasonic bath, with isopropanol, for 30 minutes.

Combining the values obtained with the two different techniques, it was possible to determine, for each specimen position in the samples holder, an average coating thickness and the corresponding weight gain. To confirm these values, some of the samples coated for calibration purposes were cross-sectioned, mounted in thermoset resin, polished and analyzed under an optical microscope to measure the coating thickness. The obtained values were in good agreement with the ones collected with the step measuring technique.

7.5 Platinum deposition procedure

The procedure for manufacturing a set of *Pt* sputtered samples is described in this paragraph. The whole process can be illustrated as a series of subsequent steps:

- Choosing the process parameters: current density and sputtering pressure;
- Carrying out the calibration run (see section 7.4);
- Preparing the CMSX-4 coupons: machining, cleaning, weighing the samples, and assessing their surface finish;
- Positioning the samples in the substrates holder;
- Venting the deposition chamber and locating the samples holder above the *Pt* target at a separation distance of 75mm;
- Pump down the chamber overnight to a base pressure below $6 \cdot 10^{-7} Torr$;
- Switching the cryopump to a throttle mode in order to reduce the pumping flow;
- Back-filling the chamber with argon, adjusting its flow to set the pressure to the working value;
- *Sputter-cleaning* the target before starting the actual deposition run (see description below);
- Starting the *Pt* deposition;
- Switching off both the power supply and the argon flow once the sputtering stage has completed its required duration;
- Pump the chamber back to the original base pressure;
- Leaving the system to cool down before unloading the samples (the target and the samples may become significantly hot during deposition);
- Venting the chamber and unloading the samples;
- Pump the chamber to high vacuum in order to prevent the targets and the chamber walls from absorbing pollutants between depositions;

- Weighing the samples and calculating the *Pt* weight gain in order to confirm that the *Pt* layer thickness was within the required tolerance.

The preliminary operations on the CMSX-4 coupons (machining, cleaning, weighing, and surface finish assessment) were always carried out within 24 hours from the loading of the samples into the sputtering chamber to minimise the risk of unwanted oxidation/contamination of the substrates.

Allocation of the samples within the positions of the holder was decided on the basis of the calibration data and taking into account the required *Pt* layer thickness (usually $10 \pm 0.5\mu\text{m}$). Due to the strong influence of the sample position on the amount of *Pt* deposited, such a tolerance was very strict and it was found out that only 8 out of the 23 positions available satisfied this requirement (see cartography of the *Pt* deposition in chapter 11).

The sputter-cleaning process conducted before the actual deposition has the objective of removing the first atomic layers from the target surface. This is done by gradually increasing the current from 0A up to 0.7A while a shutter, between the target and the samples, controlled by an external handle, is kept closed. The shutter protects the substrates from unwanted deposition of potentially contaminated platinum. Based on prior experience, the sputter-cleaning process is believed to be completed after approximately three minutes. Once the ‘cleaning’ is completed, the current density is gradually decreased to the working value. The deposition starts when the shutter is moved away, leaving the samples exposed to the plasma.

Chapter 8

Bondcoat manufacturing

Before proceeding with the detailed description of the manufacturing process, it is essential to illustrate the general aspects of the heat treatment necessary to generate the bondcoat and the furnace used. This will be done in section 8.1.

After platinum deposition, the samples are divided into two sets in order to carry out the production of the two types of bondcoat. Accordingly, two sections will be dedicated to the description of the manufacturing processes leading to the production of the two types of bondcoat:

- Production of a *Pt*-diffused bondcoat (section 8.2),
- Production of a *Pt*-modified Aluminide bondcoat (section 8.3).

8.1 Vacuum furnace and heat treatment procedure

All the heat treatments were carried out under high vacuum atmosphere in a vacuum furnace. This consists of a working chamber connected to a pumping system, equipped with both a rotary and a diffusion pump. The samples were loaded into the chamber on an alumina plate which was located between the two L-shaped carbon electrodes (figure 8.1). This arrangement guaranteed a homogeneous distribution of the heating energy on the samples. After loading the samples the chamber was pumped to $1 - 2 \cdot 10^{-6} \text{ mbar}$. Each heat treatment involved three phases:

1. heating up to working temperature,
2. dwelling at constant temperature,

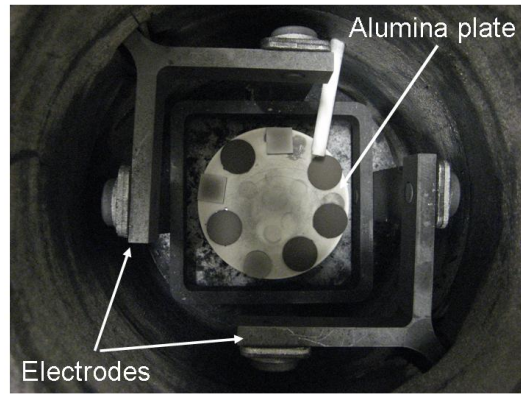


Figure 8.1: Vacuum furnace chamber. The samples, loaded on the alumina plate, are placed between the two L-shaped carbon electrodes.

3. cooling down to room temperature.

The heating up phase was carried out in three steps, progressively increasing the temperature. Table 8.1 shows details of the heat treatment procedure; the temperature, the heating up/cooling down rate, and the dwelling time are specified for each phase. Several different heat treatments have been carried out during this program. Each of

		TEMPERATURE [°C]	RATE [°C/MIN]	DWELLING [MIN]
Phase 1	Heating up	40	10	1
Phase 1	Heating up	200	40	10
Phase 1	Heating up	450	15	10
Phase 2	Dwelling	Working temperature	20	Dwelling at working temperature
Phase 3	Cooling down	20	100	

Table 8.1: Heat treatment procedure

them had its own characteristic Phase 2, while Phase 1 and Phase 3 were the same for all of them. Detailed description of the Phase 2 will be given in the appropriate sections.

8.2 Production of a *Pt*-diffused bondcoat

Production of a *Pt*-diffused bondcoat required one single heat treatment. Its characteristic Phase 2 (see previous section) consisted of a dwelling at 1190°C for one hour.

8.3 Production of a *Pt*-modified Aluminide bondcoat

Manufacturing of the *Pt*-modified Aluminide bondcoat involved two heat treatments and one further deposition step, in the following order:

1. Pre-aluminising heat treatment,
2. Aluminising by Chemical Vapour Deposition,
3. Post-aluminising heat treatment.

8.3.1 Pre-aluminising heat treatment

The pre-aluminising heat treatment was carried out under full vacuum, and in this case the Phase 2 described in table 8.1 consisted of a dwelling for two hours at 1040°C.

8.3.2 Aluminising by Chemical Vapour Deposition

8.3.2.1 CVD equipment

The CVD equipment includes two fixed stations, indicated as ‘Station A’ and ‘Station B’, and a separate bell furnace. Each station consists of a deposition chamber containing a retort on a stand. In the retort, the specimens are either surrounded by or immersed in the coating source material, thus this is the area in which the aluminising reactions occur.

During an aluminising run, the bell furnace is first heated up to temperature and then positioned over one of the two stations. The deposition chamber and its content are then brought up to temperature and held there for the required time whilst the coating process takes place. At the end of this period, the furnace is switched off, lifted up from the station, and positioned either on the other station to start a new process, or on its trolley and moved away from the chamber, while this cools down. Figure 8.2 shows the bell furnace on its trolley at the end of a run; figure 8.3 shows the Station A, the only one used in this project, before closure.

The deposition chamber consists of a vessel with two main elements: the ‘bell shaped’ lid and the ‘base’. To open the chamber, the lid has to be lifted using a hoist; when the base and the lid are in contact the chamber can be closed by means of four clamps equally distributed along the base perimeter; an O-ring, positioned between the base and the lid, assures a gas tight closure.



Figure 8.2: Bell Furnace on its trolley

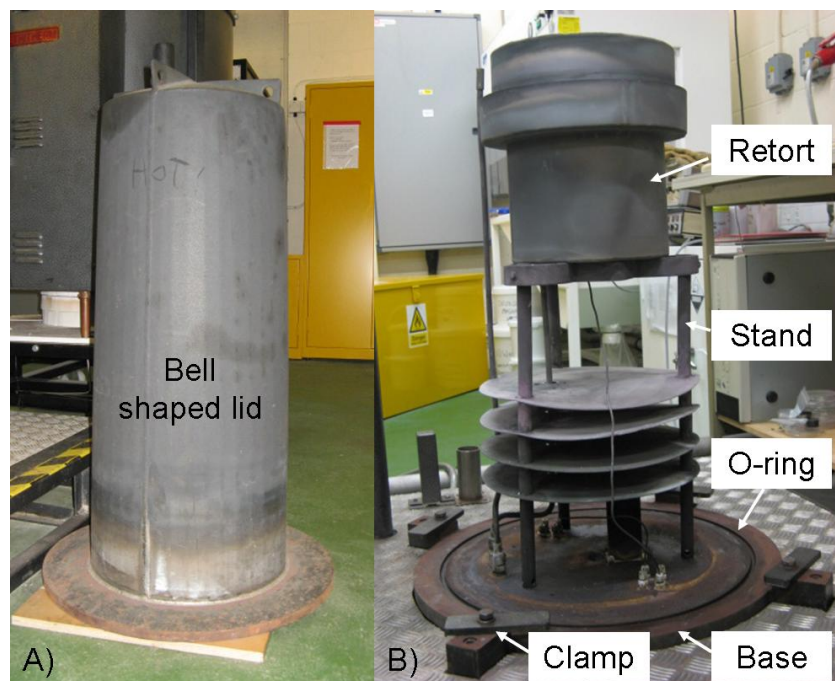


Figure 8.3: Station A opened. A) Chamber bell shaped lid; B) Stand and the retort positioned on the chamber base

Inside the chamber, the stand (figure 8.4) has two main purposes: on one hand, positioning the retort in the hottest area of the station and, on the other, preventing the base from overheating being provided with four insulating baffles.



Figure 8.4: Stand

The retort consists of a cylindrical container, to which a sealing channel is welded, and a cylindrical loose fixing lid (figure 8.5A). The sealing channel is filled with 20 mesh alumina granules that play the role of a mechanical barrier to the escape of the aluminising gases from the retort; when the retort is closed, in fact, the free edge of the lid is embedded into the granules. Inside, the retort is equipped with a ring shaped gas feeder, for an homogeneous distribution of the gases, a samples holder or tray, and three spacer bars that allow positioning the tray at different distances from the retort base. Figure 8.5B shows a top view of the opened retort before loading the aluminising reagents and the tray with the samples. Figure 8.5C shows the same view after loading with details of the tray consisting of a mesh welded to a metallic ring-shaped support. Underneath the tray, through the tray mesh, the aluminising reagents are visible (8.3.2.2).

Figure 8.6 shows a schematic representation of the Station A and the gas lines connected to it. Through the chamber base the station is connected to five gas inlet/outlet lines:

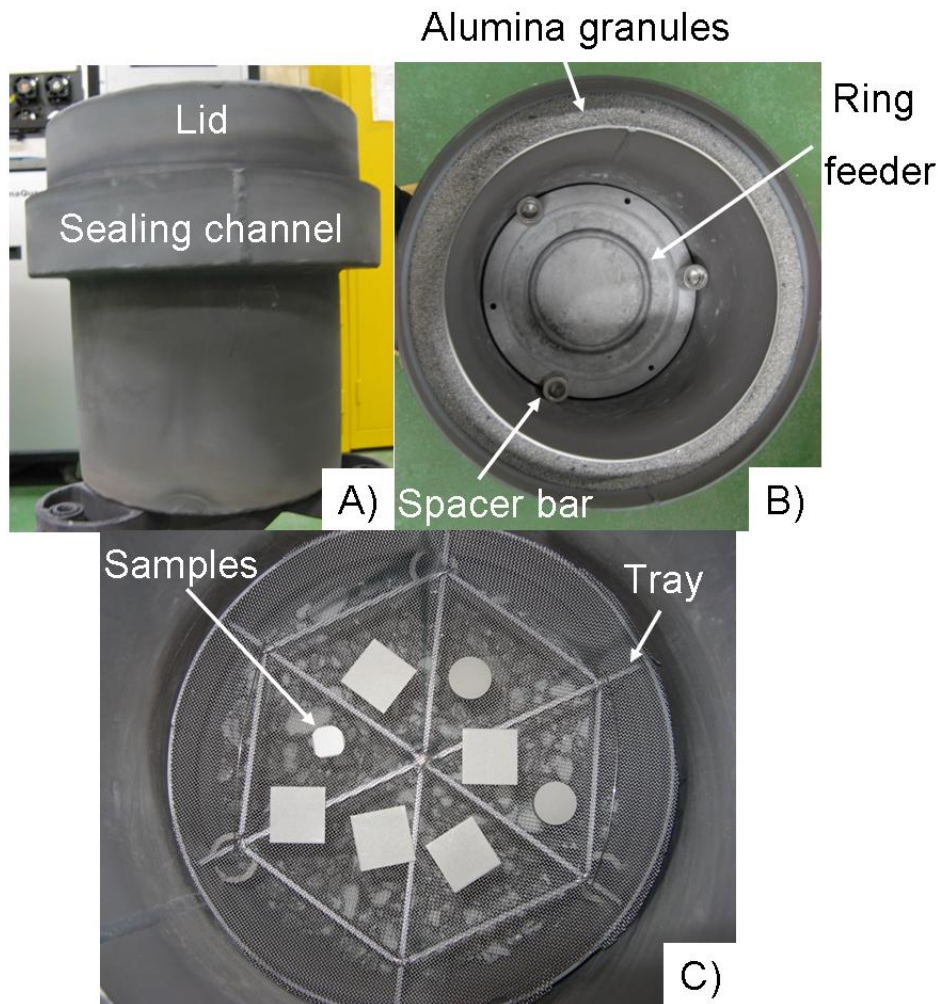


Figure 8.5: Retort. A) Retort closed; B) View from the top of the opened retort before loading the aluminising reagents and the tray with the samples. The picture shows: the sealing channel full of alumina granules, the three spacer bars and the ring shaped gases feeder; C) View from the top of the opened retort after loading. In the picture, the tray is the fully welded mesh and ring assembly. Underneath the tray, through the tray mesh, it is possible to see the aluminising reagents.

- a connection to a vacuum system (V),
- an inlet line for the retort which is connected to the ring shaped gas feeder (I_R),
- an inlet line for the chamber (I_C),
- an operative exhaust line (E_O),
- an emergency exhaust line (E_E).

The vacuum line is provided with a rotary pump which allows reaching a soft vacuum in the chamber. Each inlet gas line allows feeding the system with N4.8 argon (99.998% pure), N6.0 argon (99.9999% pure), or a combination of hydrogen and either of them. Four analog Mass Flow Controllers (MFC) allow controlling the flows on each line independently. The exhaust lines, as their name suggests, allow purging the exhaust gases out of the chamber. The ‘operative exhaust line’ is the one normally used during the process; it is kept closed with a cap at any time except during the process, when the cap is removed and the line is manually connected to a wet scrubber system. This consists of two sealed plastic tanks, indicated as ‘suck-back chamber’ and ‘bubbler’, connected in series: the first is kept empty while the second is filled with 10 liters of water. During the process the flue of acid gases coming out of the chamber is forced through the two tanks and, hence, through the water before being released in air. As a result, the gases are neutralised and a light overpressure corresponding to the ten litres of water is built up in the chamber. The suck-back tank has the purpose of collecting any back stream of water in case, during the process, a light vacuum builds into the deposition chamber. The ‘emergency exhaust line’ works as a back-up for the operative exhaust line: it is activated either manually or automatically in case the pressure inside the chamber exceeds $+0.5bar$.

During the run the temperature of the station is monitored by four thermocouples: one applied to the retort and three to the chamber base.

8.3.2.2 Reagents

The aluminising source material is an aluminium-chromium alloy (40wt%Cr-60wt%Al), in the form of chips (figure 8.7), supplied by ReadingAlloys[®]. The activator is aluminium fluoride powder supplied by PrinceMinerals[®]. In this project a weight ratio of 66:1 (chips to activator) was adopted, corresponding to 2000g of chips and 30g of salt.

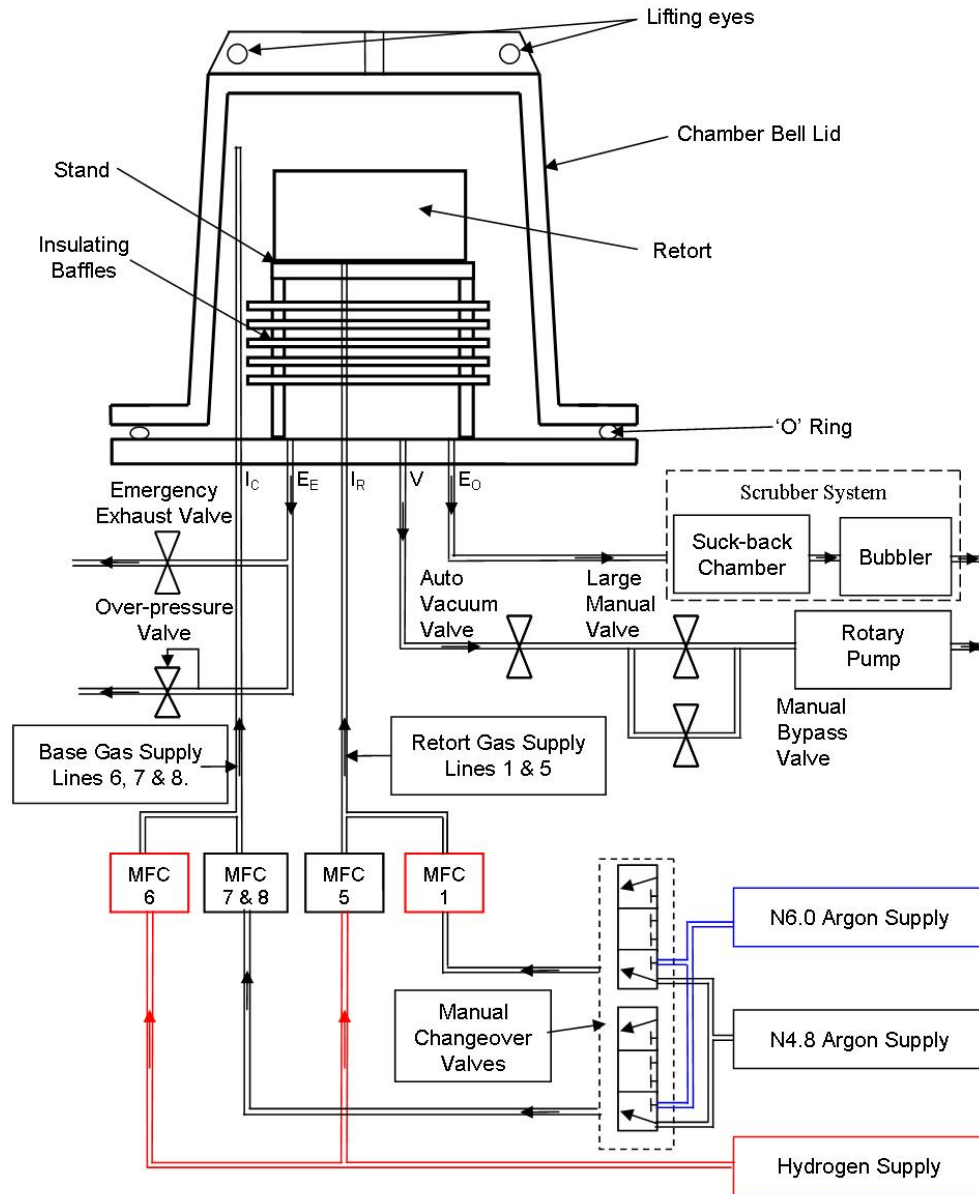


Figure 8.6: CVD equipment overview: the picture shows both the Station A and the five inlet/exit gases lines connected to it. (Adapted from material courtesy of Dr K. Long)



Figure 8.7: Aluminium-chromium alloy (40%Cr-60%Al) chips

8.3.2.3 CVD procedure

The aluminising run is described in this paragraph as a series of steps which, overall, lasted approximately 36 hours.

- Preheating the furnace at 800°C overnight.
- Increasing the temperature of the furnace to 1050°C and allowing at least one hour to stabilise the temperature before moving it over the station.
- Loading the retort.
The bottom of the retort was filled with the *Al-Cr* chips first, which were then evenly covered by a thin layer of AlF_3 . The samples were laid on the tray which was then positioned in the retort at a distance of 80mm from the *Al-Cr* chips.
- Sealing the retort by making sure the edges of its lid are fully embedded into the alumina granules bed.
- Closing the chamber by clamping its lid onto the chamber base.
- Creating an inert environment in the station.
The station was evacuated and back filled with argon for three cycles to make sure it was fully purged from any residue of oxygen before commencing the CVD. The argon flow was set at $25\text{l}/\text{min}$ in the chamber and $10\text{l}/\text{min}$ in the retort.

- *Purge phase*

After the station was filled with argon for the 3rd time, the exhaust line was opened and connected to the wet scrubber system, the hydrogen flow was then started and set at 10% of the argon flow. The gases were left running for one hour. This and the following phases of the CVD run are detailed in table 8.2.

PROCESS PHASE	SAMPLE TEMPERATURE [$^{\circ}C$]	FURNACE POSITION	GAS FLOW IN THE CHAMBER		GAS FLOW IN THE RETORT	
			Ar flow [l/min]	H ₂ flow [l/min]	Ar flow [l/min]	H ₂ flow [l/min]
Purge	Room temperature	trolley	25	2.5	10	1
Reaction	750 \rightarrow 1030	station	5	0.5	1	0.1
Cool down 1	1030 \rightarrow 400	trolley	15	0.5	10	0.1
Cool down 2	400 \rightarrow 250	trolley	15	0	10	0
Cool down 3	250 \rightarrow 25	trolley	0	0	0	0

Table 8.2: Aluminising process divided into phases. For each phase are indicated: sample temperature, position of the furnace, gas flows, in the retort and in the chamber.

- Setting up a system to collect temperature data comprising four thermocouples, which recorded the temperature at 10 seconds intervals.

- *Reaction phase*

Moving the furnace over the station and reducing the gas flow as detailed in table 8.2. The aluminising process technically started when the retort temperature reached 1030 $^{\circ}C$. In practice aluminising starts before this, in the heat up phase of the aluminising process, albeit at a low rate.

- Switching off the furnace after 5 hours of aluminising, and moving it from the station to the trolley.

- *Cool down phases*

Cooling down of the station followed the three steps described in table 8.2. When the retort temperature reached 400 $^{\circ}C$, the hydrogen lines were closed; while the argon lines were left opened until the temperature was below 250 $^{\circ}C$.

- Opening the chamber to prevent the water in the bubbler from being sucked into it because of the vacuum created by cooling down of the station without any gas supply.

- Leaving the station to cool down to room temperature overnight.
- Removing the specimens.
- Cleaning and maintaining the CVD equipment.

After each run the whole station needed to be dismantled and cleaned of fluoride and oxide residues. These precipitates needed to be abraded off the surfaces with grinding paper and then removed with a vacuum cleaner equipped with filters for acid waste. The used *Al-Cr* chips were sifted to remove most of the fluorides, then washed with water and eventually left to dry overnight at a temperature between 70°C and 100°C .

8.4 Post aluminising heat treatment

After aluminising, the manufacture of the *PtAl* bondcoat was completed by a ‘post aluminising heat treatment’, which follows the steps listed in table 8.1 where Phase 2 consisted of two stages. During stage one the samples were kept at 1140°C for two hours and then, after reducing the temperature to 870°C at a rate of $20^{\circ}\text{C}/\text{min}$, they underwent a second dwelling stage of 20 hours.

Chapter 9

Ceramic deposition

9.1 Coating equipment

The Electron Beam Physical Vapour Deposition (EB-PVD) unit consists of two chambers: the *working* or *deposition chamber* and, underneath it, the *Electron Beam (EB) gun chamber*. Each chamber has its own pumping system which allows the two units to work at different pressure during the deposition; in this particular case, the working chamber pressure will be varied between $10^{-2}mbar$ and $10^{-7}mbar$ while the gun chamber will be kept at $6 \cdot 10^{-4}mbar$.

Figure 9.1 shows the working chamber layout. The two substrate holders (or blades) are fixed on the deposition chamber back wall, onto the axes of a rotation mechanism. This enables the holders to rotate perpendicularly to the ceramic ingot, which is the evaporation source (figure 9.1A). For this project a rotation speed of 20rpm was chosen, which represents an acceptable compromise between the need of a lower speed, for a longer coating lifetime, and a higher speed, for a lower coating anisotropy. Unlike full scale commercial coaters, the unit available in the Cranfield University laboratory does not have a powerful enough EB gun to sustain a high temperature, hence an arc shaped furnace is positioned around the samples holders in order to heat up the specimens prior to the deposition (figure 9.1B).

The EB gun chamber accommodates an electron beam gun inclined by 270° with respect to the ceramic rod. The power source works at $40kW$ with a voltage of $10kV$. During deposition, the generated electron beam is accelerated to a high kinetic energy and focused towards the ingot by a magnetic field. The kinetic energy of the electrons, converted into thermal energy as the beam bombards the surface of the ingot, allows

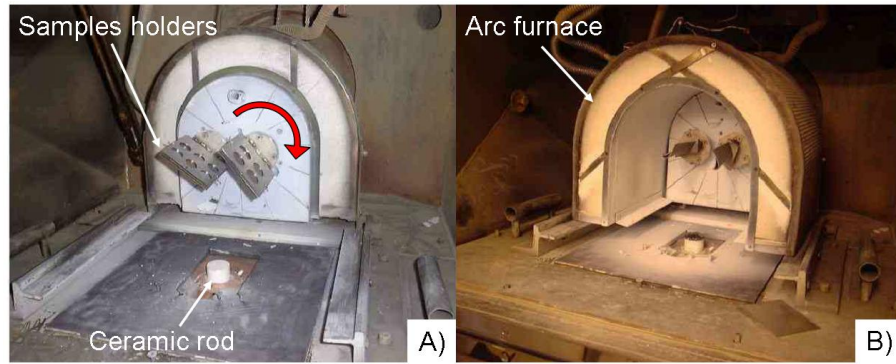


Figure 9.1: EB-PVD working chamber layout. A) Two substrate holders fixed on the deposition chamber back wall, perpendicularly to the ceramic ingot. The red arrow indicates the rotation direction. B) The arc-shaped furnace placed over the sample holders.

the surface temperature of the ingot to increase, resulting in the formation of a liquid pool of ceramic material that evaporates under vacuum. The ingot, enclosed in a water cooled copper crucible, is provided with an ingot feed mechanism. This pushes the ceramic rod from the bottom into the chamber and allows to keep the level of the molten liquid pool on the surface of the ingot constant. A controlled blend of oxygen (90%) and argon (10%) is pumped into the deposition chamber in order to achieve the required Zirconia stoichiometry. The deposition temperature ranges between 871°C and 1093°C [28] and the condensation rate of the vapours on the substrates is typically $2 - 3\mu\text{m}/\text{min}$.

9.2 The EB-PVD substrates holders

The substrate holders for the EB PVD chamber (figure 9.2) adopted in this study have been especially designed and commissioned for the present work. They must guarantee that, during the deposition, the samples are central with respect to the melted ceramic pool and that the resulting deposition on all the specimens is as homogeneous as possible. Each holder consists of two parts assembled together with five bolts. The holders and the bolts are manufactured using Nimonic 75 (table 7.1) to guarantee stability at the deposition temperature. Nimonic 75 melts between 1340°C and 1380°C .



Figure 9.2: EB-PVD substrates holders

9.3 The evaporation source

In this study, Y-PSZ rods (or ingots), supplied by Phoenix Coating Resources (USA), were used as an evaporation source. Table 9.1 reports both dimensions and nomi-

Ingot name	Dimension		Description	Y_2O_3 [mol %]
	Diameter [mm]	Length [mm]		
Y-PSZ	33	201	7wt% Y_2O_3 - ZrO_2	15.6

Table 9.1: Dimensions and nominal chemical composition of Y-PSZ ingot

nal chemical composition for the ingot. The rod composition was chosen in order to guarantee a metastable single phase in the coated samples (see section 4.2).

9.4 Ceramic deposition procedure

An established practice of the engine manufacturers requires grit blasting the blade/samples prior ceramic deposition. In this study, the samples were not grit blasted immediately prior to ceramic deposition in order to preserve their original surface finish. Each ceramic deposition involved the following steps:

- Venting the deposition chamber.
- Positioning the samples on the holders and connecting them to the rotating system.
- Loading the Y-PSZ rod and putting the arc furnace in place.

- Closing the deposition chamber and pump it down to a high vacuum level (typically between 10^{-5} and 10^{-7} mbar).
- Heating the furnace up to approximately $500^{\circ}C$.
- Leaving the system to stabilise overnight.
- Feeding the chamber with a gas mixture of 10% argon and 90% oxygen. The gas flow is adjusted to set the pressure to the working value of 10^{-2} mbar. The presence of oxygen in the chamber assures that fewer oxygen vacancies are formed in the ceramic coating guaranteeing the correct stoichiometry for zirconia formation.
- Increasing the furnace temperature to a minimum of $850^{\circ}C$ prior to deposition.
- Starting the samples holders rotation.
- Triggering the electron beam gun to the operative conditions of $10kV/0.54A$. This operation raises the temperature to the working temperature (between $900^{\circ}C$ and $1020^{\circ}C$).
- Evaporate ceramic for the required duration. In the present study the required TBC thickness was $200\mu m$, which corresponds to a deposition time of 83 minutes. During evaporation, the consumption of the ceramic rod was controlled through the control aperture; the rod was raised manually approximately every 5 minutes.
- Leaving the samples to cool down and finally unloading them.

Chapter 10

Testing methods

10.1 Surface texture characterisation

10.1.1 Profilometer

The specimens surface was assessed using a Form Talysurf manufactured by Taylor-Hobson. The instrument consists of a diamond stylus with a small tip (radius of $2\mu m$), a laser gauge or transducer, a traverse datum and a processor. The machine measures the surface by drawing the stylus across the surface and measuring its vertical displacement as a function of the position. Figure 10.1 shows a schematic representation of the profilometer while measuring the sample surface. For correct data collection, only the

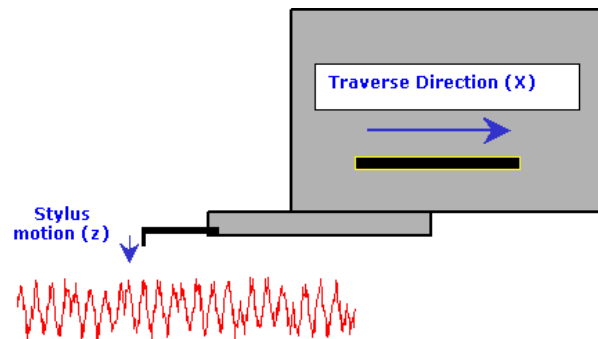


Figure 10.1: Schematic representation of the profilometer while measuring a surface

stylus tip should be following the surface to be tested while the gauge passes over the surface along a straight line. This is obtained using a straightness datum, which consists of a datum bar lapped to a high straightness tolerance. As the stylus moves up and down along the surface, its movement is converted first into a signal by the transducer

and then into a visual profile (measured profile) by the processor.

10.1.2 Procedure for surface texture assessment

The surface texture assessment consists of measuring the sample surface along the direction perpendicular to the lay of the irregularities. On ground surfaces the lay is perpendicular to one of the coupon edges (see section 6.2.1), which could then be used as a reference for the direction of the texture measurement. The sample surface was assessed with four measurements running parallel to the reference, and evenly distributed over the surface; each measurement was done over a length of 10mm.

On grit blasted surfaces, the irregularities do not have a particular lay, so the surface was assessed according to a grid of eight measurements: following the same procedure adopted for the ground samples, four measurements were taken along one of the coupon edges while the other four were taken after rotating the sample by 90°.

The real profile of a surface can be thought of as the sum of many different individual functions, each with its own wavelength. In order to separate *form* from *waviness* and *roughness*, the profilometer filters the measured profile. The filters adopted allow separating and removing the wavelength components of the surface outside the range of interest and obtaining a modified profile; such a profile is then used to calculate the surface parameters. Based on the wavelength components that have been extracted from the measured profile, the calculated parameters may be: form parameters, waviness parameters or roughness parameters.

In this study, a Gaussian filter was applied and a band-pass type filtering operation was adopted to extract the roughness profile of the surface. A band-pass filter involves the application of both high-pass and low-pass filters. The former lets the short wavelength (high frequency) components through, while the latter eliminates the noise. The high-pass and low-pass limits are expressed, numerically, as ‘cut off’ values: they were chosen according to the procedure described in the paragraph 7.2 of the BS EN ISO 4288:1998.

After extracting the roughness profile the profilometer calculates the roughness parameters as described in the standard protocol BS EN ISO 3274:1998. This procedure provides one set of parameters per measurement, hence four were obtained from the ground surfaces and eight from the grit blasted surfaces. For each sample a single, final set of parameters, representative of the whole surface, was calculated as an average of the corresponding parameters in the various sets.

10.2 Coating characterisation

The following section describes the apparatus and the analysis performed to characterise the coating at different stages of manufacturing and after the cyclic oxidation test. Microscopy was used for observing surface and cross sections of as deposited samples or samples exposed to oxidation, in order to understand the behaviour of the coating being aged.

10.2.1 Optical Microscopy

An optical microscope was used to inspect the coating top surface after each manufacturing step. The apparatus used was a Nikon direct optical microscope equipped with a JVC CCD sensor camera for picture acquisition.

10.2.2 Scanning electronic microscopy (SEM) and Energy Dispersive X-ray Spectroscopy (EDS)

The SEM equipment used in this study was a FEI XL30 SFEG equipped with an energy dispersive X-ray spectrometer or EDS system. In a scanning electron microscope, high-resolution images of the samples surface are produced by scanning the sample surface with a beam of electrons, indicated as *primary electrons*. The electrons, generated by a Field Emission Gun (FEG), are accelerated with a voltage comprised between 10 and 30kV, and then focused on the sample surface with electromagnetic lenses. The interaction between the electrons and the atoms in the sample produces signals like Secondary Electrons (SE), Back-Scattered Electrons (BSE) and characteristic X-rays; each of these signals can be detected by a specialised detector. SE give topographic information of the sample surface; they are produced by inelastic scattering of the beam electrons. Backscattered electrons are instead generated by elastic scattering, and they provide information about the distribution of different elements in the sample, by atomic number contrast. The BSE signal is related to the atomic number (Z) of the elements in the specimen and it is stronger when the electrons are reflected by atoms with a higher Z ; as a result in BS images the brighter areas are the ones containing elements with higher Z . All the micrographs reported in this work are back-scattered images. Characteristic X-rays are emitted when the primary electrons remove an inner shell electron from the atoms in the sample, causing an electron from an outer, higher-energy shell to fill the hole and release energy. The emitted X-rays are characteristic of the

difference in energy between the two shells, and of the atomic structure of the element from which they were emitted. By using an energy dispersive X-ray spectrometer it is possible to measure the number and the energy of the X-rays and, as a consequence, to characterize the chemical composition of the sample.

10.2.2.1 SEM samples preparation

The analysis with the SEM/EDS technique was conducted on the top surface of the samples and on their cross section. When examining the top surface, the sample preparation was limited to cleaning it with IPA in an ultrasonic bath; when the cross-section was investigated, preparation involved moulding the samples in phenolic resin supports and polishing them as illustrated in table 7.2.

The SEM technique requires electrically conductive and grounded samples. In a TBC system only the Y-PSZ layer is not conductive, hence the ceramic coatings and the cross sections had to be coated with a thin (less than $50nm$) layer of carbon.

10.2.3 Focused Ion Beam (FIB)

The FIB is a technique used in materials science for site-specific analysis, deposition, and ablation of materials. The FIB instrument used in this study was a FEI FIB 200; it operates in a similar way to a scanning electron microscope but, instead of using a focused beam of electrons, it uses a focused beam of ions that can be operated at low beam currents, for sample imaging, or at high beam currents, for sputtering or milling.

The instrument uses a gallium Liquid-Metal Ion Source (LMIS). The gallium metal is placed in contact with a tungsten needle and heated, the resulting melted metal wets the tungsten, and an electric field (greater than 10^8 volts per centimetre) causes ionization and field emission of the gallium atoms. The source ions are then accelerated to an energy between 5 and $50keV$ (kiloelectronvolts), and focused onto the sample by electrostatic lenses. Figure 10.2 shows the interaction between the gallium ion beam (Ga^+), or primary ion beam, and the sample surface. When the primary ion beam hits the sample, it produces the sputtering of a small amount of material, which leaves the surface as either secondary ions (i^+) or neutral atoms (n^0). The primary ion beam produces also secondary electrons (e^-). As the primary beam rasters on the sample surface, the signal from the sputtered ions or secondary electrons is collected to form an image.

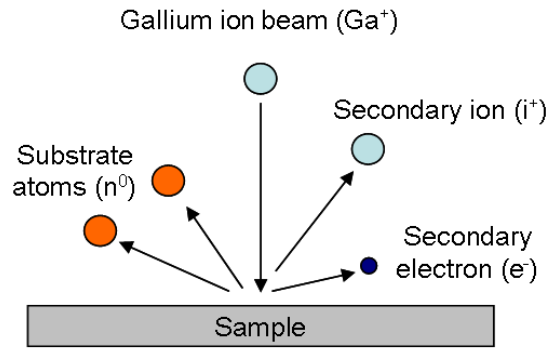


Figure 10.2: Schematic of the interactions between the gallium ion beam (Ga^+) and the sample surface

An electromagnetic aperture situated after the ion gun allows the user to choose beam current from $1pA$ to $11500pA$. At low currents, typically between 1 and $70pA$, the FIB is used for imaging, as limited amounts of material are sputtered at these current values. Above $70pA$ the beam is energetic enough to allow precision milling of the specimen down to a sub-micron scale. The choice of the beam current is strictly dependent on the type of material that is to be milled. For a given milling volume, in fact, increasing the current corresponds to an increment of the energy transferred to the sample surface, which results in a reduction of the milling time but also in a larger thermally affected zone around the milled section.

If the sample is non-conductive, a low energy electron flood gun can be used to provide charge neutralisation; thus even highly insulating samples may be imaged and milled without a conducting surface coating, as would be required in a SEM.

In addition to primary ion beam sputtering, the FIB system permits local ‘flooding’ of the specimen with a variety of gases. The interaction of these gases with the primary gallium beam allows either selective gas assisted chemical etching or selective deposition of material. Very common is the deposition of a thin *Pt* strip (1 to $3\mu m$ thick) that works as a sacrificial layer, protecting the underlying sample from the destructive sputtering by the ion beam.

In this work the FIB technique was used to study the structure of the sputtered *Pt* layer (see Chapter 7); the aim was to analyse the cross section of the as-deposited coating without any artifacts linked to sample cutting, mounting, and polishing. The sample top surface was first scanned at low currents to find a suitable area for the analysis; then the primary beam current was increased and, the selected area was milled according to a pre-defined pattern. The milling resulted in a parallelepiped shaped hole

in the *Pt* layer, where the base and the height of the parallelepiped were respectively parallel and perpendicular to the sample top surface. In order to image the coating cross section the sample was then tilted *in situ* and scanned with a low current beam.

10.3 Cyclic oxidation

After manufacturing, the lifetime of both types of TBC systems was assessed via cyclic oxidation test. The lifetime is defined as the time a component or a system operates before failure. When tested in isothermal tests, the TBC system lifetime is measured as the time at top temperature before failure, while, when tested in cyclic test, the lifetime is normally measured in terms of number of cycles.

Studies conducted on TBC systems with a *Pt*-modified aluminide bond coat highlighted that the time at temperature more than the number of cycles influences the TBC system lifetime. Nevertheless, in this work it was decided to study the TBC systems oxidation resistance adopting the industrial approach, which consists of testing the turbine components for high temperature application in cyclic oxidation tests and in determining their lifetime as number of cycles to failure. This approach aims to simulate the thermal cycles that such components endure in service. For TBC systems, it emphasises the failure generated by the thermal stress that is built up at each cycle due to the difference in thermal expansion between the superalloy, the bondcoat, the TGO and the ceramic topcoat. It should be noted that, given that a fixed cyclic regime was chosen (see section 10.3.3), the number of cycles can be easily converted in time at temperature before failure.

10.3.1 Cycling oxidation rig

The cyclic oxidation test was carried out in a thermal cycling rig manufactured by Pyrox. The rig is equipped with a furnace that can reach an operating temperature of 1450°C . A pneumatic device, connected to the samples holder, cyclically moves the samples between a ‘hot position’, inside the furnace, and a ‘cold position’, outside the furnace, in a laboratory environment; as a consequence the samples are submitted to a succession of cycles where each cycle is the sum of a ‘furnace time’ and a ‘cooling time’. The samples cooling rate can be increased using a forced air cooling system. When the samples holder is in the ‘cold position’, it is surrounded by four vertical nozzles connected to four electric fans (figure 10.3). The air, blown into the nozzle by the fans,

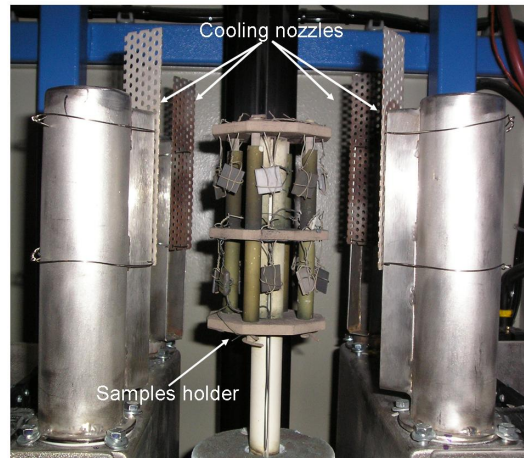


Figure 10.3: Samples holder outside the furnace in the ‘cold position’: it is surrounded by four vertical nozzles connected to four electric fans.

creates a cooling air vortex around the samples holder that increases the cooling rate. The fan rotating speed can be adjusted with a potentiometer, thus different levels of cooling speed can be achieved.

10.3.2 Samples holder for cycling oxidation

The samples holder consists of three circular plates connected by four metal rods. Twelve hooks are hung to the top and middle plates. Each hook can accommodate one sample for a total of twenty-four specimens per run. Samples are attached to the hooks via ‘baskets’ crafted in high temperature resistant wire (Kanthal AF). This *FeCrAl* alloy has a temperature capability of 1300°C (the melting point is 1500°C), and excellent oxidation resistance in combination with good form stability.

10.3.3 Oxidation testing procedure

In this study the ‘time to failure’ or ‘lifetime’ of a specimen tested in a cycling oxidation test is defined as the number of cycles that generated in the sample a 20% TBC spallation. The lifetime depends not only on the testing temperature but also on the time the samples are held in the hot and cold positions as well as on the heating and cooling rates. In this study each cycle consisted of:

- a testing temperature of 1150°C ;
- 45 minutes *exposure time* (see definition below);

- a forced air cooling;
- a minimum of 10 minutes dwell at temperatures lower than 100°C .

The *exposure time* is defined as the length of time during which the samples are exposed to a temperature higher than 97% of the testing temperature. During the cooling time the sample temperature drops from the testing temperature to the laboratory temperature. A forced cooling guarantees a high cooling rate that, in turn, allows avoiding significant creep stress relief in the samples at temperature above 800°C . When the temperature is below 100°C the samples are subject to the ambient moisture that alters the bonding across the $\alpha - \text{Al}_2\text{O}_3$ scale/bondcoat interface by stress-corrosion cracking. This phenomenon is taken into account in this study by keeping the samples for at least 10 minutes at a temperature lower than 100°C . Given the chemical reactions expected to occur at this temperature, such a portion of the oxidation test will be referred to as ‘alumina hydration’.

10.3.4 Oxidation rig programming

The oxidation rig requires a time-based programme, input via its control panel, in order to be instructed as to when to shift the samples between the hot and cold positions. Identification of the duration of the ‘furnace time’ and of the ‘cooling time’ required mimicking an oxidation cycle in which mock coupons made of 15mm squares of Ni-monic75 were used instead of the real samples and their temperature monitored during a complete oxidation cycle. Several cycles had to be run in order to achieve a setting that would comply with the requirements listed in section 10.3.3. The calibration run showed that to achieve the required testing conditions the working temperature in the furnace had to be set at 1165°C and that the cycle duration had to be seventy-nine minutes (64 minutes furnace time + 15 minutes cooling time).

Monitoring of the temperature within the samples holder was done using two thermocouples, welded onto CMSX-4 coupons attached onto different plates in the holder, in opposite positions with respect to the central axis of the holder. A third thermocouple was also placed in the centre of the samples holder between the top and middle plates. A typical temperature evolution recorded during a cycle is represented in figure 10.4. Figure 10.5 illustrates the temperature evolution during the first and the last 20 minutes of the cycle, while table 10.1 gives details of the heating and cooling rate during the first and the last 3 minutes of the cycle.

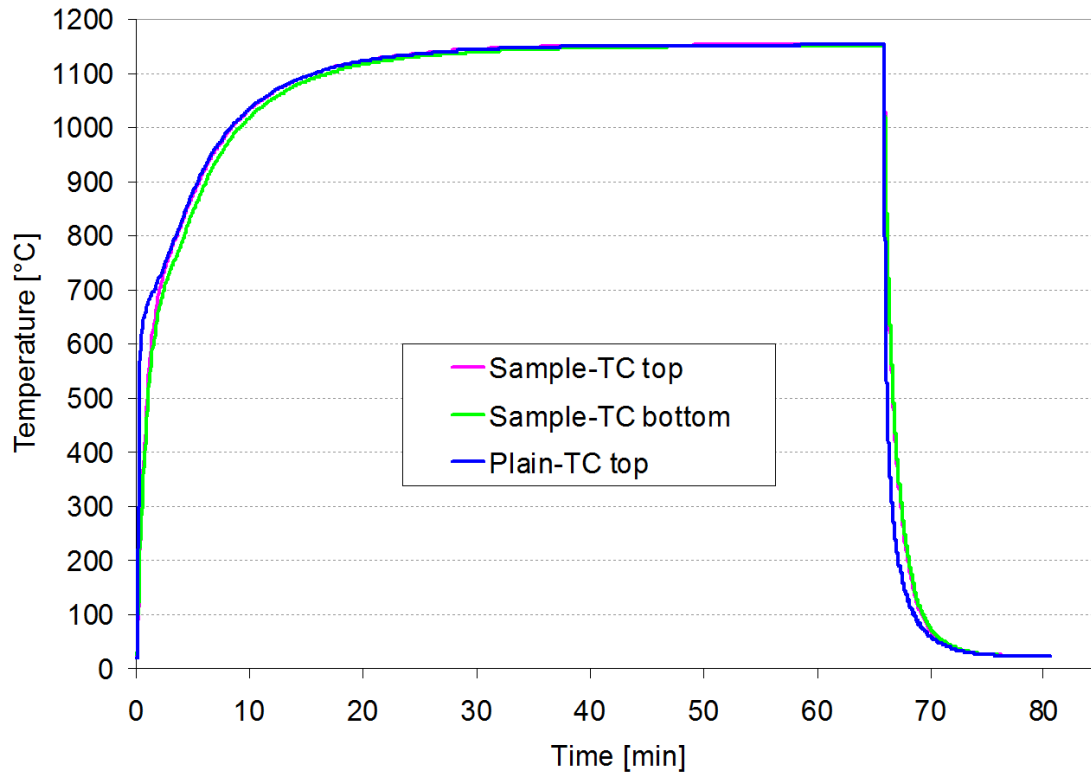


Figure 10.4: Temperature evolution during a 79 minute cycle for the three thermocouples. ‘Sample-TC top’ and ‘Sample-TC bottom’ are the two signals recorded by the thermocouples welded to the samples on the top and middle plates, respectively. ‘Plain-TC top’ is the signal recorded by the thermocouple in the centre of the samples holder.

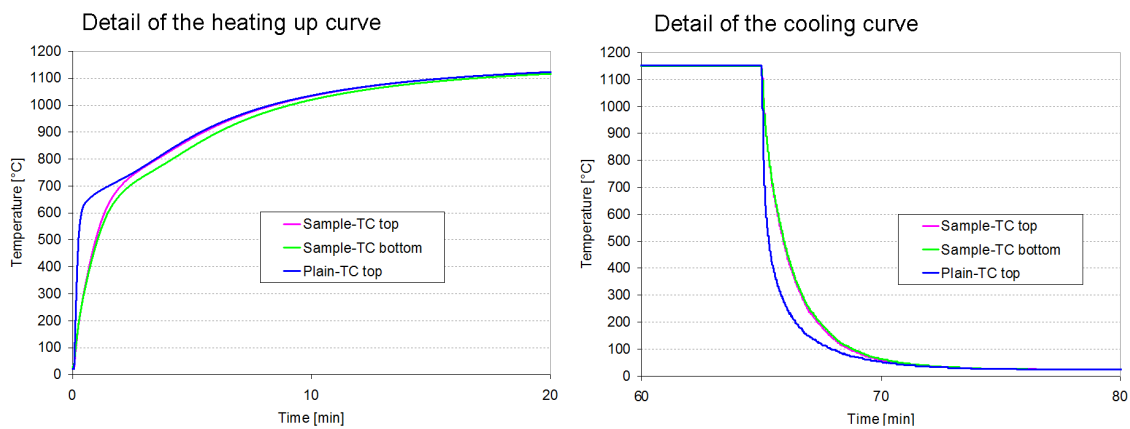


Figure 10.5: Details of the heating and cooling curves

	HEATING RATE [°C/min]		COOLING RATE [°C/min]	
	1 st minute	3 rd minute	1 st minute	3 rd minute
Sample-TC top	527	257	682	337
Sample-TC bottom	503	246	670	334
Plain-TC	677	259	886	351

Table 10.1: Heating and cooling rate during the first and last 3 minutes of the cycle, recorded for the three thermocouples. Identification of the thermocouple position is described in figure 10.4.

The results illustrated in figure 10.5 show that, apart from the initial stages of the cycle, the sample mass effect on the temperature evolution is negligible. A slight discrepancy is registered initially between the temperature of the two plates, with the middle plate showing a slower heating rate than the top one. However, after the first 14 minutes of the cycle the heating rates of the thermocouples attached to the coupons and to the samples holder are equivalent, with a difference in temperature between the three thermocouples of maximum 10°C . The top plate reaches 1115°C , which is 97% of the testing temperature, after 18 minutes, while the middle plate reaches this temperature after 20 minutes. Hence it is assumed that, after 19 minutes from the beginning of the furnace time, the exposure time starts. This allows fixing the furnace time for each cycle at 64 minutes (19 minutes ramping up to 97% maximum temperature + 45 minutes exposure time).

Once the samples are out of the furnace, they are cooled down in forced air using the highest fan speed. An initial investigation on the cooling speed showed that the cooling rate for the top plate of the samples holder was significantly higher than the rate registered for the middle plate. In order to reduce this difference, the four cooling nozzles were partially obstructed with a metallic mesh; adjusting the position of such mesh, a homogeneous cooling rate was achieved.

For the three thermocouples, the temperature dropped from 1150°C to 23°C in 15 minutes with a corresponding average cooling rate of $75^{\circ}\text{C}/\text{min}$. The cooling rate for the two plates was acceptably similar; after less than 4 minutes into the cooling time, both thermocouples registered less than 100°C . Consequently a cooling time of 15 minutes guarantees the 10 minutes required for the alumina hydration.

Part III

Results and discussion

This part of the thesis is divided into 7 chapters; chapter 12 to chapter 15 report an investigation on TBC systems with a *Pt*-diffused bond coat (or $\gamma + \gamma'$ bond coat) while, chapter 16 illustrates results regarding TBC systems with a *Pt*-modified aluminide bond coat (or *PtAl* bond coat). With the purpose of making the presentation clearer and easier to follow, each chapter presents the effect of a single factor on the lifetime of the TBC system in consideration. In particular, for TBC systems with a *Pt*-diffused bond coat:

- Chapter 12 analyses the influence of different PVD *Pt* structures;
- Chapter 13 studies the effect of the ceramic deposition temperature;
- Chapter 14 illustrates the effect of the substrate surface machining procedure with a direct comparison between an isotropic and an anisotropic surface finish;
- Chapter 15 investigates the existence of a set of roughness parameters which can characterise the substrate surface finish and can be linked to the lifetime of the system.

For TBC systems with *PtAl* bond coat:

- Chapter 16 studies the effect of different *Pt* layer morphologies;

Each chapter includes a summary of the experimental procedure adopted to manufacture the analysed specimens.

The chapters listed above are preceded by chapter 11 which investigates the correlation between the sputtering parameters and the morphology of the deposited *Pt* layer. In particular, chapter 11 describes the three types of *Pt* layer structure which were manufactured in this work and were used for both types of bond coat. Part III is closed by chapter 17, which includes an overall discussion where the two types of bond coat are compared.

Chapter 11

As-deposited platinum layer: coating morphology and density

11.1 Cartography of the platinum deposition

The TBC systems manufactured in this study required the deposition of a *Pt* layer with a thickness of $t \pm 0.5\mu m$ where t , defined as *nominal layer thickness*, is $10\mu m$ unless otherwise stated. Such a strict control of the thickness of the deposited layer was achieved by carefully mapping the amount of *Pt* deposited across the different locations in the sample holder. In fact, calibrating depositions demonstrated that the amount of *Pt* deposited on each specimen depends on the coupon position with respect to the *Pt* target. Figure 11.1 includes a picture of the samples holder (left) and a diagram with the cartography of a typical *Pt* deposition (right). In the diagram, the samples positions are represented as coloured squares: locations characterised by the same colour allow to obtain the same *Pt* thickness of $t \pm 0.5\mu m$, where the value of t can be read on the diagram scale. The adopted color scheme highlights that locations having a similar *Pt* layer thickness are arranged along concentric ellipses; this resulted in obtaining, out of each deposition run, a maximum of eight specimens (orange positions in the cartography) with acceptable specifications.

The layout of the *Pt* cartography does not vary with the sputtering parameters, but it is linked to the dimension of the magnetron underneath the *Pt* target. The ellipses, along which the sputtered *Pt* layer has equivalent thickness, have their axes aligned with the axes of the magnetron track and the ellipse with the thickest layer (orange positions) corresponds to the superposition of deposition from both of the magnetron

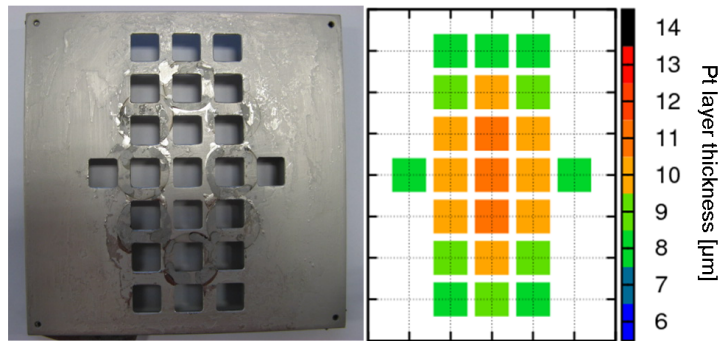


Figure 11.1: Samples holder (left) and diagram with the cartography of a typical *Pt* deposition (right). In the diagram, samples positions are represented as squares, colour coded according to the *Pt* thickness obtained.

tracks.

In this investigation, three different sets of sputtering parameters were adopted for the deposition of the *Pt* layer. For each set, table 11.1 reports:

- parameters values (current, pressure and power);
- duration of a typical deposition run;
- specimens weight gain in $\frac{mg}{cm^2}$ of *Pt*;
- type of structure of the as-deposited coating.

SPUTTERING PARAMETERS					
Current [A]	Pressure [Pa] ([mTorr])	Power [W]	Deposition time [min]	Weight gain [mg/cm ²]	<i>Pt</i> layer morphology
0.7	0.67 (5)	315	84	20.0	Dense
0.7	10.00 (75)	275	93	14.6	Open
0.2	0.67 (5)	68	410	19.9	Dense

Table 11.1: Sputtering parameters and deposition run characteristics to deposit a nominal $10\mu m$ coating thickness

The set of parameters in the first row of table 11.1 (0.7A and 0.67Pa) represents the conditions previously adopted at Cranfield University for the deposition of *Pt* thin film (i.e. less than $2\mu m$). In this work, such a set of parameters was adopted as a starting point, with the intention of identifying the conditions for the deposition of *Pt* layers with a nominal thickness of $10\mu m$. The other two configurations were obtained modifying

either the pressure or the current of the reference set, in the attempt of investigating the effect that such variations have on the *Pt* layer morphology and eventually on the TBC systems performance. The current and the pressure values were chosen at the extremes of the operative range of the sputtering equipment.

The deposition time and the *Pt* weight gain are relative to a coating thickness of $10 \pm 0.5 \mu\text{m}$ and were calculated by the *step measuring* technique (see section 7.4.1) and the *weight gain* technique (see sections 7.4.2), respectively.

Analysis of the as-deposited *Pt* layers revealed that two different types of microstructure were obtained, which were identified as ‘*Dense*’ and ‘*Open*’ structure. Figure 11.2 shows micrographs of the coating top surface (A and C) and of the ion-beam milled sections (B and D) for each of these microstructures, including, as a reference, the micrographs of an electroplated *Pt* layer (E and F). The latter represents the standard product of the industrial process for depositing *Pt* on turbine hardware. The *Pt* layer with a dense structure shows a dense and uniform topography (Figure 11.2A) with fine, elongated grains (Figure 11.2B), whereas the open structure is characterised by a spiky top surface (Figure 11.2C) and well defined columnar grains (Figure 11.2D).

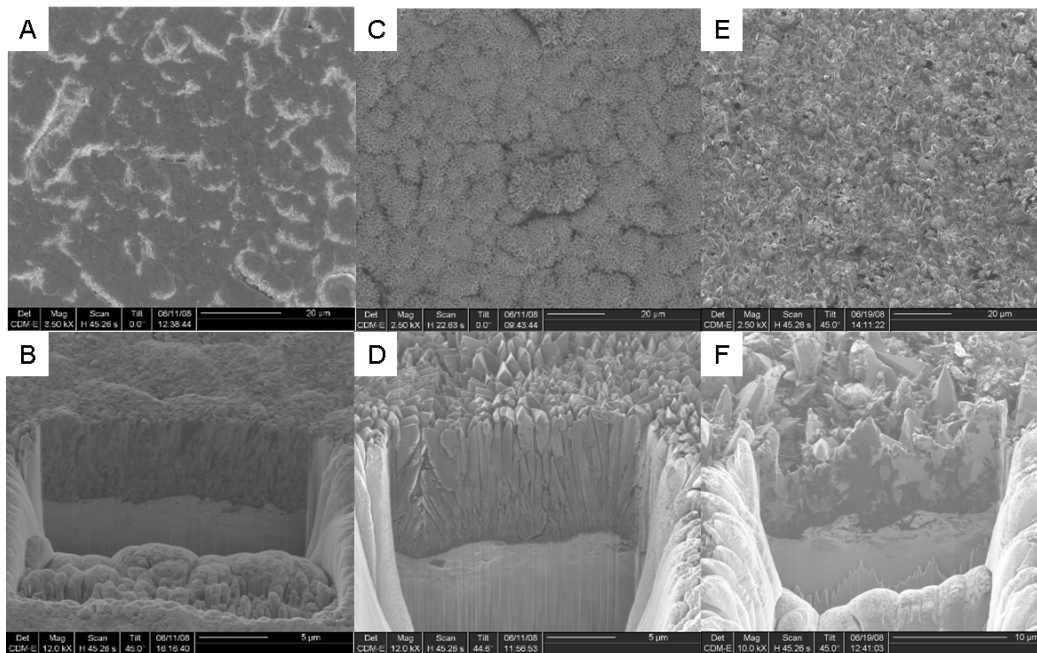


Figure 11.2: Micrographs of the topography (top row) and of FIB-milled sections (bottom row) of the as-deposited *Pt* layer on CMSX-4 substrate grit blasted at 0.2MPa : Dense structure (A and B); Open structure (C and D); Electroplated *Pt* coating (E and F).

The morphologies shown in figure 11.2 suggest that the layers deposited with dense and open structures have different densities. A simple comparison between the weight gain and the deposited volume of *Pt* on each sample confirmed this hypothesis: the amount of *Pt* sputtered varies from $14.6 \frac{mg}{cm^2}$ in an open structure to $\sim 20 \frac{mg}{cm^2}$ in a dense structure. These values correspond to a coating density of $14.6 \frac{g}{cm^3}$ and $20 \frac{g}{cm^3}$, respectively. Considering that *Pt* density is $21.46 \frac{g}{cm^3}$, it can be concluded that the dense structure contains less than 10% voids, while the open structure contains approximately 30% voids. As a comparison, an electroplated *Pt* layer contains around 40% voids.

Previous studies have demonstrated that the change in *Pt* microstructure is the result of a change in sputtering pressure more than a change in sputtering current [169]. This is confirmed by the results detailed in table 11.1, which show that coatings manufactured at low pressure ($0.67Pa$) retain their dense structure whatever the current level. An increased pressure in the deposition chamber results in shorter mean-free-path of the flux, which leads to the increase of the oblique component of the flux, and in the reduction of the energetic-particle bombardment of the deposit, causing low adatom mobility. Both these factors contribute to the production of a coating with an open structure. The open and dense microstructures can be both recognised on the Thornton diagram shown in figure 4.6 in section 4.3.2: the open structure corresponds to a Zone 1 type, characterised by a reduced densification due to a higher number of voids and pore density, whereas the dense structure can be identified as a Zone T type.

It should be noted that an increment in sputtering pressure from $0.67Pa$ to $10Pa$, while keeping the current constant, although results in the production of a different coating microstructure, has only a negligible effect on the deposition time, which is reduced by approximately 10%. On the other hand, increasing the current level from $0.2A$ to $0.7A$, while keeping the pressure constant, has the effect of reducing the sputtering time of almost a factor of 5, as previously observed also by Thornton [107]. The low or high currents adopted when depositing at low pressure, and therefore the different deposition rates achieved, will characterise two dense structures which, in the rest of the thesis, will be referred to as ‘*Dense Low Rate*’ (DLR) and ‘*Dense High Rate*’ (DHR), respectively.

Chapter 12

Effect of the platinum layer morphology on the lifetime of TBC systems with a $\gamma + \gamma'$ bond coat

This chapter presents the effect of the morphology of the *Pt* layer, deposited via PVD, on the lifetime of TBC systems with a *Pt*-diffused (or $\gamma + \gamma'$) bond coat. Three different *Pt* layer structures were studied: an open structure, a DLR structure and a DHR structure. Detailed description of both the sputtering procedures adopted to deposit the *Pt* layers and the achieved structures is provided in chapter 11.

The studied specimens were manufactured depositing a $10 \pm 0.5\mu m$ thick layer of *Pt* on CMSX-4 coupons adopting the three sets of sputtering parameters listed in table 11.1. Before *Pt* deposition, the *Ni* based substrates were machined to achieve two different surface finishes: a 0.2MPa grit blasted surface and a coarse ground surface (see chapter 6). After *Pt* deposition, the specimens were first heat treated at 1190°C for one hour under vacuum to allow the formation of the *Pt*-diffused bond coat, and then coated with Y-PSZ (see chapter 9). During the ceramic deposition, the ground samples were placed with the lay of the surface irregularities parallel to the rotation axis of the samples holder. The TBC systems were finally tested in cyclic oxidation at 1150°C (see section 10.3.3).

12.1 Bond coat characterisation in as-deposited conditions

Manufacture of the *Pt*-diffused bond coat was successful on all combinations of *Pt* layer structures and substrate surface finishes except in one case (table 12.1): visual inspection by naked eye of the specimens after heat treatment highlighted the presence of blisters in bond coats produced with a DHR *Pt* layer structure deposited on ground surfaces. Blistering resulted in catastrophic failure of these specimens before completion of the manufacturing process. For this analysis, the *Pt* with an open structure was not deposited on samples with a ground surface for a shortage of ground substrates.

TYPE OF <i>Pt</i> STRUCTURE	VISUAL INSPECTION OF DIFFUSED COATING	
	Grit blasted surface	Ground surface
Open	Ok	n/a
Dense High Rate (DHR)	Ok	Blistering
Dense Low Rate (DLR)	Ok	Ok

Table 12.1: Results of visual inspection of coatings after diffusion: the DHR coating, when deposited on ground surface, was affected by blistering. The *Pt* with an open structure was not deposited on samples with a ground surface.

SEM micrographs of top surface and cross section of the DHR *Pt* structure on a ground surface after heat treatment, blistered coating, are shown in figure 12.1A and 12.1B, respectively. Figure 12.1B gives a clear indication of when and where the coating failure occurred. The micrograph shows a fully diffused coating, even underneath the blisters, and a delamination surface which runs along the original *Pt* layer/substrate interface. This suggests that the coating failed after the diffusion heat treatment during the cool down to room temperature from $1190^{\circ}C$. The accommodation of the CTE mismatch between the coating and the substrate may have caused the formation of compressive residual stress in the coating which was relieved by the formation of blisters. This hypothesis does not justify, however, why the DHR *Pt* structure on ground surfaces is the only type of coating suffering from blisters. All the studied specimens underwent the same heat treatment, therefore, if the thermal stress is assumed to be the only cause of blistering, then the same *Pt* coating would be expected to fail also when deposited on grit blasted specimens.

This observation suggest that there must be some contribution to the occurrence of blistering linked to the type of substrate surface finish. The surfaces investigated in this

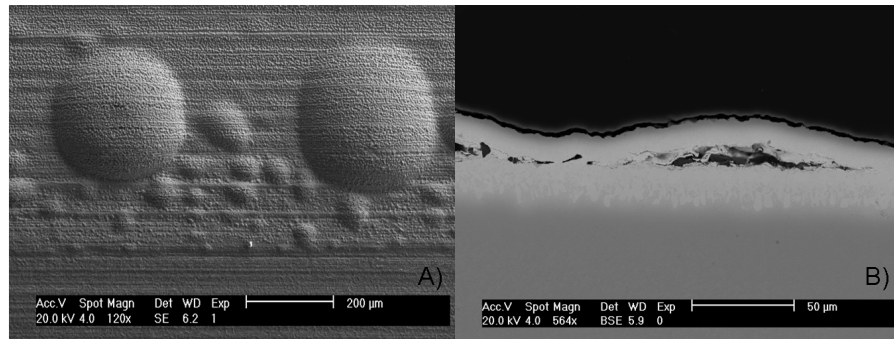


Figure 12.1: SEM micrographs of the DHR Pt structure on a ground surface after heat treatment: coating top surface (A) and cross section (B).

study are significantly different: grit blasted surfaces are characterised by irregularities which do not show any particular pattern, whereas the ground surfaces are characterised by a series of grooves running parallel to each other, which give them a higher anisotropy. The two surfaces have also different surface roughness, compared in table 12.2. The ground surface has a symmetrical profile, in respect of the mean line, and has $R_a = 0.72\mu m$. The grit blasted surface has also an almost symmetrical profile (R_{sk} value is not significantly lower than zero) but has an $R_a = 1.39\mu m$. In other words, the grit blasted surface is rougher than the ground surface. A rougher surface has a larger surface area than a smoother surface, therefore, the stress at the coating/substrate interface is distributed over a wider area, resulting in a lower interfacial strain energy. This may explain why the rougher surface of the grit blasted substrate tolerates a higher level of stress before the strain energy stored into the coating overcomes the fracture toughness of the interface, resulting in coating failure (and blistering).

ROUGHNESS PARAMETER	SURFACE FINISH	
	Ground	Grit blasted
R_a	$0.72\mu m$	$1.39\mu m$
R_q	$0.91\mu m$	$1.76\mu m$
R_v	$2.46\mu m$	$5.11\mu m$
R_p	$2.55\mu m$	$4.39\mu m$
R_{sk}	0.06	-0.31
R_{ku}	3.04	3.37
RSm	$70.42\mu m$	$76.89\mu m$

Table 12.2: Roughness parameters values for a ground and grit blasted surface finish; the chosen set of parameters is the one usually adopted to describe surfaces.

An experimental confirmation that different surface finishes (or roughnesses) have different levels of critical stress was found in another piece of work carried out by the author outside of the scope of this thesis. In that study the deposition of a $10\mu\text{m}$ thick *Pt* layer with a DHR structure on a mirror polished surface ($R_a = 0.2\mu\text{m}$) resulted in the failure of the *Pt* deposit by film spallation immediately after the completion of the PVD deposition, confirming that, when a highly polished surface is coated, the residual internal stress of the deposited structure may be sufficient to overcome the critical stress value that brings the coating to failure.

The suggestion that blistering is caused by CTE mismatch and that it is more likely to occur on smoother substrates still does not clarify why the DLR *Pt* structure was successfully deposited both on ground and grit blasted samples.

A possible explanation to this may be found in the fact that a reduction in the coating deposition rate causes a reduction in the level of internal residual stress. In this work the DLR *Pt* structure was produced reducing the sputtering rate by a factor of almost five with respect to that of the DHR structure (see table 11.1), and it seems to have been effective in eliminating the risk of blistering altogether.

As already mentioned in section 11.1, the dense structure (identified as the Zone T structure in the Thornton diagram [19]) is characterised by a high compressive internal stress. To prevent the blisters formation in dense coatings deposited on smooth surfaces, a reduction in the level of residual stress is critical. Based on the observations above, such a reduction can be achieved either by increasing the sputtering pressure, which in turn results in changing the deposit structure, or, for a given structure, by reducing the coating deposition rate.

Another effective way to reduce the stress level in the coating consists in reducing the thickness of the deposit. Although this method was not contemplated in the present study (due to the strict tolerance requested to the coating thickness - $\pm 0.5\mu\text{m}$), the author has attempted experimentally at depositing a DHR *Pt* structure without incurring coating failure by reducing the coating thickness down to $7.5\mu\text{m}$.

12.2 Oxidation test results

Figure 12.2 shows the TBC systems lifetime as a function of the *Pt* layer morphology (DHR, open, or DLR) for the two substrate surface finishes investigated. For each of the five TBC systems investigated, the diagram reports the number of specimens tested

as well as the average, maximum and minimum lifetime values expressed as number of oxidation cycles.

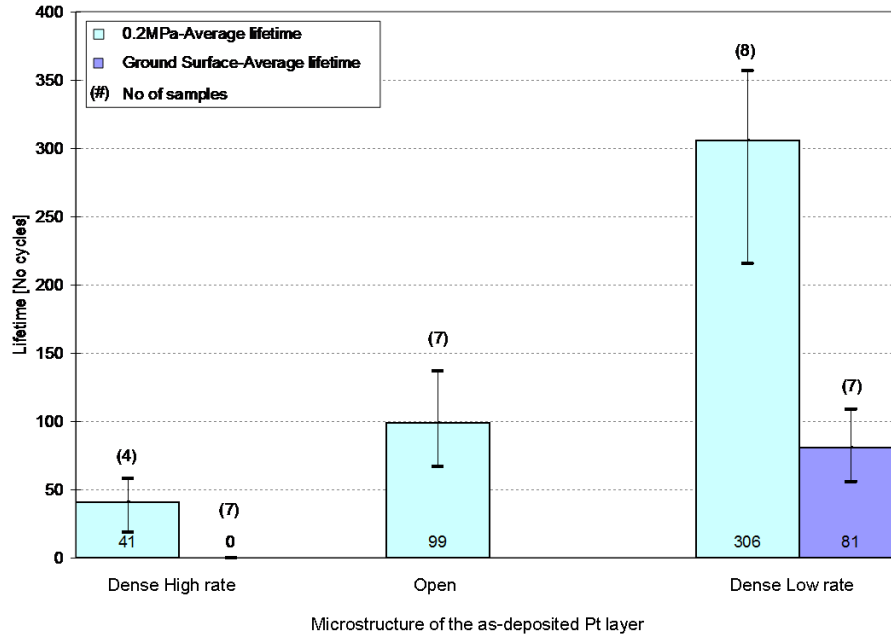


Figure 12.2: Oxidation test results for TBC systems with a *Pt*-diffused bond coat as a function of the *Pt* layer structure (DHR, open, or DLR) for two different substrate surface finishes (0.2MPa or ground surface). For each TBC system, the number of specimens tested, the average, maximum and minimum lifetime values (expressed as number of oxidation cycles) are reported.

The TBC systems with a DHR *Pt* structure exhibited the shortest time to failure. In this category of specimens, the samples with a ground surface have a nominal lifetime of zero cycles. Such a value was arbitrarily assigned to highlight the fact that all samples effectively failed before completing the manufacturing process due to blisters formation.

The lifetime of the TBC systems with a grit blasted surface increased by a factor of two when the *Pt* was deposited with an open structure rather than with a DHR structure and by a factor of seven when the *Pt* layer had a DLR structure. The beneficial effect of the DLR structure over a DHR structure was observed also on samples with a ground surface. None of the specimens with a DLR *Pt* structure, in fact, was affected by blistering and the coupons tested showed an average lifetime of 81 cycles. Independently of the type of *Pt* structure deposited, the TBC systems with a grit blasted surface always showed the longest life. The influence of the substrate

surface finish on the TBC systems lifetime is reported in detail in chapter 14.

Weibull analysis was performed on the life data collected from the TBC systems with a $0.2MPa$ surface finish; the resulting plots are pictured in figure 12.3. The shape parameter of the Weibull distribution (β , which is a measure of reliability) increases by a factor of almost two changing the Pt structure from a DHR to an open structure; such increment reaches a factor of three when the DLR structure is used. The beneficial effect of changing the Pt structure is even more evident when the characteristic life is evaluated: η increases by a factor of two or almost seven, respectively, when the open or the DLR structures are used. The combination of a high η and a high β results in the increment of B(10)life: this value was increased by a factor of 4 or 15 when the open or the DLR structures were used, instead of a DHR structure.

This progressive improvement in the TBC system performance depends on the progressive reduction of the residual stress in the bond coat due to the change in sputtering conditions. In section 12.1 it was inferred that the DHR Pt structure is characterised by a high level of residual stress, significantly higher than that of the DLR Pt structure. The open structure too appears to have a lower level of stress than the DHR Pt structure due to its higher number of voids and pore density. Although in none of these structures the stress level is high enough to cause coating failure at the original Pt layer/substrate interface, the different levels of residual stress may affect the life of the TBC system to different extents. When these coatings are used as bond coats, their top surface will be constrained under the TGO and TBC. During oxidation tests, the residual stress in the bond coat represents an additional contribution to the residual stress that is already building up in the TGO because of the oxide growth and because of the CTE mismatch between the TGO and the metallic bond coat. Given the important role played by the total stress in the TGO in determining the TBC durability, it can be concluded that a higher contribution to stress level in the TGO caused by the residual stress in the bond coat should be expected to shorten the TBC system lifetime.

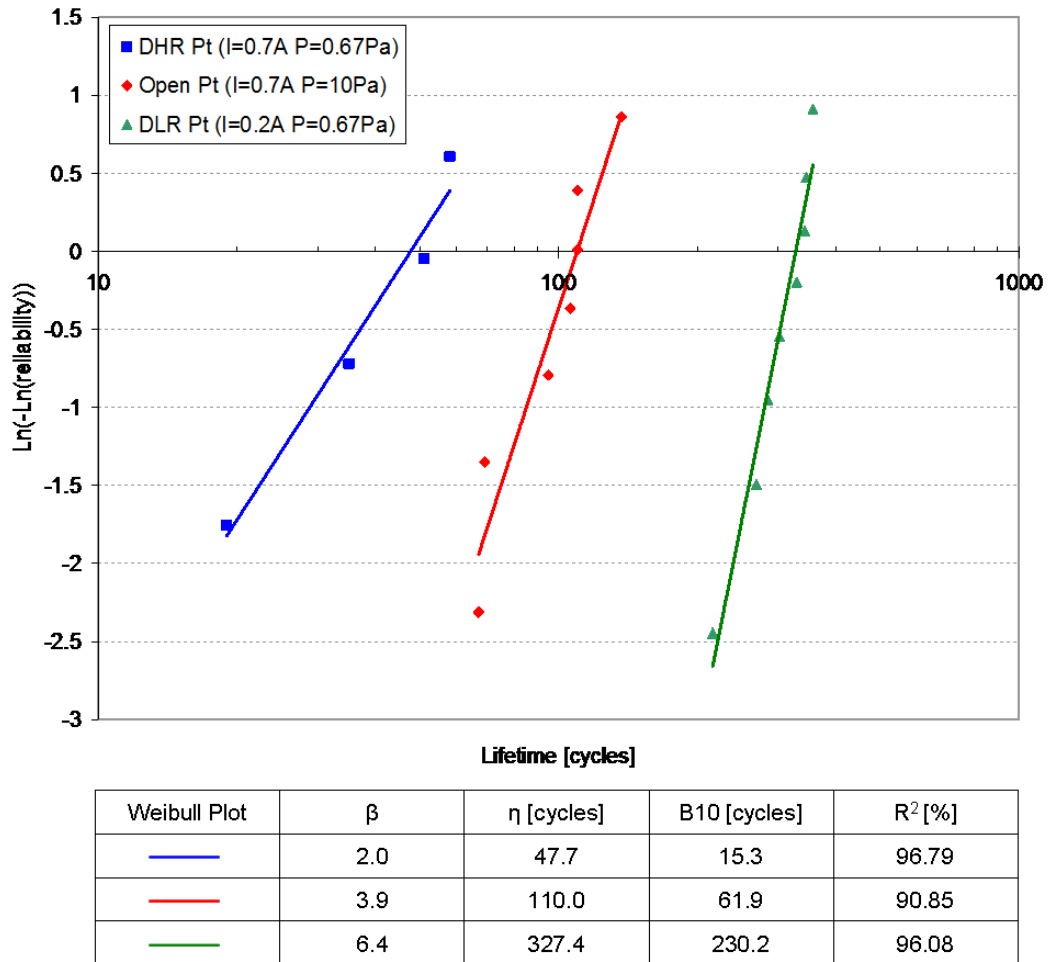


Figure 12.3: Weibull plots of the influence of the *Pt* layer morphology on the lifetime of TBC systems with grit blasted substrates and *Pt*-diffused BC. For each Weibull plot, the table reports the values of: β , η , B(10)life and R^2 .

12.3 Conclusions on the role of *Pt* layer morphology on the lifetime of TBC systems with a $\gamma + \gamma'$ bond coat

The three *Pt* structures investigated are thought to be characterised by different levels of compressive residual stress. Such stress, combined with the stress that arises from the accommodation of the CTE between the coating and the substrate, can overcome the critical stress value beyond which the coating fails due to blisters formation at the original *Pt* layer/substrate interface. For a given coating thickness, the critical stress level depends on the substrate surface finish; in particular such a level is lower for smooth surfaces than for rough surfaces. For a given surface finish, reducing the *Pt* layer sputtering rate is an effective way to reduce the residual stress in the coating and, in turn, to manufacture successfully *Pt*-diffused coatings on smooth surfaces, such as the ground surfaces.

When a $\gamma + \gamma'$ coating is used as a bond coat, the residual stress in the coating influences the TBC systems performance in cyclic oxidation, even if such a stress is below the critical stress value for the substrate surface in consideration. In a TBC system, the bond coat external surface is constrained underneath the TGO and the TBC. Therefore, the residual stress in the bond coat contributes to the increase of the residual stress in the TGO which, in turn, causes the ceramic to spall. TBC systems with a dense *Pt* structure and the anticipated highest level of stress (DHR *Pt* structure) showed the shortest life and lowest reproducibility in life. On the other hand, when the DLR *Pt* structure was used, the TBC systems showed the longest life and the highest reproducibility.

Chapter 13

Effect of the TBC deposition temperature on the lifetime of TBC systems with a $\gamma + \gamma'$ bond coat

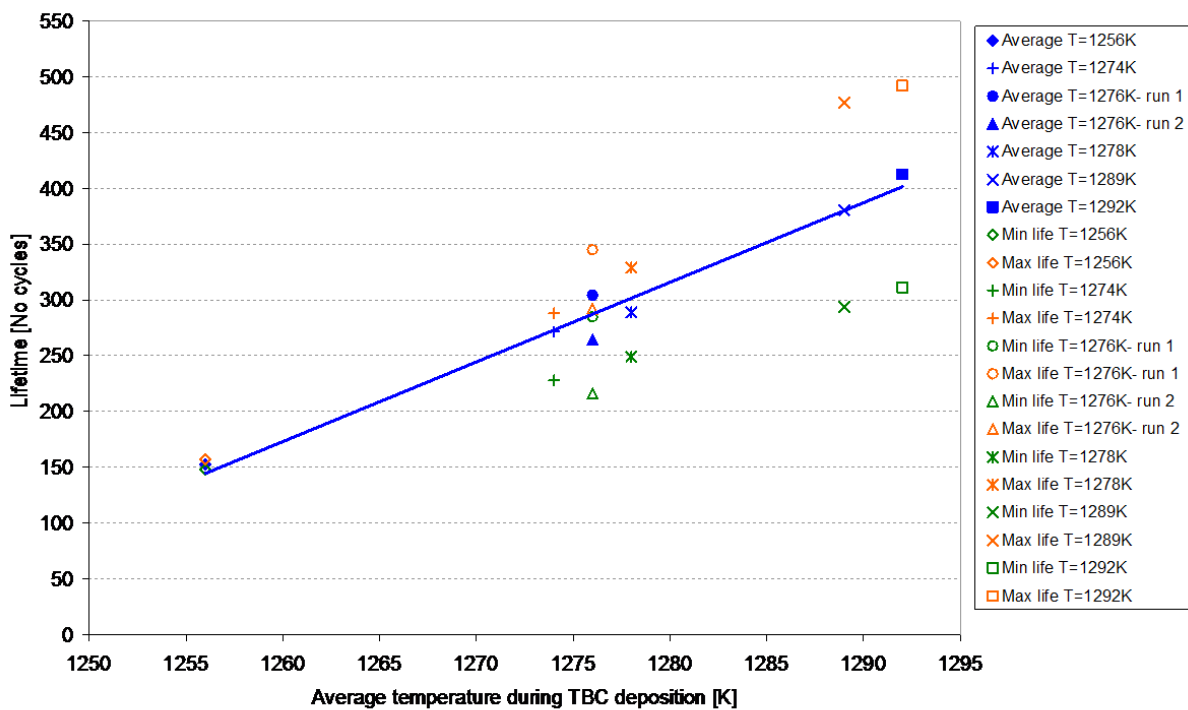
This section aims to discuss the influence that a variation of the ceramic deposition temperature has on the lifetime of TBC systems with a *Pt*-diffused bond coat. The study was carried out comparing the life data of a total of 26 specimens, the manufacture of which consisted of depositing a $10 \pm 0.5\mu m$ thick *Pt* layer with a DLR structure on grit blasted CMSX-4 coupons, heat treating the coupons at $1190^{\circ}C$ for 1 hour, and eventually coating them with Y-PSZ. The specimens were tested in cyclic oxidation at a temperature of $1150^{\circ}C$.

A total of seven EB-PVD runs were conducted to deposit the ceramic on the 26 specimens. Table 13.1 reports, for each run, the average deposition temperature and the number of samples coated. It should be noted that all the EB-PVD runs were carried out at a pre-defined temperature within the interval of temperature typically used in industrial production processes for the ceramic deposition (1144K and 1366K) [28].

A summary of the results of the oxidation tests are presented in figure 13.1, where the average lifetime of the specimens produced in each of the seven TBC deposition runs is plotted as a function of the average ceramic deposition temperature. The plot shows a linear dependence of lifetime with respect to the TBC deposition temperature, with the lifetime increasing monotonically when the TBC deposition temperature increases.

AVERAGE TBC DEPOSITION T [K]	NUMBER OF SAMPLES
1256	2
1274	2
1276	6
1276	5
1278	5
1289	3
1292	3

Table 13.1: Details of the EB-PVD runs carried out for depositing TBC on 26 specimens with a *Pt*-diffused bond coat



Trend line equation: $y=ax+c$			
Trend line	a	c	R ² [%]
	7.1491	-8834.7	96.67

Figure 13.1: Lifetime, expressed as average, maximum and minimum for each of the seven EB-PVD TBC run, as a function of the average ceramic deposition temperature.

There is no data available in the literature regarding the dependence of TBCs oxidation lifetime as a function of the deposition temperature; thus this is believed to be the first work investigating this aspect, at least in the public domain. Some limited comparison can be drawn based on the data provided in the work of Wu *et al.*, where the oxidation performance of TBC systems on a CMSX-4 substrate and with a *Pt*-diffused bond coat is described [24]. Wu's data differ from the results presented here in that his samples were manufactured within industrial setups (therefore the platinum layer was deposited via electroplating) and his oxidation tests were performed at 1135°C rather than 1150°C . In order to make a direct comparison, a diffusion based model developed by Nicholls *et al.* [170] can be used to extrapolate the life of Wu's samples had his tests been performed at 1150°C . The calculated extrapolations have been plotted together with all the data points obtained in the present work in figure 13.2, where the whole dataset has been modelled adopting a 2-parameters Weibull distribution (see chapter 5 for details of the analysis).

The R^2 value is often used to measure how well a distribution fits the experimental data. The Weibull plot in figure 13.2 shows a R^2 value higher than 97% , which means that more than 97% of the variation in the data is represented by the fit of the trend line. Such a good fit of the experimental data confirms that the 2-parameter Weibull distribution can be adopted to model TBC systems life data, and that the custom made samples produced on a laboratory scale at Cranfield University represent very well those produced in the industrial processes.

SEM analysis of the TBC top surface highlighted a significant variation of the columnar structure with the deposition temperature. Three different types of surface topography have been identified and are presented in Figure 13.3, which includes the micrographs of the top surface of TBC deposited at 1256K (figure 13.3A), 1278K (figure 13.3B) or 1298K (figure 13.3C). The type of column tops depicted in figure 13.3A are cusped, whereas the other two have the typical pyramidal shape. Grain dimension in figure 13.3C varies over a wider range of sizes with predominantly large elements.

On the basis of these observations, the seven EB-PVD runs and the seven sets of samples can be divided into three groups:

- Runs carried out at 'Low temperature' ($1256\text{K} \pm 2$) - surface type as in figure 13.3A;
- Runs carried out at 'Medium temperature' ($1276\text{K} \pm 2$) - surface type as in figure 13.3B;

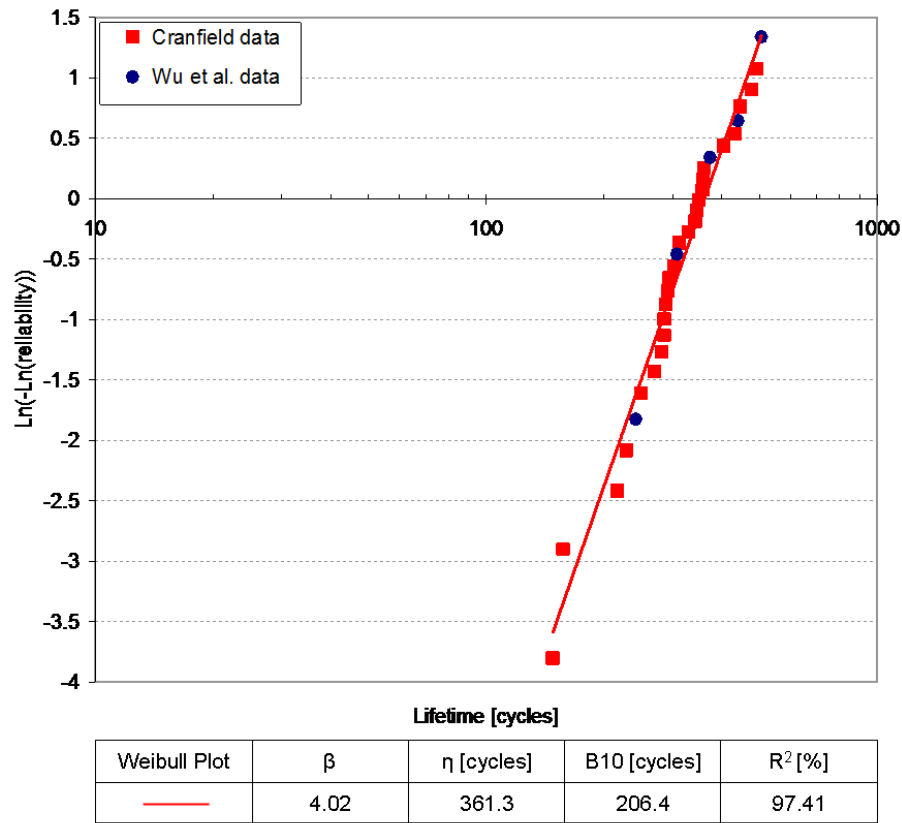


Figure 13.2: Lifetime analysis conducted on a population of samples including specimens studied in the present work (*Cranfield data*) and results extrapolated from literature (*Wu et al. data* [24])

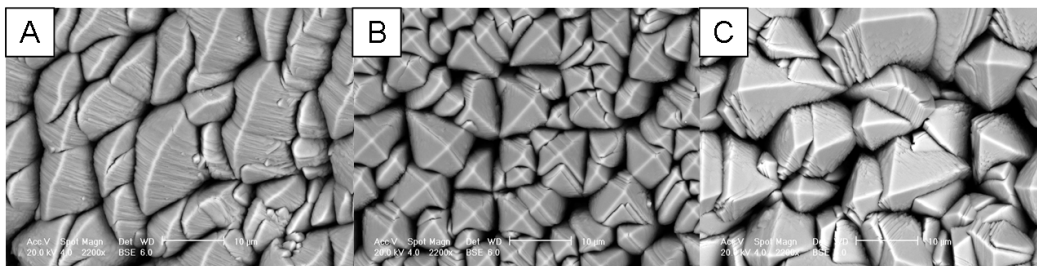


Figure 13.3: SEM micrographs of the top surface of TBC deposited at three different temperature: A) 1256K, B) 1278K, C) 1289K.

- Runs carried out at ‘High temperature’ ($1291K \pm 2$) - surface type as in figure 13.3C.

This classification is reflected in the notation used to identify each group of samples (i.e. samples manufactured during any of the ‘Low temperature’ runs are referred to as ‘TBC deposition T=1256K’). Life data analysis was repeated within each of these three groups, the resulting Weibull plots being shown in figure 13.4 together with a table reporting the values of β , η , B(10)life, and R^2 . The plots at 1276K and 1291K show good fit of the data, with R^2 values well above the minimum required to guarantee goodness of fit (89% for the 1276K plot and 87% for the 1291K plot [166]).

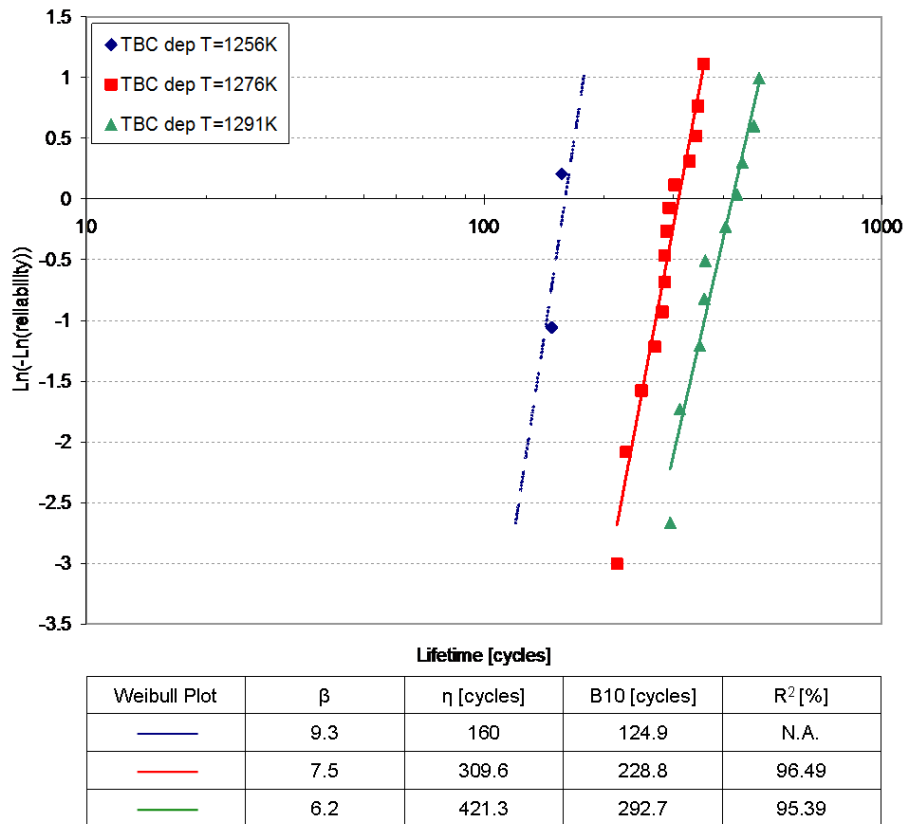


Figure 13.4: Weibull plots of different families of samples, classified according to the nominal ceramic deposition temperature.

The dashed line used in figure 13.4 to represent the Weibull plot for the samples deposited at 1256K points out that, for this group, not enough datapoints were available to perform a full life data analysis, therefore its trend had to be hypothesized and determined according to the following two step procedure (detailed in the subsequent paragraphs):

1. estimating the value of the shape parameter at 1256K (β_{1256}), based on the hypothesis that the Weibull shape parameter varies linearly with temperature;
2. fitting the general expression of the Weibull plot ($y = \beta_{1256}x - \beta_{1256}\ln(\eta_{1256})$) through the experimental data to determine η_{1256} .

Step 1 The β_{1256} value is estimated assuming that the Weibull shape parameter is a linear function of the TBC deposition temperature. The Weibull analysis, conducted on the lifetime data at 1276K and 1291K, allows calculation of the β values at these temperatures; in particular $\beta_{1276} = 7.5$ and $\beta_{1291} = 6.2$. In figure 13.5, these experimental data (filled symbols) are plotted as a function of the TBC deposition temperature and extrapolated with a linear model to β_{1256} . The value of β_{1256} determined through linear extrapolation at 1256K is 9.3.

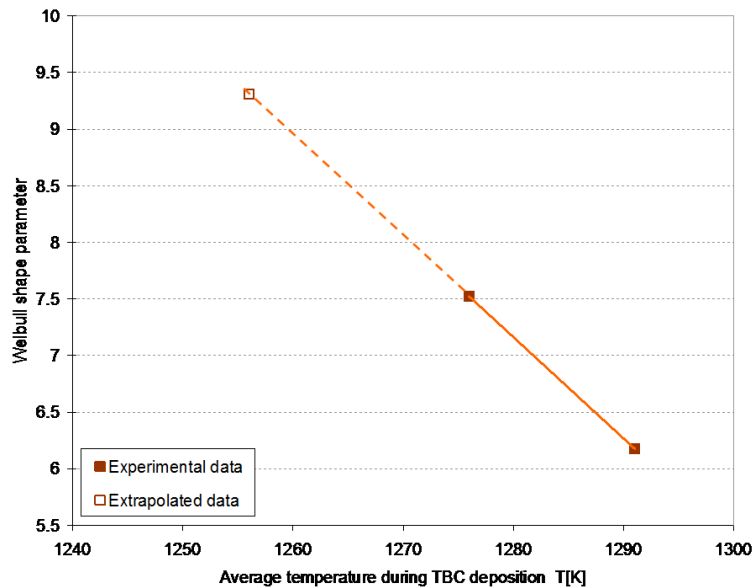


Figure 13.5: Weibull shape parameter versus TBC deposition temperature. The solid line in the diagram is an interpolation of the experimental data (β_{1276} and β_{1291}) while the dashed line is a linear extrapolation of the data to determine β_{1256} .

Step 2 The value of β_{1256} allows to identify a family of parallel curves having equation:

$$y = 9.3x - 9.3\ln(\eta_{1256}) \tag{13.1}$$

The Weibull plot at 1256K is the curve that provides the best fit to the limited

experimental data at 1256K, the equation of which is:

$$y = 9.3x - 47.18 \tag{13.2}$$

and it is drawn as a dashed line in figure 13.4.

From this data and the experimental data at 1276K and 1291K, figure 13.6 shows the variation of the characteristic life and of the B(10)life as a function of the TBC deposition temperature.

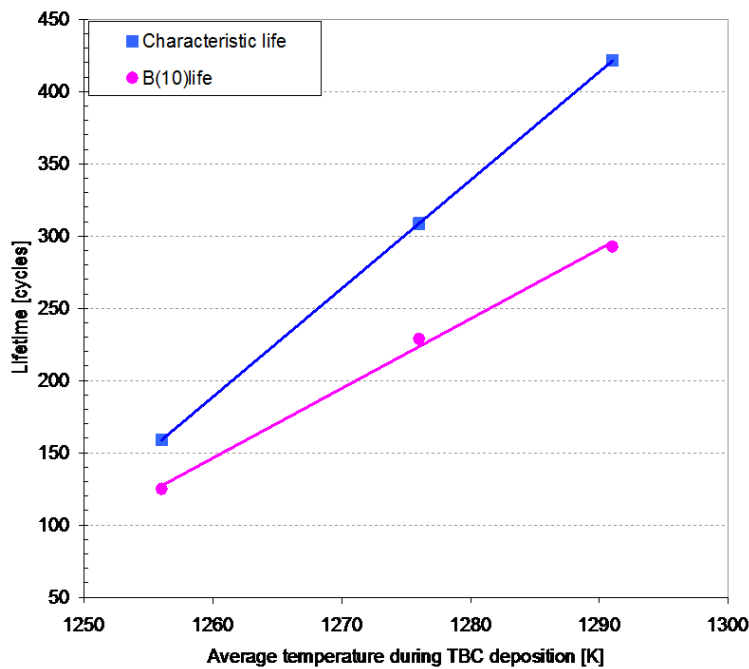


Figure 13.6: Variation of characteristic life and B(10)life as function of the TBC deposition temperature

The diagram shows that a higher TBC deposition temperature results in an increase of both η and B(10)life: in particular, raising the temperature from 1256K to 1291K results in an increment of characteristic life from 160 cycles to 421 cycles and of B(10)life from 125 cycles up to 293 cycles. Although both parameters increase linearly with the temperature, B(10)life increases at a lower rate. This is believed to depend on the reduction of the shape parameter with temperature showed in figure 13.5, which shows a monotonic decrease of β with the temperature.

Direct observation of the surface topology has demonstrated clearly that a change in TBC deposition temperature results in a modification of the resulting TBC struc-

ture. Variation of time to failure and life data reproducibility with ceramic deposition temperature suggests that there must exist a link between these characteristics and the TBC structure, the identification of which is, however, very difficult. XRD studies conducted on ceramic layers with different morphologies showed that the amount of residual stress level in the as-deposited EB-PVD ceramics is negligible (no more than a few hundred MPa) and therefore non influential on the TBC system lifetime[171]. However, this observation may not necessarily be translated directly in systems undergoing cyclic oxidation.

In general, a high stress level within the TGO is believed to be the principal cause of TBC failure. Such a stress, associated with the surface angulation, results in the formation of out-of-plane stresses, the direction of which is normal to the ceramic/metal interface eventually can cause the TBC to spall. Many factors contribute to the build up of stress in the TGO, however two main mechanisms have been identified: the oxide layer growth and the thermal mismatch between the bond coat and the oxide scale. The TBC systems analysed in this work are nominally identical in terms of substrate surface finish and bond coat chemical composition, therefore the contribution to the total amount of residual stress in the TGO due to the oxide scale growth is expected to be the same for all samples. On the other hand, the different TBCs produced may respond differently to the ageing phenomena taking place when the specimens are under test, and it is plausible that the observed ceramic structures lose compliance at different rates upon ageing, with those deposited at lower temperature producing higher levels of stress in the TGO due to the thermal mismatch with the bond coat.

It is possible that the structure produced by low temperature deposition is more susceptible to spallation due to a low compliant ceramic, which causes all these samples to fail within a relatively small range of cycles and according to the same mechanism. A variation in deposition temperature might induce a shift in the predominant mechanism for TBC spallation, with other temperature (and time) dependent mechanisms contributing to the failure of those deposited at higher temperature.

To date these hypothesis have not found experimental confirmation, and a detailed analysis of the level of stress in the TGO in the as-deposited condition and its evolution during oxidation would be required. This would require a high temperature XRD study, which is not available at Cranfield University and is beyond the work anticipated in this thesis.

13.1 Conclusions on the role of the TBC deposition temperature on the lifetime of TBC systems with a $\gamma + \gamma'$ bond coat

The 2-parameter Weibull distribution can be used successfully to model the time to failure of TBC systems with a Pt -diffused bond coat. It has been demonstrated that the specimens manufactured for the present work, although produced according to a custom made production procedure, can be used as a good representation of the industrial product. In fact, they belong to the same population as those manufactured according to the standard commercial procedure, albeit with different methods to deposit the Pt layer used to form the bond coat.

The experimental analysis carried out in the present study has shown that the ceramic deposition temperature has a significant effect on the TBC system lifetime. Within the interval of temperature usually adopted for the ceramic deposition via EB-PVD, an increase of the deposition temperature from 1256K to 1291K may more than double both the characteristic life and the B(10)life. Moreover, a closer control on the TBC deposition temperature may result into an increase of β from 4 up to 9.3.

From a structural point of view, a variation of ceramic deposition temperature results in the deposition of a TBC layer with different morphologies; the effect of the ceramic structure on the TBC system lifetime needs further investigation. The study of the stress evolution within TGO at different stages of the cycle test is also desirable.

Chapter 14

Influence of substrate surface preparation on the lifetime of TBC systems with a $\gamma + \gamma'$ bond coat

This section aims at investigating the effect that the substrate surface preparations have on the lifetime of TBC systems with a *Pt*-diffused bond coat by comparing the life data of a total of 80 specimens. The sample manufacture procedure consisted of coating the substrates with a $10 \pm 0.5 \mu m$ thick layer of *Pt* with a DLR structure, heat treating the coupons at $1190^\circ C$ for 1 hour and then coating them with Y-PSZ. The manufactured TBC systems were eventually tested in cyclic oxidation at $1150^\circ C$. The only nominal difference among the 80 specimens is the substrate surface preparation before *Pt* deposition, which is summarised in table 14.1 and detailed in the following paragraphs. Disk-shaped coupons were used as substrates for the studied TBC systems; such coupons were obtained by slicing CMSX-4 superalloy rods via Wire Electrical Discharge Machining (WEDM). During the cutting procedure the superalloy experiences significant heating across the cut, which results in the formation of a layer of recast material on the coupon surfaces. Such a type of surface, identified as *WEDM surface*, is the surface finish of the substrate in the as-received conditions (table 14.1- column 1).

Before *Pt* deposition, the substrates were submitted to a surface preparation procedure that included either one or two steps (columns 2 and 3 in table 14.1). In the single step procedure, the WEDM surface was either ground or grit blasted as described in sections 6.2.1 and 6.2.2, respectively. In the two-step procedure, the samples were first

As-received substrate surface finish	Surface preparation		Number of samples	Sample ID
	Step 1	Step 2		
WEDM surface	none	grit blasting at 0.05MPa	8	0.05-n
WEDM surface	none	grit blasting at 0.1MPa	9	0.1-n
WEDM surface	none	grit blasting at 0.2MPa	14	0.2-n
WEDM surface	none	grit blasting at 0.4MPa	12	0.4-n
WEDM surface	polishing	grit blasting at 0.05MPa	3	P0.05-n
WEDM surface	polishing	grit blasting at 0.1MPa	2	P0.1-n
WEDM surface	polishing	grit blasting at 0.2MPa	2	P0.2-n
WEDM surface	polishing	grit blasting at 0.4MPa	2	P0.4-n
WEDM surface	none	grinding (B46 wheel)	14	B46-n
WEDM surface	none	grinding (B91 wheel)	14	B91-n

Table 14.1: Summary of specimens surface preparation including total number of samples manufactured for each surface finish and samples identification codes

polished to a mirror finish and then grit blasted as described in section 6.2.2. The total number of specimens tested for each surface finish and the sample identification code are listed in columns 4 and 5 of table 14.1. The sample labels comprise two parts: the first refers to the surface preparation for the group of specimens, while the second is a serial number; e.g. the code P0.05-3 refers to the sample number 3 of the series of surface polished coupons grit blasted at 0.05MPa.

14.1 TBC systems characterisation at different stages of the manufacture

Figure 14.1 shows 3D optical images of a ground (left) and grit blasted (right) surface obtained using a confocal optical microscope. The grit blasted surfaces do not show any particular pattern, whereas the ground surfaces are characterised by a series of grooves running parallel to each other; the main direction of which is defined as the *lay* of the surface irregularities.

The substrate surface texture is not erased by the manufacture of the bond coat, the surface of which seems to replicate closely that of the substrate. Figure 14.2 shows the cross section micrographs of the *Pt*-diffused bond coat produced on a ground surface (figure 14.2A) and on a grit blasted surface (figure 14.2B). Different surface finishes do not affect the bond coat formation; in both cases, in fact, the bond coat consists of 25 μ m of a *Pt* enriched layer which shows two distinct phases. Analysis by EDX revealed

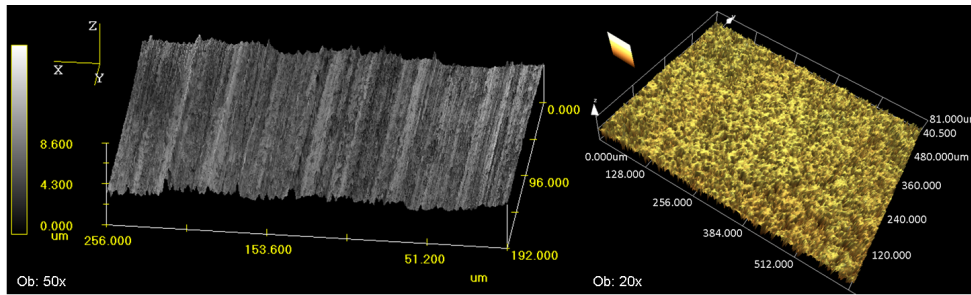


Figure 14.1: 3D optical images of a ground (left) and grit blasted (right) substrate surface

that the lighter phase is Pt -enriched $\gamma' - Ni_3Al$ and that the dark phase is Pt -enriched $\gamma - Ni$. In comparison to the γ' phase, the γ phase contains a lower amount of Pt and Al , but a higher amount of Cr , Co and W impurities. These results are in agreement with previous studies conducted on similar TBC systems [172]. The coating deposited on the grit blasted surface (figure 14.2B) shows dark inclusions roughly aligned along its middle plane. Such inclusions are residues of the alumina grits used during the substrate blasting process, and, in fact, cannot be observed in the bond coat manufactured on the ground surface (figure 14.2A).

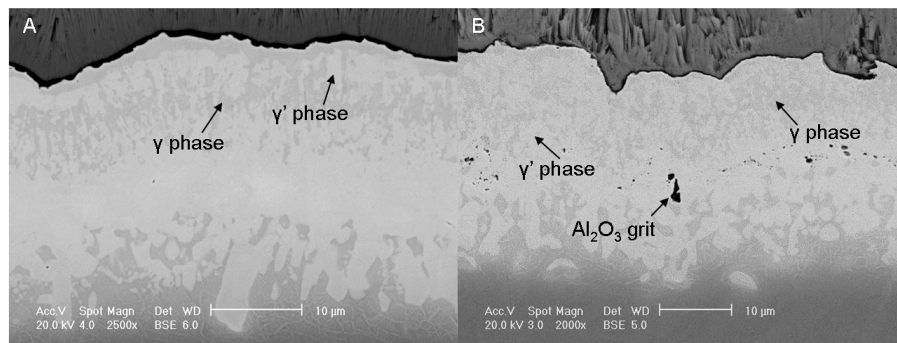


Figure 14.2: SEM micrographs of the cross section of a $\gamma + \gamma'$ bond coat deposited on a ground surface (A) and on a grit blasted surface (B). The latter micrograph shows the presence of dark inclusions at a distance of approximately 50% from the TGO/bond coat interface. Such inclusions are residues of the alumina grits used during the substrate blasting process.

Figure 14.3 shows the concentration profiles of the $\gamma + \gamma'$ bond coat on a ground surface (figure 14.3A) and on a grit blasted surface (figure 14.3B) as a function of the distance from the TGO/bond coat interface. The compositional analysis reveals that only the Pt profiles show some limited difference, while the content of the other

components is quite similar between the two types of TBC systems.

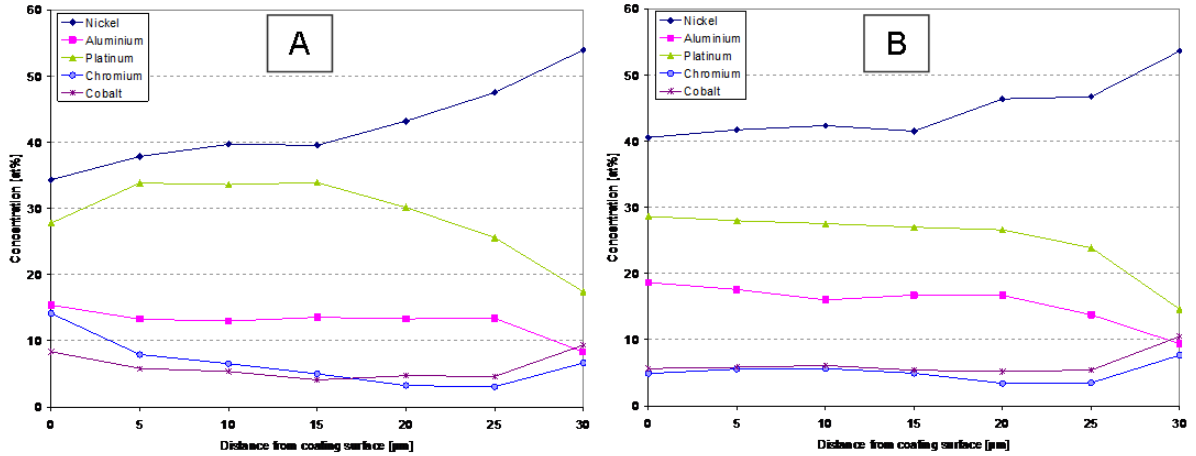


Figure 14.3: EDX compositional analysis of the cross section of a $\gamma + \gamma'$ bond coat deposited on a ground surface (A) and on a grit blasted surface (B).

The bond coat production is followed by the ceramic deposition; a well established practice prescribes grit blasting the bond coat before performing such operation. This step aims at cleaning the bond coat surface from any eventual oxide or contaminant, and it is typically carried out using a medium size of *220grit* and a pressure of 0.14MPa (20psi). In this study, the bond coat surfaces were not grit blasted before TBC deposition in order not to introduce any modification in the surface finish.

The TBC manufacture via EB-PVD requires constant rotation of the samples holder during the ceramic deposition (see section 4.3.2). The orientation of the specimens surface, with respect to the rotation axis of the samples holder, is irrelevant for isotropic surfaces such as the grit blasted surfaces; nevertheless, it may have an influence on the lifetime of TBC systems if the substrate has been ground. Therefore, during ceramic deposition, half of the samples for each type of ground surface finish were placed with the lay parallel to the rotation axis of the samples holder, and the other half with the lay perpendicular. As a result, at the end of the manufacturing procedure, the initial 28 samples were divided into four groups identified as: Coarse-parallel (or B91-parallel), Coarse-perpendicular (or B91-perpendicular), Fine-parallel (or B46-parallel), and Fine-perpendicular (or B46-perpendicular).

Figure 14.4 shows the top surface of a TBC deposited on three different surfaces. On ground samples, the lay of the irregularities is still visible after ceramic deposition, although it is more evident on coarse surfaces (figure 14.4B) than on fine surfaces (figure

14.4A). No difference was observed between samples having the lay perpendicular or parallel to the rotation axis. As expected, the columns grown on grit blasted surfaces do not show any pattern (figure 14.4C).

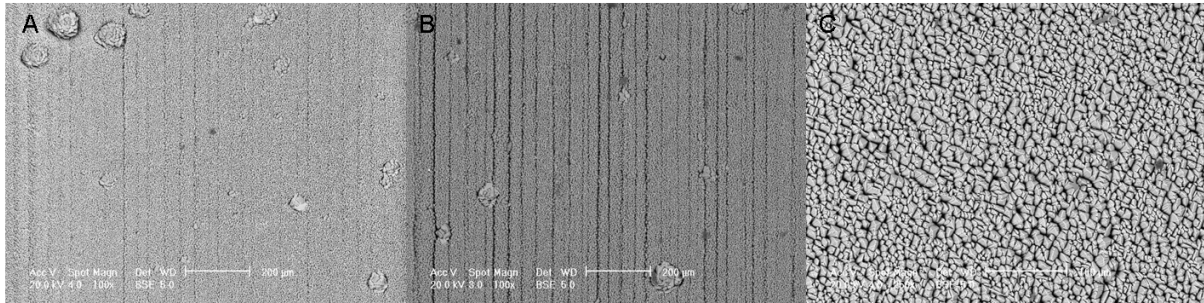


Figure 14.4: SEM micrographs of the top surface of a EB-PVD TBC deposited on three different surfaces: A) fine ground surface; B) coarse ground surface; C) grit blasted surface.

14.2 Cyclic oxidation test results

All manufactured specimens were tested under cyclic oxidation at 1150°C. Figure 14.5 shows the life data as a function of the substrate surface preparation. Each column in the diagram corresponds to a single type of surface as indicated in table 14.1 and reports average, maximum, and minimum values of lifetime. Columns are colour coded according to the category to which the single type of surface belongs: ground, polished and grit blasted (polished+grit blasted), or grit blasted only.

The ground surfaces are the worst performing. Within this category, the time to failure is not significantly affected neither by the change in surface texture, nor by the direction of the lay with respect to the rotation axis. In comparison to the other ground surfaces, a slight improvement in life was observed in coarse samples with the lay parallel to the rotation axes. The substrate surface preparation has a major influence on the life of grit blasted surfaces. Regardless of the pre-blasting surface treatment, the two categories of grit blasted surfaces show a similar dependence of the life from the blasting pressure: increasing the pressure results in an incremental increase, up to a factor of almost 7, of the TBC time to failure. Polishing the surface before grit blasting has a detrimental effect on the lifetime: all the polished+grit blasted surfaces, in fact, show a life up to 4 times shorter than that of the correspondent grit blasted only surface. The two step procedure was found to reduce the scatter in lifetime data. All the grit

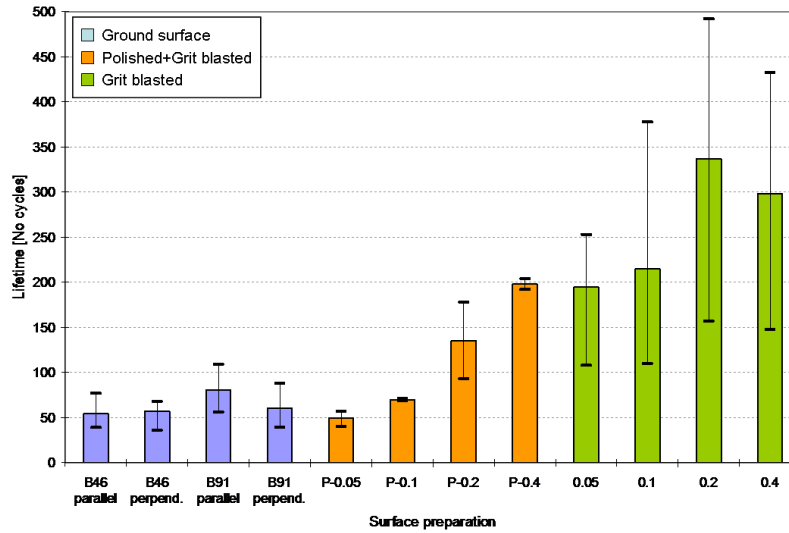


Figure 14.5: Average lifetime as a function of surface preparation. Each column corresponds to a single type of surface and reports average, maximum, and minimum values of lifetime expressed as a number of cycles to failure. Columns are colour coded according to the category to which the type of surface belongs: ground, polished and grit blasted or grit blasted only.

blasted only surfaces, in fact, show quite a poor reproducibility, with a lifetime scatter that can be of the same order of magnitude of the average life. However, it should be pointed out that such a high variability in life within each surface finish may have more than one single contributing factor other than the substrate surface preparation.

In chapter 13 it was highlighted that the ceramic deposition temperature has a significant influence on the TBC system lifetime. Therefore, the data in figure 14.5 were replotted as a function of the TBC deposition temperature for the four different grit blasting pressures; the resulting diagram is shown in figure 14.6. This diagram does not include ground and polished+grit blasted surfaces because these two categories of samples were coated adopting only a single deposition temperature (1276K).

Grouping the specimens according to the ceramic deposition temperature resulted in a significant reduction in life scatter for the specimens the substrates of which were grit blasted at 0.2MPa and 0.4MPa. On the other hand, the scatter reduction is limited in TBC systems with a 0.1MPa surface, and absent in specimens with a 0.05MPa surface. Therefore, it can be concluded that the latter category might have a lifetime independent of the ceramic deposition temperature.

Similarly to figure 14.5, figure 14.6 shows that the blasting pressure influences the

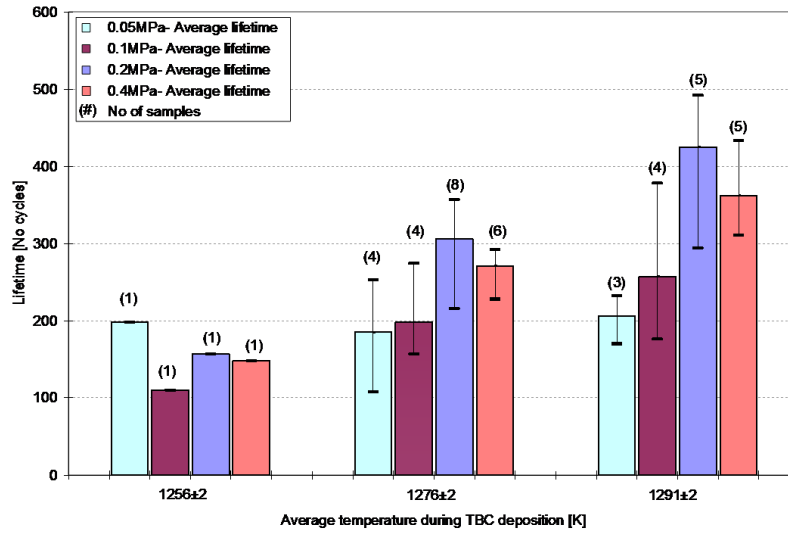


Figure 14.6: Average lifetime as a function of the TBC deposition temperature for four different surface finishes. Each column reports the number of specimens tested as well as the average, maximum and minimum values of lifetime expressed as number of cycles to failure. Columns are colour coded according to the pressure adopted during the blasting procedure.

TBC systems lifetime; however, such an effect is only significant at high TBC deposition temperature: at 1256K the life is almost independent of the surface finish. For each TBC deposition temperature the samples grit blasted at 0.2MPa and 0.4MPa appear to have a comparable life, and all of the 0.4MPa specimens have a life within the scatter of the 0.2MPa category. As a consequence, it is believed that these two surface finishes may well belong to the same samples population.

14.3 Post failure analysis

After failure of the TBC system, SEM and EDX analysis were carried out on both fracture surfaces (i.e. on the exposed substrate surface and on the bottom side of the spalled ceramic flake) to investigate the crack failure path. Figure 14.7 includes micrographs of the substrate exposed surface (figure 14.7A) and of the bottom side of the TBC spalled fragment (figure 14.7B) for a TBC system with a ground substrate.

Generally speaking, TBC systems with a ground surface fail at the bond coat/TGO interface. The crack runs along the interface leaving the bond coat evident on the substrate (indicated by ‘BC’ in figure 14.7A) and the TGO at the back of the spalled TBC

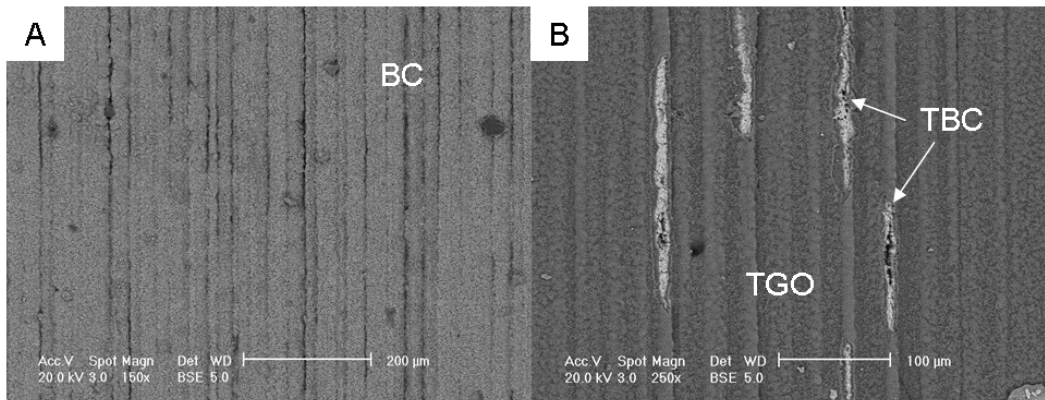


Figure 14.7: Post failure SEM analysis of a TBC system with a ground surface: A) substrate exposed surface and B) bottom side of the ceramic spalled fragment.

(figure 14.7B). However, while the failure leaves a perfectly bare bond coat on the substrate of TBC systems with a fine ground surface, some traces of ceramic can be found embedded into the bond coat of TBC systems with a coarse surface. To investigate this slightly different failure path, SEM analysis were carried out on metallographically prepared cross sections of a TBC system with a fine surface (figure 14.8A) and a coarse surface (figure 14.8B) before failure. The specimens were cut perpendicularly to the lay of the irregularities.

Unfortunately, perhaps due to the shrinkage of the mounting resin during preparation of the microscopy samples, the TBC in all examined samples was fully debonded from the bond coat, making it impossible to study cracks nucleation. Figure 14.8A shows that the TBC system with a fine finish has an almost flat bond coat/TGO interface; the surface undulations are, in fact, barely visible. On the other hand, the TBC systems with a coarse finish show a rougher interface, the surface is characterised by pronounced peaks spaced by an almost flat profile (see figure 14.8B). These features are believed to play a key role in crack propagation. In specimens with a fine finish, the very smooth surface allows the cracks, initiated at the bond coat/TGO interface, to propagate and to coalesce without being stopped. In specimens with a coarse finish, instead, the crack failure path is interrupted by the presence of the peaks on the bond coat surface. Due to the sudden change in curvature of the surface, the cracks are forced to run through the TBC. This results in a longer time to failure and in the presence of TBC fragment on the bond coat after failure (see arrows in figure 14.8B). Due to the peculiar pattern in the surface irregularities, the TBC fragments are aligned and fill the

trenches of the bond coat surface.

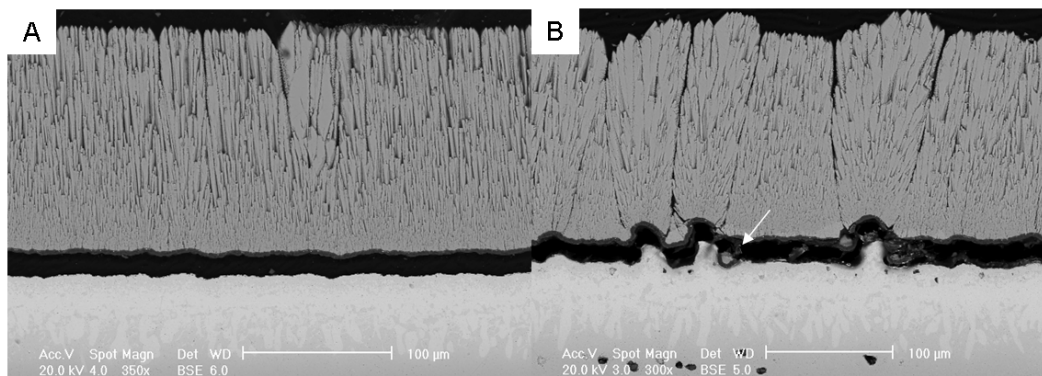


Figure 14.8: SEM micrographs of the cross section of a TBC system with a fine ground surface (A) and a coarse ground surface (B).

A similar investigation was conducted on TBC systems with grit blasted surface: figure 14.9 includes micrographs of the exposed substrate surface (figure 14.9A) and of the bottom side of the spalled TBC fragment (figure 14.9B). The substrate surface is characterised by large areas of exposed bond coat in which several islands of TBC surrounded by TGO are embedded. The analysis of the spalled fragment revealed that the back face is almost completely covered by the TGO layer, with only limited areas of ceramic left visible. These observations confirm the crack propagation mechanism suggested above, and the higher amount of TBC residues found on the substrate surface suggests that the crack path deviates from the bond coat/TGO interface more often when the substrate surface has a rougher finish.

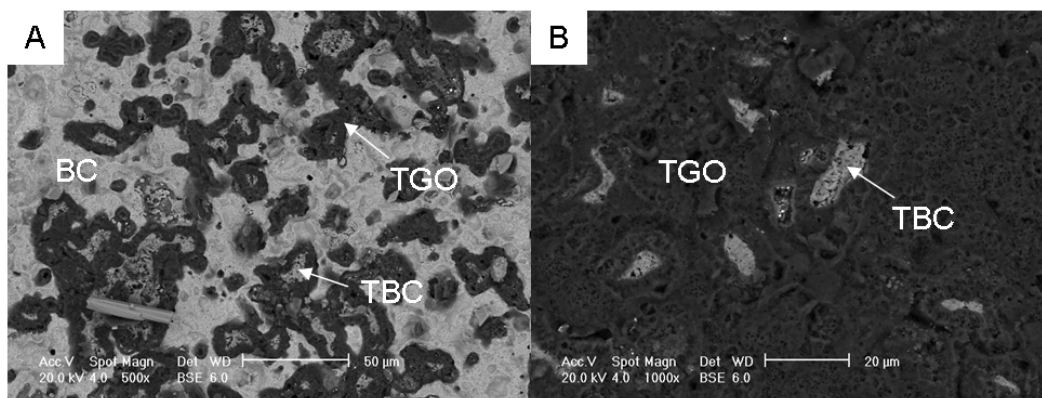


Figure 14.9: Post failure SEM analysis of a TBC system with a grit blasted surface: A) substrate exposed surface and B) bottom side of the ceramic spalled fragment.

14.4 Conclusions on role of surface preparation on the lifetime of TBC systems with a $\gamma + \gamma'$ bond coat

The substrate surface texture does not change the composition or the aspect of the bond coat, but it changes the TBC system failure mode. The lifetime of TBC system with a *Pt*-diffusion bond coat is strongly influenced by the surface texture of the substrate. An anisotropic surface obtained by grinding the substrate surface was shown to be detrimental for the TBC system lifetime. The longest life is achieved by adopting an isotropic surface obtained by grit blasting of the surface. For this category of specimens, the lifetime increases by increasing the blasting pressure.

The history of the substrate influences the lifetime too. Polishing the surface before grit blasting may reduce the TBC system lifetime up to a factor of 7. In this category of specimens, the highest blasting pressure adopted (0.4MPa) allows an increment in life, but the achieved improvement is still a factor 2 lower than the corresponding unpolished surface.

Post-mortem direct observation of the failure surfaces suggests that deviation of the crack propagation path from the TGO/bond coat initial interface is responsible for the improved lifetime of the grit blasted samples. The overall conclusion is that, in general, a coarser substrate surface finish promotes a longer lifetime, all other variables being the same.

Chapter 15

Effect of substrate surface texture on the lifetime of TBC systems with a $\gamma + \gamma'$ bond coat

Chapter 14 highlighted that the substrate surface preparation and the resulting surface finish have a significant effect on the TBC resistance to spallation. Moreover, within a group of ten different procedures, two methods were identified as the most suitable for manufacturing TBC systems with improved performance; they consist of grit blasting a WEDM surface either at $0.2MPa$ or at $0.4MPa$. However, these procedures are not easily applicable on an industrial scale. The WEDM surface is the result of a specific cutting process and therefore is very different from the surface of a turbine blade. The blasting procedure itself may as well be quite difficult to be replicated closely. Some process variables such as the particulate incident angle, the surface/gun nozzle distance, or the type of medium are relatively easy to control, whereas others, which also influence the process outcome, are extremely difficult to monitor and may jeopardise the surface reproducibility. Examples of these variables are: the amount of medium in the blaster, the shape of the grits, the amount of contaminant in the medium resulting from previous blasting operations, as well as the type of equipment adopted and the experience of the operator.

This chapter aims at assessing quantitatively the surfaces machined in chapter 14, looking for a measurable characteristic of the surface which can be correlated to the TBC system lifetime. The study was carried out comparing the life of 80 specimens, the manufacture of which was described in chapter 14. The substrate surface preparation

followed before the *Pt* deposition is summarised in table 14.1 on page 140.

15.1 Surface texture assessment

The specimens surface texture was assessed with a laser profilometer at two stages in the manufacturing procedure: after completing the substrate surface preparation, before *Pt* deposition, and after *Pt* deposition plus heat treatment. Assessment involved scanning the sample surface along the direction perpendicular to the lay of the irregularities (see section 10.1.2). The surface of the ground samples was assessed with four measurements running perpendicular to the lay and evenly distributed over the surface. Each measurement was done over a length of 10mm and provided a representation of the surface profile. The surface of grit blasted surfaces, whose irregularities do not have a particular lay, was assessed with eight measurements, evenly distributed over a 10mm side square grid.

The obtained profile, referred to as *raw profile*, was filtered with a low-high pass filter, according to the BS ISO 4288:1998 and BS ISO 3274:1998 standards. The filtered profile, *modified profile*, was used to determine a set of surface roughness parameters. At the completion of the surface assessment procedure, each ground sample was characterised by 4 sets of roughness parameters, while each grit blasted sample by 8 sets. Finally, for each sample, the average, minimum, and maximum values of each parameter were calculated.

For the purpose of this study, three statistical parameters were chosen to characterise the substrate surface roughness (BS EN ISO 4287:2000):

- the root mean square roughness, R_q
- the tortuosity, τ
- the root mean square average wavelength of the surface undulations, Rlq .

The parameter R_q is proportional to the profile amplitude, although the exact relationship depends on the specific geometry of the undulations:

$$R_q = \sqrt{\frac{1}{l_r} \int_0^{l_r} Z^2(x) dx} \quad (15.1)$$

where $Z(x)$ is the height of the assessed profile at any position x , and l_r is the sampling length.

The parameter τ is a measure of the increase of the surface profile due to the blasting procedure:

$$\tau = \frac{RL_0}{L} \quad (15.2)$$

where RL_0 is the actual length of the profile and L the projected profile length.

The parameter Rlq is determined by combining both the amplitude and the spacing parameters of the profile. Rlq provides a measure of the spacings between local peaks and valleys, taking into account their relative amplitudes and individual spatial frequencies. Numerically:

$$Rlq = 2\Pi \frac{R_q}{\Delta_q} \quad (15.3)$$

where Δ_q is the root mean square slope defined as $\Delta_q = \sqrt{\frac{1}{l_r} \int_0^{l_r} \left(\frac{dz(x)}{dx}\right)^2 dx}$.

15.2 Grit blasted surfaces

15.2.1 Before *Pt* deposition surface assessment: surface parameters versus grit blasting pressure

Figures 15.1, 15.2 and 15.3 show the root mean square roughness (R_q), the tortuosity (τ), and the average wavelength (Rlq) for a total of 33 grit blasted specimens before *Pt* deposition. The surface preparation for these samples involved grit blasting of the WEDM surface (without polishing). In the diagrams, each column corresponds to a single specimen and includes: the average, the maximum and the minimum value of the roughness parameter in consideration. Columns are colour coded according to the pressure adopted during the blasting procedure.

All diagrams show a small spread in roughness data measured at different locations within the same specimen, which is expected for this kind of measurement. The limited data spread indicates that the surface irregularities are homogeneously distributed over the analysed substrate surface, confirming that the average value of each parameter can be considered as a meaningful representation of each sample surface texture. Equivalent conclusions in terms of repeatability of the results can be drawn from the analysis of the set of samples whose WEDM surface was polished before grit blasting: the R_q , τ , and Rlq diagrams, reported in Appendix A, show very limited data spread for all measured parameters. However, figures 15.1, 15.2 and 15.3 show that the parameters may not change within each sample but they change significantly from sample

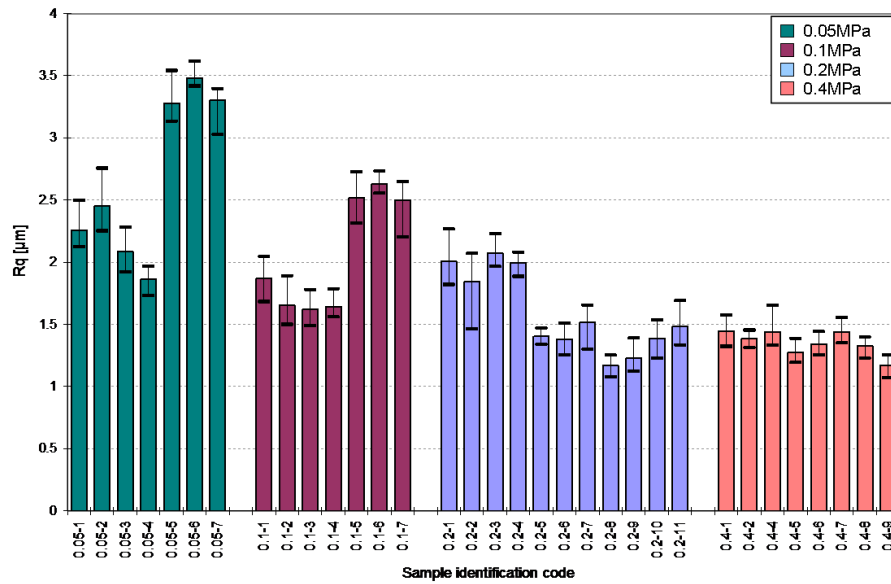


Figure 15.1: Root mean square roughness (R_q) value of the grit blasted samples before Pt deposition: each column corresponds to one sample and plots the average, minimum and maximum R_q value.

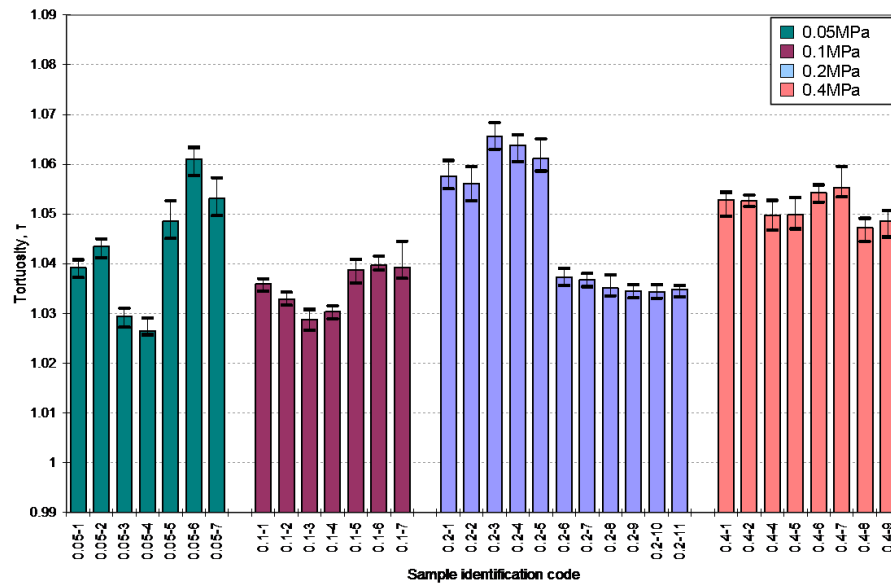


Figure 15.2: Tortuosity (τ) value of the grit blasted samples before Pt deposition: each column corresponds to one sample and plots the average, minimum and maximum τ value.

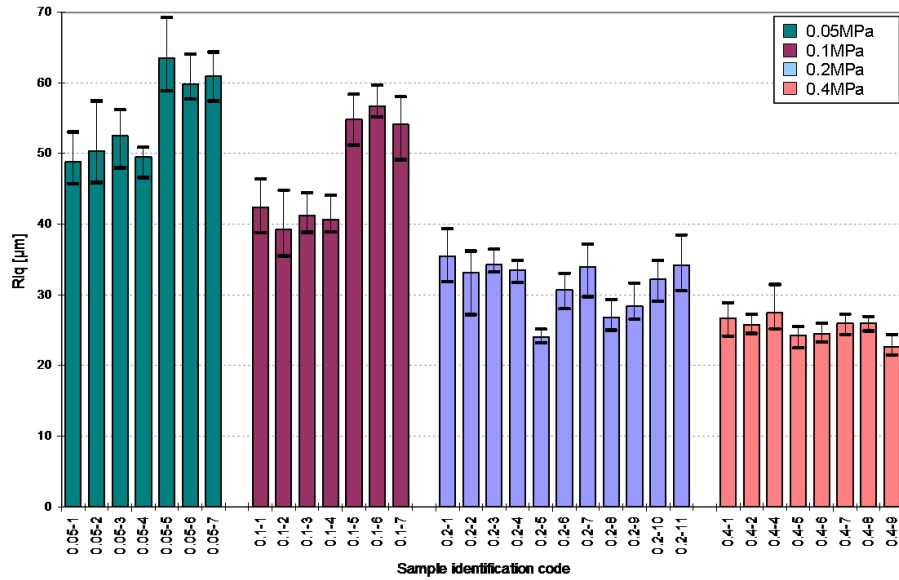


Figure 15.3: Root mean square average wavelength (Rlq) value of the grit blasted samples before Pt deposition: each column corresponds to one sample and plots the average, minimum and maximum (Rlq) value.

to sample within the same group. This difference reflects batch to batch variation in samples preparation: coupons manufactured within the same batch, in fact, tend to share equivalent roughness values while samples belonging to different batch may have significantly different surface texture.

Figures 15.4, 15.5 and 15.6 show the variation of the roughness parameters (averaged within each batch) measured before Pt deposition as a function of the blasting pressure, for different batches and surface preparation processes.

The grit blasted only samples and the polished+grit blasted samples follow different R_q profiles (figure 15.4). The former show a steep reduction in R_q (although with different, batch dependent rates) when the blasting pressure is increased up to $0.2MPa$, while, for higher pressure, R_q plateaus at values between 1.3 and $1.4\mu m$. This suggests that, at pressure higher than $0.2MPa$, the profile amplitude becomes less sensitive to pressure variations and to differences between batches. The polished+grit blasted samples show in the whole range of pressure analysed an increase in R_q ; such increment, however, is not constant, but it occurs at a rate that slowly decreases with increasing blasting pressure. This may indicate that also this category of samples will reach eventually an R_q plateau value of $\sim 1.3\mu m$, although possibly at pressure levels outside the range investigated here.

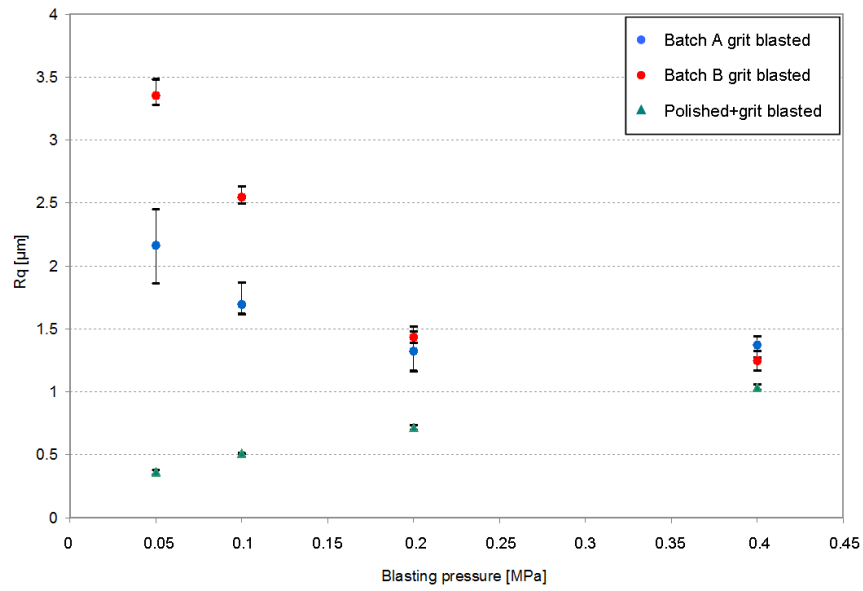


Figure 15.4: R_q (measured before Pt deposition) for three batches of coupons plotted as a function of grit blasting pressure

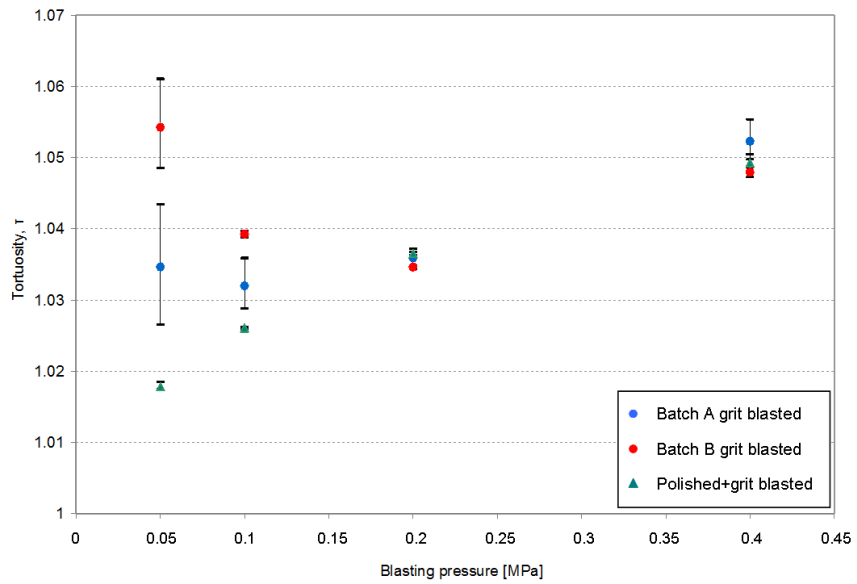


Figure 15.5: τ (measured before Pt deposition) for three batches of coupons plotted as a function of grit blasting pressure

Figure 15.5 shows that the two batches of grit blasted only specimens share a similar tortuosity trend: τ initially decreases, to start increasing over $0.2MPa$. The tortuosity of the polished samples instead steadily increases with the blasting pressure, and, over $0.2MPa$, it is comparable to that of the grit blasted only specimens. Therefore, above $0.2MPa$ the tortuosity is only a function of the blasting pressure.

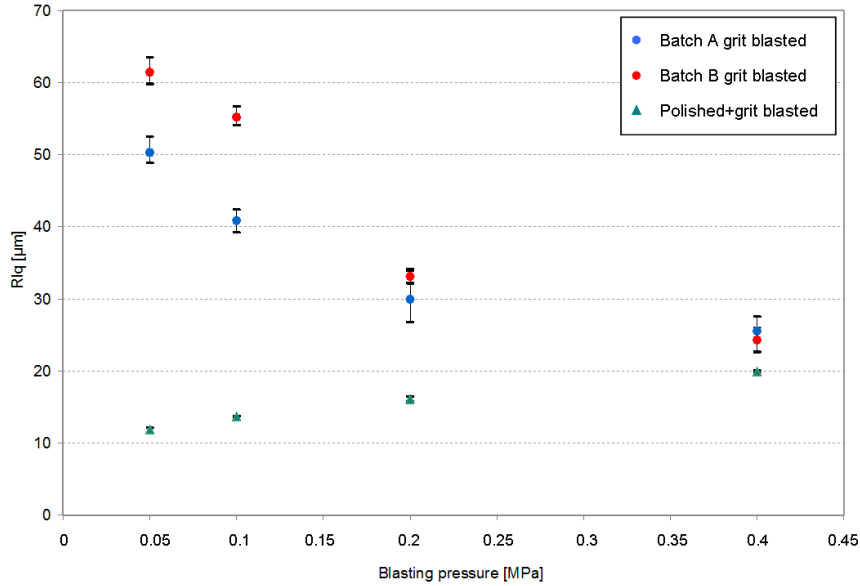


Figure 15.6: Rl_q (measured before Pt deposition) for three batches of coupons plotted as a function of grit blasting pressure

The trends of the Rl_q profiles shown in figure 15.6 are qualitatively equivalent to those of R_q : values are initially very sensitive to the grit blasting pressure, only to stabilise at higher pressure, both in case of polished and non polished samples.

To appreciate better the effect of the blasting pressure on the surface texture, figure 15.7 compares the profile of a $0.05MPa$ surface (figure 15.7A) and that of a $0.4MPa$ surface (figure 15.7B). The $0.05MPa$ surface is characterised by sharp troughs superimposed onto a pseudo-sinusoidal profile with a $\sim 130\mu m$ wavelength. Similar sharp troughs are present on the $0.4MPa$ surface, but the profile is generally flatter. The difference between the two textures is visible in figure 15.8, which includes micrographs of the two surfaces taken at an angle of 45° . While the $0.4MPa$ surface appears flat and relatively homogeneous (figure 15.8B), the $0.05MPa$ surface shows an array of ridges (figure 15.8A) the spacing of which corresponds to the sinusoidal wavelength identified in figure 15.7A. Optical inspection of grit blasted surfaces highlighted that the ridges are



Figure 15.7: Profiles of a 0.05MPa surface (A) and of a 0.4MPa surface (B). The measures are in microns

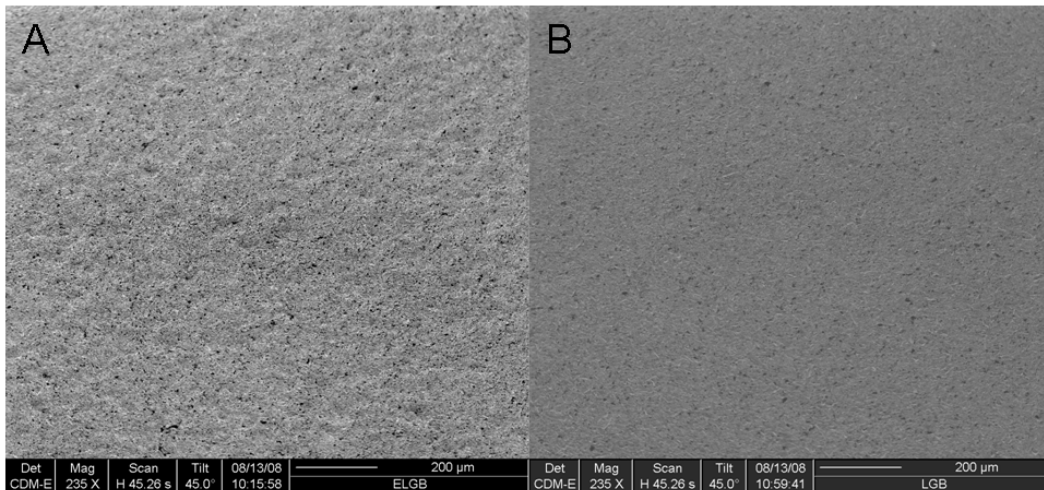


Figure 15.8: Secondary electrons micrographs of the 0.05MPa surface (A) and of the 0.4MPa surface (B) inclined by 45°

visible on all the $0.05MPa$ and the $0.1MPa$ surfaces, although they are less marked on the latter. All specimens grit blasted at either $0.2MPa$ or $0.4MPa$ appear flat. Such a pressure dependent difference in surface texture is believed to be linked to a lower efficiency of the low pressure blasting flux in carrying the blasting medium, which causes random agglomerates of grits to hit the surface, locally removing only some of the surface asperities and causing the ridges formation (figure 15.8A). Increasing the blasting pressure results in a more homogeneous distribution of the grits in the blasting flux and in higher energy impacts. As a result, the process allows to knock out all surface irregularities and to obtain a flatter surface (figure 15.8B). An equivalent result can be achieved also at low pressure by increasing the blasting time or by reducing the distance between the nozzle and the surface. Such modifications are believed to be the main cause of the batch to batch variation observed in figures 15.4, 15.5 and 15.6 for specimens grit blasted at low pressure.

Actually, the same procedure was followed to grit blast all samples, but the operator dependency of the fully manual blasting process as well as the fact that two consecutive batches of samples might have been produced over a relatively long time span, might have introduced small but significant variations in the process. Such variations do not affect the surface achieved when a high pressure is adopted, due to the fact that impacts are so energetic that a flat surface is obtained after just a few seconds of blasting; on the other hand, they influence the surfaces grit blasted at low pressure as they cause a variable material removal which translates in a poor repeatability in surface finish.

These considerations are also valid when a polished surface is grit blasted. The polishing procedure removes all the irregularities of the WEDM surface and an almost perfectly smooth surface is obtained. The following grit blasting at low pressure barely modifies the specimen surface re-introducing some irregularities; however, the surface is still very smooth (figure 15.4, 15.5 and 15.6). The amount of asperities introduced increases with increased blasting pressure and, for a pressure of $0.4MPa$, the surface is not significantly dissimilar from that achieved adopting the same pressure on a WEDM surface.

15.2.2 After *Pt* diffusion surface assessment: bond coat surface parameters versus grit blasting pressure

In the TBC system manufacturing procedure, the *Pt* deposition is followed by a heat treatment which allows the *Pt* to diffuse in the substrate, thereby forming the *Pt*-

diffused bond coat. Figures 15.9, 15.10 and 15.11 show R_q , τ , and Rlq for a total of 33 grit blasted specimens at this stage of the manufacturing. Contrary to the procedure adopted in the industrial practice, the manufactured procedure adopted in this study does not contemplate any grit blasting of the specimens surface between the diffusion heat treatment and the ceramic deposition. Therefore, measuring the surface texture of the specimens after heat treatment corresponds to the assessment of the bond coat surface before the EB-PVD TBC deposition. In the diagrams, each column corresponds to a single specimen and includes: the average, the maximum and the minimum value of the roughness parameter in consideration. Columns are colour coded according to the pressure adopted to grit blast the substrate before Pt deposition.

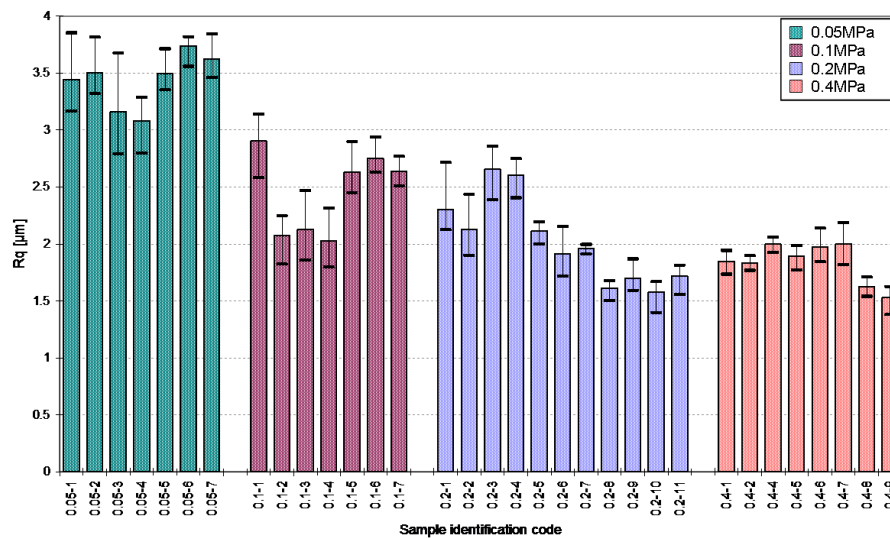


Figure 15.9: R_q value of the grit blasted samples after heat treatment; each column corresponds to one sample and report the average, the minimum and the maximum R_q value.

Similarly to that observed for the roughness values before Pt deposition, all diagrams show a small spread in roughness data within the same specimen, therefore the average value of each parameter can be considered as a meaningful representation of each sample surface texture. Moreover, coupons manufactured within the same batch still tend to share equivalent roughness values. Equivalent conclusions in terms of repeatability of the results can be drawn from the analysis of the set of samples whose WEDM surface was polished before grit blasting: the R_q , τ , and Rlq diagrams, reported in Appendix B, show very limited data spread for all measured parameters.

Figures 15.12, 15.13 and 15.14 show the variation of the roughness parameters (av-

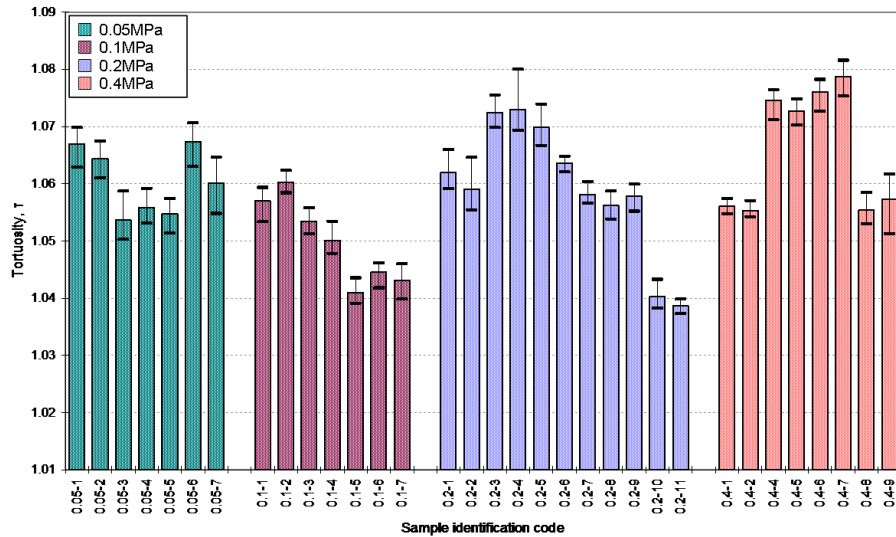


Figure 15.10: Tortuosity (τ) value of the grit blasted samples after *Pt* diffusion: each column corresponds to one sample and plots the average, minimum and maximum τ value.

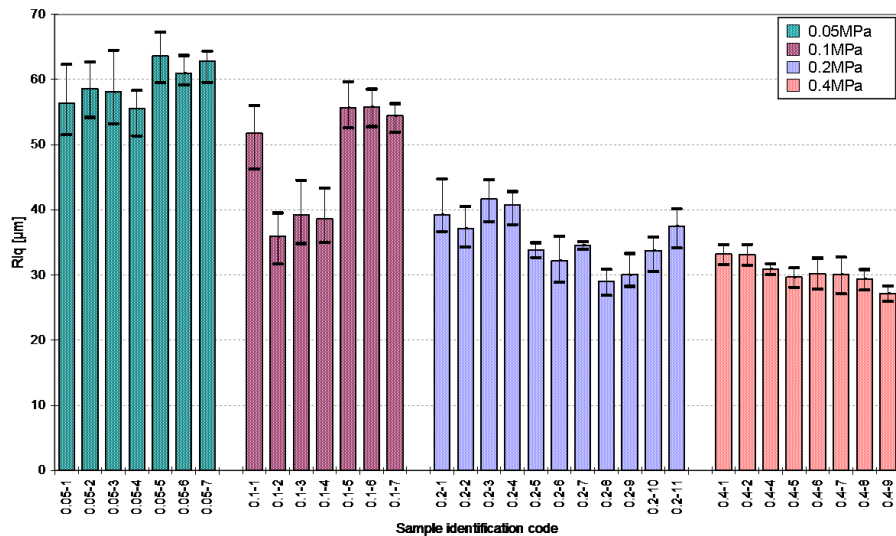


Figure 15.11: Root mean square average wavelength (Rlq) value of the grit blasted samples after *Pt* diffusion: each column corresponds to one sample and plots the average, minimum and maximum (Rlq) value.

eraged within each batch) measured after heat treatment as a function of the blasting pressure, for different batches and surface preparation processes (batch A and B are two randomly selected batches of specimens produced according to an equivalent grit blasting procedure).

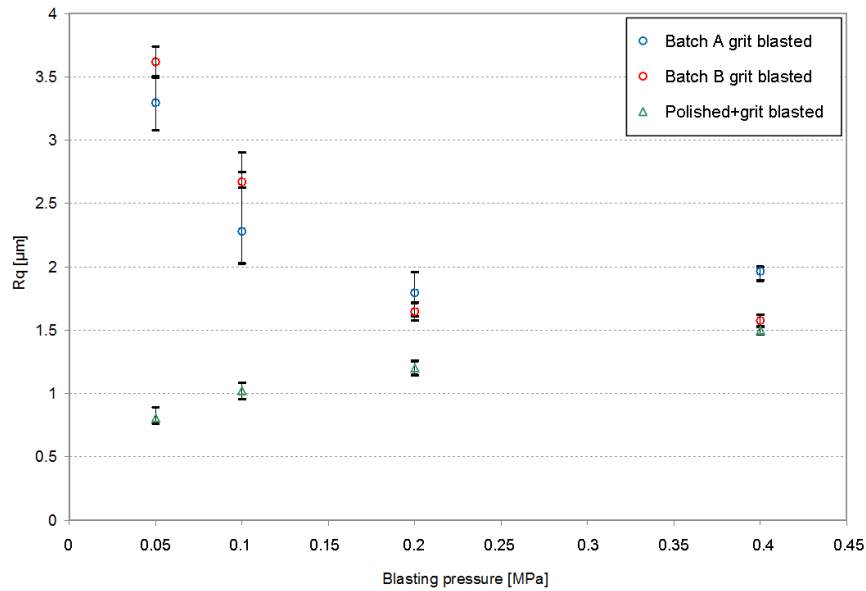


Figure 15.12: R_q (measured after Pt diffusion) for three batches of coupons plotted as a function of the pressure adopted to grit blast the substrate before Pt deposition

The trends of all roughness parameters are qualitatively equivalent to those of the correspondent parameters measured before Pt deposition, both in case of polished and non polished samples. However, grit blasted only samples show less variation in roughness values between different production batches.

15.2.3 Surface texture evolution: comparison between substrate and bond coat surface parameters

Figures 15.15, 15.16 and 15.17 show how the samples surface texture changes from the pre-sputtering to the after heat treatment conditions. The evolution is described in terms of variation of R_q , τ , and Rlq (indicated as ΔR_q , $\Delta\tau$, and ΔRlq , respectively) plotted as a function of the blasting pressure, for three different batches of samples and for different surface preparations. In the diagrams, each column represents the difference

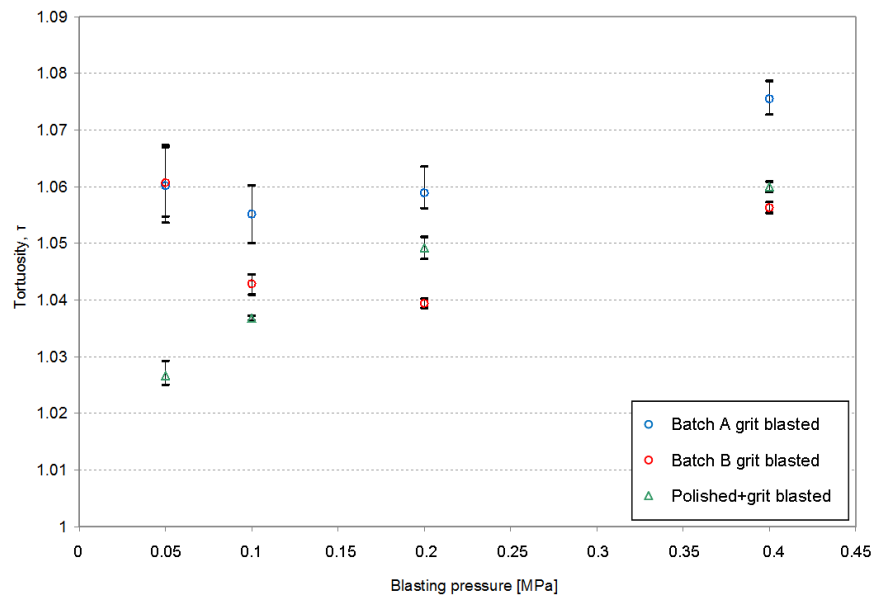


Figure 15.13: τ (measured after *Pt* diffusion) for three batches of coupons plotted as a function of the pressure adopted to grit blast the substrate before *Pt* deposition

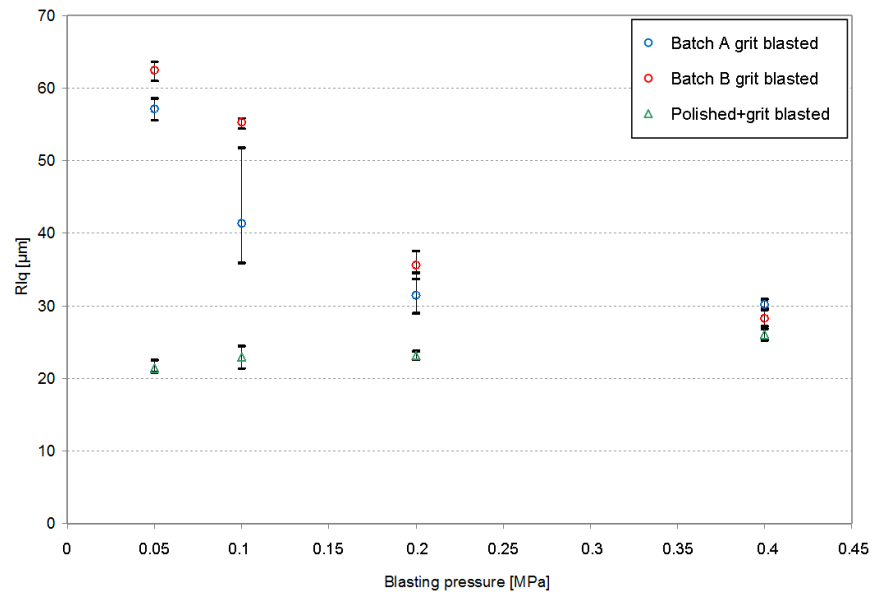


Figure 15.14: Rlq (measured after *Pt* diffusion) for three batches of coupons plotted as a function of the pressure adopted to grit blast the substrate before *Pt* deposition

between the average value of the roughness parameter in consideration, assessed after heat treatment, and the corresponding value before Pt deposition.

All diagrams show that the value of the roughness parameters increases after diffusion. The increment in R_q and τ may be batch dependent, while it is almost independent of the blasting pressure within each batch. The increments in Rlq have a more erratic appearance, however, the increase in wavelength suggests that some of the existing irregularities in the pre-sputtering surface do not evolve into large undulations but disappear under the Pt deposit. This means that, although the Pt layer follows the substrate geometry, the sputtering process itself introduces a certain level of asperities which combine with the already existing substrate roughness.

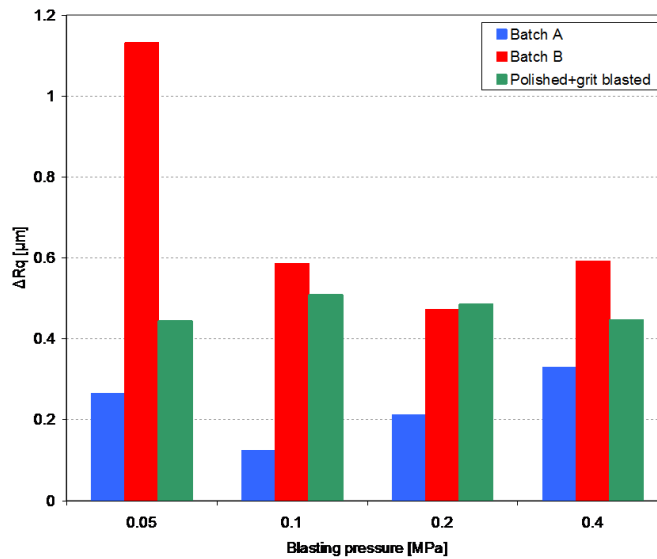


Figure 15.15: Increment of the R_q value for three batches of coupons. The increment is determined as the difference between the R_q measured after Pt diffusion and the corresponding value measured before Pt deposition. ΔR_q is plotted as a function of the pressure adopted to grit blast the coupons before sputtering the Pt .

15.2.4 Correlation between surface roughness parameters and TBC system lifetime

Figure 15.18 shows the variation of the specimens lifetime as a function of the Rlq of the surface before Pt deposition, for three different TBC deposition temperatures. This classification takes in consideration the results illustrated in chapter 13 where it

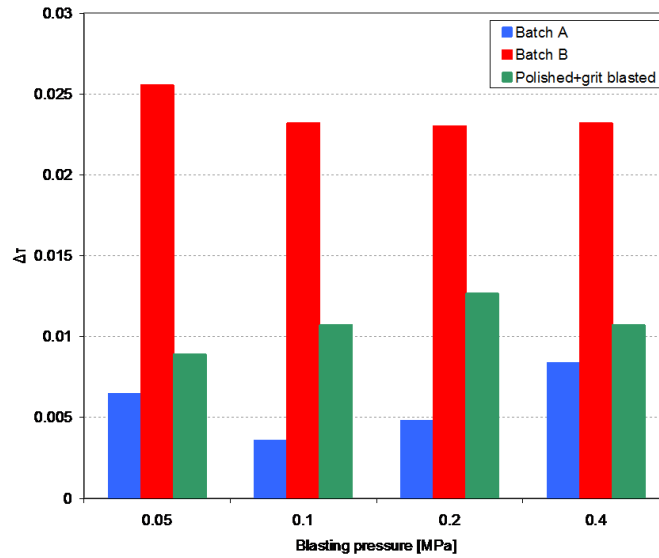


Figure 15.16: Increment of the τ value for three batches of coupons. The increment is determined as difference between the τ measured after Pt diffusion and the corresponding value measured before Pt deposition. $\Delta\tau$ is plotted as a function of the pressure adopted to grit blast the coupons before sputtering the Pt .

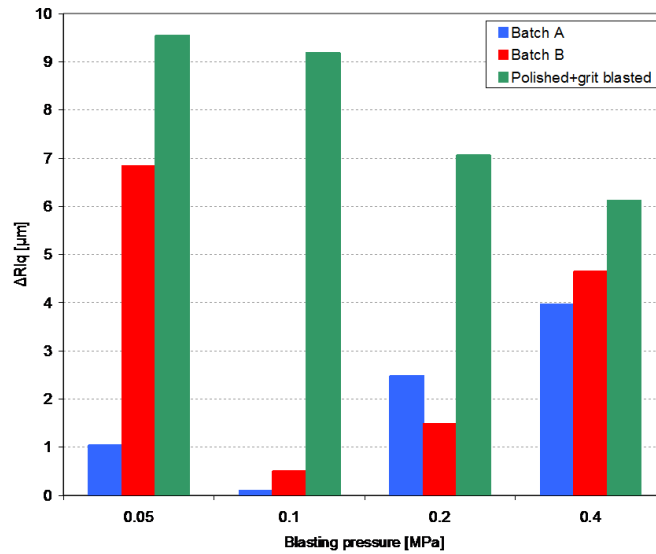


Figure 15.17: Increment of the Rlq value for three batches of coupons. The increment is determined as difference between the Rlq measured after Pt diffusion and the corresponding value measured before Pt deposition. ΔRlq is plotted as a function of the pressure adopted to grit blast the coupons before sputtering the Pt .

has been shown that the ceramic deposition temperature has an effect on the TBC systems lifetime. The diagram includes data obtained from all grit blasted samples: polished+grit blasted and grit blasted only specimens. Samples grit blasted at the same pressure, but having a different type of pre-blasting surface finish (i.e. WEDM or polished), are represented with the same symbol which is filled for grit blasted only samples and empty for polished+grit blasted specimens. Data points are colour coded according to the TBC deposition temperature. In section 15.2.1 it was shown that specimens grit blasted at the same pressure within each production batch share similar roughness parameters; therefore, those specimens in figure 15.18 which were tested, but the surface of which was not assessed, were given an Rlq value equal to the average Rlq of their production batch.

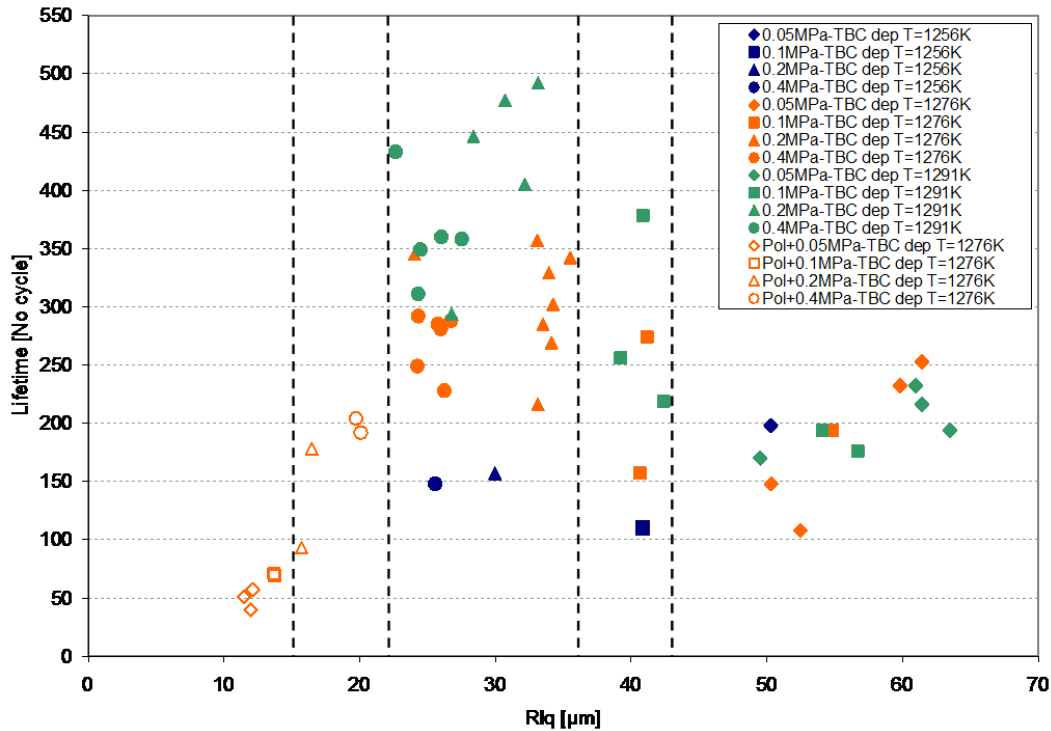


Figure 15.18: Variation of the TBC system lifetime as a function of the substrate surface Rlq , for three different TBC deposition temperatures.

Grit blasting produces surface finishes with an average wavelength between $11\mu\text{m}$ and $64\mu\text{m}$; in particular, those specimens with a polished pre-blasting surface have a Rlq between $11\mu\text{m}$ and $22\mu\text{m}$, while the grit blasted only samples have an Rlq between $22\mu\text{m}$ and $64\mu\text{m}$. Therefore, although the blasting pressure adopted (0.05MPa , 0.1MPa , 0.2MPa , or 0.4MPa) is the same for both categories of samples, the pol-

ishing treatment narrows the range of achievable wavelength, and shifts such a range towards smaller Rlq values.

The whole Rlq range obtained can be divided into three main intervals, with peculiar characteristics, spaced out by two further smaller intervals defined as ‘transition Rlq ranges’. The main intervals are:

- $Rlq < 15\mu m$.
- $22\mu m \leq Rlq \leq 36\mu m$
- $Rlq > 43\mu m$.

while the transition intervals are:

- $15\mu m \leq Rlq \leq 22\mu m$
- $36\mu m \leq Rlq \leq 43\mu m$

The $Rlq < 15\mu m$ range includes specimens the surface of which was polished and then grit blasted either at $0.05MPa$ or $0.1MPa$. All samples in this range failed between 40 and 70 cycles.

The $22\mu m \leq Rlq \leq 36\mu m$ range includes samples grit blasted either at $0.2MPa$ or $0.4MPa$. In this range of wavelength the TBC system lifetime ranges between 148 cycles and 492 cycles. However, the scatter in life does not depend on the Rlq value, but it is strictly dependent on the TBC deposition temperature.

The $Rlq > 43\mu m$ range includes all samples grit blasted at $0.05MPa$ and one-third of the specimens grit blasted at $0.1MPa$. In this range of Rlq , the TBC system life data varies between 108 cycles and 253 cycles. As opposed to the previous range, in this case the TBC deposition temperature does not significantly influence the TBC resistance to spallation.

The transition $15\mu m \leq Rlq \leq 22\mu m$ range includes specimens the surface of which was polished and then grit blasted either at $0.2MPa$ or $0.4MPa$, while the $36\mu m \leq Rlq \leq 43\mu m$ range includes the remaining two-third of the specimens grit blasted at $0.1MPa$. These two quite narrow Rlq intervals are similar in size and characterised by a significant scatter in lifetime. The specimens falling into these two ranges of wavelength allow a continuous transition between the best performing samples, in the $22\mu m \leq Rlq \leq 36\mu m$ range, and the shorter-life samples in either the $Rlq < 15\mu m$ range or the $Rlq > 43\mu m$ range.

No quantitative correlation between lifetime and the other roughness parameters (i.e. Rq and τ) were found; the diagrams are included in Appendix C.

15.2.5 Lifetime analysis

Section 15.2.4 showed that the TBC system lifetime depends on the roughness parameter (Rlq) of the substrate surface and that, in the range of wavelength investigated, five Rlq intervals with common lifetime characteristics can be identified. Section 13 showed that the lifetime is also dependent on the deposition temperature of the ceramic. In this section, the 2-parameter Weibull distribution will be adopted to model the life data for each interval of Rlq , and for three different TBC deposition temperatures. Figures 15.19, 15.20, and 15.21 show the Weibull plots for three intervals of Rlq : $Rlq < 22$, $22 < Rlq < 36$, and $Rlq > 36$, respectively. The Rlq interval in figures 15.19 and 15.21 is split further and the data are represented with an empty or filled symbol. In these diagrams, symbols with different shapes are used to represent the different pressure values adopted to blast the substrate; in particular, a diamond is used for $0.05MPa$, a square for $0.1MPa$, a triangle for $0.2MPa$, and a circle for $0.4MPa$. The symbols are colour coded according to the TBC deposition temperature: blue for $1256K$, orange for $1276K$ and green for $1291K$. All these diagrams show evidence of a very good fit between the experimental data and the calculated Weibull plots.

The characteristic life, the B(10)life and the shape parameter for the five Weibull distributions identified and plotted in the previous diagrams are compared in the charts in figures 15.22 and 15.23. Observation of figure 15.22 shows that the Weibull plots of the specimens in the transition Rlq intervals have similar η and B(10)life values. Such values, in fact, are only marginally higher in the $36 < Rlq < 43$ range in comparison to the corresponding values in the $15 < Rlq < 22$ range. The plots for the main Rlq intervals, instead, show significantly different values for both the characteristic life and the B(10)life, with the specimens in the $22 < Rlq < 36$ range being the best performing.

Figure 15.23 shows that the Weibull plots in the two transition Rlq ranges share similar β value (~ 2.5). For this value of β , the Weibull pdf becomes almost symmetrical and approaches the normal distribution [162]. Therefore, in the transition Rlq ranges, the failure can be described as a random phenomenon, due to the coexistence of two different distributions. As already mentioned, in fact, specimens in these ranges may have the characteristics of either the high performing or the low performing samples.

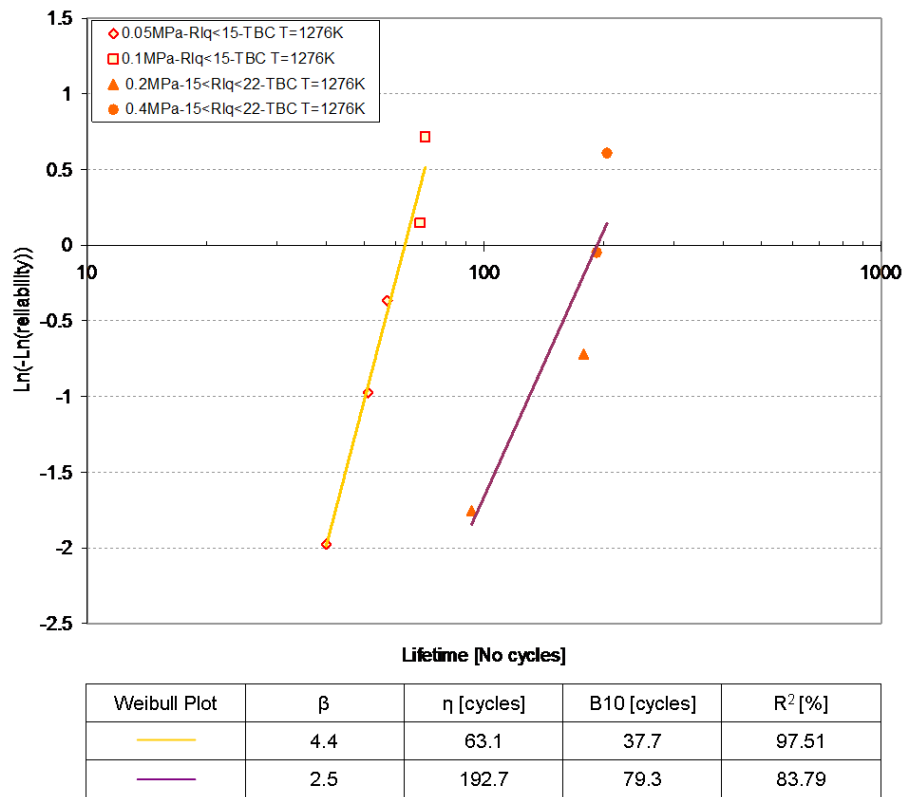


Figure 15.19: Weibull plots including the lifetime of specimens with $Rlq < 15$ (empty symbol) and $15 < Rlq < 22$ (filled symbol). Ceramic deposition temperature was 1276K. For each Weibull plot, the table reports the values of β , η , B(10)life and R^2 .

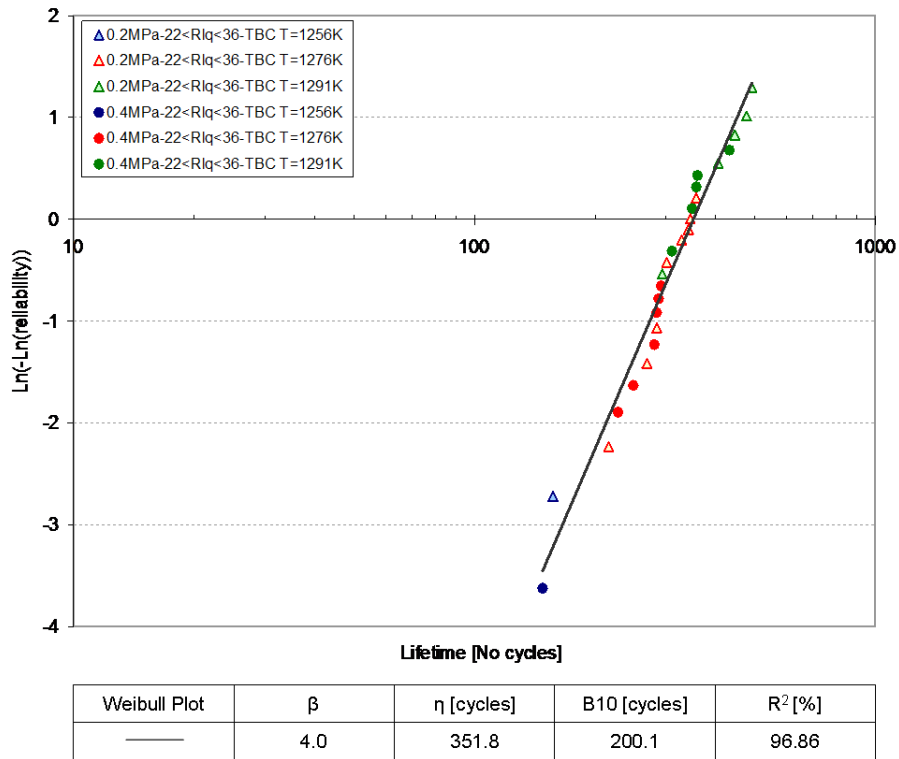


Figure 15.20: Weibull plot including the lifetime of specimens with $22 < Rlq < 36$; the plot includes specimens which were coated at three different TBC deposition temperatures. The table reports the values of β , η , B(10)life and R^2 .

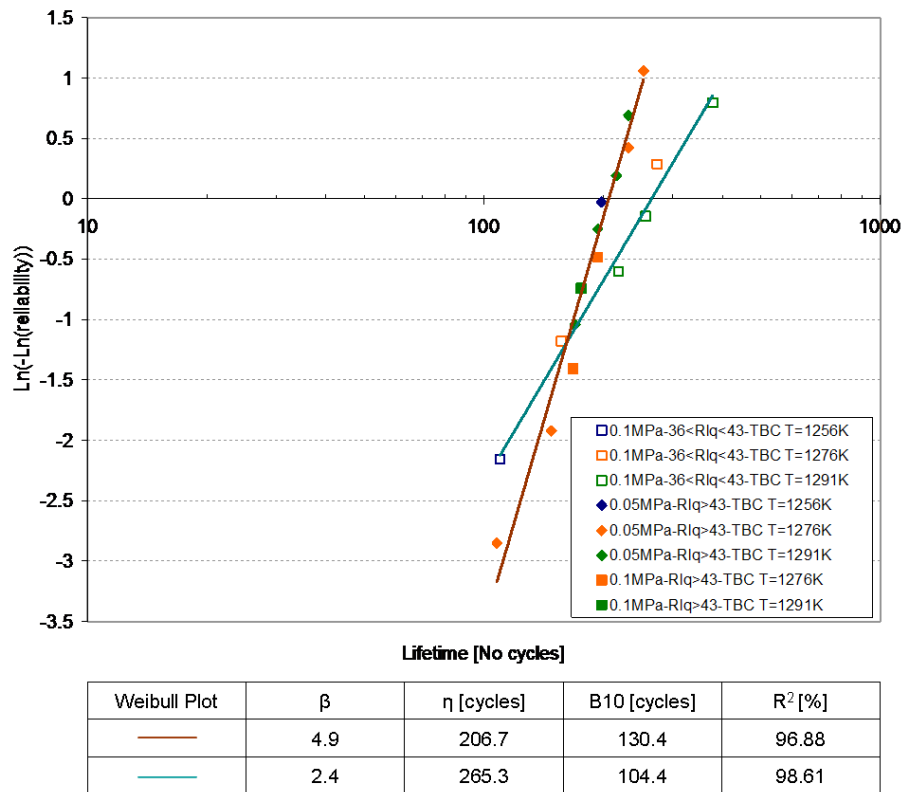


Figure 15.21: Weibull plots including the lifetime of specimens with $36 < Rlq < 43$ (empty symbol) and $Rlq < 43$ (filled symbol); each plot includes specimens coated at three different TBC deposition temperatures. For each Weibull plot, the table reports the values of β , η , B(10)life and R^2 .

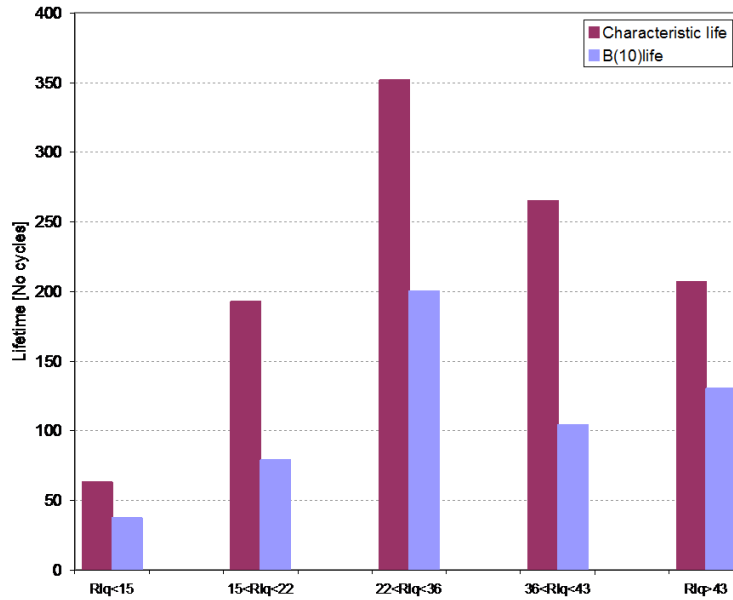


Figure 15.22: Characteristic life and B(10)life for the Weibull distribution as a function of Rlq intervals

In the three main Rlq intervals, the plots also share a similar shape parameter which value varies between 4 and 4.9. A β value higher than 3.7 means that the selected pdf has the characteristic of a Weibull distribution which is negatively skewed (see section 5.4.1.1). The similarity in β value means that the specimens in these intervals share a similar failure mode that, in this case, is determined by the substrate surface roughness and in particular by the value of the average wavelength.

However, while the surface texture is believed to be the main controlling factor that causes the TBC system failure in the $Rlq < 15$ and $Rlq > 43$ intervals, in the best performing Rlq range ($22 < Rlq < 36$) an optimization of the TBC deposition temperature allows a further improvement of the TBC system performance. The time to failure of the specimens in the $22 < Rlq < 36$ interval were, therefore, divided according to the temperature adopted during the TBC deposition, and a life data analysis was performed on each group (figure 15.24). The details of the procedure followed to build the plots is described in chapter 13.

Figures 15.25 and 15.26 show the characteristic life, the B(10)life and the shape parameter for the five Rlq intervals and for the three different TBC deposition temperatures. In the optimum Rlq range strict control of the ceramic deposition temperature allows an increase in β from 4 up to 9.3 (figure 15.26) and the characteristic life from 352 to 421 cycles (figure 15.25).

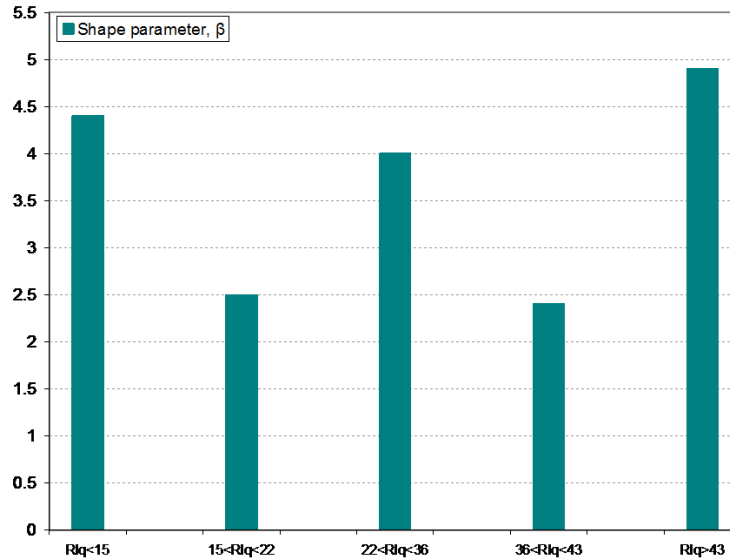


Figure 15.23: Shape parameter for the Weibull distribution as a function of Rlq intervals

15.3 Ground samples

The analysis carried out on the grit blasted specimens and presented in section 15.2 is performed here on ground samples. All fine and coarse surfaces were assessed at two different stages of the TBC system manufacturing procedure: before Pt deposition and after the bond coat forming heat treatment, and then compared in terms of the roughness parameters R_q , τ , and Rlq . The sample to sample comparison is followed by the comparison between the two types of surface (coarse versus fine surface) and by the life data analysis.

15.3.1 Ground surface characterisation before Pt deposition

Figure 15.27, figure 15.28, and figure 15.29 show R_q , τ , and Rlq for all ground surfaces before Pt deposition. In the diagrams, each column corresponds to a single specimen and includes the average, the maximum and the minimum value of the roughness parameter in consideration. Columns are colour coded according to their surface finish.

All diagrams show a very limited data spread in roughness data within the same specimen and a small spread within each of the two types of surface. These results are not unexpected: the grinding procedure adopted to machine the samples is, in fact, a recognised method for machining surfaces with a high degree of reproducibility.

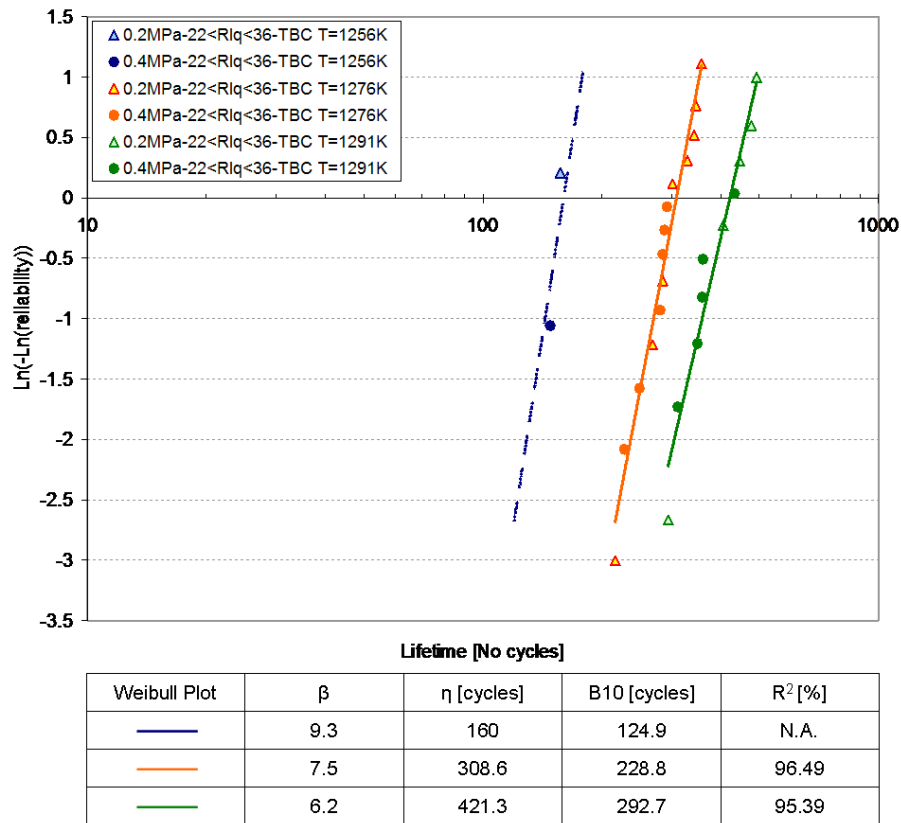


Figure 15.24: Weibull plots including the lifetime of specimens with $22 < Rlq < 36$; each plot includes specimens which were coated at a similar TBC deposition temperatures. For each Weibull plot, the table reports the values of β , η , B(10)life and R^2 .

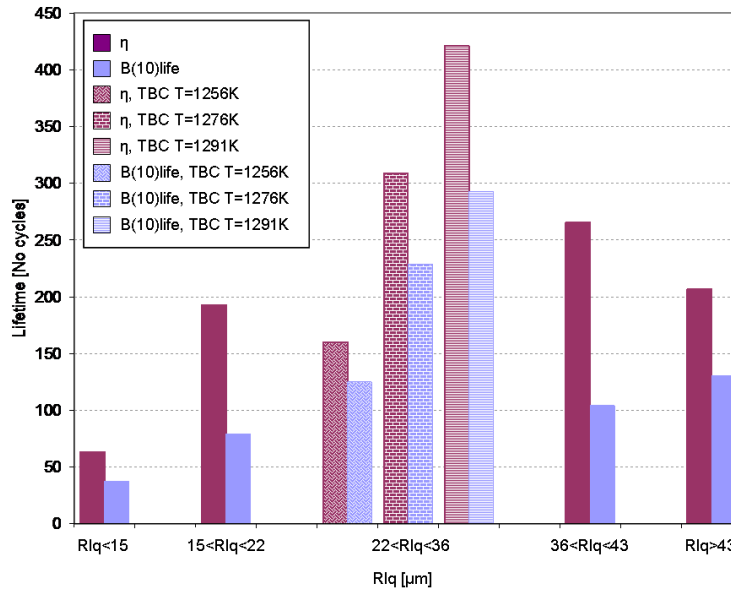


Figure 15.25: Characteristic life and B(10)life for the Weibull distribution for the five Rlq intervals and for three different TBC deposition temperature

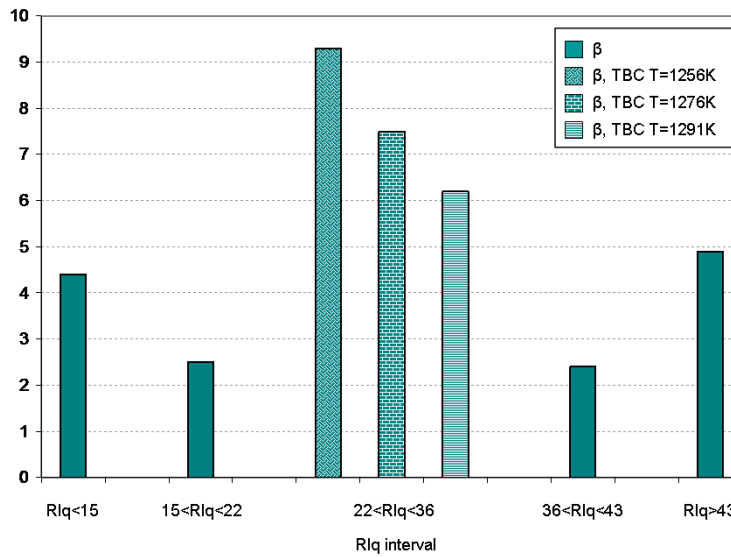


Figure 15.26: Shape parameter for the Weibull distribution for the five Rlq intervals and for three different TBC deposition temperature

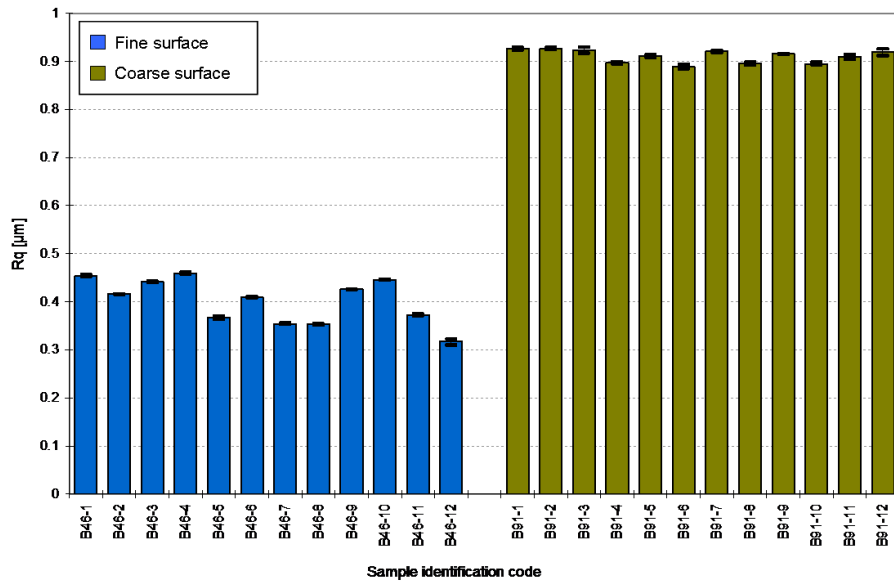


Figure 15.27: R_q value of the ground samples before Pt deposition; each column corresponds to one sample and report the average, the minimum and the maximum R_q value.

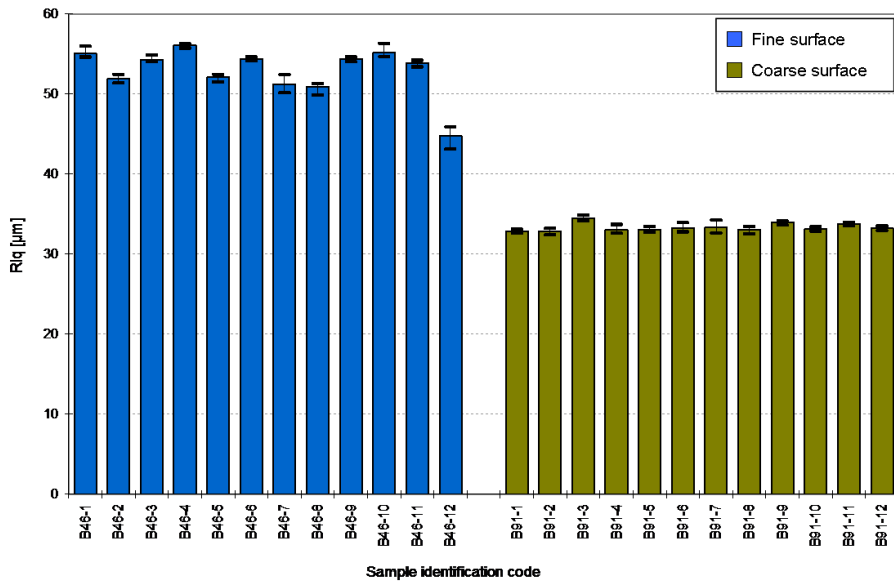


Figure 15.28: R_{lq} value of the ground samples before Pt deposition; each column corresponds to one sample and report the average, the minimum and the maximum R_{lq} value.

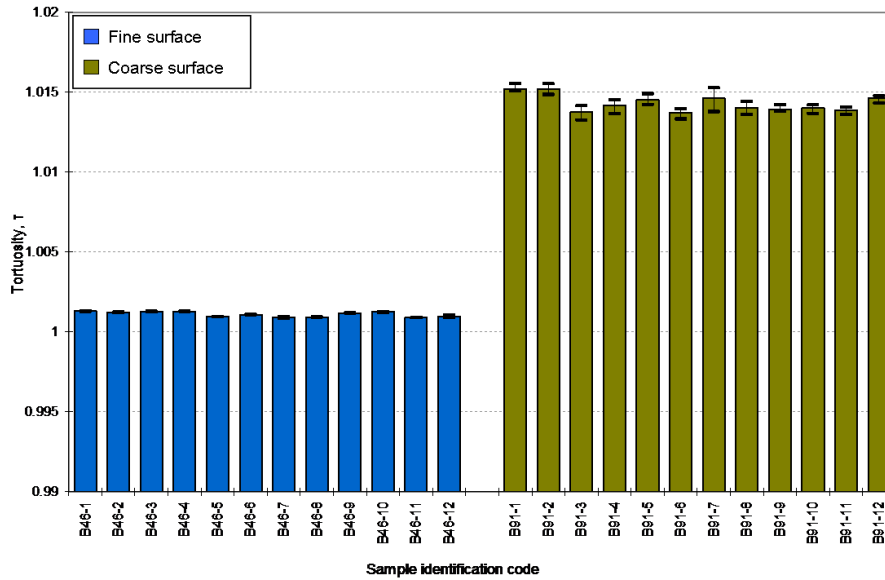


Figure 15.29: τ value of the ground samples before Pt deposition; each column corresponds to one sample and report the average, the minimum and the maximum τ value.

Although all the ground samples share a similar pattern of surface irregularities, they do not have equivalent surface roughness. In comparison to the fine surface, the coarse surfaces are characterised by undulations with higher peaks and shorter spacing, which result in a higher R_q and a lower Rlq , respectively. However, the grinding procedure in both cases results in a minor modification of the substrate surface: in the coarse specimens, the actual length of the surface profile is less than 3% longer than the projected profile, while these two profiles are almost identical in the fine surfaces.

15.3.2 After heat treatment characterisation: bond coat surface assessment

Figures 15.30, 15.31 and 15.32 show R_q , τ , and Rlq for all the machined ground surfaces after heat treatment. Similarly to the procedure followed to produce TBC systems with grit blasted surfaces, the surface of the specimens with a ground substrate was not grit blasted before ceramic deposition, therefore, the data reported in figures 15.30, 15.31 and 15.32 refer to the roughness parameters of the bond coat. In the diagrams, each column corresponds to a single specimen and includes the average, the maximum and the minimum value of the roughness parameter in consideration. Columns are colour coded according to the substrate surface finish before Pt deposition. All diagrams show

that the bond coat manufacturing resulted in an increase in the spread of roughness value both within each specimens and within each group of specimens.

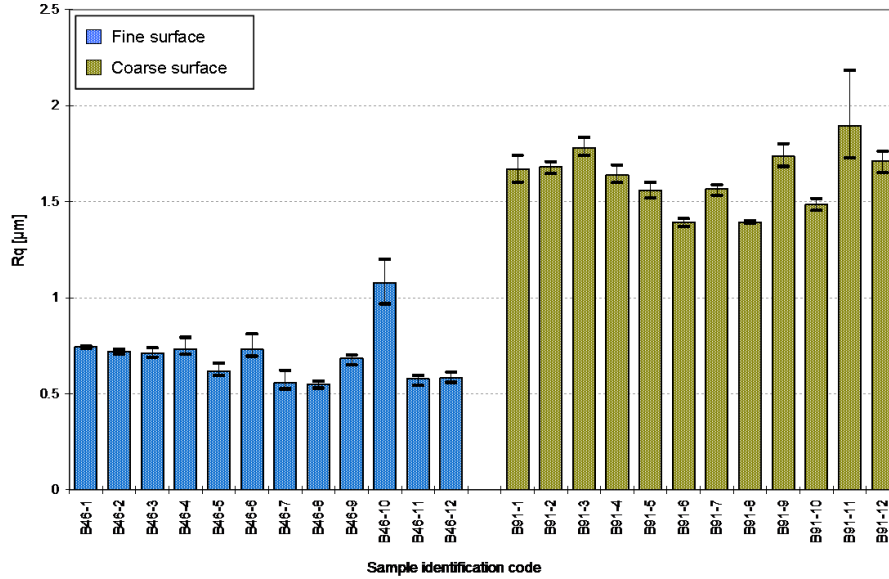


Figure 15.30: R_q value of the ground samples after heat treatment; each column corresponds to one sample and reports the average, the minimum and the maximum R_q values.

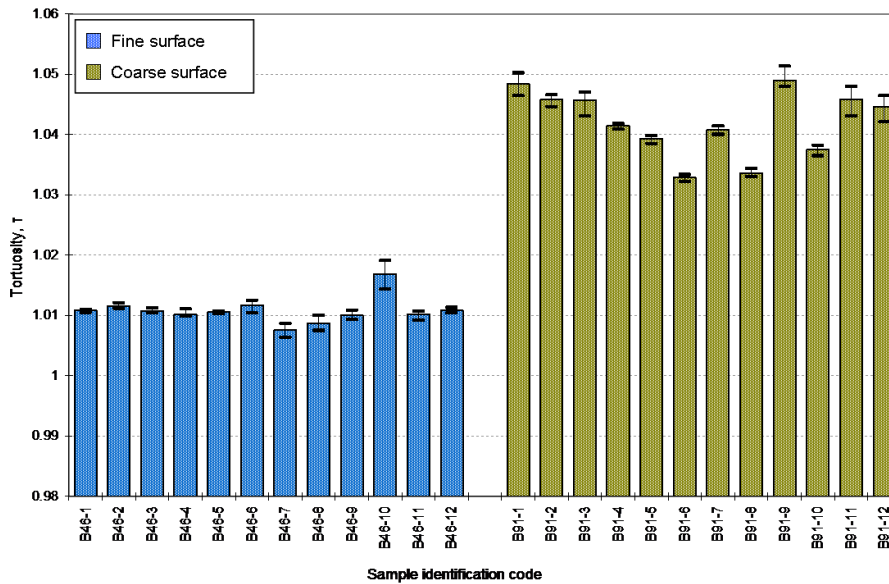


Figure 15.31: τ value of the ground samples after heat treatment; each column corresponds to one sample and reports the average, the minimum and the maximum τ values.

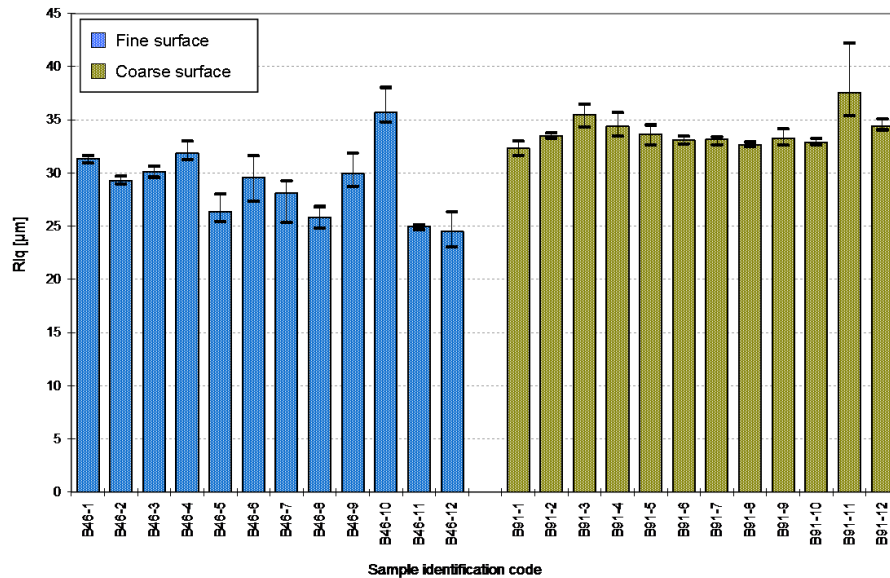


Figure 15.32: Rlq value of the ground samples after heat treatment; each column corresponds to one sample and reports the average, the minimum and the maximum Rlq values.

15.3.3 Comparison between substrate and bond coat surface parameters in ground samples

For the two types of ground surface investigated, figures 15.33, 15.34, and 15.35 show the variation of the roughness parameters (averaged within each type of surface finish) measured before Pt deposition and after heat treatment. In comparison to the pre-sputtering conditions, the bond coat on both fine and coarse ground specimens show higher R_q and τ ; Rlq , instead, remains unchanged for coarse surfaces while decreases for fine surfaces.

15.3.4 Correlation between surface roughness parameters and TBC system lifetime

Figure 15.36 shows the variation of the specimens lifetime as a function of the Rlq of the surface before Pt deposition. All specimens were coated at a TBC deposition temperature of 1276K.

The two grinding procedures adopted produce surface textures with an average wavelength between $33\mu m$ and $56\mu m$. Due to the limited amount of different types of ground surfaces machined, it is impossible to identify any particular trend in the dia-

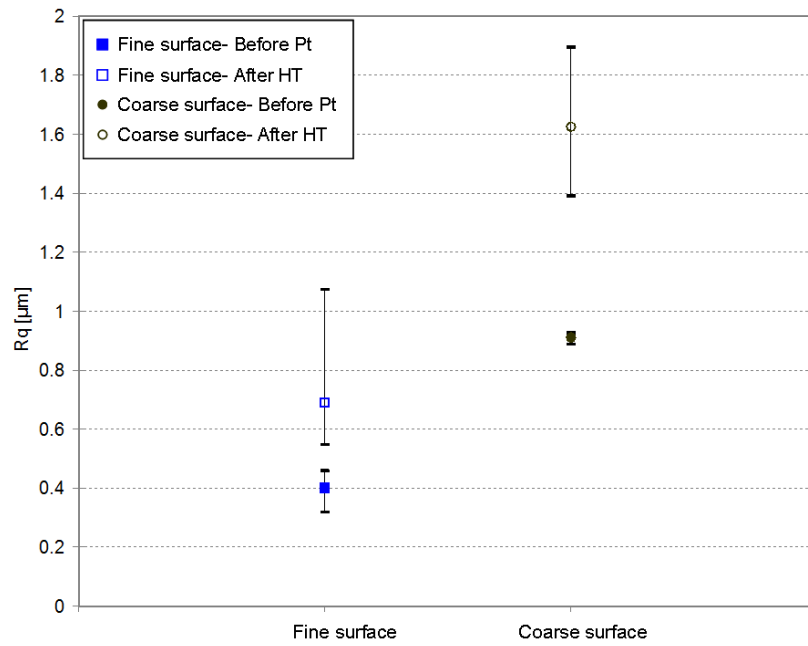


Figure 15.33: Comparison of R_q (averaged for fine and coarse surface finish) measured before Pt deposition and after heat treatment

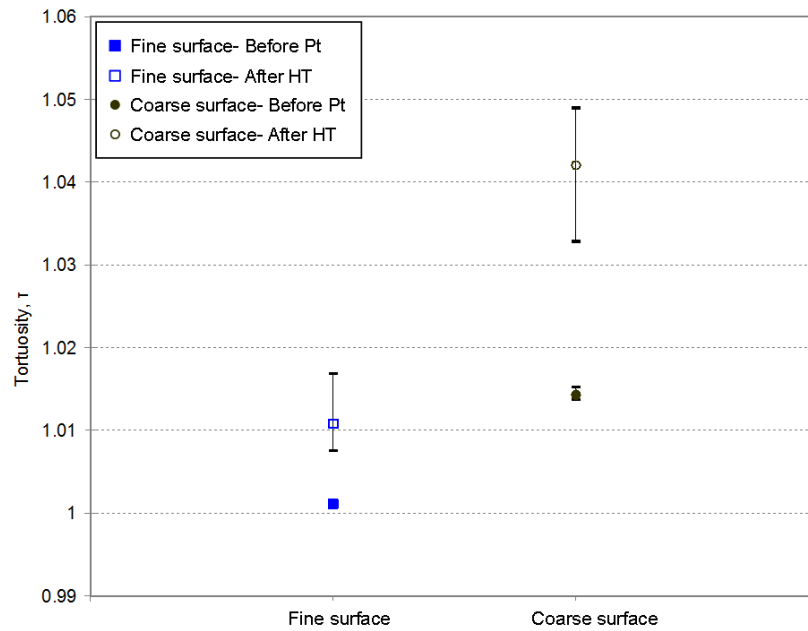


Figure 15.34: Comparison of τ (averaged for fine and coarse surface finish) measured before Pt deposition and after heat treatment

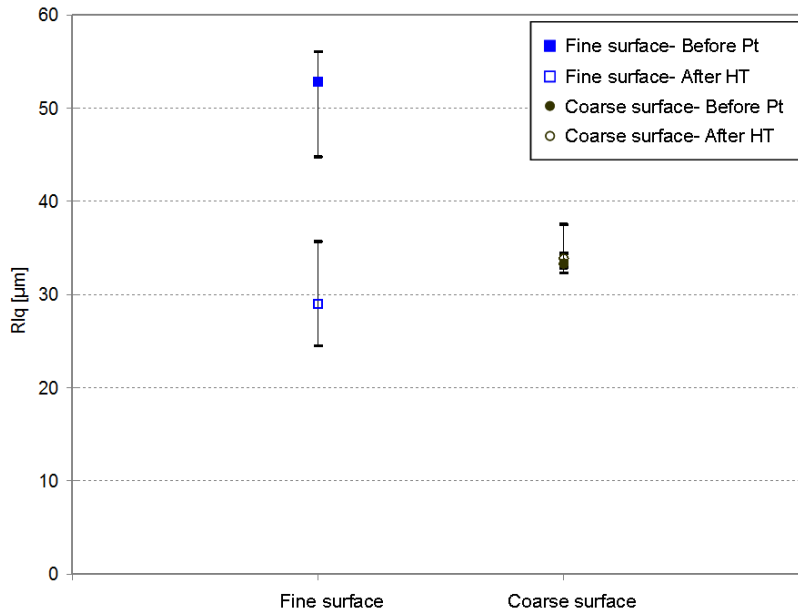


Figure 15.35: Comparison of Rlq (averaged for fine and coarse surface finish) measured before Pt deposition and after heat treatment

gram between specimens lifetime and Rlq . For the same reason, no correlation between the lifetime and the other roughness parameters can be observed (these diagrams are included in Appendix D).

Observation of the diagram in figure 15.36 indicates that all ground specimens have an average wavelength which belongs to two of the three main Rlq intervals identified in figure 15.18 on page 164. In particular, the fine surfaces have an Rlq in the $Rlq > 43$ interval, while the coarse surfaces have Rlq in the $22 < Rlq < 36$ range. Nevertheless, in opposition to what was observed for grit blasted surfaces, ground surfaces belonging to different Rlq ranges do not show significantly different time to failure.

Further comparison between the diagrams in figure 15.36 and in figure 15.18 on page 164 indicates that, although the ground surfaces share similar wavelengths with the grit blasted surfaces, ground surface finishes cause a lifetime reduction. Such a reduction exceeds a factor of 3 in the $Rlq > 43$ range and a factor of 4 in the $22 < Rlq < 36$ interval. Given that in the latter range the systems lifetime is highly dependent on the ceramic deposition temperature, the comparison was based only on those specimens coated at equivalent temperature (1276K). It is believed that the different performance of the grit blasted and ground finishes depend on the surface anisotropy which characterises the latter.

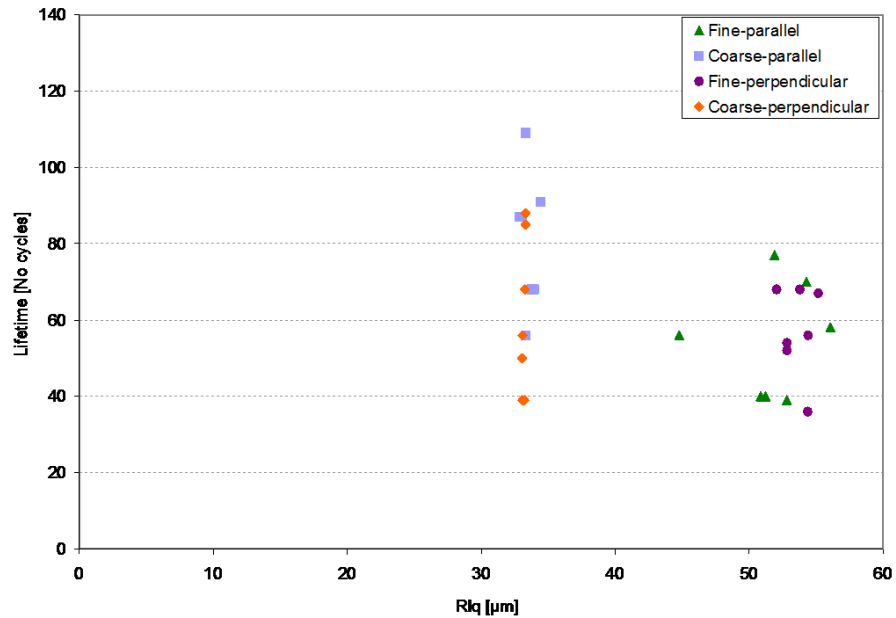


Figure 15.36: Variation of the TBC system lifetime as a function of the substrate surface Rlq for ground specimens.

Lifetime analysis was carried out on the time to failure of the specimens falling into the two Rlq intervals: $22 < Rlq < 36$ and $Rlq > 43$. On the basis of the observations above, such an analysis corresponds to the comparison between coarse and fine surfaces. The Weibull plots are presented in figure 15.37. The two Weibull plots show good fit of the data, with R^2 values well above the minimum required to guarantee goodness of fit (88% for both plots [166]).

15.4 Conclusions on role of surface texture on the TBC system lifetime

In this chapter the surface texture obtained by ten different surface preparation procedures was analysed to find a correlation between surface finish before Pt deposition and TBC system lifetime. Four of these procedures involved grit blasting a previously polished surface, four of them consisted solely of grit blasting the specimens surface, while the remaining two consisted of grinding the surface in one direction, to achieve a bidimensional surface texture. The pressures adopted to grit blast the surface were either $0.05MPa$, $0.1MPa$, $0.2MPa$, or $0.4MPa$ while the ground surfaces were ma-

chined adopting either a B91 or a B46 wheel. The surface texture for all the specimens was assessed using a profilometer; three different roughness parameters (R_q , Rlq and τ) were chosen to characterise the surface.

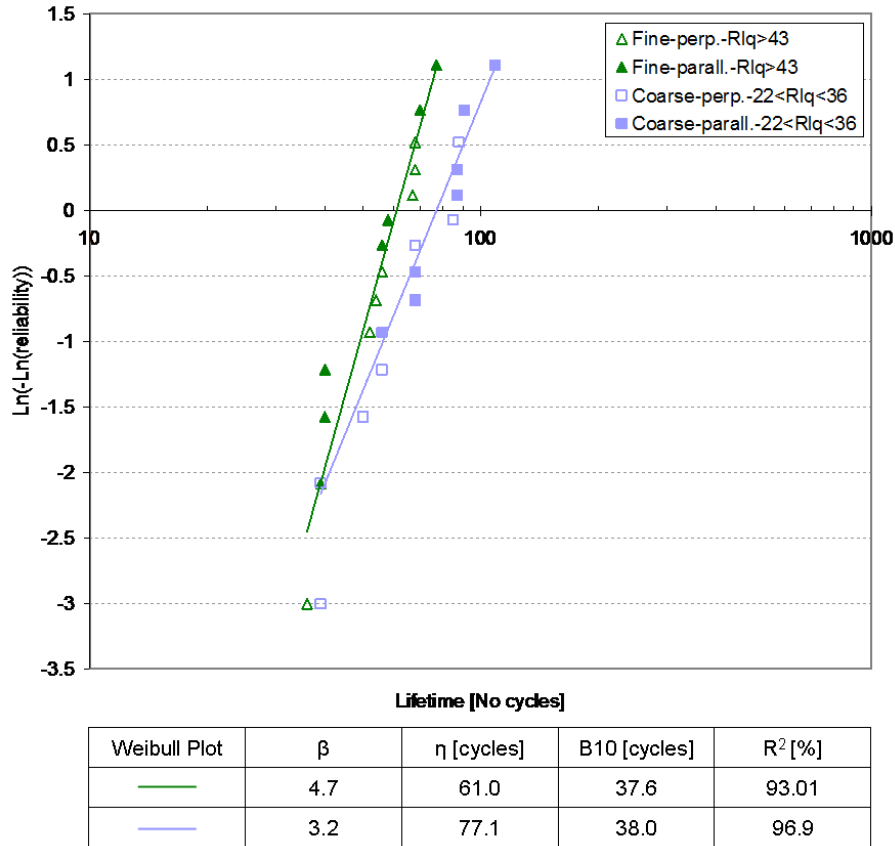


Figure 15.37: Weibull plots including the lifetime of fine and coarse ground specimens. For each Weibull plot, the table reports the values of β , η , B(10)life and R^2 .

Although the pressures adopted in the grit blasting procedure were the same for the two groups of grit blasted surfaces, polishing the surface before grit blasting affected the surface texture obtained, which appears smoother than that of the corresponding non-polished category. Even the highest pressure adopted in this study ($0.4MPa$) was ineffective in erasing the specimens surface history. The pre-blasting treatment had the advantage of increasing the surface texture reproducibility. The grit blasted only specimens in fact showed a significant batch to batch variation in surface texture, particularly when grit blasted at lower pressure ($0.05MPa$ and $0.1MPa$). Such a variation is believed to depend on the fact that the blasting procedure was a fully manual process,

therefore operator dependent, and inherently difficult to reproduce perfectly. However, these uncontrollable variations in process do not affect the surface texture when higher pressures (0.2MPa and 0.4MPa) are adopted. Surfaces produced at a pressure higher than 0.2MPa seem to be not only insensitive to unintended variations to the blasting procedure, but also to further increase in pressure. The surface finishes produced at a pressure higher than 0.2MPa are, in fact, all remarkably similar. The grinding procedures produced two types of surface finish (fine and coarse) both characterized by a series of grooves running parallel to each other. The surface measurement, carried out in a direction perpendicular to the grooves, revealed the highest reproducibility within each group experienced in this work. Although the coarse surfaces showed a profile amplitude and an average wavelength almost twice as big as that of the corresponding value for the fine surfaces, both type of surfaces were very smooth when compared to the grit blasted surfaces.

A bond coat surface assessment was carried out for all categories of samples. The comparison between the specimens surface texture before Pt deposition and after heat treatment revealed an increase in value for almost all roughness parameters for all samples categories. Only the average wavelength value of the bond coat on ground surfaces was either smaller or unchanged when the bond coat was produced either on fine or coarse surfaces, respectively. This means that, although the Pt layer follows the substrate geometry, the sputtering process itself introduces a certain level of asperities which combine with the already existing substrate roughness.

For grit blasted surfaces, a correlation between the average wavelength of the specimens substrate, before Pt deposition, and the TBC system lifetime in cyclic oxidation test was found. In particular five intervals of *Rlq* were identified: three main ranges with peculiar characteristics, spaced by two further *Rlq* intervals which showed not so distinctive properties, and the characteristics of which could be interpreted as a transition between the two main ranges that they separate.

A 2-parameters Weibull distribution was adopted to analyse the data in each *Rlq* range. In all cases the plots show good fit of the data, therefore the chosen distribution can be adopted successfully to model TBC systems failure data. The plots were compared in terms of the distribution parameters (characteristic life and shape parameter) and B(10)life, namely the number of cycles at which 90% of the analysed population has not yet failed.

The plots for the two transition *Rlq* range shared a shape parameter of ~ 2.5 ; for such a value, the Weibull distribution becomes almost symmetrical and approaches the

Gaussian distribution. Therefore, in the transition range, the TBC system failure can be interpreted as a random phenomenon. Also the plots in the three main Rlq intervals share a similar shape parameter, but the value is much higher and varies between 4 and 4.9. For these values, the distribution assumes the shape of a Weibull distribution with a left tail. This implies a high reproducibility in time to failure in the sample population under analysis. Although the shape parameter was similar, the three populations of samples had a significantly different characteristic life and the specimens having Rlq between $22\mu m$ and $36\mu m$ were the best performing.

However, strict control of the ceramic deposition temperature allowed further improvements in the performance of samples belonging to this Rlq range. The combination of an Rlq between $23\mu m$ and $36\mu m$ with a ceramic deposition temperature at $1291K$ produced TBC systems with the longest life. This process condition may result in a lifetime 3 times greater than expected to an average life in commercial production.

Chapter 16

Effect of the platinum layer morphology on the lifetime of TBC systems with a *PtAl* bond coat

In this chapter the effect of the *Pt* layer morphology on the lifetime of TBC systems with a *PtAl* bond coat will be investigated. Three different *Pt* layer structures were studied: an open structure, a DLR structure and a DHR structure. Detailed description of both the sputtering procedures adopted to deposit the *Pt* layers and the achieved structures is provided in chapter 11.

The TBC systems studied were manufactured depositing $20 \frac{mg}{cm^2}$ of *Pt* on CMSX-4 coupons adopting the three sets of sputtering parameters listed in table 11.1. Before *Pt* deposition, the *Ni* based substrates were machined to achieve two different surface finishes: a $0.2MPa$ grit blasted surface and a coarse ground surface (see chapter 6). After *Pt* deposition, the production of the *PtAl* bond coat required three further steps: an heat treatment at $1040^\circ C$ for two hours under vacuum, a vapour aluminising, and a post aluminising heat treatment at $1140^\circ C$ for 2 hours followed by a recovery heat treatment at $870^\circ C$ for twenty hours (see chapter 8). The samples were finally TBC coated (see chapter 9), and tested in cyclic oxidation at $1150^\circ C$ (see section 10.3.3).

16.1 TBC system with *PtAl* bond coat

Table 16.1 summarises the outcome of the coating inspections carried out at various stages of the manufacturing/testing process.

TYPE OF <i>Pt</i> STRUCTURE	VISUAL INSPECTION AFTER PRE-CVD HT		SEM ON CROSS SECTION AFTER POST-CVD HT		VISUAL INSPECTION AFTER FAILURE	
	0.2MPa surface	Ground surface	0.2MPa surface	Ground surface	0.2MPa surface	Ground surface
DHR	Ok	Blisters	Ok	n/a	Buckling	n/a
Open	Ok	Ok	Ok	Ok	Ok	Ok
DLR	Ok	n/a	Ok	n/a	Buckling	n/a

Table 16.1: Results of visual inspection of the coating after diffusion: the dense high rate coating, when deposited on the ground surface, failed the inspection due to the presence of blisters. The *Pt* with an open structure was not deposited on ground surface.

The coating produced depositing a DHR *Pt* layer on ground substrates failed the visual inspection after heat treatment: similarly to the *Pt*-diffused bond coat, the coating was damaged by an array of blisters distributed over the surface (see chapter 12). All remaining specimens were tested under cyclic oxidation at 1150°C.

Figure 16.1 presents the oxidation test results for the TBC systems with a *PtAl* bond coat as a function of the *Pt* layer structure (DHR, open, or DLR) for the two substrate surface finishes investigated (0.2MPa grit blasted and ground surface). For each of the five TBC systems analysed, the diagram reports the number of specimens tested as well as the average, maximum and minimum lifetime values expressed as number of oxidation cycles. The TBC systems with an open *Pt* structure showed the longest lifetime. Within this category, the specimens with a ground finish were the best performing. The shortest time to failure was experienced by specimens with a DHR *Pt* structure; the zero cycles lifetime of the specimens with ground surface represents failure while manufacturing due to blistering. The time to failure increased by a factor of two when a *Pt* layer with a DLR structure was adopted; a further improvement in life, almost by a factor of six, was reached using an open structure in conjunction with a substrate with a ground finish.

A post failure visual inspection pointed out that the specimens failed according to two different failure modes (see table 16.1): all TBC systems with a dense *Pt* structure failed due to coating buckling that eventually causes the ceramic to spall, whereas all the TBC systems with an open structure failed due to TBC delamination at TBC/TGO interface, following a mechanism identical to that often described in literature for *PtAl* bond coats [173, 88, 174, 175]. In order to understand the causes of such different failure modes, a TBC system with a DHR *Pt* layer structure was analysed at various stages

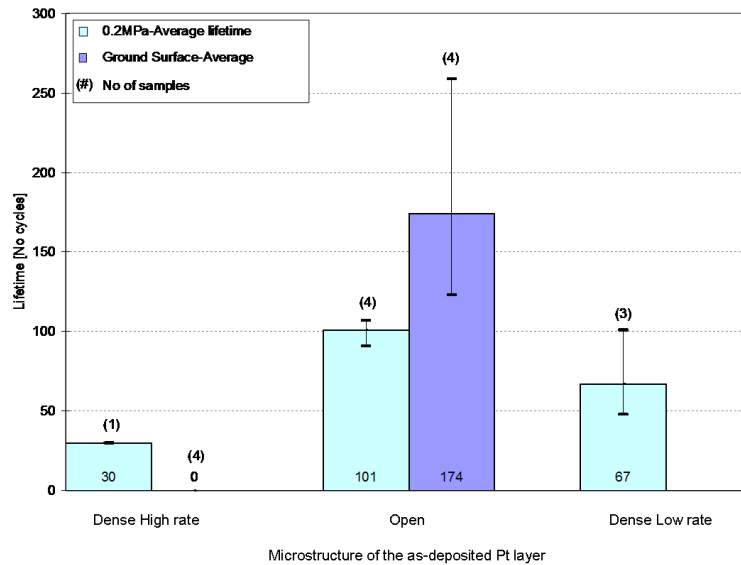


Figure 16.1: Oxidation test results for TBC systems with a *PtAl* bond coat as a function of the *Pt* layer structure (DHR, open, or DLR) for two different substrate surface finishes (0.2MPa grit blasted and ground surface). For each TBC system, the number of specimens tested, the average, maximum and minimum lifetime values (expressed as number of oxidation cycles) are reported.

of the manufacturing process as well as after failure, and compared to a TBC system with an open *Pt* layer structure. The outcome of such comparison is presented in the following section. Both TBC systems have a substrate with a 0.2MPa grit blasted surface finish.

16.2 Bond coat characterisation in various stages of the manufacturing process

Figure 16.2 includes SEM micrographs of the cross section of specimens with a DHR *Pt* structure (left column) and an open *Pt* structure (right column) at various stages of the manufacturing process.

Figure 16.2A and 16.2D show the two studied TBC systems before aluminising, after being *Pt* coated and heat treated at 1040°C. Different *Pt* layer morphologies do not affect the bond coat formation in this initial stage; in both cases, in fact, the bond coat consists of a *Pt* enriched layer which shows the two distinctive γ' and γ

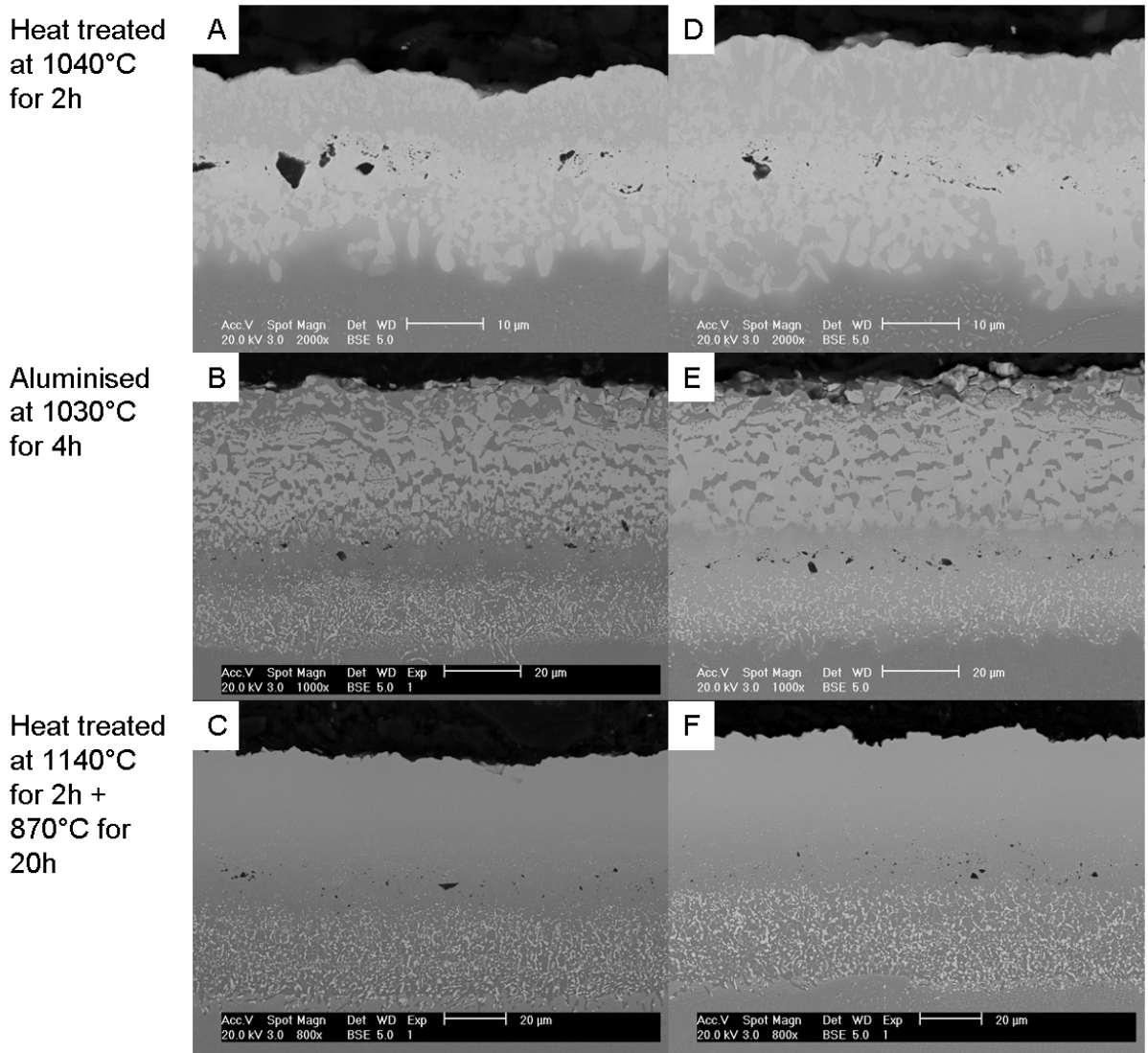


Figure 16.2: SEM micrographs of the coating cross section at various stages of the manufacturing process. Proceeding from the top row to the bottom, the pictures show: the coating after *Pt* deposition and pre-aluminising heat treatment, after aluminising and at the end of *PtAl* bond coat manufacturing (therefore after post-aluminising heat treatment). Pictures A, B, C (left column) are relative to specimens with a DHR *Pt* structure while picture D, E, F (right column) are relative to specimens with an open *Pt* structure.

phases. The overall coating thickness is between $25\mu\text{m}$ and $30\mu\text{m}$. In both coatings alumina inclusions (dark particles) are present at a distance of approximately 50% of the total coating thickness. The shape and dimension of the Al_2O_3 grains suggest that they are residues of the grit blasting procedure. therefore they are a clear indication of the Pt layer/substrate interface location before heat treatment. In the cross section of the specimen with a DHR Pt structure (Figure 16.2A), the distance between the original interface and the coating top surface is $\sim 40\%$ shorter than in the corresponding specimen with an open structure (figure 16.2D). This difference in coating thickness is due to the difference in density between the two investigated Pt layers (see section 11.1). The specimens in figures 16.2A and 16.2D, were coated with $20\frac{\text{mg}}{\text{cm}^2}$ of Pt which corresponds to a $\sim 10\mu\text{m}$ thick layer of DHR Pt structure and to a $\sim 14\mu\text{m}$ thick layer of open Pt structure.

Figure 16.2B and 16.2E show the cross section micrographs of the two types of coatings after aluminising. The coating in the as-aluminised conditions has a $\sim 45\mu\text{m}$ thick outer layer which consists of two-phase structure with PtAl_2 (bright phase) and Pt-rich $\beta\text{-NiAl}$ grains, both phases also contain Co and Cr. The inner layer, $20\text{--}25\mu\text{m}$ thick, consists of Al-rich $\beta\text{-NiAl}$ and intermetallic precipitates containing refractory elements. Figure 16.2C and 16.2F show the two TBC systems at the end of the bond coat manufacturing process. The post-aluminising heat treatment converted the two-phase structure into a single β -phase layer.

Figure 16.3 shows the results of the EDX analysis conducted on the cross sections of specimens with either a DHR or an open Pt structure at two different stages of the bond coat production: after Pt deposition and heat treatment (figures 16.3A and 16.3D) and after aluminising and heat treatment (figures 16.3C and 16.3F). The compositional analysis was performed in several aligned points starting from the coating surface up to the substrate. The distance between two consecutive points was either $5\mu\text{m}$ or $10\mu\text{m}$.

The compositional analysis shows that at every stage of bond coat production the specimens are very similar. This result is confirmed in table 16.2, which reports the average composition of the outer layer of the coatings; which was calculated as an average over three areas having a surface of $10\mu\text{m} \times 5\mu\text{m}$ and set at a distance of $5\mu\text{m}$ from the coating surface.

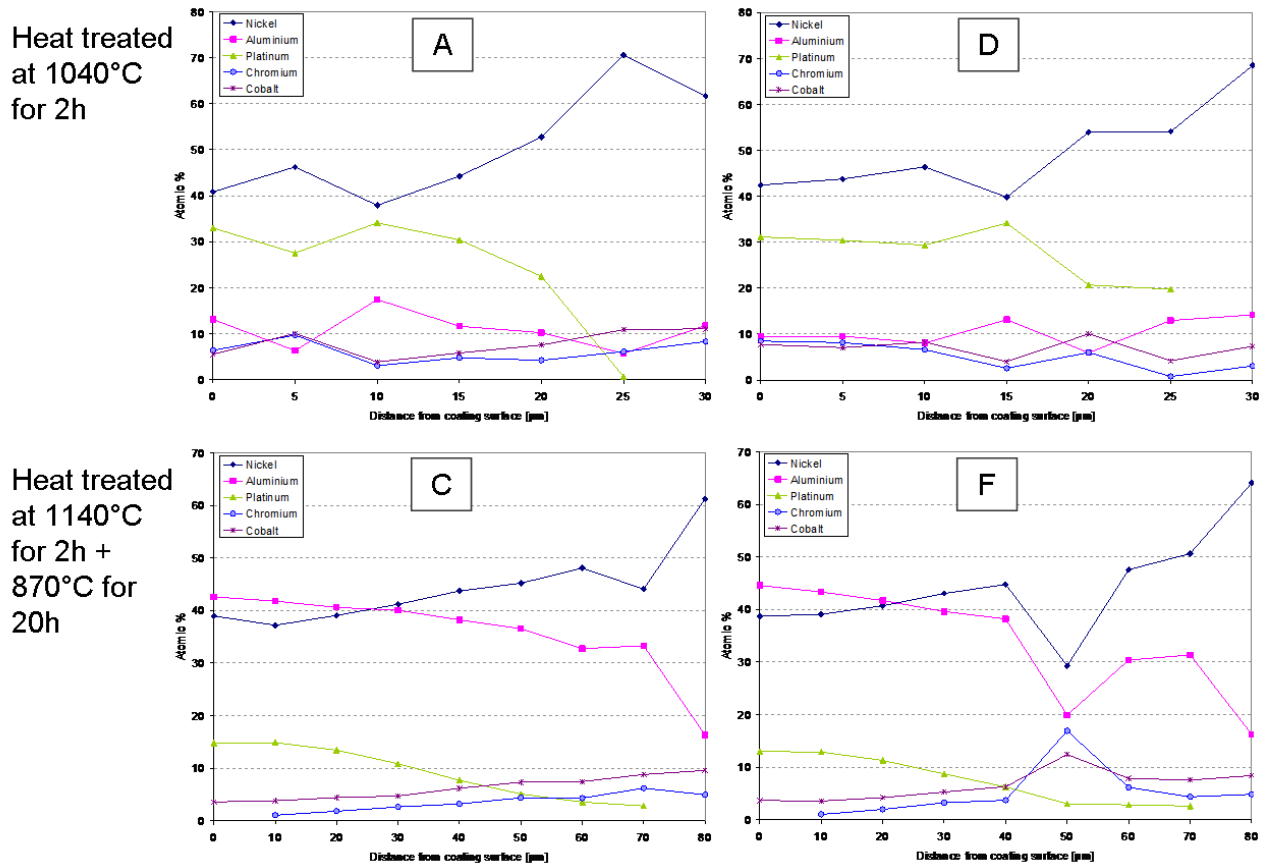


Figure 16.3: EDX compositional analysis of the cross sections of specimens with either a DHR or an open *Pt* structure at two different stages of the bond coat production: after *Pt* deposition and heat treatment at 1040°C (A and D) and at the end of *PtAl* bond coat manufacturing (C and F). Pictures A and C (left column) are relative to specimens with a DHR *Pt* structure while picture D and F (right column) are relative to specimens with an open *Pt* structure.

MANUFACTURING STAGE	<i>Pt</i> STRUCTURE	COATING COMPOSITION [AT%]					
		Ni	Pt	Al	Cr	Co	Ti
Heat treated at 1040°C for 2h	DHR	42.7	31.0	10.9	7.5	6.9	1.0
	Open	43.4	30.3	9.2	8.9	7.7	1.1
Aluminised at 1030°C for 4h	DHR	31.4	10.9	53.9	0.9	2.9	n.d.
	Open	29.6	12.6	54.5	0.8	2.6	n.d.
Heat treated at 1140°C for 2h +870°C for 20h	DHR	38.8	13.3	43.4	0.8	3.6	n.d.
	Open	39.4	13.0	43.0	0.8	3.8	n.d.

Table 16.2: Average composition of the cross section of coatings, with either a DHR or an open *Pt* structure, at different stages of the bond coat manufacture. The EDX analysis was performed on areas of the coatings having a 10 μ m x 5 μ m dimension and set at a distance of 5 μ m from the coating surface. The coating composition was determined as the average composition over three areas.

16.3 Post failure analysis

The post failure analysis of the specimens revealed two completely different failure modes depending on the structure of the platinum: open or dense (figure 16.4). The TBC systems with a open *Pt* structure failed with separation at the ceramic/TGO interface; the cross section micrograph of a failed specimen is shown in figure 16.4B. Following aluminising, the surface of the *PtAl* bond coat shows a geometrical array of ridges corresponding to the grain boundaries in the β phase. Although the ridges evolution with oxidation time was not investigated, based on other studies, it is reasonable to assume that, with thermal cycling, the ridges are transformed into cavities, which then may lead to localised debonding between the TBC and the bond coat [173, 88, 174, 175]. Several neighbouring debonded areas subsequently merge, creating fewer flaws of several millimetres in size. These flaws induce buckling at first, and then ceramic spallation when the TBC system is cooled from testing to room temperature.

The TBC systems with dense *Pt* structure failed due to the formation of voids in the central part of the bond coat, at the original *Pt* layer/substrate interface (figure 16.4A). Contrary to what was observed in TBC systems with open structure, TBC systems with dense *Pt* structure show a superficial indication of the evolving damage. Several cycles before failure, the coating starts swelling and forming a blister which keeps growing until it reaches a critical size that causes either the TBC to spall or the entire external part of the bond coat to peel.

The formation of internal voids in *PtAl* coatings was observed previously by other

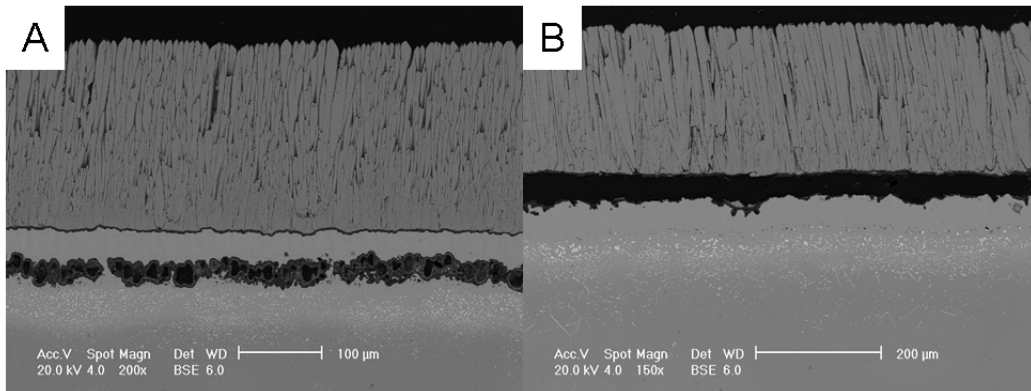


Figure 16.4: Cross section micrograph of the failed specimens. A) *PtAl* bond coat with a DHR *Pt* structure B) *PtAl* bond coat with an open *Pt* structure

authors[176, 177, 178, 12, 179], but it has never been identified as the sole responsible for the coating failure. The common explanation for the formation of the voids refers to the Kirkendall mechanism. During the exposure to high temperature, three different diffusion fluxes occurs: the *Al* diffusion towards the surface to form or replenish the alumina scale, the *Al* diffusion into the substrate, and the *Ni* diffusion towards the surface. The balance of such fluxes results in a flux of vacancies which condensate below the original *Pt* layer/substrate interface to form pores.

It is believed that the Kirkendall mechanism is also responsible for the voids nucleation in the *PtAl* coatings with a dense *Pt* structure studied here. However, Kirkendall porosities are typical of outward diffusion coating, and therefore they should be present both in *PtAl* bond coat with a dense *Pt* structure and in *PtAl* bond coat with an open *Pt* structure. As observed by Tolpygo *et al.*, it is possible that in the *PtAl* bond coat with an open *Pt* structure, the pores form but collapse during thermal cycling; therefore no pore is observed after failure.

The formation of voids only in the *PtAl* bond coat with a dense *Pt* structure observed in the present study is believed to depend on the fact that the interdiffusion behaviour associated with the dense coating causes the formation of pores which are too big to collapse. With thermal cycling and/or oxidation time, the voids grow and merge together, and the resulting separation area causes the penetration of oxygen from the specimen edge; which, in turn, causes the oxidation of the voids surface. This theory has been confirmed by X-ray photoelectron spectroscopy analysis conducted on the products found on delaminated surfaces; which confirmed the presence of oxides of aluminium, tungsten and titanium. The presence of tungsten and titanium is not

unexpected when considering the area where the voids formed in the coating. The volume increment related to the conversion of a high density intermetallic to a low density oxide causes the coating to swell, until the size of the damage reaches a critical size which causes the TBC system failure. The different stages of the damage evolution are shown, from left to right, in figure 16.5.

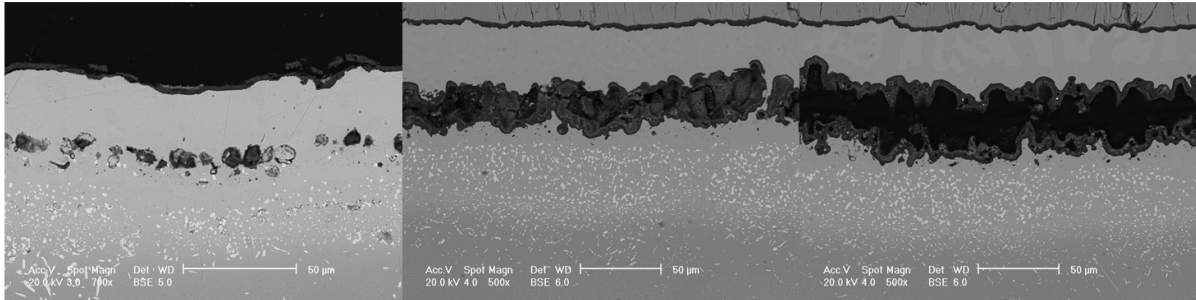


Figure 16.5: Damage evolution in a *PtAl* bond coat with a dense *Pt* structure. In the first stage, isolated voids are formed along the original grit line, with fully bonded material between them. With thermal cycling and/or oxidation time the voids grow and merge together. The voids surface oxidise due to oxygen penetration into the coating from the coating edges. Subsequently, the volume increase due to the oxidation causes the coating to swell until failure.

Other studies carried out in Cranfield University seem to confirm the Kirkendall mechanism being at the origin of the voids formation. All the outward diffusion *PtAl* coatings manufactured with a dense *Pt* structure, in fact, experience this peculiar failure mode independently of the testing conditions (isothermal or cyclic oxidation) [180, 181]. On the other hand, inward *PtAl* coatings manufactured with the same *Pt* structure fail at the TGO/TBC interface [182]: in inward diffusion coating the main flux consists of *Al* diffusing into the substrate without formation of Kirkendall voids.

16.4 Conclusion on the role of *Pt* layer morphology on the lifetime of TBC systems with a *PtAl* bond coat

Similarly to the *Pt*-diffused bond coat, the post-sputtering heat treatment results in catastrophic failure of the coating, due to blisters formation, when a *Pt* deposit with a DHR structure was formed over ground surfaces. A detailed explanation of this

behaviour is reported in chapter 12. The *PtAl* bond coat was manufactured successfully on grit blasted surfaces starting from DHR, DLR, or open *Pt* structures, and on ground surfaces adopting an open *Pt* structure. *PtAl* bond coat with a DLR *Pt* structure was not produced on ground surfaces. SEM and EDX analysis were performed on TBC systems with dense and open *Pt* structure; in both cases the obtained bond coat showed the characteristics of an outward diffusion *PtAl* bond coat.

Cyclic oxidation testing investigated the effect of the three *Pt* structures and the substrate surface finish (either grit blasted or ground) on the TBC system lifetime. Results showed that TBC systems with an open *Pt* structure were the best performing. Within this category, the specimens with a ground finish showed the longest life. The shortest time to failure was experienced by specimens with a DHR *Pt* structure; within this category specimens with ground surface failed due to blisters formation before completion of the TBC system manufacturing process. Direct comparison among the three *Pt* structure deposited on the grit blasted surfaces showed that, with respect to TBC systems with a DHR *Pt* structure, the time to failure increased by a factor of two and three when a *Pt* layer with a DLR and open structure were adopted, respectively. However, an improvement of a factor of almost six in life was obtained by using an open structure in conjunction with a substrate with a ground finish.

The compositional analysis showed that the TBC systems with either an open or a dense *Pt* structure were extremely similar, however, the two types of TBC system showed completely different failure modes. All TBC systems with an open structure failed due to TBC delamination at TBC/TGO interface, following a mechanism identical to that often described in literature for *PtAl* bond coats. On the other hand, all TBC systems with a dense *Pt* structure failed due to the formation of voids in the central part of the bond coat along the original *Pt* layer/substrate interface. It is believed that the Kirkendall mechanism is the cause of the voids nucleation. With thermal cycling and/or oxidation time the voids grow and merge together. Oxygen infiltration into the coating from the specimen edge causes the oxidation of the voids surface. The volume increment due to the oxides formation causes the coating to swell, until the damage reaches a critical size which causes the TBC to spall or the entire outer part of the bond coat to peel.

Chapter 17

Conclusions

17.1 Contribution to knowledge

This work investigated the possibility to increase the reproducibility in TBC system time to failure by improving the outcome of each of the steps involved in the TBC system manufacture. The TBC systems lifetime was determined in a cyclic oxidation test and the data were modelled with the Weibull distribution. Two types of TBC system were studied: a TBC system with a *Pt*-diffused bond coat and a TBC system with a *PtAl* bond coat; where possible identical production steps were used to manufacture the two systems. The production of the *PtAl* bond coat involved an extra step consisting of vapour aluminising. The entire specimens production was undertaken in the facilities of Cranfield University and, except for the TBC deposition, it was personally carried out by the author. The approach adopted in this work consisted first in the understanding the effect that variations in each manufacturing step had on the TBC systems lifetime, and then in the production of TBC systems with the best outcome from all previous trials.

Three different *Pt* layer morphologies were produced via PVD: an ‘open’ structure and two ‘dense’ structures identified respectively as a Zone 1 type and a Zone T type of the structures in the Thornton diagram [107]. The structures names were chosen with reference to the percentage of voids in the deposited *Pt* layer; approximately 30% in the open structure and less than 10% in the dense structure. Although the two dense structures shared a similar morphology, they were produced at significantly different deposition rates: hence they were identified as *Dense Low Rate* (DLR) and *Dense High Rate* (DHR) structures.

Layers of *Pt*, $10\mu\text{m}$ thick, and exhibiting one of the three structures described above were deposited on nickel-based superalloy substrates with two different surface finishes: one with $R_a = 1.39\mu\text{m}$ and another with $R_a = 0.72\mu\text{m}$. All depositions were successful, however, the coating with a DHR structure deposited on the smoothest surface failed after diffusion heat treatment due to the formation of blisters. This phenomenon is believed to be due to the interaction of three different factors:

- the CTE mismatch between the coating and the substrate,
- the residual stress built in the coating during deposition,
- the substrate surface roughness.

The first two factors contribute to the overall compressive stress which builds up in the coating. It was also demonstrated that, in order to avoid blister formation, two different approaches can be adopted: increasing the surface roughness of the substrate or reducing the stress in the coating. In fact, a rougher substrate tolerates higher levels of stress before the strain energy stored into the coating overcomes the fracture toughness of the interface, resulting in coating failure (or blistering). The level of internal stress in the coating can be reduced either modifying the coating structure introducing more voids (i.e. producing an open *Pt* structure), or reducing the deposition rate (i.e. producing a DLR structure).

The study of the effect of the *Pt* layer structure on the TBC system lifetime produced different outcomes depending on the type of bond coat involved. TBC systems with a *Pt*-diffused bond coat showed the longest life and highest reproducibility when a DLR structure was used: these systems performed 3 times better than the corresponding ones with an open *Pt* structure. On the other hand, TBC systems with a *PtAl* bond coat showed the best performance when an open structure was deposited. Moreover, while these system failed at the TGO/bond coat interface with a well known mechanism, the systems with dense *Pt* structure failed due to the formation of voids along the original substrate/*Pt* interface.

Another investigated aspect was the effect of the type of surface finish (and therefore surface roughness) before *Pt* deposition on the TBC system lifetime. This study was carried out comparing up to ten different substrate surface finishes on which was deposited the *Pt* structure which was expected to provide the best performance based on the results above: a DLR structure for the *Pt*-diffused bond coat and an open structure for the *PtAl* bond coat. The ten different surface finishes were obtained adopting ten

different surface preparation procedures, they were assessed using a profilometer, and characterised using three roughness parameters: R_q , Rlq and τ . Surface assessment was repeated after platinum deposition and subsequent heat treatment. Despite the industrial practice requires grit blasting the bond coat prior to ceramic deposition, in this study the TBC was deposited on the bond coat as formed during the heat treatment, with no further surface machining. Comparison between the substrate (before Pt deposition) and the bond coat surface textures showed an increment in the value of almost all roughness parameters for all samples categories. The only exception was the value of the average wavelength of the roughness of the bond coat on ground surfaces. This means that, although the Pt layer follows the substrate geometry, the sputtering process itself introduces a certain level of asperities which combine with the already existing substrate roughness.

For grit blasted surfaces, a correlation between the average wavelength of the specimens substrate (before Pt deposition) and the TBC system lifetime in cyclic oxidation test was found. In particular five interval of Rlq were identified: three main ranges with peculiar characteristics, spaced by two further Rlq intervals with no distinctive properties, and the characteristics of which could be interpreted as a transition between the two main ranges that they separate. A 2-parameters Weibull distribution was adopted to analyse the data in each Rlq range. In all cases the plots show good fit of the data, demonstrating that the chosen distribution can be successfully adopted to model the TBC systems failure data. The plots were compared in terms of the distribution parameters (characteristic life and shape parameter) and B(10)life (namely the estimated number of cycles when the reliability in the specimens population is 90%).

The plots for the two transition Rlq ranges shared a shape parameter of ~ 2.5 ; for such a value the Weibull distribution becomes almost symmetrical and approaches the Gaussian distribution. Therefore in the transition ranges the TBC system failure can be interpreted as a random phenomenon. The plots in the three main Rlq intervals share a similar shape parameter but the value is much higher and varies between 4 and 4.9. For these values, the distribution assume the shape of a Weibull distribution with a left tail. This implies a high reproducibility in time to failure in the population of TBC system under analysis. Although the shape parameter was similar, the three populations of samples had a significantly different characteristic life and the specimens having Rlq between $22\mu m$ and $36\mu m$ were the best performing.

A further observation of the data highlighted also that the TBC systems lifetime may be affected by the TBC deposition temperature too. In the range of temperature

commercially identified as suitable for the production of TBC via EB-PVD, three different ceramic deposition temperatures were selected for the TBC deposition. Such a temperature variation had little effect on the TBC system lifetime for almost all the TBC systems manufactured, with the exception of the TBC systems the substrate of which had an average wavelength between $22\mu\text{m}$ and $36\mu\text{m}$. In this case, a strict control of the ceramic deposition temperature allowed to further improve the samples performance. The combination of an Rlq between $23\mu\text{m}$ and $36\mu\text{m}$ with a ceramic deposition temperature at 1291K produced TBC systems with the longest life. In practical terms, adoption of these process conditions may result in a lifetime three times longer than the average life of equivalent high temperature coatings in commercial production.

A correlation between the substrate surface roughness and the TBC system lifetime for ground surfaces was not found, and the samples did not show a significant difference in performance, whether the substrate was fine or coarse ground. Comparison between ground and grit blasted samples showed that, despite a marked similarity in average wavelength of the surface texture, the lifetime of the ground specimens was much shorter than that of the grit blasted: the coarse ground more than 4 times shorter, and the fine ground more than 3 times shorter.

The performance of the platinum aluminide bondcoat was not as sensitive to the surface finish as that of the platinum diffused bond coat. Interestingly, however, while the lifetime of the TBTBCC system with Pt -diffused bond coat was longer on grit blasted substrates than on ground, when $PtAl$ bondcoat is produced, the TBC system on ground substrates outlast the grit blasted. These findings are consistent with and justified by the different failure mechanisms identified for the two types of bondcoat.

17.2 Suggestion for further work

- The deposition of a Pt layer with a DLR structure is quite time consuming, lasting up to seven hours. This has a significant impact on the overall duration of the TBC system manufacturing process. In order to reduce it, it is suggested to attempt Pt deposition at a higher current; it is likely that a current of $0.35A$ would reduce the deposition time without significantly increasing the residual stress in the deposited Pt layer, although this needs to be verified.
- A variation in the ceramic deposition temperature results in the deposition of a TBC layer with different morphologies. The effect of the ceramic structure on the

TBC system lifetime needs further investigation. The study of the stress evolution within the TGO at different stages of the cycle test is also desirable.

- A more detailed study of the TBC systems at failure would be required. Such a study should aim at understanding where the cracks nucleate and how they evolve; the study should also be supported by an investigation of TBC systems at different stages of the oxidation tests (i.e. 10%, 25%, 50%, 75% of their life). It would be also desirable an evaluation of the TGO thickness at failure for the cases considered.
- Further investigation of the variation of the bond coat chemical composition (if any) with the different substrate preparations would be useful.
- The technique adopted in this work to deposit the *Pt* layer, sputtering, is not a technique usually adopted as a standard industrial practice, which is typically electroplating. Further efforts should be dedicated in replicating the results achieved here when the *Pt* layer has been electroplated.
- An analysis of the behaviour of the best performing TBC systems identified in this study under CMAS attack as well as their erosion resistance would contribute to assess their practical and industrial viability.

References

- [1] M. Peters, C. Leyens, U. Schulz, and W. A. Kaysser. EB-PVD thermal barrier coatings for aeroengines and gas turbines. *Advanced Engineering Materials*, 3(4):193–204, 2001.
- [2] T. Sourmail. Coatings for turbine blades. www.msm.cam.ac.uk/phase-trans/2003/Superalloys/coatings/index.html, (accessed on the 25 of July 2011), 2003.
- [3] M Cervenka. The Rolls-Royce trent engine. www.msm.cam.ac.uk/phase-trans/mphil/Trent1/sld001.htm, (accessed on the 9 of June 2011), 2000.
- [4] S. Bose. Substrate alloys. *High temperature coatings*, pp. 17-27, Elsevier Butterworth-Heinemann, USA, 2007.
- [5] H. J. T. Ellingham. Reducibility of oxides and sulfides in metallurgical processes. *Journal of the Society of Chemical Industry, London*, 63:125–133, 1944.
- [6] Cambridge University. Ellingham Diagrams. www.doitpoms.ac.uk/tlplib/ellingham-diagrams/index.php, (accessed on the 17 of August 2011), 2006.
- [7] S. Bose. Oxidation. *High temperature coatings*, pp. 29-52, Elsevier Butterworth-Heinemann, USA, 2007.
- [8] B. M. Warnes. Reactive element modified chemical vapor deposition low activity platinum aluminide coatings. *Surface and Coatings Technology*, 146-147:7–12, 2001.
- [9] R. Pichoir. Influence of the mode of formation on the oxidation and corrosion behaviour of the NiAl-type protective coatings. *Materials and coatings to resist*

- high temperature corrosion*, pp. 271-291, Eds. D. R. Holmes and A. Rahmel, Applied Science Publishers, London, 1978.
- [10] P. Nash, M. F. Singleton, and J. L. Murray. Aluminum-Nickel. *Phase diagrams of binary Nickel alloys*, pp. 3-11, Ed. P. Nash, ASM International, Materials Park, Ohio, 1991.
- [11] J. Angenete. Aluminide diffusion coatings for Ni based superalloys (PhD Thesis). Chalmers University of Technology, Goteborg University, Goteborg, Sweden, 2002.
- [12] V. K. Tolpygo and D. R. Clarke. Surface rumpling of a (Ni,Pt)Al bond coat induced by cyclic oxidation. *Acta Materialia*, 48(13):3283–3293, 2000.
- [13] B. Chapman. *Glow discharge processes*. John Wiley and Sons, USA, 1980.
- [14] M. Yashima, M. Kakihana, and M. Yoshimura. Metastable-stable phase diagrams in the zirconia-containing systems utilized in solid-oxide fuel cell application. *Solid State Ionics*, 86-88(2):1131–1149, 1996.
- [15] U. Schulz, C. Leyens, K. Fritscher, M. Peters, B. Saruhan-Brings, O. Lavigne, J. Dorvaux, R. Poulain, M. Mevrel, and M. Caliez. Some recent trends in research and technology of advanced thermal barrier coatings. *Aerospace Science and Technology*, 7:73–80, 2003.
- [16] C. R. Lima and J. M. Guilemany. Adhesion improvements of thermal barrier coatings with HVOF thermally sprayed bond coats. *Surface and Coatings Technology*, 201(8):4694–4701, 2007.
- [17] T. J. Lu, C. G. Levi, H. N. G. Wadley, and A. G. Evans. Distributed porosity as a control parameter for oxide thermal barriers made by physical vapor deposition. *Journal of the American Ceramic Society*, 84(12):2937–2946, 2001.
- [18] B. A. Movchan and A. V. Demchishin. Investigation of the structure and properties of thick vacuum-deposited films of nickel, titanium, tungsten, alumina and zirconium dioxide. *Fizika Metallov I Metallovedenie*, 28(4):653–660, 1969.
- [19] J. A. Thornton. Influence of apparatus geometry and deposition conditions on the structure and topography of thick sputtered coatings. *Journal of Vacuum Science and Technology*, 11(4):666–670, 1974.

-
- [20] W. A. Kaysser, M. Peters, K. Fritscher, and U. Schulz. Processing, characterisation and testing of EB-PVD thermal barrier coatings. *AGARD report 823*, pp. 9/1-9/11, 1998.
- [21] D. V. Rigney, R. Viguie, D. J. Wortman, and D. W. Skelly. PVD thermal barrier coating applications and process development for aircraft engines. *NASA Conf. Publ. 3312*, pp. 135-149, 1995.
- [22] C. A. Johnson, J. A. Ruud, R. Bruce, and D. Wortman. Relationships between residual stress, microstructure and mechanical properties of electron beam-physical vapor deposition thermal barrier coatings. *Surface and Coatings Technology*, 108-109(1-3):80-85, 1998.
- [23] S. Kramer, J. Yang, C. G. Levi, and C. A. Johnson. Thermochemical interaction of thermal barrier coatings with molten CaO-MgO-Al₂O₃-SiO₂ (CMAS) deposits. *Journal of the American Ceramic Society*, 89(10):3167-3175, 2006.
- [24] R. T. Wu, X. Wang, and A. Atkinson. On the interfacial degradation mechanisms of thermal barrier coating systems: effects of bond coat composition. *Acta Materialia*, 58:5578-5585, 2010.
- [25] P. Caron and Khan T. Evolution of Ni-based superalloys for single crystal gas turbine blade applications. *Aerospace Science and Technology*, 3(8):513-523, 1999.
- [26] N. Pickard. Efficient and environmentally friendly aero-engine (EEFAE) targeted research action. *Air and Space Europe*, 3(3-4):161-162, 2001.
- [27] Dossier. Europe's aeroengine community targets major environmental improvements. *Air and Space Europe*, 2(3):51, 2000.
- [28] T. E. Strangman. Thermal barrier coatings for turbine airfoils. *Thin Solid Films*, 127(1-2):93-105, 1985.
- [29] P. Morrell and D. S. Rickerby. Advantages/disadvantages of various TBC systems as perceived by the engine manufacturer. *AGARD report 823*, pp. 20/1-20/9, 1998.
- [30] M. Goulette. Materials technology for aero gas turbines. *World Aerospace technology International*, pages 74-78, 1995.

- [31] H. Ohnabe, S. Masaki, M. Onozuka, K. Miyahara, and T. Sasa. Potential application of ceramic matrix composites to aero-engines components. *Composites Part A*, 30(4):489–496, 1999.
- [32] H. K. D. H. Bhadeshia. Nickel based superalloys. www.msm.cam.ac.uk/phase-trans/2003/Superalloys/superalloys.html, (accessed on the 15 of June 2011), 2003.
- [33] M. Gell, D. N. Duhl, D. K. Gupta, and K. D. Sheffler. Advanced superalloy airfoils. *JOM*, 39(7):11–15, 1987.
- [34] G. L. Erickson. The development and application of CMSX-10. *Superalloys 1996*, pp. 35-44, Eds. R. D. Kissinger, D. J. Deye, D. L. Anton, A. D. Cetel, M. V. Nathal, T. M. Pollock and D. A. Woodford, The Minerals, Metals and Materials Society, USA, 1996.
- [35] A. Sato, Y. Koizumi, T. Kobayashi, T. Yokokawa, H. Harada, and H. Imai. TTT diagram for TCP phases precipitation of fourth generation Ni-base superalloys. *Journal of the Japan Institute of Metals*, 68(8):507–510, 2004.
- [36] P. Silvestroni. *Fondamenti Di Chimica- IX edition*. Masson S.p.A., Milano, 1992.
- [37] K. R. Lawless. The oxidation of metals. *Reports on Progress in Physics*, 37:231–316, 1974.
- [38] C. Wagner. Reaktionstypen bei der Oxydation von Legierungen. *Zeitschrift für Elektrochemie, Berichte der Bunsengesellschaft für physikalische Chemie*, 63:772–782, 1959.
- [39] J. L. Smialek and G. H. Meier. High temperature oxidation. *Superalloys II. High Temperature Materials for Aerospace and Industrial Power*, pp. 293-326, Eds. C. T. Sims, N. S. Stoloff and W. C. Hagel, Wiley-Interscience Publication, USA, 1987.
- [40] J. R. Nicholls. Designing oxidation-resistant coating. *JOM*, 52(1):28–35, 2000.
- [41] C. Sarioglu, M. J. Stiger, J. R. Blachere, R. Janakiraman, E. Schumann, A. Ashary, F. S. Pettit, and G. H. Meier. The adhesion of alumina films to metallic alloys and coatings. *Materials and Corrosion*, 51:358–372, 2000.

- [42] K. Kawagishi, H. Harada, A. Sato, A. Sato, and T. Kobayashi. The oxidation properties of fourth generation single-crystal Nickel-based superalloys. *JOM*, 58(1):43–46, 2006.
- [43] T. Izumi, N. Mu, L. Zhang, and B. Gleeson. Effects of targeted gamma-Ni+gamma'-Ni₃Al-based coating compositions on oxidation behaviour. *Surface and Coatings Technology*, 202(4-7):628–631, 2007.
- [44] U. Schulz, M. Menzebach, C. Leyens, and Y. Q. Yang. Influence of substrate material on oxidation behaviour and cyclic lifetime of EB-PVD TBC systems. *Surface and Coatings Technology*, 146-147:117–123, 2001.
- [45] S. Hayashi and B. Gleeson. Early stage oxidation behaviour of Pt modified gamma'-Ni₃Al based alloys with and without Hf addition. *Oxidation of Metals*, 71:5–19, 2009.
- [46] B. A. Pint. The role of chemical composition on the oxidation performance of aluminide coatings. *Surface and Coatings Technology*, 188-189:71–78, 2004.
- [47] J. A. Haynes, B. A. Lance, M. J. and Pint, and I. G. Wright. Characterization of commercial EB-PVD TBC systems with CVD (Ni,Pt)Al bond coatings. *Surface and Coatings Technology*, 146-147:140–146, 2001.
- [48] J. A. Haynes. Potential influences of bond coat impurities and void growth on premature failure of EB-PVD TBCs. *Scripta Materialia*, 44:1147–1152, 2001.
- [49] Y. Zhang, W. Y. Lee, J. A. Haynes, I. G. Wright, B. A. Pint, K. M. Cooley, and P. K. Liaw. Synthesis and cyclic oxidation behavior of a (Ni, Pt) Al coating on a desulfurized Ni-Base superalloy. *Metallurgical and Materials Transactions A*, 30A(10):2679–2687, 1999.
- [50] J. D. Kiely, T. Yeh, , and D. A. Bonnell. Evidence for the segregation of sulfur to Ni-alumina interfaces. *Surface Science*, 393(1-3):L126–L130, 1997.
- [51] L. Rivoaland, V. Maurice, P. Josso, M. P. Bacos, and P. Marcus. The effect of sulfur segregation on the adherence of the thermally-grown oxide on NiAl. I: Sulfur segregation on the metallic surface of NiAl(001) single-crystals and at NiAl(001)/Al₂O₃ interfaces. *Oxidation of Metals*, 60(1-2):137–157, 2003.

- [52] L. Rivoaland, V. Maurice, P. Josso, M. P. Bacos, and P. Marcus. The effect of sulfur segregation on the adherence of the thermally-grown oxide on NiAl. II: The oxidation behavior at 900C of standard, desulfurized or sulfur-doped NiAl(001) single-crystals. *Oxidation of Metals*, 60(1-2):159–178, 2003.
- [53] J. L. Smialek, D. T. Jayne, J. C. Schaeffer, and W. H. Murphy. Effects of hydrogen annealing, sulfur segregation and diffusion on the cyclic oxidation resistance of superalloys: a review. *Thin Solid Films*, 253(1-2):285–292, 1994.
- [54] S. Sarioglu, J. R. Blachere, F. S. Pettit, G. H. Meier, J. L. Smialek, and C. Mennicke. The effect of reactive element additions, sulfur removal, and specimen thickness on the oxidation behaviour of Alumina-forming Ni- and Fe-base alloys. *Materials Science Forum*, 251-254:405–412, 1997.
- [55] H. J. Grabke and H. J. Kurbatov, G. and Schmutzler. Segregation beneath oxide scales. *Oxidation of Metals*, 43(1-2):94–114, 1995.
- [56] J. G. Smeggil, A. W. Funkenbusch, and N. S. Bornstein. A relationship between indigenous impurity elements and protective oxide scale adherence characteristics. *Metallurgical Transactions A*, 17A:923–932, 1986.
- [57] J. R. Nicholls and M. J. Bennett. Cyclic oxidation - guidelines for test standardization, aimed at the assessment of service behaviour. *Materials at High Temperatures*, 17(3):413–428, 2000.
- [58] J. R. Vargas, N. E. Ulion, and J. A. Goebel. Advanced coating development for industrial/utility gas turbine engines. *Thin Solid Films*, 73(2):407–413, 1980.
- [59] J. R. Nicholls and P. Hancock. Advanced high temperature coatings for gas turbines. *Industrial Corrosion*, 5(4):8–17, 1987.
- [60] J. R. Nicholls, K.A. Long, and N. J. Simms. Diffusion coatings. *Shreir's Corrosion*, Vol. 4, pp. 2532-2555, Eds. T. Richardson, B. Cottis, M. Graham, R. Lindsay, S. Lyon, D. Scantlebury and H. Scott, Elsevier Science, 2010.
- [61] G.W. Goward. Progress in coatings for gas turbine airfoils. *Surface and Coatings Technology*, 108-109:73–79, 1998.

- [62] M. G. Hocking, V. Vasantasree, and P. S. Sidky. *Metallic and ceramic coatings: production, high temperature properties and applications*. Longman Scientific and Technical, Great Britain, 1989.
- [63] G. W. Goward and L. W. Cannon. Pack cementation coatings for superalloys: a review of history, theory and practice. *Journal of Engineering for Gas Turbines and Power*, 110:150–154, 1998.
- [64] R. Mevrel, C. Duret, and R. Pichoir. Pack cementation processes. *Material Science and Technology*, 2:201–206, 1986.
- [65] H. Omar, D. P. Papadopoulos, S. A. Tsipas, and H. Lefakis. Aluminizing nickel foam by a slurry coating process. *Materials Letters*, 63(16):1387–1389, 2009.
- [66] R. S. Parzuchowski. Gas phase deposition of Aluminum on Nickel alloys. *Thin Solid Films*, 45(2):349–355, 1977.
- [67] H. J. Lin, W. P. Sun, and M. H. Hon. Gas phase aluminide coatings on nickel-base superalloy IN713. *Thin Solid Films*, 156:259–264, 1988.
- [68] G. Gauge and R. Morbioli. Vapor phase aluminizing to protect turbine airfoils. *High Temperature Protective Coating*, pp. 13-26, Ed. S.C. Singhal, Metallurgical Society of AIME, Warrendale, PA, 1983.
- [69] A. Squillace, R. Bonetti, N. J. Archer, and J. A. Yeatman. The control of the composition and structure of aluminide layers formed by vapour aluminising. *Surface and Coatings Technology*, 120-121:118–123, 1999.
- [70] J. R. Nicholls and D. J. Stephenson. High temperature coatings for gas turbines. *Intermetallic compounds, principles and practice*, pp. 489-500, Eds. J. H. Westbrook and R. L. Fleisher, John Wiley and Sons, Chichester, UK, 1995.
- [71] R. Sivakumar and L. L. Seigle. On the kinetics of the pack-aluminization process. *Metallurgical Transactions A*, 7A:1073–1079, 1976.
- [72] D. C. Tu and L. L. Seigle. Kinetics of formation and microstructure of aluminide coatings on Ni-Cr alloys. *Thin Solid Films*, 95(1):47–56, 1982.
- [73] G. W. Goward and D. H. Boone. Mechanisms of formation of diffusion aluminide coatings on Nickel-base superalloys. *Oxidation of Metals*, 3(5):475–495, 1971.

- [74] J. M. Coulson and J. F. Richardson. Mass transfer. *Chemical Engineering-Fluid Flow, Heat Transfer and Mass Transfer- 6th edition*, Vol. 1, pp. 573-659, Butterworth-Heinemann, Oxford (UK), 1999.
- [75] A. L. Purvis and B. M. Warnes. The effects of platinum concentration on the oxidation resistance of superalloys coated with single-phase platinum aluminide. *Surface and Coatings Technology*, 146-147:1-6, 2001.
- [76] G. Lehnert and H. W. Meinhardt. A new protective coating for nickel alloys. *Electrodeposition and Surface Treatment*, 1(3):189-197, 1973.
- [77] G. R. Krishna, D. K. Das, V. Singh, and S. V. Joshi. Role of Pt content in the microstructural development and oxidation performance of Pt aluminide coatings produced using a high-activity aluminizing process. *Materials Science and Engineering A*, 251:40-47, 1998.
- [78] J. Benoist, K. F. Badawi, A. Malie, and C. Ramade. Microstructure of Pt modified aluminide coatings on Ni-based superalloys without prior Pt diffusion. *Surface and Coatings Technology*, 194:48-57, 2005.
- [79] J. Angenete and K. Stiller. A comparative study of two inward grown Pt-modified Al diffusion coatings on a single crystal Ni base superalloy. *Materials Science and Engineering A*, 316(1-2):182-194, 2001.
- [80] C. Guerre, R. Molins, and L. Remy. Study of the coating stability of a TBC system. *Materials at High Temperatures*, 17(2):197-203, 2000.
- [81] K. Bouhanek, O. A. Adesanya, F. H. Stott, P. Skeldon, D. G. Lees, and G. C. Wood. Isothermal and thermal cyclic oxidation behaviour of thermal barrier coatings: Pt aluminide bond coats. *Materials at High Temperatures*, 17(2):185-196, 2000.
- [82] J. Angenete and K. Stiller. Comparison of inward and outward grown Pt-modified aluminide diffusion coatings on a Ni based single crystal superalloy. *Surface and Coatings Technology*, 150(2-3):107-118, 2002.
- [83] J. H. Chen and J. A. Little. Degradation of the platinum aluminide coating on CMSX-4 at 1100C. *Surface and Coatings Technology*, 92(1-2):69-77, 1997.

-
- [84] Y. Zhang, J. A. Haynes, B. A. Pint, I. G. Wright, and W. Y. Lee. Martensitic transformation in CVD NiAl and (Ni,Pt)Al bond coatings. *Surface and Coatings Technology*, 163-164:19–24, 2003.
- [85] M. W. Chen, M. L. Glynn, R. T. Ott, T. C. Hufnagel, and K. J. Hemker. Characterization and modeling of a martensitic transformation in a platinum modified diffusion aluminide bond coat for thermal barrier coatings. *Acta Materialia*, 51:4279–4294, 2003.
- [86] M. W. Chen, K. J. T. Livi, P. K. Wright, and K. J. Hemker. Microstructural characterization of a Platinum-modified diffusion aluminide bond coat for thermal barrier coatings. *Metallurgical and Materials Transactions A*, 34A(10):2289–2299, 2003.
- [87] M. W. Chen, R. T. Ott, T. C. Hufnagel, P. K. Wright, and K. J. Hemker. Microstructural evolution of platinum modified nickel aluminide bond coat during thermal cycling. *Surface and Coatings Technology*, 163-164:25–30, 2003.
- [88] D. R. Mumm, A. G. Evans, and I. T. Spitsberg. Characterization of a cyclic displacement instability for a thermally grown oxide in a thermal barrier system. *Acta Materialia*, 49(12):2329–2340, 2001.
- [89] R. Panat, S. Zhang, and K. J. Hsia. Bond coat surface rumpling in thermal barrier coatings. *Acta Materialia*, 51(1):239–249, 2003.
- [90] D. S. Rickerby and R. G. Wing. Thermal barrier coating for a superalloy article and a method of application thereof. United States Patent: US5942337, 24 August 1999.
- [91] D. S. Rickerby, S. R. Bell, and R. G. Wing. Article including thermal barrier coated superalloy substrate. United States Patent: US5981091, 9 Nov. 1999.
- [92] J. R. Nicholls. Advances in coating design for high-performance gas turbines. *MRS Bulletin*, 28(9):659–670, 2003.
- [93] B. Gleeson, W. Wang, S. Hayashi, and D. Sordelet. Effects of Platinum on the interdiffusion and oxidation behavior of Ni-Al-based alloys. *Materials Science Forum*, 461-464:213–222, 2004.

- [94] O. A. Adesanya, K. Bouhanek, F. H. Scott, P. Skeldon, D. G. Lees, and G. C. Wood. Cyclic oxidation of two bond coats in thermal barrier coating systems on CMSX-4 substrates. *Materials Science Forum*, 369-372:639–646, 2001.
- [95] S. Hayashi, T. Narita, and B. Gleeson. Early-stage oxidation behavior of gamma'-Ni₃Al-based alloys with and without Pt addition. *Materials Science Forum*, 522-523:229–238, 2006.
- [96] F. Qin, J. W. Andereg, C. J. Jenks, B. Gleeson, D. J. Sordelet, and P. A. Thiel. The effect of Pt on Ni₃Al surface oxidation at low-pressures. *Surface Science*, 601(1):146–154, 2007.
- [97] N. Mu, T. Izumi, L. Zhang, and B. Gleeson. Compositional factors affecting the oxidation behavior of Pt-modified gamma-Ni+gamma'-Ni₃Al-based alloys and coatings. *Materials Science Forum*, 595-598(1):239–247, 2008.
- [98] T. Izumi and B. Gleeson. Oxidation behaviour of Pt + Hf-modified gamma-Ni+gamma'-Ni₃Al alloys. *Materials Science Forum*, 522-523:221–228, 2006.
- [99] C. Jiang, D. J. Sordelet, and B. Gleeson. Site preference of ternary alloying elements in Ni₃Al: A first-principles study. *Acta Materialia*, 54(4):1147–1154, 2006.
- [100] E. Copland. Partial thermodynamic properties of gamma'-(Ni,Pt)₃Al in the Ni-Al-Pt system. *Journal of Phase Equilibria and Diffusion*, 28(1):38–48, 2007.
- [101] S. Bose. Oxidation- and corrosion- resistant coatings. *High temperature coatings*, pp. 71-154, Elsevier Butterworth-Heinemann, USA, 2007.
- [102] X. Zhao and P. Xiao. Effect of platinum on the durability of thermal barrier systems with a gamma+gamma' bond coat. *Thin Solid Films*, 517(828-834), 2008.
- [103] M. G. Hocking, V. Vasantasree, and P. S. Sidky. Physical vapour deposition (PVD). *Metallic and ceramic coatings: production, high temperature properties and applications*, pp. 49-102, Longman Scientific and Technical, UK, 1989.
- [104] R. F. Bunshah. Evaporation: processes, bulk microstructures and mechanical properties. *Handbook of Deposition Technologies for Films and Coatings - Sci-*

- ence, *Technology and Applications- 2nd edition*, pp. 157-206, Ed. R. F. Bunshah, William Andrew Publishing/Noyes, 1994.
- [105] D. M. Mattox. Physical vapor deposition (PVD) process. *Metal Finishing*, 100(1A):394–408, 2002.
- [106] R. F. Bunshah. Deposition Technologies: An Overview. *Handbook of Deposition Technologies for Films and Coatings - Science, Technology and Applications- 2nd edition*, pp. 27-54, Ed. R. F. Bunshah, William Andrew Publishing/Noyes, 1994.
- [107] J. A. Thornton and J. E. Greene. Sputter Deposition Processes. *Handbook of Deposition Technologies for Films and Coatings - Science, Technology and Applications-2nd edition*, pp. 275-345, Ed. R. F. Bunshah, William Andrew Publishing/Noyes, 1994.
- [108] F. Cernuschi, P. Bianchi, M. Leoni, and P. Scardi. Thermal diffusivity/microstructure relationship in YPSZ thermal barrier coating. *Journal of Thermal Spray Technology*, 8(1):102–109, 1999.
- [109] K. E. Wilkes and J. F. Lagedrost. Thermophysical properties of plasma sprayed coatings. *NASA CR-121144*, 1973.
- [110] L. W. Sink, G. S. Hoppin, and M. Fujii. Low-cost directionally solidified turbine blades. *NASA CR-159464*, 1979.
- [111] Y. Du, Z. Jin, and P. Huang. Thermodynamic assessment of the ZrO₂-YO_{1.5} system. *Journal of the American Ceramic Society*, 74(7):1569–1577, 1991.
- [112] M. H. Bocanegra-Bernal and S. Diaz De La Torre. Phase transitions in zirconium dioxide and related materials for high performance engineering ceramics. *Journal of Material Science*, 37(23):4947–4971, 2002.
- [113] R. C. Garvie, R. H. Hannink, and R. T. Pascoe. Ceramic steel? *Nature*, 258(5537):703–704, 1975.
- [114] P. Kountouros and G. Petzow. Defect chemistry, phase stability and properties of Zirconia polycrystals. *Science and Technology of Zirconia V*, pp. 30-48, Eds. S. P. S Badwal, M.J. Bannister and R. H. J. Hannink, Technomic Publishing, 1993.

- [115] R. Taylor, J. R. Brandon, and P. Morrell. Microstructure, composition and property relationships of plasmasprayed thermal barrier coatings. *Surface and Coatings Technology*, 50(2):141–149, 1992.
- [116] U. Schulz, B. Saruhan, K. Fritscher, and C. Leyens. Review on advanced EB-PVD ceramic topcoats for TBC applications. *International Journal of Applied Ceramic Technology*, 1(4):302–315, 2004.
- [117] A. Azzopardi, R. Mevrel, B. Saint-Ramond, E. Olson, and K. Stiller. Influence of aging on structure and thermal conductivity of Y-PSZ and Y-FSZ EB-PVD coatings. *Surface and Coatings Technology*, 177-178:131–139, 2004.
- [118] R. A. Miller. Current status of thermal barrier coatings: An overview. *Surface and Coatings Technology*, 30(1):1–11, 1987.
- [119] R. A. Miller. Thermal barrier coatings for aircraft engines: History and directions. *Journal of Thermal Spray Technology*, 6(1):35–42, 1997.
- [120] S. Stecura. Optimization of the NiCrAl-Y/ZrO₂-Y₂O₃ thermal barrier system. *NASA/TM-86905*, 1985.
- [121] U. Schulz, K. Fritscher, C. Leyens, M. Peters, and W. A. Kaysser. The thermocyclic behavior of differently stabilized and structured EB-PVD TBCs. *JOM-e*, 49(10), Available at <http://www.tms.org/pubs/journals/JOM/9710/Schulz/Schulz-9710.html>, 1997.
- [122] J. R. Brandon and R. Taylor. Phase stability of zirconia-based thermal barrier coatings Part I. Zirconia-Yttria alloys. *Surface and Coatings Technology*, 46(1):75–90, 1991.
- [123] V. Lughì and D.R. Tolpygo, V. K. and Clarke. Microstructural aspects of the sintering of thermal barrier coatings. *Materials Science and Engineering A*, 368(1-2):212–221, 2004.
- [124] U. Schulz. Phase transformation in EB-PVD yttria partially stabilized zirconia thermal barrier coatings during annealing. *Journal of the American Ceramic Society*, 83(4):904–910, 2000.
- [125] H. Herbert. Plasma-sprayed coatings. *Scientific American*, 259(3):112–117, 1988.

-
- [126] P. Chagnon and P. Fauchais. Thermal spraying of ceramics. *Ceramics International*, 10(4):119–131, 1984.
- [127] J. Singh, D. E. Wolfe, and J. Singh. Architecture of thermal barrier coatings produced by electron beam-physical vapor deposition (EB-PVD). *Journal of Materials Science*, 37(11):3261–3267, 2002.
- [128] H. E. Evans. Oxidation failure of TBC systems: An assessment of mechanisms. *Surface and Coatings Technology*, 206(7):1512–1521, 2011.
- [129] B. A. Movchan. EB-PVD technology in the gas turbine industry: present and future. *JOM*, 48(11):40–45, 1996.
- [130] U. Schulz and M. Schmucker. Microstructure of ZrO₂ thermal barrier coatings applied by EB-PVD. *Materials Science and Engineering A*, 276(1-2):1–8, 2000.
- [131] B. D. Kernan, A. He, and A. H. Heuer. Microstructural evolution and microhardness in Zirconia-based EB-PVD thermal barrier coatings. *Journal of the American Ceramic Society*, 86(6):959–968, 2003.
- [132] F. H. Stott and G. C. Wood. Growth and adhesion of oxide scales on Al₂O₃-forming alloys and coatings. *Materials Science and Engineering A*, 87:267–274, 1987.
- [133] F. C. Toriz, A. B. Thakker, and S. K. Gupta. Flight service evaluation of thermal barrier coatings by physical vapor deposition at 5200H. *Surface and Coatings Technology*, 39-40:161–172, 1989.
- [134] R. M. Watt, J. L. Allen, N. C. Baines, J. P. Simons, and M. George. A study of the effects of thermal barrier coating surface roughness on the boundary layer characteristics of gas turbine aerofoils. *Journal of Turbomachinery*, 110(1):88–93, 1998.
- [135] J. R. Nicholls, M. J. Deakin, and D. S. Rickerby. A comparison between the erosion behaviour of thermal spray and electron beam physical vapour deposition thermal barrier coatings. *Wear*, 233-235:352–361, 1999.
- [136] X. Chen, M. Y. He, I. T. Spitsberg, N. A. Fleck, J. W. Hutchinson, and A. G. Evans. Mechanisms governing the high temperature erosion of thermal barrier coatings. *Wear*, 256(7-8):735–746, 2004.

- [137] X. Chen, R. Wang, N. Yao, A. G. Evans, J. W. Hutchinson, and R. W. Bruce. Foreign object damage in a thermal barrier system: mechanisms and simulations. *Materials Science and Engineering A*, 352(1-2):221–231, 2003.
- [138] R. G. Wellman and C. Allen. The effects of angle of impact and material properties on the erosion rates of ceramics. *Wear*, 186-187(1):117–122, 1995.
- [139] R. G. Wellman, Deakin M.J., and J. R. Nicholls. The effect of TBC morphology on the erosion rate of EB PVD TBCs. *Wear*, 258(1-4):349–356, 2005.
- [140] X. Chen. Calcium-magnesium-alumina-silicate (CMAS) delamination mechanisms in EB-PVD thermal barrier coatings. *Surface and Coatings Technology*, 200(11):3418–3427, 2006.
- [141] C. Mercer, S. Faulhaber, A. G. Evans, and R. Darolia. A delamination mechanism for thermal barrier coatings subject to calcium-magnesium-alumino-silicate, CMAS, infiltration. *Acta Materialia*, 53(4):1029–1039, 2005.
- [142] H. J. Grabke. Oxidation of aluminides. *Materials Science Forum*, 251-254(1):149–161, 1997.
- [143] J. Doychak, J. L. Smialek, and T. E. Mitchell. Transient oxidation of single crystal beta-NiAl. *Metallurgical Transactions*, 20A:499–518, 1989.
- [144] K. M. N. Prasanna, A. S. Khanna, R. Chandra, and W. J. Quadackers. Effect of delta-alumina formation on the growth kinetics of alumina-forming superalloys. *Oxidation of Metals*, 43(5-6):465–480, 1996.
- [145] F. H. Stott. The oxidation of Alumina-forming alloys. *Materials Science Forum*, 251-254:19–32, 1997.
- [146] C. Leyens, U. Schulz, B. A. Pint, and I. G Wright. Influence of electron beam physical vapor deposited thermal barrier coating microstructure on thermal barrier coating system performance under cyclic oxidation conditions. *Surface and Coatings Technology*, 120-121:68–76, 1999.
- [147] P. K. Wright and A. G. Evans. Mechanisms governing the performance of thermal barrier coatings. *Current Opinion in Solid State and Materials Science*, 4(3):255–265, 1999.

-
- [148] Y. H. Sohn, K. Vaidyanathan, M. Ronski, E. H. Jordan, and M. Gell. Thermal cycling of EB-PVD/MCrAlY thermal barrier coatings: II. Evolution of photo-stimulated luminescence. *Surface and Coatings Technology*, 146-147:102–109, 2001.
- [149] R. J. Christensen, D. M. Lipkin, and D. R. Clarke. The stress and spalling behavior of the oxide scale formed on polycrystalline Ni3Al. *Acta Materialia*, 44(9):3813–3821, 1996.
- [150] R. M. Cannon and P. Y. Hou. Diffusion induced stress generation during oxidation. *High Temperature Corrosion and Materials Chemistry*, Eds. P. Y. Hou, M. McNallan, R. Oltre, E. S. Opila and D. A. Shorer, The Electrochemical Society Inc., New Jersey, 1998.
- [151] S. Bose. Thermal barrier coatings (TBCs). *High temperature coatings*, pp. 155-232, Elsevier Butterworth-Heinemann, USA, 2007.
- [152] D. W. Jordan and K. T. Faber. X-ray residual stress analysis of a ceramic thermal barrier coating undergoing thermal cycling. *Thin Solid Films*, 235(1-2):137–141, 1993.
- [153] D. Kececioglu. *Reliability Engineering Handbook*. vol.1, Prentice Hall, Inc., Englewood Cliffs, New Jersey, 1991.
- [154] ReliaSoft Corporation. Life data analysis (Weibull analysis). *Life Data Analysis Online Reference*, www.weibull.com/basics/lifedata.htm, (accessed on the 11 of December 2011).
- [155] ReliaSoft Corporation. What is accelerated life testing? *Accelerated Life Testing Online Reference*, www.weibull.com/AccelTestWeb/what is accelerated life testing.htm, (accessed on the 11 of December 2011).
- [156] ReliaSoft Corporation. Types of accelerated tests. *Accelerated Life Testing Online Reference*, www.weibull.com/AccelTestWeb/types of accelerated tests.htm, (accessed on the 11 of December 2011).
- [157] ReliaSoft Corporation. The probability density and cumulative distribution functions. *Life Data Analysis Online Reference*, www.weibull.com/LifeDataWeb/the

- probability density and cumulative distribution functions.htm, (accessed on the 11 of December 2011).
- [158] W. Weibull. A statistical distribution function of wide applicability. *ASME Journal of Applied Mechanics*, (293-297), 1951.
- [159] R. B. Abernethy. *The New Weibull Handbook*. R. B. Abernethy, USA, 2007.
- [160] ReliaSoft Corporation. The Weibull distribution. *Life Data Analysis Online Reference*, www.weibull.com/LifeDataWeb/lifedataweb.htm, (accessed on the 11 of December 2011).
- [161] ReliaSoft Corporation. The exponential distribution. *Life Data Analysis Online Reference*, [www.weibull.com/LifeDataWeb/the exponential distribution.htm](http://www.weibull.com/LifeDataWeb/the%20exponential%20distribution.htm), (accessed on the 11 of December 2011).
- [162] ReliaSoft Corporation. The normal distribution. *Life Data Analysis Online Reference*, [www.weibull.com/LifeDataWeb/the normal distribution.htm](http://www.weibull.com/LifeDataWeb/the%20normal%20distribution.htm), (accessed on the 11 of December 2011).
- [163] ReliaSoft Corporation. Statistical background. *Life Data Analysis Online Reference*, www.weibull.com/LifeDataWeb/lifedataweb.htm, (accessed on the 11 of December 2011).
- [164] R. B. Abernethy. Maximum likelihood estimates and other alternative methods. *The New Weibull Handbook*, pp. 83-98, R. B. Abernethy, USA, 2007.
- [165] L.G. Johnson. Median ranks of sample values in their populations with an application to certain fatigue studies. *Industrial Mathematics*, Vol. 2, pp. 1-9, 1951.
- [166] R. B. Abernethy. Dirty data, bad Weibulls, and uncertainties. *The New Weibull Handbook*, pp. 31-48, R. B. Abernethy, USA, 2007.
- [167] W. Dorner. Using Microsoft Excel for Weibull analysis. www.qualitydigest.com/jan99/html/weibull.html, (accessed on the 27 February 2009), 1999.
- [168] ReliaSoft Corporation. The lognormal distribution. *Life Data Analysis Online Reference*, www.weibull.com/LifeDataWeb/lifedataweb.htm, (accessed on the 11 of December 2011).

- [169] J. E. Greene. Nucleation, film growth, and microstructural evolution. *Handbook of Deposition Technologies for Films and Coatings - Science, Technology and Applications- 2nd edition*, pp. 707-765, Ed. R. F. Bunshah, William Andrew Publishing/Noyes, 1994.
- [170] J. R. Nicholls, L. Chirivi, and K. Long. Life prediction of high temperature thermal barrier coatings. ISHOC-10, 8-11 November 2010, Zushi, Japan, 2010.
- [171] Y. Jaslier and S. Alperine. Electron beam physical vapour deposition thermal barrier coatings a comparative evaluation of competing deposition technologies. *AGARD report 823*, pp. 8/1-8/10, 1998.
- [172] X. Zhao, I. P. Shapiro, and P. Xiao. Spinel formation in thermal barrier systems with a Pt-enriched γ -Ni + γ' -Ni₃Al bond coat. *Surface and Coatings Technology*, 202(13):2905–2916, 2008.
- [173] M. Gell, E. Jordan, K. Vaidyanathan, K. McCarron, B. Barber, Y. H. Sohn, and V. K. Tolpygo. Bond strength, bond stress and spallation mechanisms of thermal barrier coatings. *Surface and Coatings Technology*, 120-121:53–60, 1999.
- [174] I. T. Spitsberg, D. R. Mumm, and A. G. Evans. On the failure mechanisms of thermal barrier coatings with diffusion aluminide bond coatings. *Materials Science and Engineering A*, 394(1-2):176–191, 2005.
- [175] V. K. Tolpygo and D. R. Clarke. The effect of oxidation pre-treatment on the cyclic life of EB-PVD thermal barrier coatings with platinum-aluminide bond coats. *Surface and Coatings Technology*, 200:1276–1281, 2005.
- [176] G. M. Kim, N. M. Yanar, F. S. Hewitt, E. N. and Pettit, and G. H. Meier. The effect of the type of thermal exposure on the durability of thermal barrier coatings. *Scripta Materialia*, 46(489-495), 2002.
- [177] Y. Zhang, J. A. Haynes, W. Y. Lee, I. G. Wright, B. A. Pint, K. M. Cooley, and P. K. Liaw. Effects of Pt incorporation on the isothermal oxidation behavior of chemical vapor deposition aluminide coatings. *Metallurgical and Materials Transactions A*, 32A(7):1727–1741, 2001.
- [178] D. H. Boone, D. A. Crane, and D. P. Whittle. The structure and interdiffusional degradation of aluminide coatings on oxide-dispersion-strengthened alloys. *Thin Solid Films*, 84(1):39–47, 1981.

- [179] V. K Tolpygo. Development of internal cavities in platinum-aluminide coatings during cyclic oxidation. *Surface and Coatings Technology*, 202(617-622), 2007.
- [180] K. Long. Unpublished work. Cranfield University.
- [181] A. Vande Put, D. Oquab, J.R. Nicholls, and D. Monceau. Hf addition by sputtering in NiPtAl bond coating for TBC systems and its effect on thermal cycling behaviour. 2009 TMS Annual Meeting and Exhibition, Collected Proceedings.
- [182] S. Gray. Unpublished work. Cranfield University.

Appendix A

Substrate surface assessment of polished/grit blasted specimens before Pt deposition

Figure 17.1 shows the R_q value for each sample before Pt: Figure 17.2 shows the τ

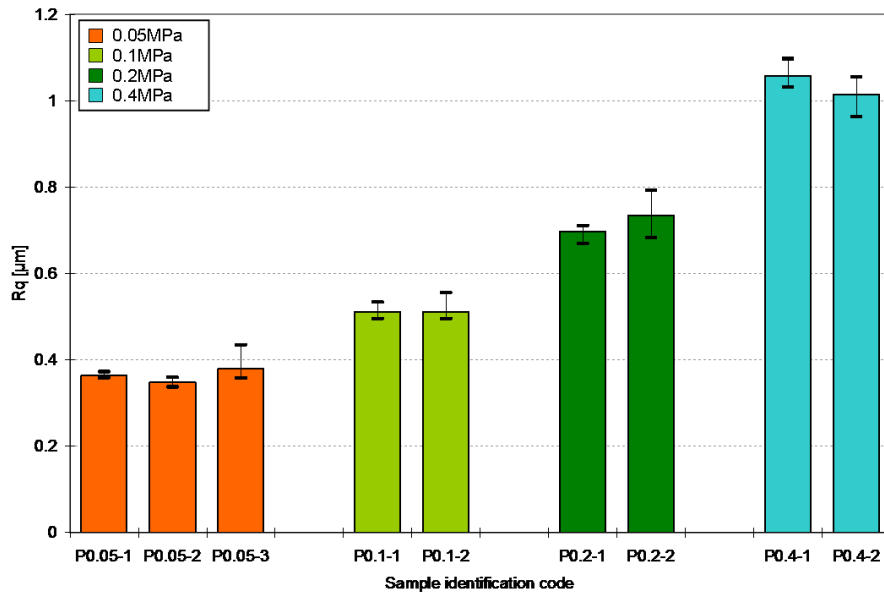


Figure 17.1: Root mean square roughness (R_q) value of the polished plus grit blasted samples before Pt deposition: each column corresponds to one sample and plots the average, minimum and maximum R_q value

value for each sample before Pt:

Figure 17.3 shows the Rlq value for each sample before Pt:

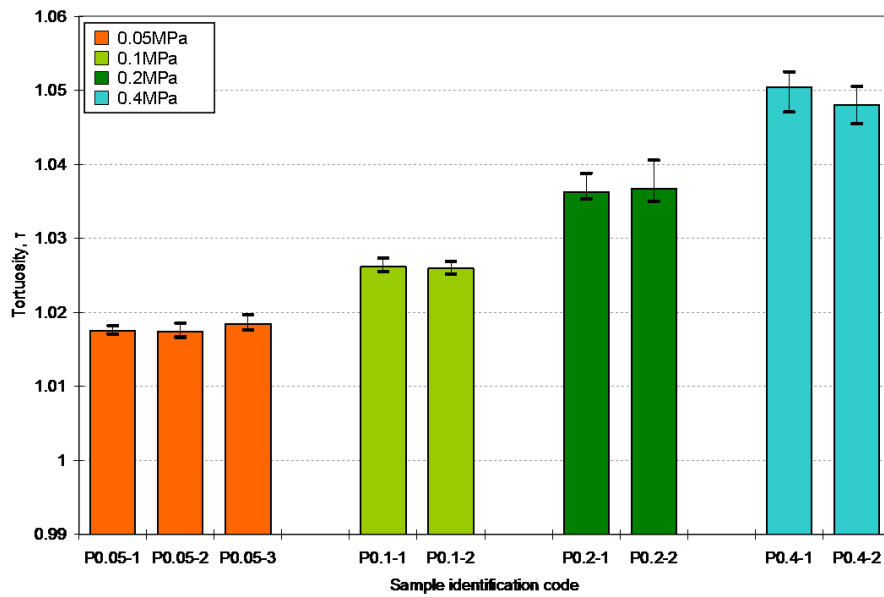


Figure 17.2: Tortuosity (τ) value of the polished plus grit blasted samples before Pt deposition: each column corresponds to one sample and plots the average, minimum and maximum τ value.

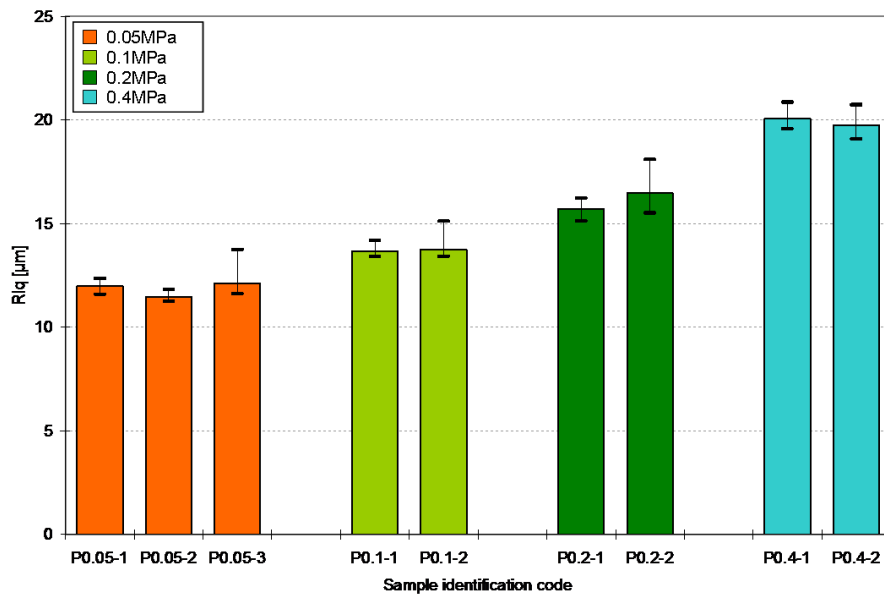


Figure 17.3: Root mean square average wavelength (Rlq) value of the polished plus grit blasted samples before Pt deposition: each column corresponds to one sample and plots the average, minimum and maximum (Rlq) value.

Appendix B

Surface assessment of bond coat on polished/grit blasted specimens

Figure 17.4 shows the R_q value for each sample after Pt diffusion:

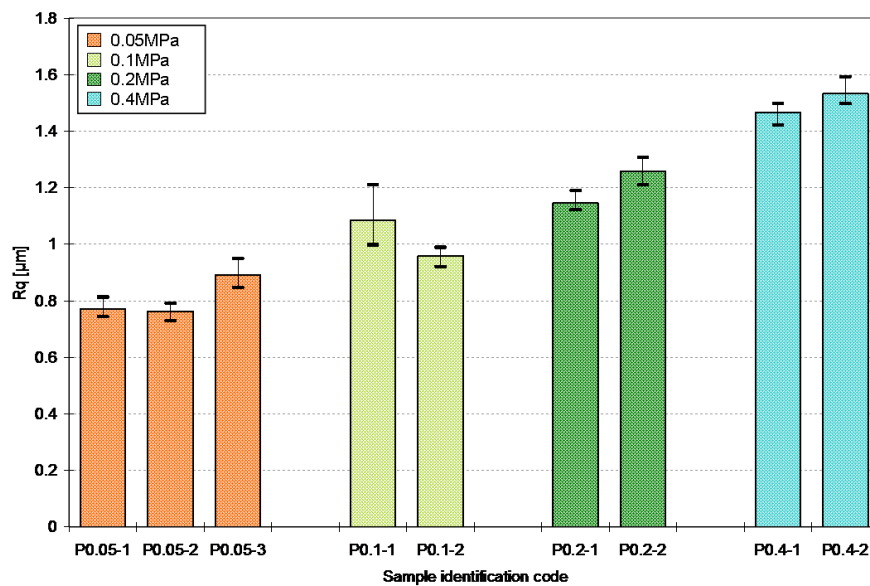


Figure 17.4: Root mean square roughness (R_q) value of the polished plus grit blasted samples after Pt diffusion: each column corresponds to one sample and plots the average, minimum and maximum R_q value

Figure 17.5 shows the τ value for each sample after Pt diffusion:

Figure 17.6 shows the Rlq value for each sample after Pt diffusion:

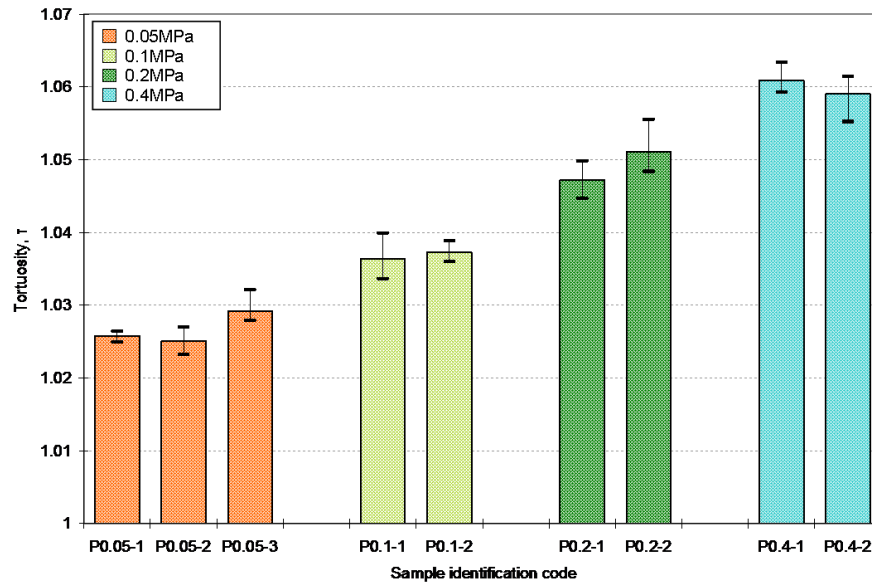


Figure 17.5: Tortuosity (τ) value of the polished plus grit blasted samples after Pt diffusion: each column corresponds to one sample and plots the average, minimum and maximum τ value.

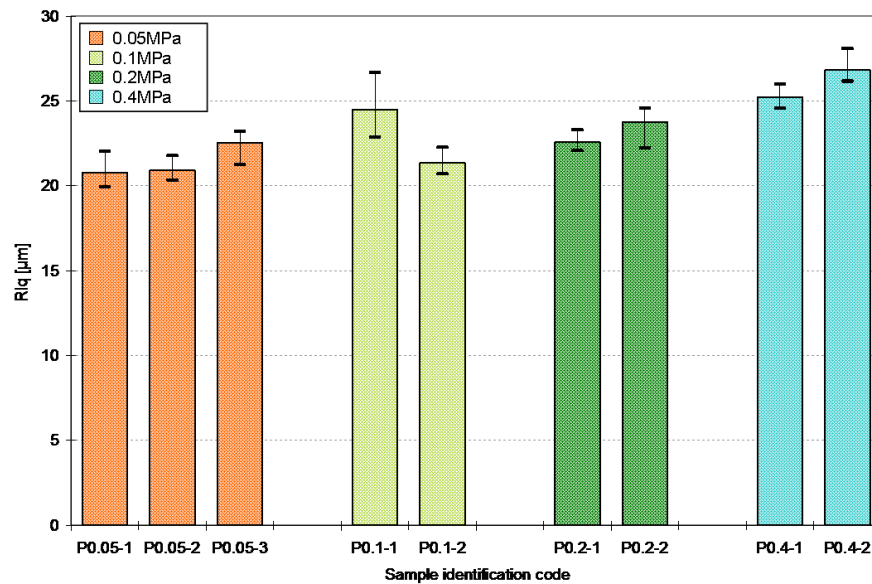


Figure 17.6: Root mean square average wavelength (Rlq) value of the polished plus grit blasted samples after Pt diffusion: each column corresponds to one sample and plots the average, minimum and maximum (Rlq) value.

Appendix C

Correlation between substrate roughness parameters and TBC lifetime: grit blasted samples

Figure 17.7 and figure 17.8 show the variation of the TBC systems lifetime as a function of the R_q and tortuosity of the surface before Pt deposition, for three different ceramic deposition temperatures.

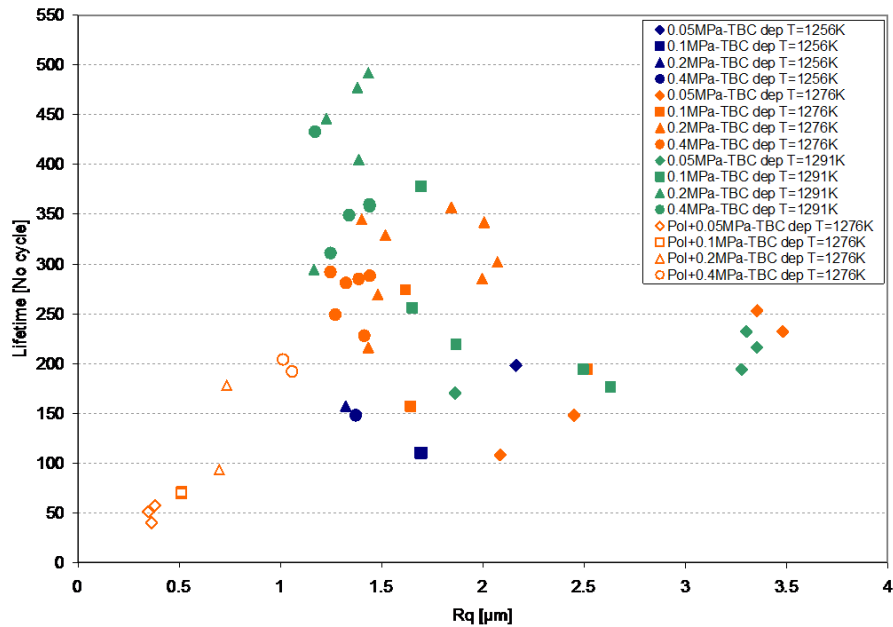


Figure 17.7: Variation of the TBC system lifetime as a function of the substrate surface R_q , for three different TBC deposition temperatures

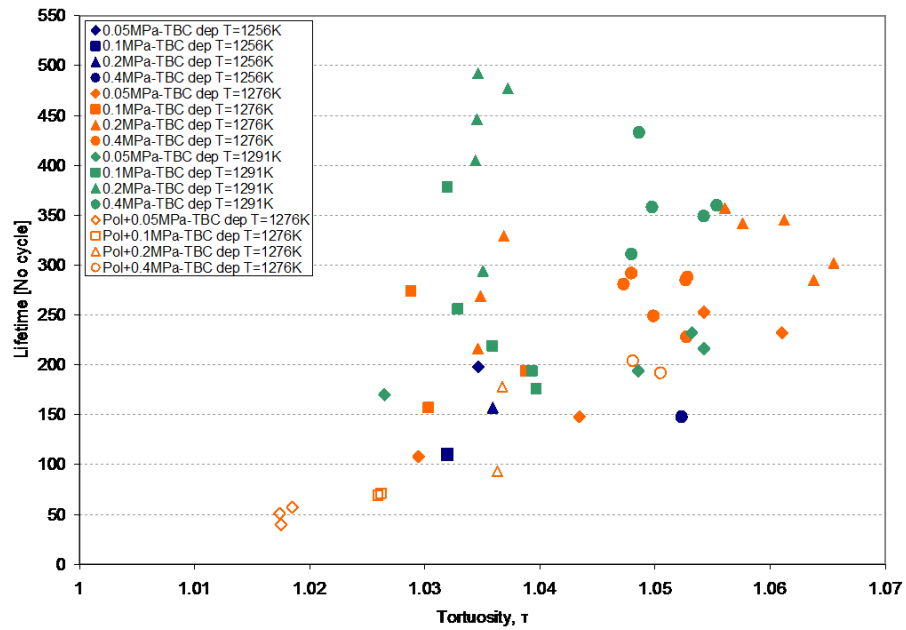


Figure 17.8: Variation of the TBC system lifetime as a function of the substrate surface τ , for three different TBC deposition temperatures

Appendix D

Correlation between substrate roughness parameters and TBC lifetime: ground samples

Figure 17.9 and figure 17.10 show the variation of the TBC systems lifetime as a function of the R_q and tortuosity of the surface before Pt deposition. For all specimens the ceramic deposition temperature was 1276K.

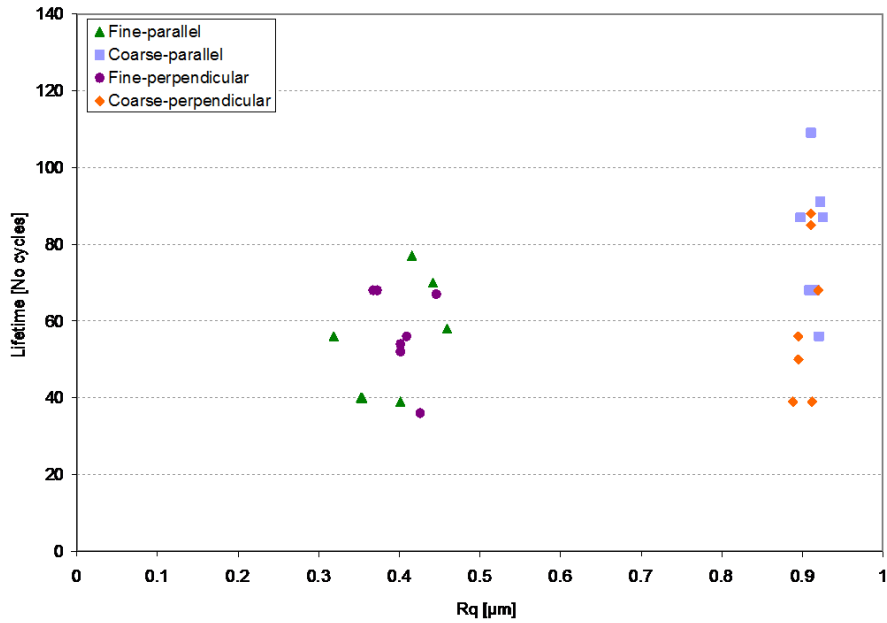


Figure 17.9: Variation of the TBC system lifetime as a function of the substrate surface R_q .

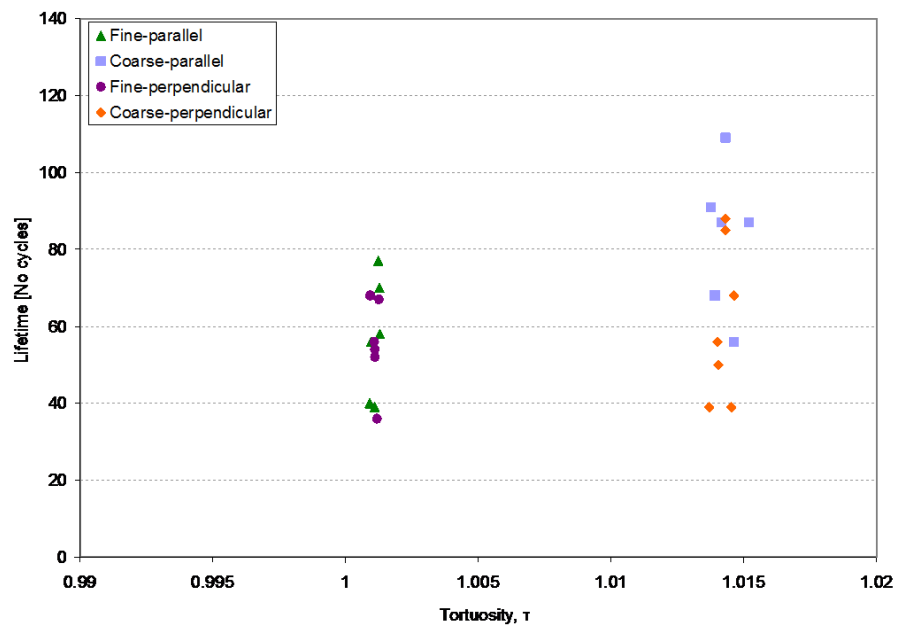


Figure 17.10: Variation of the TBC system lifetime as a function of the substrate surface τ .